Adsorption and Ion Exchange with Synthetic Zeolites

Adsorption and Ion Exchange with Synthetic Zeolites

Principles and Practice

William H. Flank, EDITOR

Union Carbide Corporation

Based on a symposium

sponsored by the Division of

Industrial and Engineering

Chemistry at the

180th Meeting of the

American Chemical Society,

San Francisco, California,

August 25–26, 1980.

ACS SYMPOSIUM SERIES **135**

ACS Symposium Series

M. Joan Comstock, *Series Editor*

FOREWORD

The ACS Symposium Series was founded in 1974 to provide
a medium for publishing symposia quickly in book form. The
format of the Series parallels that of the continuing Advances
in Chemistry Series except that in order to save time the
papers are not typeset but are reproduced as they are sub-
mitted by the authors in camera-ready form. Papers are re-
viewed under the supervision of the Editors with the assistance
of the Series Advisory Board and are selected to maintain the
integrity of the symposia; however, verbatim reproductions of
previously published papers are not accepted. Both reviews
and reports of research are acceptable since symposia may
embrace both types of presentation.

PREFACE

It has been more than a quarter of a century since synthetic molecular sieve zeolites first became a commercial reality. The magnitude and importance of this new technology, as is often the case, initially grew at a modest pace by absolute standards. This growth rate exploded almost 20 years go, however, with the widespread application of these materials in petroleum cracking catalysts. Another sharp increase occurred about 10 years ago with the development of relatively sophisticated adsorptive processes for drying and purification in the petrochemical and natural gas industries. And now, in recent years, we have seen the emergence of large-scale uses for synthetic zeolites as ion exchangers, and the development of complex high-technology systems employing these porous crystals in bulk separations of commodity-type liquids and gases.

The number of publications dealing with zeolites has grown similarly by leaps and bounds. A very rough estimation of the number of issued U.S. patents in which zeolites and their uses are disclosed rose from more than 2000 at the end of 1972 to over 5500 by the end of 1979. A similar approximation of the number of technical papers shows a rise from more than 7000 in 1972 to about 25,000 by 1980.

Although a number of books now contain chapters or sections dealing with zeolites, this subject has been the primary focus in very few volumes. The most noteworthy of these is the treatise by D. W. Breck, *Zeolite Molecular Sieves,* published by Wiley in 1974. The earliest modern ones are the Russian texts on *Molecular Sieves and Their Use,* published by V. A. Sokolov, N. S. Torocheshnikov, and N. V. Kel'tsev in 1964, and S. P. Zhdanov's *Chemistry of Zeolites* in 1968. Other significant works include the 1976 ACS Monograph on *Zeolite Chemistry and Catalysis* edited by J. A. Rabo, and the volume on *Zeolites and Clay Minerals as Sorbents and Molecular Sieves* by R. M. Barrer, published in England in 1978.

A number of conferences have now been held whose focus has been molecular sieve zeolites. The International Zeolite Association will have held the Fifth International Conference on Zeolites in Naples in June, 1980. The first such conference was organized by R. M. Barrer in London in 1967, and was followed by others in Worcester, Massachusetts in 1970, Zurich in 1973, and Chicago in 1977. Preceding these were the All-Union Conferences held in the USSR in 1961 and 1964; other European conferences have included the First All-Union Conference · on Molecular Sieves in Catalysis held in Novosibirsk in 1976, the Symposium on Zeolites held in Szeged, Hungary in 1978, and the Symposium on Catalysis by

ix

Zeolites to be held in Lyon in September, 1980. Also, a conference on natural zeolites was held in Tuscon, Arizona in 1976. Sessions on zeolites have become a regular feature at large technical meetings like those of the ACS and AIChE, and at smaller specialized ones like those of the Catalysis Society, the Clay Minerals Society, and the Gordon Conferences.

While zeolite catalysis represents the largest application area for molecular sieve zeolites to date, and has been addressed separately in several recent symposia and books, adsorption and ion exchange with zeolites, the other major fields of application, have not been so treated. They have been considered either in conjunction with catalytic aspects, or as subsets of unit operations or materials used therein. As the number and size of applications for zeolites in these noncatalytic areas prepare to take a great leap forward, this is an appropriate time to gather together current work dealing with the principles and practice relating to adsorption and ion exchange applications of synthetic zeolites, and to consider them in some kind of perspective before specialized fragmentation renders such an attempt too overwhelming to contemplate.

This, then, is the rationale behind the organization of this symposium. Among the principles addressed are those involving single and multicomponent adsorption modeling, mass transfer and surface diffusion in packed beds, and competitive sorption effects. A number of basic phenomena in adsorption and ion exchange are examined and discussed, including structural stability considerations, oxygen adsorption and energy transfer in copper-exchanged zeolite Y, and ion exchange behavior in zeolites A and Y. Applications include both simple and complex pressure-swing adsorption processes for bulk separations, recent advances in purification and drying, and selective separations of various types of adsorbates with some of the newer zeolites possessing high silica to alumina ratios in their framework composition. The sophistication and innovation evident in some of this work (e.g., the 1979 Kirkpatrick honors award-winning Polybed hydrogen separation process and the applications of high-silica zeolites) are indicative of the continuing growth and broad applicability of zeolites in an increasing number of fields.

Thanks are due to several of my colleagues, particularly R. A. Anderson, D. W. Breck, M. N. Y. Lee, and J. D. Sherman, for helpful suggestions and discussions in the organization of this symposium. The encouragement of the program committee of the Industrial and Engineering Chemistry Division of the ACS also is acknowledged. Finally, I want particularly to thank the reviewers, who contributed their valuable time and effort to the advancement of zeolite science and technology.

Molecular Sieve Department   WILLIAM H. FLANK
Union Carbide Corporation
Tarrytown, NY
April, 1980

The Solution Theory Modeling of Gas Adsorption on Zeolites

ARTHUR W. WOLTMAN[1] and WILLIAM H. HARTWIG

The University of Texas at Austin, Austin, TX 78712

The adsorption of gas molecules on the interior surfaces of zeolite voids is an ionic interaction with a characteristic potential energy called the heat of adsorption. The molecular adsorption process results in an exothermic attachment of the gas molecules to the surface of the voids, and is characterized by a high order of specificity. Zeolites exhibit a high affinity for certain gases or vapors. Because of their "effective" anionic frameworks and mobile cations, the physical bonds for adsorbed molecules having permanent electric moments (N_2, NH_3, H_2O) are much enhanced compared with nonpolar molecules such as argon or methane.

The functional relationship of amount of adsorption versus temperature and pressure for various zeolite-gas pairs is extremely complex, and as such, empirical or semi-empirical methods are commonly used to generate adsorption data.

Recent work (1, 2, 3) by the junior author and his colleagues on thermally cycled gas compression by adsorption/desorption of N_2O and other gases in zeolites created a need for a theory derived from first principles. Such a theory would be capable of accounting for the detailed physical behavior over a wide range of pressures, and thereby establish a reliable formalism to predict behavior and design apparatus. More important, however, is the need for a unifying theory to support and accelerate further work on all aspects of zeolite research and their applications.

Derivation of a Lattice Solid Solution Model

A lattice theory of solutions has been proposed (4) to describe the adsorption-desorption phenomena in zeolites. There are several reasons for this choice: (a) forming a solid solution by two substances is analogous to the forming of an adsorbed phase in the cavities of a zeolite, (b) the theory of solutions is well understood and its mathematical techniques powerful, and (c) since the state-of-the-art in description of adsorption phenomena in

[1]Current address: Shell Development Corp., Houston, Texas 77001

zeolites is basically empirical, solution theory could provide
constants that are pleasing because they are physically related to
the actual phenomena. An implicit reason for this choice is that
a lattice solution model will correspond to a localized adsorption
model – i.e., adsorption will occur at localized points on the
surface just as a lattice solution is formed at the various lat-
tice points. Therefore, a lattice "adsorption" model will consid-
er small-scale, localized gradients in the electrostatic field.
The mobile adsorption equations of Ruthven (5), and others (6,7),
by their very nature, do not consider fine structure in the elec-
trostatic field.

The solution is assumed ideal. It is incompressible; all
lattice sites are filled with some species of molecule. All
species of molecules at the lattice sites are of equal (or nearly
equal) size. For physical reasons, only one molecule can occupy
each lattice site. Since there is a distribution of adsorptive
energies within the zeolite, corresponding to the locally varying
electrostatic field, the adsorption problem is approached from the
standpoint of a superposition of several solutions – all the sites
in each being identical. The number of solutions that must be
considered equals the number of different adsorptive energy sites
that are found within the zeolite.

The canonical ensemble partition function for a binary solu-
tion is

$$Q(N_A,N_B,T) = q_A(T)^{N_A} q_B(T)^{N_B} \sum_{N_{AB}} g(N_B,N_A+N_B,N_{AB})e^{-W/kT} \qquad [1]$$

where (a) there are N_A A molecules and N_B B molecules in solution,
(b) each molecule vibrates about a lattice site with a three-di-
mensional partition function of $q_A(T)$ or $q_B(T)$ independent of the
state of occupation of neighboring sites, (c) the total energy of
solution is W, given by

$$W = N_{AA}\omega_{AA} + N_{AB}\omega_{AB} + N_{BB}\omega_{BB} \qquad [2]$$

and where the N_{AA}, N_{AB} and N_{BB} are the number of nearest neighbor
pairs of type AA, AB, and BB in the solution and where the ω_{AA},
ω_{AB}, and ω_{BB} are the corresponding nearest neighbor interaction
energies (more distant interaction energies assumed to be insig-
nificantly small), and (d) $g(N_B,N_A+N_B,N_{AB})$ is the number of ways
in which N_B B solution molecules can be distributed among the
N_A+N_B positions in the lattice so that there are N_{AB} nearest
neighbor pairs of type A-B. The presence of nearest neighbor in-
teractions indicates that adjacent sites, although they are char-
acterized by partition functions which are independent of the
state of occupation of their neighbors, are not independent en-
tities.

According to Hill (8), due to the small correction for ex-
cess entropy Δs_e, "the approximation of random mixing can approp-
riately be introduced, for molecules of like size, in lattice or
cell solution theories that are otherwise fairly sophisiticated."

Making use of the random mixing theory, the canonical ensemble partition function becomes

$$Q(N_A, N_B, T) = [q_A(T)e^{-c\omega_{AA}/2kT}]^{N_A}[q_B(T)e^{-c\omega_{BB}/2kT}]^{N_B}$$

$$\frac{(N_A+N_B)!}{N_A!N_B!} \exp[\frac{c\omega N_A N_B}{2kT(N_A+N_B)}] \qquad [3]$$

where c is the coordination number (number of nearest neighbors) and ω is the mixing energy of solution and is defined as

$$\omega \equiv \omega_{AA} + \omega_{BB} - 2\omega_{AB} \qquad [4]$$

This canonical ensemble partition function predicts a first-order two dimensional phase transition as shown by Hill (8).

The chemical potential μ_B of species B in binary solution is found by the standard thermodynamic formula

$$\frac{\mu_B(\text{binary solution})}{kT} = [\frac{-\partial \ln Q(N_A, N_B, T)}{\partial N_B}]_{N_A, T}$$

or

$$\frac{\mu_B(\text{binary solution})}{kT} = -\ln(q_B e^{-c\omega_{BB}/2kT}) + \ln X_B - \frac{c\omega}{2kT}(1-X_B)^2 \qquad [5]$$

where X_B is the molar concentration of component B in solution and is defined as

$$X_B = \frac{N_B}{N_A+N_B} \qquad [6]$$

Similarly the chemical potential μ_B of species B in a pure solution of B is

$$\frac{\mu_B(\text{pure solution})}{kT} = -\ln(q_B e^{-c\omega_{BB}/2kT}) \qquad [7]$$

The chemical potential of species B in a binary gas mixture above the solution is

$$\frac{\mu_B(\text{binary gas})}{kT} = \frac{\mu_{Bo}(T)}{kT} + \ln p_B \qquad [8]$$

where $\mu_{Bo}(T)$ is an integration constant and is only a function of T, and p_B is the partial pressure of species B in the gaseous phase.

The chemical potential of species B in the unitary gas phase above a pure solution of B is

$$\frac{\mu_B(\text{one component gas})}{kT} = \frac{\mu_{Bo}(T)}{kT} + \ln p_{Bo} \qquad [9]$$

where the o subscript on p_{Bo} designates a pressure due only to the one component B, i.e., the partial pressure due to B above the solution is equivalent to the total pressure above the solution.

The solution problem is solved for the equilibrium condition. This is formally equivalent to stating that

$$\frac{\mu_B(\text{binary gas})}{kT} = \frac{\mu_B(\text{binary solution})}{kT} \qquad [10]$$

and

$$\frac{\mu_B(\text{one component gas})}{kT} = \frac{\mu_B(\text{pure solution})}{kT} \qquad [11]$$

The following adsorption law is obtained by combining Equations [6-9]:

$$\ln(\frac{p_B}{p_{Bo}}) = \ln X_B - \frac{c\omega}{2kT}(1-X_B)^2$$

or

$$\frac{p_B}{p_{Bo}} = X_B \exp[\frac{-c\omega}{2kT}(1-X_B)^2] \qquad [12]$$

There is a corresponding equation for species A.

Development of the Adsorption Equation Parameters

The two species in the binary solution are designated as B and A. B is the adsorbate molecule and A is the absence of an adsorbed molecule at a particular adsorption site on the zeolite surface, called a "vacancy". Because of its definition, A is equal in size to the B species molecule. As the gas pressure above the zeolite (i.e., p_B) goes to larger values ($p_B \rightarrow p_{Bo}$) the solution composition within the cavity goes toward a pure solution of adsorbed gas ($X_B \rightarrow 1$). As the gas pressure above the zeolite goes to smaller values (i.e., $p_A \rightarrow p_{Ao}$), the amount of adsorption becomes less ($X_B \rightarrow 0$) and the solution composition within the cavity goes toward a pure solution of vacancies ($X_A \rightarrow 1$). This choice of solution species has the proper asymptotic nature.

It has been stated that zeolites exhibit a distribution of adsorptive energies. This is due to the complex structure within the zeolitic micropores and the strong dependence of electrostatic energies upon structure geometry. A discrete number of types of adsorption sites can be considered; the finite number is dependent upon electrostatic and steric considerations. The most strongly adsorbing sites correspond to locations near the cations (SII, SIII, etc.). After these positions are filled, the adsorbate molecules seek positions in the framework structure to minimize repulsive forces between them on the zeolite surface, and at the same time to maximize adsorptive forces with the framework.

This further adsorption must occur on the weakly charged "anionic" framework. The term "anionic" is used in that each oxygen atom in the framework must display a fractional negative charge for the zeolite crystal to be neutral. This fractional charge or "effective" charge implies the covalent character of the oxygen framework. The zeolite can be easily handled with solution theory if the ionic/covalent physical nature of the zeolite is treated mathematically as an ionic crystal lattice of cationic sites and "effective" anionic sites. The weak adsorption sites (or "ionic" sites) are in secondary coordination spheres around the cations and in positions corresponding to minimum-energy configuration and favorable steric location.

The mixing energy term ω is defined as the energy difference between (a) a pair of AA nearest neighbors and a pair of BB nearest neighbors, and (b) two pairs of AB nearest neighbors. In the subtraction, the adsorbate-adsorbent interactions are exactly cancelling and ω is equal to the adsorbate-adsorbate interaction. For most gas species the adsorbate-adsorbate interaction is given by the Lennard-Jones potential equation

$$\omega(r) = 4\epsilon[(\sigma/r)^{12}-(\sigma/r)^{6}] \qquad [13]$$

where σ and ϵ are constants characteristic of the chemical species of colliding molecules. For polar gases (such as NH_3) the interaction energy is given by the Stockmayer Potential ($\underline{9}$)

$$\omega(r,\theta_A,\theta_B,\psi_A,\psi_B) = 4\epsilon[(\sigma/r)^{12}-(\sigma/r)^{6}] - \frac{\mu_B\mu_B^{'}}{r^3}$$

$$[2\cos\theta_B\cos\theta_B^{'}-\sin\theta_B\sin\theta_B^{'}\cos(\psi_B-\psi_B^{'})] \qquad [14]$$

where the last term is the dipole-dipole interaction energy, μ_B and $\mu_B^{'}$ are the dipole moments of the BB pair, θ_B and $\theta_B^{'}$ are the angles of inclination of the polar axes to the line of centers, and ψ_B and $\psi_B^{'}$ are the angles subtended between the polar axes and perpendiculars passing through their centers.

The molar concentration term, defined by Equation [6], is the ratio of the number of adsorbate molecules in a cavity to the total number of adsorbate molecules that could be in one cavity at temperature T. This may be related to the mass of gas adsorbed per unit mass of zeolite (the x/m commonly found in adsorption graphs) by the following equation for a heteroenergetic surface:

$$\left(\frac{x}{m}\right)_j = \left(\frac{M_g N_o N_{mj}}{M_o}\right)X_{Bj} = A_j X_{Bj} \qquad [15]$$

where N_o = number of cavities/unit cell of zeolite
M_o = mass of a unit cell of zeolite
M_g = mass/molecule of gas adsorbed
N_{mj} = number of sites per cavity with adsorptive energy particular to the jth solution
X_{Bj} = molar concentration of B species in the jth solution

and $(\frac{x}{m})_j$ = the x/m contribution (to the total adsorption) due to the jth solution.

This equation must be solved subject to the boundary condition

$N_m = \sum\limits_j N_{mj}$ = total number of adsorption sites, and the total number of adsorbed B molecules in the cavity when all solutions within the cavity go to saturation.

This value of N_m is solved by considering steric limitations of adsorbed molecules in the volume of the cavity as saturation is approached. The total x/m becomes

$$\frac{x}{m} = \sum_j(\frac{x}{m})_j = \sum_j A_j X_{Bj} \qquad [16]$$

The term $p_{Bo}(U_j,T)$ is the pressure at which the jth solution becomes one-component B. This "saturation" pressure has been shown in standard statistical mechanics texts ([10]) to be

$$p_{Bo}(U_j,T) = const(T)exp[U_j/kT] \qquad [17]$$

where U_j is the minimum energy necessary to remove the molecule from solution j; is negative because the attachment of molecules to the zeolite surface is exothermic; and is not affected by nearest-neighbor interactions ([10]).

Several researchers ([11], [12], [13], [14]) have found that the zeolite cavities totally fill with gas molecules at pressures corresponding to saturation pressures for their corresponding vapors. This saturation pressure, $p_{Bo}(U_i,T)$, follows the semilogarithmic formula

$$\ln p_{Bo}(U_i,T) = C-D/T \qquad [18]$$

where C and D are constants to be solved for, and $p_{Bo}(U_i,T)$ is the saturation pressure corresponding to the particular solution with the smallest adsorptive potential and labelled i. Therefore, the saturation pressure for any solution j is immediately found with the following formulae:

$$p_B(U_j,T)/p_{Bo}(U_i,T) = exp[(U_j-U_i)/kT] \qquad [19]$$

and

$$p_{Bo}(U_j,T) = exp(C-D/T)exp[(U_j-U_i)/kT] \qquad [20]$$

The adsorbate-adsorbent interactions U_j, U_i are found by summing all relevant electrostatic interactions.

Ion-dipole energy: $W_{I\mu} = -\dfrac{(Ze)\mu}{r^2}\cos\theta \qquad [21a]$

Ion-quadrupole energy: $W_{IQ} = \dfrac{(Ze)Q}{4r^3}(3\cos^2\theta-1) \qquad [21b]$

Polarization energy:
$$W_{pol} = -\frac{1}{2}\frac{\alpha_g(Ze)^2}{r^4} \qquad [21c]$$

Dispersion-Repulsion energy:
$$W_{DR} = \frac{6mc^2\alpha_I\alpha_g}{(\frac{\alpha_I}{X_I} + \frac{\alpha_g}{X_g})} \cdot \frac{1}{2r^6} \qquad [21d]$$

where Ze = ionic charge

    r = gas-ion distance

    μ = dipole moment of gas molecule

    Q = quadrupole moment of gas molecule

    m = mass of electron

    c = speed of light in vacuum

α_g,α_I = polarizabilities of gas and ion respectively

X_g,X_I = susceptibilities of gas and ion respectively

and θ = angle subtended by a line connecting the centers of the ion and gas molecule and the line of axis of the dipole or quadrupole.

Summarizing, in the idealized lattice theory of solutions, the system is a condensed, incompressible solid solution containing N_A and N_B molecules of types A and B at temperature T. The Woltman-Hartwig model treats the A and B species as vacant and occupied adsorption sites, respectively, in the zeolite cage. The B molecules in solution (adsorbed) are in equilibrium with the B molecules in the gas above the solution. The Bragg-Williams approximation is used in which the distribution of molecules at the various sites in the solution, and also their average nearest neighbor interaction energy, are both treated as random.

The molar concentration $X_B = N_B/(N_A + N_B)$, and the solution equation relating equilibrium pressure of component B above the solution to its molar concentration in solution is

$$p_B = p_{Bo}X_B \exp\frac{-c\omega}{2kT}(1-X_B)^2 \qquad [22]$$

where T is the absolute temperature, ω is mixing energy, and c is the coordination number appropriate to each adsorption site. The mixing energy is the energy difference when two nearest neighbor A-B pairs are destroyed to form an AA pair and a BB pair. The mixing energy is calculated on the basis of forces between molecules on a line parallel to the void surface. This yields $\omega = \omega_{AA} + \omega_{BB} - 2\omega_{AB}$. The value of p_{Bo} is pressure, corresponding to the filling of the last sites to be occupied. The value of p_{Bo} is a function of the interaction energy between the molecule

B and the ions in the zeolite, and the force vector is normal to the void surface. It has the form

$$p_{Bo} = \exp(C-D/T)\exp\left[(U_J - U_o)/kT\right]$$ [23]

The values of C and D are evaluated at the critical point and normal boiling point. U_J is the vertical molecule-cation inter-action energy and U_o is the corresponding molecule-anion term. U and ω are calculated as the sums of all the appropriate dielectric and Lennard-Jones potentials. The actual calculation of an x/m isotherm is the superposition of several solution models. The principal one corresponds to the partial filling by molecules on the cation sites. The value of x/m is a constant times X_B, summed over all sites, where the constant is the molecular weight ratio.

The solution model is implemented for various gas-zeolite combinations (4). Where calculations are similar for the various gases, unnecessary repetition is avoided. Sample calculations are given below in abbreviated form.

Adsorption Isotherms of Argon on Synthetic Zeolite LiX

Experimental isotherms from Barrer and Stuart (15) are used as a check on the present theory. Following the liquid filling theory of Dubinin (11) and other (12, 13, 14), saturation values of $\frac{x}{m}$ for Argon on LiX at the various experimental temperatures are as follows:

$$\frac{x}{m}_{SAT} (173^{\circ}K) = 0.393$$

$$\frac{x}{m}_{SAT} (183^{\circ}K) = 0.386$$

$$\frac{x}{m}_{SAT} (194.5^{\circ}K) = 0.378$$

$$\frac{x}{m}_{SAT} (218^{\circ}K) = 0.362$$

Using these limiting values, the saturation pressures, p_{Bo}, at which the zeolite cavities are completely filled are determined by the saturated vapor pressure-temperature semi-logarithmic formula extrapolated into the super-critical region (8, 9, 10, 11). These pressures correspond to the filling of the weakly adsorbing sites-the anionic sites.

$$p_{Bo}(173^{\circ}K) = 9.8 \times 10^3 kPa$$

$$p_{B_0}(183^\circ K) = 1.26 \times 10^4 kPa$$
$$p_{B_0}(194.5^\circ K) = 1.64 \times 10^4 kPa$$
$$p_{B_0}(218^\circ K) = 2.55 \times 10^4 kPa$$

Calculation of interaction energies at the various lattice sites calls for evaluation of the interactions of Equation [21]. The argon atoms are adsorbed one per cationic site due to steric and electrostatic reasons. The remaining argon atoms are adsorbed on the anionic sites. The gas kinetic diameter of the adsorbed atoms and the geometric distribution of cations within the cavity determine the favorable anionic lattice solution sites. The cationic and anionic lattice solution sites are illustrated in Figure 1. The line of sight into the page is equivalent to a perpendicular to the connecting frame forming a section of the supercavity wall. Adsorption of the cation at SI, and the geometric arrangement of oxygen atoms and Li atom are illustrated in Figures 2 and 3 respectively. For this geometry, the interactions given in Table 1 occur.

TABLE 1

$$W_{pol}(\overset{+}{Li}-Ar) = -21.5 \text{ kJ/mole}$$

$$W_{disp}(\overset{+}{Li}-Ar) = -0.222 \text{ kJ/mole}$$

$$W_{ion-\mu}(\overset{+}{Li}-Ar) = W_{ion-Q}(\overset{+}{Li}-Ar) = 0 \text{ kJ/mole}$$

$$W_{pol}(O(2)-Ar) = -0.205 \text{ kJ/mole}$$

$$W_{disp}(O(2)-Ar) = -0.732 \text{ kJ/mole}$$

$$W_{pol}(O(4)-Ar) = -0.272 \text{ kJ/mole}$$

$$W_D(O(4)-Ar) = -1.12 \text{ kJ/mole}$$

Charge shielding is the resultant repelling force of the oxygen atoms O(2) and O(4) upon the induced dipole moment of the argon atom.

$$W_{ind\mu}(O(2)-Ar) = 2.88 \text{ kJ/mole}$$

$$W_{ind\mu}(O(4)-Ar) = 3.55 \text{ kJ/mole}$$

The net SII site interaction energy is -13.15 kJ/mole. The net SIII site interaction energy is approximately that of site II and is taken as being equal to it.

For the anionic site shown in Figure 1, the net interaction energy is -6.90 kJ/mole. The subscript j in Equation [19] refers here to sites SII, SIII; the subscript i refers to the anionic sites. Therefore,
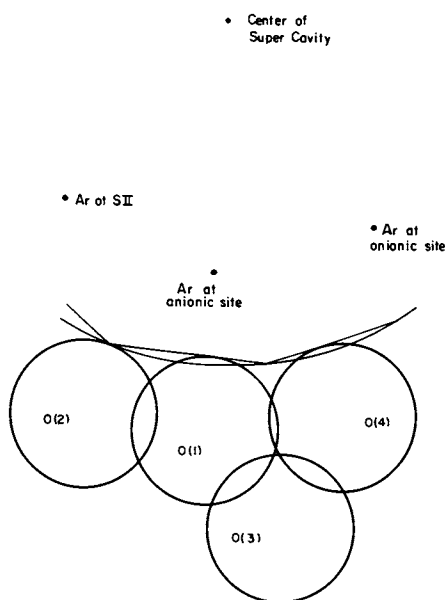
Figure 1.   Cross section of a supercavity in zeolite LiX with adsorption on the anionic sites and site SII. The various oxygen distances are as given by Broussard and Shoemaker (16) and are O(1)–O(2) = 2.8Å, O(1)–O(3) = 2.7Å, O(1)–O(4) = 2.64Å, and O(3)–O(4) = 2.8Å. The centers of the O(1) and O(4) oxygen anions lie 1.45Å out of and into the plane of the paper. The centers of the O(2) and O(3) anions lie on the plane of the paper.

Figure 2. Spatial arrangement of oxygen atoms, cation, and adsorbed gas atom at site SII. The Li⁺ atom lies on the 6-membered ring.

Figure 3. The geometric arrangement of oxygen anions and lithium cation at site SII. The distances are from Broussard and Shoemaker (16), with the Li⁺ cation on the 6-membered ring.

$$p_{Bo}(U_i, 173^{\circ}K) = 9.8 \times 10^3 kPa \text{ and } p_{Bo}(U_j, 173^{\circ}K) = 128 \text{ kPa}$$

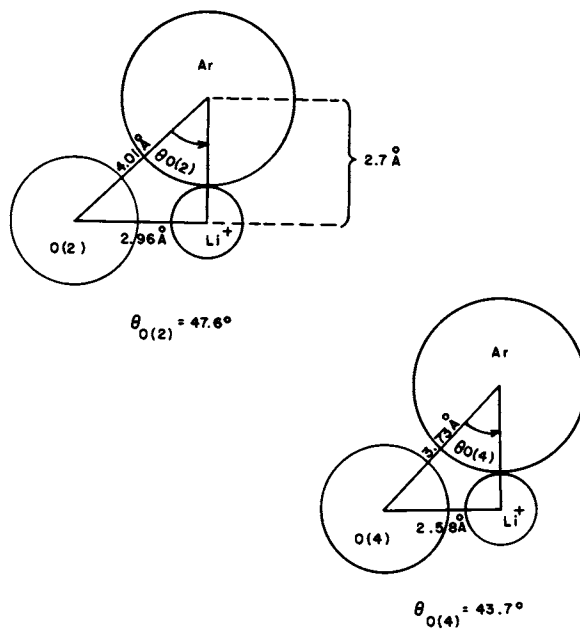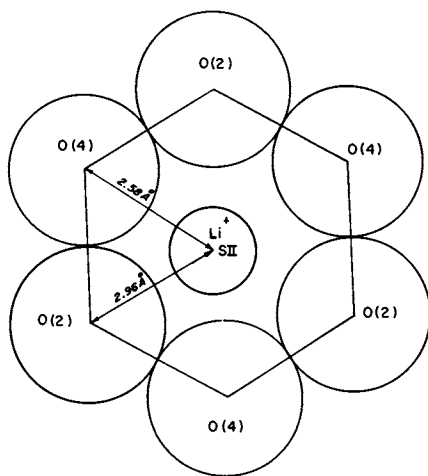$$p_{Bo}(U_i, 183^{\circ}K) = 1.26 \times 10^4 kPa \text{ and } p_{Bo}(U_j, 183^{\circ}K) = 208 \text{ kPa}$$

$$p_{Bo}(U_i, 194.5^{\circ}K) = 1.64 \times 10^4 kPa \text{ and } p_{Bo}(U_j, 194.5^{\circ}K) = 345 \text{ kPa}$$

$$p_{Bo}(U_i, 218^{\circ}K) = 2.55 \times 10^4 kPa \text{ and } p_{Bo}(U_j, 218^{\circ}K) = 811 \text{ kPa}$$

Calculation of the <u>nearest neighbor interactions</u> takes into account the coordination number as well as the energies determined from Equations [13,14], as appropriate, so in general

$$c_i\omega_i = c_{ii}\omega_{ii} + c_{ij}\omega_{ij}. \qquad [24]$$

The term ω_{ii} is the nearest-neighbor adsorbate-adsorbate interaction energy between two anionic sites and is calculated using the Lennard-Jones equation; ω_{ij} is that between site SII and the anionic site, and $\omega_{ii} = \omega_{ij} = \omega_i$.

The term c_i is the number of nearest neighbors an adsorbate atom has when it is sited on the <u>anionic</u> site. For adsorption, the term c_i is the number of atoms adsorbed on the solution sites which are nearest neighbor to a particular <u>anionic</u> site when the "solution" becomes saturated. The c_i are composed of two terms –

$$c_i = c_{ii} + c_{ij} = \frac{N_{Bi,sat}}{N_{Ai}+N_{Bi}} + 1 \qquad [25]$$

The first term is the number of nearest neighbors at anionic sites and is temperature-dependent. The second term is the number of nearest neighbors at site SII, and is temperature-independent, and has a value of 1 since the site would then become more unfavorable than any other adsorption site.
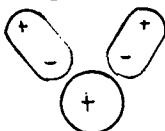
unfavorable situation

The nearest-neighbor interaction between two adsorbed Ar atoms on the surface is repulsive and equal to 4.27 kJ/mole. Thus,

$$c_i(173^{\circ}K) = \frac{10.28}{11} + 1 = 1.935$$

and for $173^{\circ}K$ $c_i\omega_i = (1.935)(4.27) = 8.26$ kJ/mole

for $183^{\circ}K$ $c_i\omega_i = 8.16$ kJ/mole

for $194.5^{\circ}K$ $c_i\omega_i = 8.03$ kJ/mole

for $218°K$ $c_i\omega_i$ = 7.81 kJ/mole

For the sites SII, SIII, the product $c_j\omega_j$ is calculated in the following manner: $c_j\omega_j = c_{jj}\omega_{jj} + c_{ji}\omega_{ji}$

$\omega_j = \omega_{ji} = \omega_{ii}$ = 4.27 kJ/mole; $\omega_{jj} \approx 0.0$ kJ/mole.

The ω_{ji} is the nearest-neighbor adsorbate-adsorbate interaction between atoms at SII, SIII and the anionic sites.

$$c_j = \frac{3N_{Bi} \cdot N_{Bi,sat}}{N_{Ai} + N_{Bi}} \tag{26}$$

where the 3 is the three-fold coordination to any site SII, and the factor $\frac{N_{Bi}N_{Bi,sat}}{N_{Ai} + N_{Bi}}$ is the occupation factor of the anionic sites when the sites SII, SIII are filled. The product $c_j\omega_j$ for argon is so small for all temperatures of interest that it may be put equal to zero.

The equations which define the two solutions (SII, SIII and anionic)are as follows:

$$p_B(U_j,T) = p_{Bo}(U_j,T)X_{Bj}\exp[-\frac{c_j\omega_j}{2kT}(1-X_B)^2] \tag{27}$$

$$= p_{Bo}(U_i,T)\exp[(U_j-U_i)/kT]X_{Bj}\exp[\frac{-c_j\omega_j}{2kT}(1-X_{Bj})^2]$$

and

$$p_B(U_i,T) = p_{Bo}(U_i,T)X_{Bi}\exp[\frac{-c_i\omega_i}{2kT}(1-X_{Bi})^2] \tag{28}$$

Solving these equations and superimposing the results gives the adsorption isotherm of argon on zeolite LiX.

The constituent contributions due to SII, SIII sites and to anionic sites are shown in Figure 4 for the temperature T = $173°K$. Comparison of experimental curves with theoretical points is given by Figure 5.

The agreement between theoretical and experimental results is extremely good. The trend noted, that theory predicted slightly less adsorption than was found experimentally, could be due to capillary condensation, especially when p_B/p_{Bo} is appreciable.

Adsorption Isotherms of Nitrogen on Synthetic Zeolite NaX

Experimental isotherms from Barrer and Stuart (15) are used as an additional check on the present theory. Saturation values of $\frac{x}{m}$ for N_2 on NaX at the various experimental temperatures are as follows:

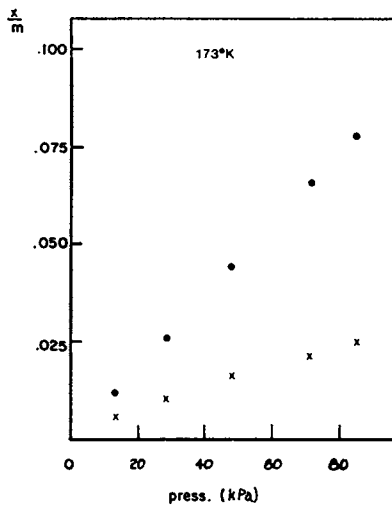| Temp.	$173°K$	$194.5°K$	$218°K$	$273°K$
$\frac{x}{m}_{SAT}$	.237	.225	.212	.186

Figure 4.   Constituent contributions due to (●) (SII, SIII) sites and (x) anionic sites
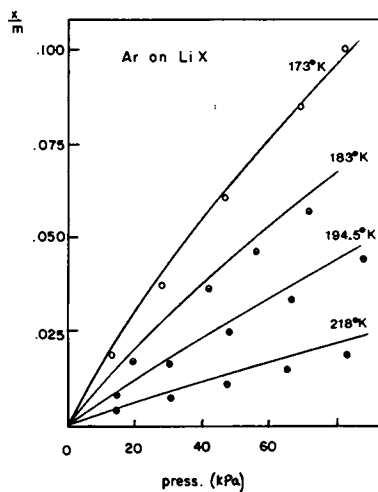

Figure 5.   Comparison of experimental curves with theoretical points (15)

The cationic and anionic lattice solution sites are illus-
trated in Figure 6. The ω_{ii} = 17.78 kJ/mole; the ω_{ji} = 10.96 kJ/
mole. The U_j = -25.65 kJ/mole; the U_i = -15.27 kJ/mole. Therefore,

$$p_{Bo}(U_i,173°K) = 1.53 \times 10^4 \text{ kPa and } P_{Bo}(U_j,173°K) = 12 \text{ kPa}$$

$$p_{Bo}(U_i,194.5°K) = 2.39 \times 10^4 \text{ kPa and } p_{Bo}(U_j,194.5) = 40 \text{ kPa}$$

$$p_{Bo}(U_i,218°K) = 3.52 \times 10^4 \text{ kPa and } p_{Bo}(U_j,218) = 120 \text{ kPa}$$

$$p_{Bo}(U_i,273°K) = 6.70 \times 10^4 \text{ kPa and } p_{Bo}(U_j,273) = 695 \text{ kPa}$$

For 173°K

$\dfrac{c_i \omega_i}{2kT} = 9.21$ where now $\omega_{ii} \neq \omega_{ij}$ and the product
                                         $c_i\omega_i$ must be used in its expanded form
                                         $c_i\omega_i = c_{ij}\,\omega_{ij} + c_{ii}\,\omega_{ii}$

$\dfrac{c_j \omega_j}{2kT} = 2.19$ where now $\omega_j = \omega_{ji} \neq \omega_{jj} = 0.0$ kJ/mole

For 194.5°K, $\dfrac{c_i \omega_i}{2kT} = 7.84$ and $\dfrac{c_j \omega_j}{2kT} = 1.81$

For 218°K, $\dfrac{c_i \omega_i}{2kT} = 6.64$ and $\dfrac{c_j \omega_j}{2kT} = 1.40$

For 273°K, $\dfrac{c_i \omega_i}{2kT} = 4.76$ and $\dfrac{c_j \omega_j}{2kT} = 0.91$

Comparison of experimental curves with theoretical points is
given by Figure 7. The agreement between theoretical and experi-
mental results is good at 194.5°K, 218°K and 273°K. For 173°K,
the theoretical results overpredict adsorption at small pressures
and underpredict adsorption at high pressures. The discrepancy
is never more than 5-6%.

Adsorption Isotherms of Ammonia on Na X

Experimental isotherms from Barrer and Gibbons ([17]) are used
as a further check on the present theory. Saturation values of
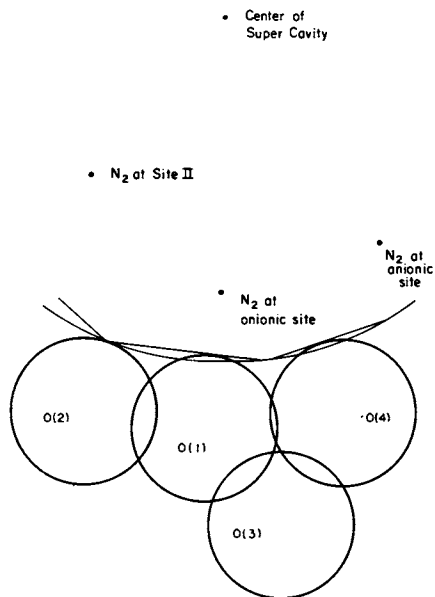$\frac{x}{m}$ for NH_3 on NaX at the various experimental temperatures are as
follows:

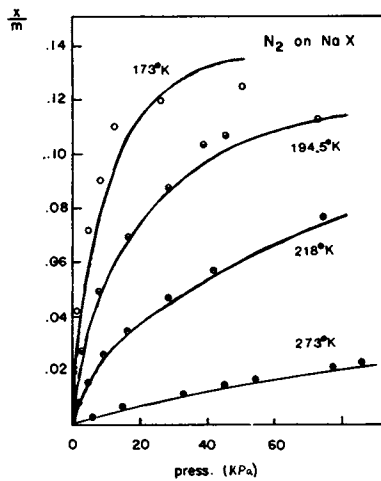*Figure 6. Cross section of supercavity in zeolite NaX; nitrogen is adsorbed as shown*

Figure 7. Comparison of experimental curves with theoretical points (15)

Temp.	$373^\circ K$	$453^\circ K$	$503^\circ K$	$563^\circ K$
$\dfrac{x}{m_{SAT}}$	0.171	0.138	0.121	0.104

These saturation values are determined assuming that the NH_3 enters the β cages of the zeolite NaX at temperatures $\geq 100^\circ C$. According to Breck ([18]) and Barrer and Gibbons ([17]), this is a good assumption.

NH_3 is similar to H_2O in that they both possess large dipole moments and are both small molecules. The presence of NH_3 in a zeolite is chemically similar to the presence of H_2O in a zeolite. Therefore, the hydrated cation distribution in zeolites is probably more typical of NH_3 adsorption in zeolites than the dehydrated cation distribution. According to Breck ([18]), for hydrated zeolite X, cations are found in sites SI, SI', SII, and SIV. Of these sites, SI', SII, and SIV would all be adsorption lattice solution sites. The cationic and anionic lattice solution sites (in the supercavity of NaX) are illustrated in Figure 8. For NH_3, the subscript j1 will refer to SII sites, the subscript j2 will refer to SI' sites, and j3 will refer to SIV sites. The anionic sites are two and are (1) in the center 4-membered ring of the connecting frame and (2) near the center of the 0(2)-0(1)-0(1) triad of oxygen atoms. For NH_3, the subscript i1 will refer to the first anionic site; the subscript i2 will refer to the second anionic site.

The U_{j1} = -69.0 kJ/mole, $U_{j2} \simeq$ -69.0 kJ/mole, and U_{j3} = -71.1 kJ/mole

The U_{i1} = -47.3 kJ/mole and U_{i2} = -32.6 kJ/mole. The ω_{i1-j3} = 9.33 kJ/mole = ω_{i2-j3}.

The $\omega_{i1-j1} = \omega_{i1-j2} = \omega_{i2-j1} = \omega_{i2-j2} \simeq$ 0.0 kJ/mole.

The $\omega_{j2-j1} = \omega_{i2-j3}$ = 0.0 kJ/mole

The $\omega_{j1-j1} = \omega_{j2-j2} = \omega_{j3-j3}$ = 0.0 kJ/mole.

The ω_{j1-j3} = 31.4 kJ/mole.

For T = $373^\circ K$

The $p_{Bo}(U_{j1},T) = p_{Bo}(U_{j2},T) < 1$ kPa

$p_{No}(U_{j3},T) < 1$ kPa

$p_{Bo}(U_{i1},T) = 56$ kPa

$p_{Bo}(U_{i2},T) = 6.3 \times 10^3$ kPa

• Center of
  Super Cavity

• NH$_3$ at
  S$\mathbf{I}$

• NH$_3$ at   • NH$_3$ at
  anionic   anionic site
  site

O(2)   O(4)

O(1)

O(3)
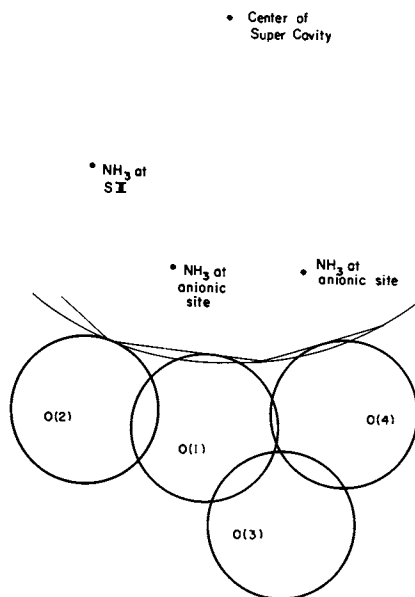
Figure 8.   Cross section of supercavity in zeolite NaX showing anionic sites for NH$_3$ adsorption

$\dfrac{x}{m}$ .2

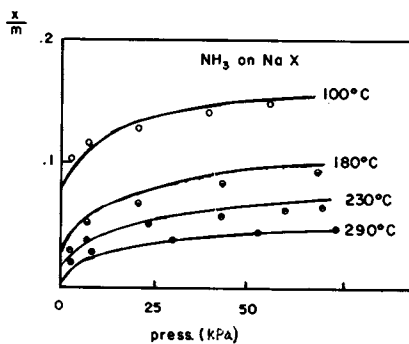NH$_3$ on Na X

100°C

.1

180°C

230°C

290°C

O   25   50

press. (kPa)

Figure 9.   Comparison of experimental curves with theoretical points (17)

Also, $p_{Bo}(U_{j1},453^{\circ}K) = p_{Bo}(U_{j2},453^{\circ}K) = 73$ kPa

$\qquad p_{Bo}(U_{j3},453^{\circ}K) = 42$ kPa

$\qquad p_{Bo}(U_{i1},453^{\circ}K) = 2.3 \times 10^{4}$ kPa

$\qquad$ There are no i2 sites filled at $453^{\circ}K$, $503^{\circ}K$, and $563^{\circ}K$. Also,

$\qquad p_{Bo}(U_{j1},503^{\circ}K) = p_{Bo}(U_{j2},503^{\circ}K) = 237$ kPa

$\qquad p_{Bo}(U_{j3},503^{\circ}K) = 144$ kPa

$\qquad p_{Bo}(U_{i1},503^{\circ}K) = 4.3 \times 10^{4}$ kPa

Also, $p_{Bo}(U_{j1},563^{\circ}K) = p_{Bo}(U_{j2},563^{\circ}K) = 743$ kPa

$\qquad p_{Bo}(U_{j3},563^{\circ}K) = 475$ kPa

$\qquad p_{Bo}(U_{i1},563^{\circ}K) = 7.7 \times 10^{4}$ kPa

For $373^{\circ}K$, $\dfrac{c_i \omega_i}{2kT} = 3.0$ and $\dfrac{c_{j2} \omega_{j2}}{2kT} = 0.0$, since $\omega_{j2} = 0.0$ kJ/mole,

and $\dfrac{c_{j1} \omega_{j1}}{2kT}$ and $\dfrac{c_{j3} \omega_{j3}}{2kT}$ are not considered since adsorption is

completed so rapidly on the sites SII and SIV.

For $453^{\circ}K$, $\dfrac{c_i \omega_i}{2kT} = 2.47$, $\dfrac{c_{j1} \omega_{j1}}{2kT} = 12.43$, and $\dfrac{c_{j3} \omega_{j3}}{2kT} = 10.32$.

For $503^{\circ}K$, $\dfrac{c_i \omega_i}{2kT} = 2.22$, $\dfrac{c_{j1} \omega_{j1}}{2kT} = 11.19$, and $\dfrac{c_{j3} \omega_{j3}}{2kT} = 9.29$.

For $563^{\circ}K$, $\dfrac{c_i \omega_i}{2kT} = 1.99$, $\dfrac{c_{j1} \omega_{j1}}{2kT} = 10.0$, and $\dfrac{c_{j3} \omega_{j3}}{2kT} = 8.3$.

$\qquad$ Comparison of experimental curves with theoretical points is given by Figure 9. The agreement between theoretical and experimental results is good at high pressures for all the temperatures considered. At low pressures (2-3 kPa) the discrepancy may be as much as 10% for the $100^{\circ}C$ experimental curve, it is less for the other temperatures.

Adsorption Isotherms of Nitrous Oxide on NaY

$\qquad$ Experimental isotherms generated by the present authors are also used as a check on the present theory. Saturation values of

$\frac{x}{m}$ for N_2O on NaY at the various experimental temperatures are as follows:

Temp.	$202^{\circ}K$	$240^{\circ}K$	$270^{\circ}K$	$300^{\circ}K$	$335^{\circ}K$	$373^{\circ}K$
$\frac{x}{m}_{SAT}$	.463	.434	.412	.394	.371	.349

The subscript i refers again to the anionic sites; the subscript j refers to the cationic site SII. The $\omega_{ii} = \omega_{ij} = 20.42$ kJ/mole. The $U_j = -29.8$ kJ/mole; the $U_i = -21.00$ kJ/mole. Therefore,

$$p_{Bo}(U_i,202^{\circ}K) = 243 \text{ kPa and } p_{Bo}(U_j,202^{\circ}K) \simeq 1 \text{ kPa}$$

$$p_{Bo}(U_i,240^{\circ}K) = 1.16 \times 10^3 \text{ kPa and } p_{Bo}(U_j,240^{\circ}K) = 14 \text{ kPa}$$

$$p_{Bo}(U_i,270^{\circ}K) = 2.86 \times 10^3 \text{ kPa and } p_{Bo}(U_j,270^{\circ}K) = 57 \text{ kPa}$$

$$p_{Bo}(U_i,300^{\circ}K) = 5.92 \times 10^3 \text{ kPa and } p_{Bo}(U_j,300^{\circ}K) = 173 \text{ kPa}$$

$$p_{Bo}(U_i,335^{\circ}K) = 1.17 \times 10^4 \text{ kPa and } p_{Bo}(U_j,335^{\circ}K) = 498 \text{ kPa}$$

$$p_{Bo}(U_i,373^{\circ}K) = 2.13 \times 10^4 \text{ kPa and } p_{Bo}(U_j,373^{\circ}K) = 1250 \text{ kPa}$$

The sites SII fill so quickly at $T = 202^{\circ}K$ and $240^{\circ}K$ that the exponent $\frac{c_j\omega_j}{2kT}$ is not considered.

Temp.	$202^{\circ}K$	$240^{\circ}K$	$270^{\circ}K$	$300^{\circ}K$	$335^{\circ}K$	$373^{\circ}K$
$\frac{c_i\omega_i}{2kT}$	12.67	10.20	8.77	7.67	6.62	5.73

Comparison of experimental points with theoretical points is shown in Figure 10. Agreement is good at low pressure (i.e., p < 100kPa), and may differ by as much as 10% at the higher pressures. This error is of the same order as that claimed by the existing, more empirical, models in the literature. A systematic agreement in shape is noted, and the actual error may be in the experimental data where "flotation" effects are serious for gravimetic measurements at elevated pressures.

Summary

The "solid-solution lattice theory" model of adsorption on zeolites has been shown to describe the experimental results in the literature with accuracy comparable to all existing theories, even though these theories are in many instances semi-empirical. Since the theory is related to actual physical phenomena, systematic studies can be made of the effect on adsorption of changing the zeolite.
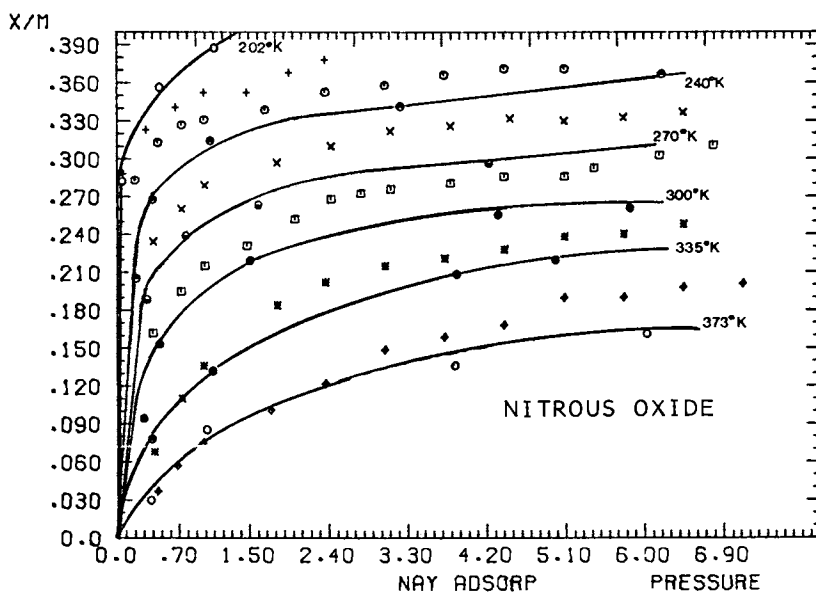
Figure 10. Comparison of experimental points with theoretical points. The experimental points are related to the temperatures at which they were taken by the caption at the lower right of the graph. The theoretical points are connected by lines that are then labeled with the correct corresponding temperatures.

The model has been tested for a wide variety of gas-zeolite combinations. Gases of increasing complexity were considered: Ar(non-polar), N_2(quadrupole moment, no dipole moment), N_2O (quadrupole moment, small dipole moment), and NH_3 (large dipole moment, small quadrupole moment). The zeolites tested were all in the synthetic faujasite family; however, they ranged from the cation-rich zeolite X to the cation-poor zeolite Y. Cation geometries considered in the tests were those typical of the dehydrated zeolite form and those typical of the hydrated geometry (associated with NH_3 adsorption). Two forms of representative cations were considered, Li^+ and Na^+.

It can be concluded that the "solid-solution lattice theory" model shows great promise in describing adsorption on zeolites. The general shape of the zeolite adsorption isotherm (i.e., the roughly linear Henry's law initial adsorption region, the exponential "knee" of the isotherm, and the slowly increasing adsorption with pressure at higher pressures) are all predicted qualitatively and with good quantitative agreement. Initial heats of adsorption agree well with experimental values in the literature. Future studies should indicate whether other thermodynamic quantities are as well predicted.

Acknowledgements

Abstract

A statistical thermodynamic equation for gas adsorption on synthetic zeolites is derived using solid solution theory. Both adsorbate-adsorbate and adsorbate-adsorbent interactions are calculated and used as parameters in the equation. Adsorption isotherms are calculated for argon, nitrogen, ammonia, and nitrous oxide. The solution equation appears valid for a wide range of gas adsorption on zeolites.

Literature Cited

1. Hartwig, W. H., Steinfink, H., Masson, J. P. and Woltman, A.W., Proc. 1976 Region V IEEE Conf., IEEE Cat. 76CH1068-6Reg5, 1976, p. 80.
2. Hartwig, W. H.,"Adv. in Cryogenic Engineering," Ed. by K. D. Timmerhouse, Plenum Publishing Co., N. Y., 1978, 23, 435-447.
3. Hartwig, W. H., Woltman, A. W., and Masson, J. P., Proc. 1978 Int'l. Cryogenic Eng'g. Conf., IPC Science and Technology Press Guildford, Surrey GU2 5AW, England.

4. Woltman, A. W., Ph.D. Dissertation, The University of Texas at Austin, Austin, Texas, March 1978.
5. Ruthven, D. M., <u>Nature, Phys. Sci.</u>, 1971, <u>232</u>(29), 70.
6. Coughlan, B., Kilmartin, S., McEntree, J., and Shaw, R. G., <u>J. Colloid Interface Sci.</u>, 1975, <u>52</u>, 386.
7. Derrak, R. I., Coughlin, K. F., and Ruthven, D. M., <u>J. Chem. Soc.</u>, <u>Faraday I</u>, 1972, <u>68</u>, 1947.
8. Hill, T. L., "An Introduction to Statistical Thermodynamics," Addison-Wesley, 1962, pp. 246, 381.
9. Hirschfelder, J. O., Curtiss, C. F., and Bird, R. B., "Molecular Theory of Gases and Liquids," Wiley, New York, N.Y., 1954.
10. Fowler, M. A. and Guggenheim, E. A., "Statistical Thermodynamics," London, England, Cambridge University Press, 1939.
11. Dubinin, M. M., <u>J. Colloid and Interface Sci.</u>, 1967, <u>23</u>, 487.
12. Harper, R. J., Stifel, G. R., and Anderson, R. B., <u>Canad. Jour. of Chem.</u>, 1969, <u>47</u>, 4661.
13. Flock, J. W. and Lyon, D. N., <u>J. of Chem. and Engin. Data</u>, 1974, <u>19</u>, 205.
14. Nakahara, T., Hirata, M. and Ohmori, T., <u>J. of Chem. and Eng. Data</u>, 1975, <u>20</u>, 195.
15. Barrer, R. M. and Stuart, W. I., <u>Proc. Roy. Soc.</u>, London, 1959, <u>249A</u>, 464.
16. Broussard, L. and Shoemaker, D.P., <u>J. Amer. Chem. Soc.</u>, 1960, <u>82</u>, 1041.
17. Barrer, R. M. and Gibbons, R. M., <u>Trans. Faraday Soc.</u>, 1963, <u>59</u>, 2569.
18. Breck, D. W., "Zeolite Molecular Sieves," Wiley-Interscience, New York, N.Y., 1974.

Mathematical Modeling of Adsorption in Multicomponent Systems

ALEXANDER P. MATHEWS

Department of Civil Engineering, Kansas State University, Manhatten, KS 66506

WALTER J. WEBER, JR.

College of Engineering, The University of Michigan, Ann Arbor, MI 48104

Adsorption is an important unit process in chemical processing, air pollution control, and water and wastewater treatment. In several applications, the adsorbate is a mixture of a number of compounds. Industrial and domestic wastewaters typically contain a wide spectrum of compounds in differing concentrations. Even in single solute systems, biological decay may result in end products that compete with the solute for the available sites on the surface of the adsorbent. It is, therefore, desirable to develop a model to describe the kinetics of multicomponent adsorption.

There have been few studies reported in the literature in the area of multi-component adsorption and desorption rate modeling (1,2,3,4,5). These have generally employed simplified modeling approaches, and the model predictions have provided qualitative comparisons to the experimental data. The purpose of this study is to develop a comprehensive model for multi-component adsorption kinetics based on the following mechanistic process: (1) film diffusion of each species from the fluid phase to the solid surface; (2) adsorption on the surface from the solute mixture; and (3) diffusion of the individual solute species into the interior of the particle. The model is general in that diffusion rates in both fluid and solid phases are considered, and no restrictions are made regarding adsorption equilibrium relationships. However, diffusional flows due to solute-solute interactions are assumed to be zero in both fluid and solid phases.

Mathematical Development

In a rapidly agitated slurry adsorber, the concentration C_k of the solute species k, and the distribution of the adsorbent particles may be assumed to be uniform throughout the reactor. The mass transfer rate of each solute across the film to the solid surface may be equated to the average uptake of the solute to give the following equation:

$$\frac{dq_j}{dt} = \frac{k'_{f_k} (C_k - Cs_k)}{V_p \, \rho \, (1 - \varepsilon)} \, , \quad k = 1, N \tag{1}$$

C_k and q_k are the concentrations of the solute in the liquid and solid phases expressed in moles/liter and moles/gm, respectively. Cs_k is the equilibrium concentration in the liquid phase at the surface, and k'_{f_k} is the mass transfer coefficient for each solute. V_p, ρ and ε are the volume, density and porosity of the particle, respectively. N is the number of adsorbing species in the mixture.

The average concentration in the particle is obtained by integrating the pointwise concentration q_{i_k} over the volume of the particle as follows:

$$q_k = \frac{3}{R^3} \, {}_0\!\int^R q_{i_k} \, r^2 dr, \quad k = 1, N \tag{2}$$

Adsorption at the surface is assumed to be rapid compared to the diffusion rates. The following relationship was developed to describe the mixture adsorption equilibria (3):

$$q_{s_j} = \frac{a_j \, (C_{s_j}/\eta_k)}{\sum\limits_{k=1}^{N} (1 + b_k (C_{s_k}/\eta_k)^{\beta_k}} \, , \quad k = 1, n \tag{3}$$

The equilibrium concentrations in the solid and liquid phases at the surface of the adsorbent particle are q_{s_k} and C_{s_k} and a_k, b_k and β_k are isotherm constants for each solute corresponding to the single solute isotherm equation (4).

$$q_s = \frac{ac_s}{1 + (bc_s)^{\beta}} \tag{4}$$

η_j are interaction factors, one for each solute species in the mixture and are obtained by correlating mixture equilibrium data.

Equation (3) allows the use of experimental equilibrium data in multicomponent rate models.

The transport of the adsorbed species into spherical particles is represented by the unsteady state diffusion equation as follows:

$$\frac{\delta q_{i_k}}{\delta t} = D_k \left(\frac{\delta^2 q_{i_k}}{\delta r^2} + \frac{2}{r} \frac{\delta q_{i_k}}{\delta r} \right), \quad k = 1, N \tag{5}$$

And, the material balance for the reactor is:

$$V \frac{dc_k}{dt} = -W \frac{dq_k}{dt}, \quad k = 1, N \tag{6}$$

D_k is the surface diffusion coefficient for each solute, V is the volume of fluid in the reactor, and W the weight of adsorbent in the reactor.

The initial and boundary conditions for the fluid and solid phases are given for k = 1, N by:

$$C_k(0) = C_{k_o} \tag{7}$$

$$q_{i_k}(r,0) = 0 \tag{8}$$

$$q_{i_k}(R,t) = q_{s_k}(t) \tag{9}$$

$$\frac{\delta q_{i_k}(0,t)}{\delta t} = 0 \tag{10}$$

The initial concentration of solute in the liquid phase is C_{k_o} and zero in the solid phase. The surface concentration on the solid phase is an unknown function of time, and the flux at the center of the particle at all times is zero.

The system of equations (1) to (10) provide the basis for predicting multicomponent rate profiles. The input parameters required are the mass transfer and diffusion coefficients for each solute, the single solute isotherm constants, and the mixture equilibria correlation coefficients. Estimation of these equilibrium and rate parameters are discussed in the following sections.

Adsorption Equilibria in Single Solute Systems

The successful representation of dynamic adsorptive separation of solute from the fluid to the solid phase is contingent upon a satisfactory description of the equilibrium separation between the two phases. Several empirical and theoretical equations are available to describe single component adsorption equilibria. Theories of adsorption considering monolayer and multilayer adsorption, homogeneous and hetrogeneous surfaces, and various equations of state for the two-dimensional adsorbed phase are available in the literature (6,7,8). Many of these isotherm expressions are too complex or provide poor representations of experimental data to be useful for practical design applications. Langmuir and Freundlich isotherms are two non-linear equations that have been used widely to represent equilibrium data over small concentration ranges. The Freundlich equation agrees well with the Langmuir equation over moderate concentration ranges, but unlike Langmuir isotherm, it does not reduce to the linear isotherm at low solute concentrations. Both the equations suffer from the disadvantage that equilibrium data over a wide concentration range cannot be fitted with a single set of parameters. An empirical equation (11), designated the three parameter equation has been proposed and utilized in this study to represent adsorption equilibria over a wide concentration range.

$$q_e = \frac{ac_e}{1+bc_e^{\beta}} \, , \; \beta \leq 1 \tag{11}$$

This equation reduces to the linear isotherm at low concentrations, to the Freundlich isotherm at high concentrations, and to the Langmuir isotherm when $\beta = 1$. However, the equation cannot be linearized for easy estimation of isotherm parameters.

Experimental isotherm data for the adsorption of four solutes, phenol, p-bromophenol, p-toluene sulfonate, and dodecyl benzene sulfonate onto activated carbon are shown in Figures 1 to 4. The isotherm constants are estimated using a nonlinear parameter estimation program, and are shown in Table 1. The parameter estimation program uses the principal axis method to obtain the parameters, a, b and β that will minimize the sum of the squares of the differences between experimental and computed isotherm data.

Adsorption Equilibria in Multicomponent Systems

Several models were evaluated to obtain a satisfactory description of equilibria for the adsorption of mixtures from dilute solutions (9,10,11). The method of Radke and Prausnitz
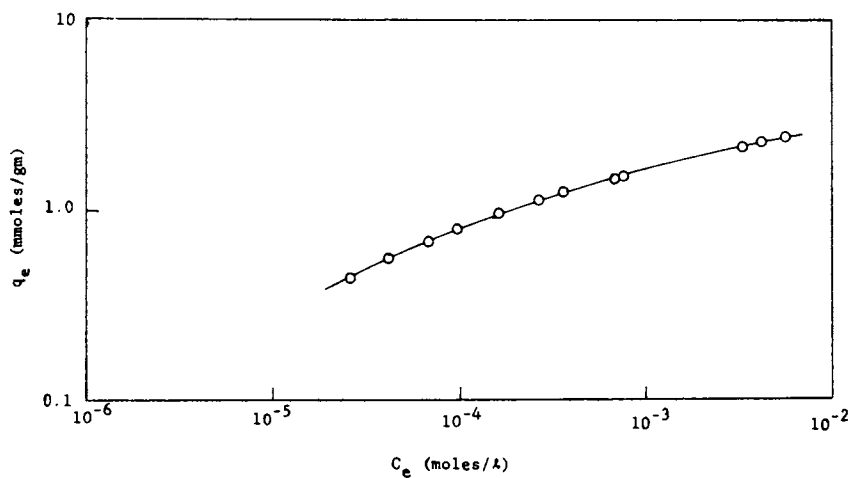
Figure 1. Adsorption isotherm for phenol: (○) experimental data, (——) 3-parameter equation
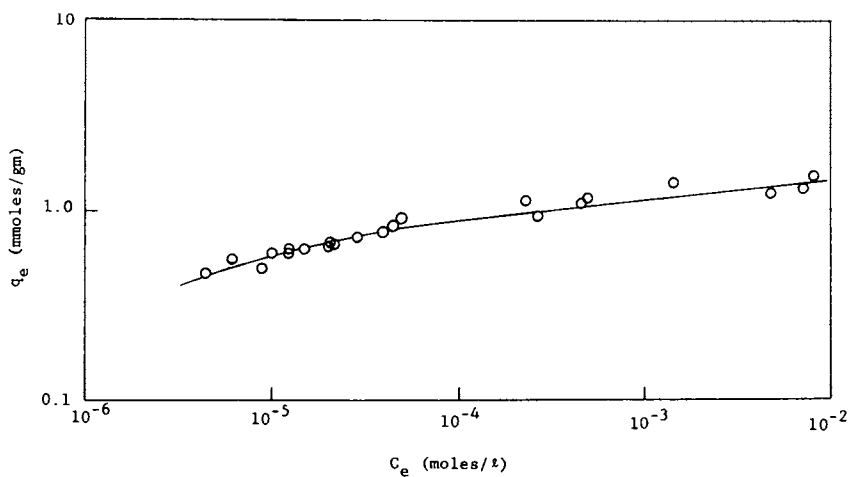
Figure 2. Adsorption isotherm for p-bromophenol: (○) experimental data, (——) 3-parameter equation
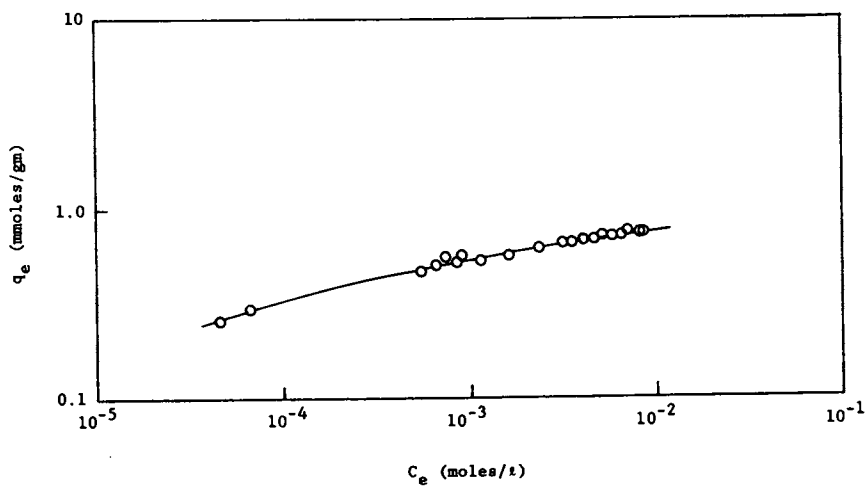
Figure 3.   Adsorption isotherm for p-toluene sulfonate: (○) experimental data, (———) 3-parameter equation
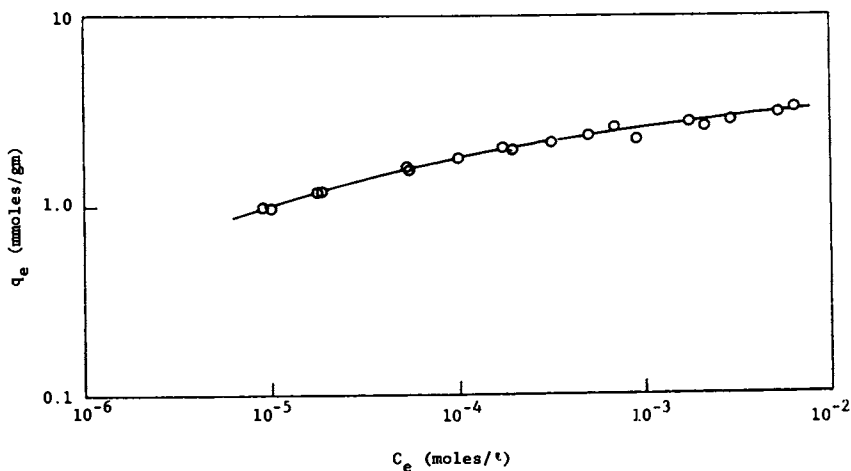
Figure 4.   Adsorption isotherm for dodecyl benzene sulfonate: (○) experimental data, (———) 3-parameter equation

Table 1

Isotherm Constants*

Solute	a	b	β
Phenol	43.29	26.34	0.7942
p-Bromophenol	333.40	133.50	0.8687
p-Toluene Sulfonate	22.23	40.41	0.8500
Dodecyl Benzene Sulfonate	284.70	248.50	0.9019

*Based on C_e and q_e expressed in mmoles/ℓ and mmoles/gm respectively

using the principles of dilute solution thermodynamics, is par-
ticularly suitable for solutes that do not adsorb strongly.
However, the computational effort required in utilizing this
model in a multicomponent rate model is substantial, particularly
for solutes that cannot be represented by easily integrable
functions. The simple extensions of the Langmuir model for
mixtures (9,10) do not satisfactorily represent mixture equil-
ibria. In this study, the three parameter equation is extended
for multisolute systems and represented by the following equa-
tion:

$$q_i = \frac{a_i \, C_i}{\sum\limits_i (1 + b_i \, C_i^{\beta_i})} \tag{12}$$

This equation was found to represent the binary equilibrium data
of Radke and Prausnitz (11) for mixtures of p-cresol and
p-chlorophenol, and acetone and propionitrile satisfactorily.
    For solute systems that are not adequately represented by
this equation, a correlational procedure is used so that mixture
equilibrium data can be used in the rate model. Schay, et al.
(12) have proposed the use of interaction terms in correlating
binary equilibrium data using the Langmuir equation for mixtures.
The Langmuir equation is derived by considering the adsorbed
phase as a two-dimensional mobile monolayer, and a correction
term analogous to the Van-der Waal's term in the three-
dimensional gas phase is applied to correct for the surface
area occupied by the adsorbed molecules. The resulting expres-
sion for the Langmuir isotherm is given by the following
equation:

$$q_i = \frac{Q_i \, b_i' \, (C_i/\eta_i)}{\sum\limits_i (1 + b_i' \, (C_i/\eta_i))} \tag{13}$$

The η_i are interaction terms, one for each solute, and are ob-
tained by correlating the mixture equilibrium data. This
approach was used by Yon and Turnock (13) to correlate equil-
ibrium data for adsorption on molecular sieves. The analogous
expression for the three parameter isotherm is given by:

$$q_i = \frac{a_i \, (C_i/\eta_i)}{\sum\limits_i (1 + b_i \, (C_i/\eta_i)^{\beta_i})} \tag{14}$$

This method, while strictly empirical, allows the use of mixture
equilibrium data in the multicomponent rate model discussed

earlier. The constants a_i, b_i and β_i for each solute are obtain-
ed from single solute equilibrium data. The n_i are obtained from
mixture equilibrium data using the above a_i, b_i and β_i developed
for each solute species in the parameter estimation procedure.

Adsorption equilibria for the systems phenol-p-toluene
sulfonate, phenol-p-bromophenol and phenol-dodecyl benzene sul-
fonate are shown in Figures 5, 6 and 7. In these figures, the
ratio of the observed equilibrium values and computed values
from equation (14) are plotted against the equilibrium liquid
phase concentration of the solute in the mixture. It is seen
that most of the data points are well within a deviation of ±20%.
The results for these diverse solute systems indicate that equa-
tion (14) is suitable for correlating binary equilibrium data
for use in multicomponent rate models.

Estimation of Rate Parameters

The rate parameters of importance in the multicomponent rate
model are the mass transfer coefficients and surface diffusion
coefficients for each solute species. For accurate description
of the multicomponent rate kinetics, it is necessary that accur-
ate values are used for these parameters. It was shown by
Mathews and Weber (14), that a deviation of ±20% in mass transfer
coefficients can have significant effects on the predicted ad-
sorption rate profiles. Several mass transfer correlation
studies were examined for estimating the mass transfer coef-
ficients (15,16,17,18,19). The correlation of Calderbank and
Moo-Young (16) based on Kolmogaroff's theory of local isotropic
turbulence has a standard deviation of 66%. The slip velocity
method of Harriott (17) provides correlation with an average
deviation of 39%. Brian and Hales (15) could not obtain super-
imposable curves from heat and mass transfer studies, and the
mass transfer data was not in agreement with that of Harriott
for high Schmidt number values.

For this study, mass transfer and surface diffusions coef-
ficients were estimated for each species from single solute
batch reactor data by utilizing the multicomponent rate equa-
tions for each solute. A numerical procedure was employed to
solve the single solute rate equations, and this was coupled
with a parameter estimation procedure to estimate the mass
transfer and surface diffusion coefficients (20). The program
uses the principal axis method of Brent (21) for finding the
minimum of a function, and searches for parameter values of mass
transfer and surface diffusion coefficients that will minimize
the sum of the square of the difference between experimental and
computed values of adsorption rates. The mass transfer and
surface coefficients estimated for each solute are shown in Table
2. These estimated coefficients were tested with other single
solute rate experiments with different initial concentrations
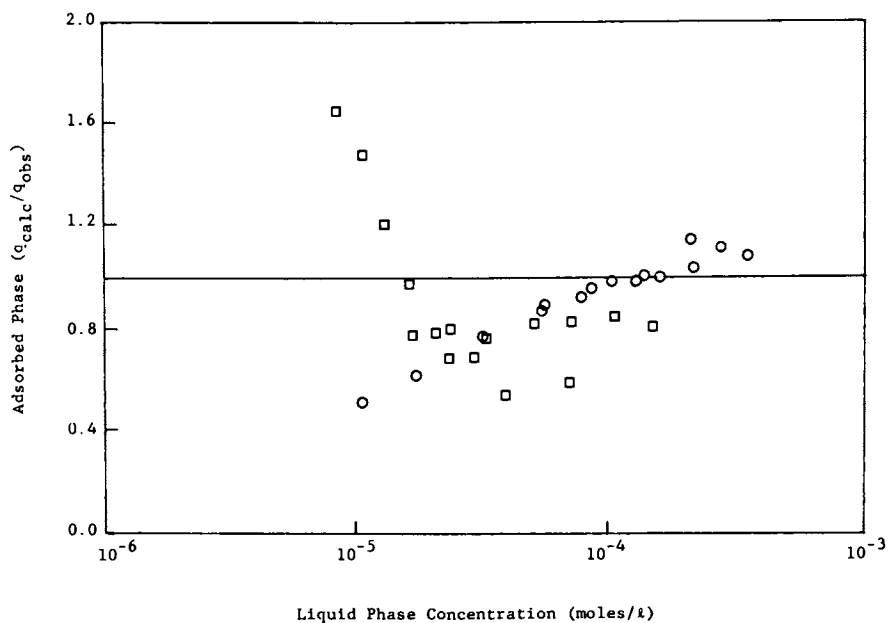and different amounts of adsorbent and were found to predict

Figure 5. Adsorption equilibria for phenol and p-toluene sulfonate mixtures: (□) phenol, (○) p-toluene sulfonate
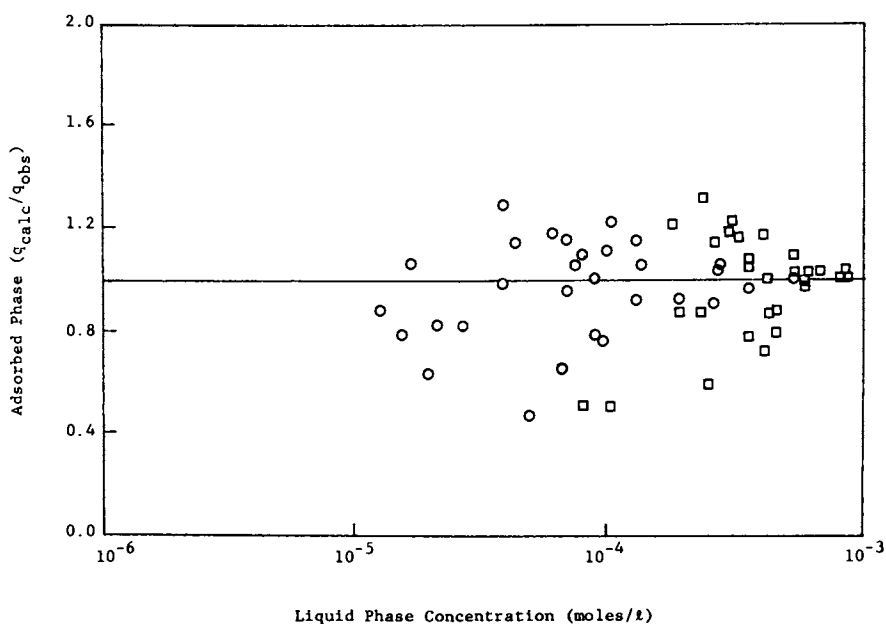

Figure 6. Adsorption equilibria for phenol and p-bromophenol mixtures: (□) phenol, (○) p-bromophenol
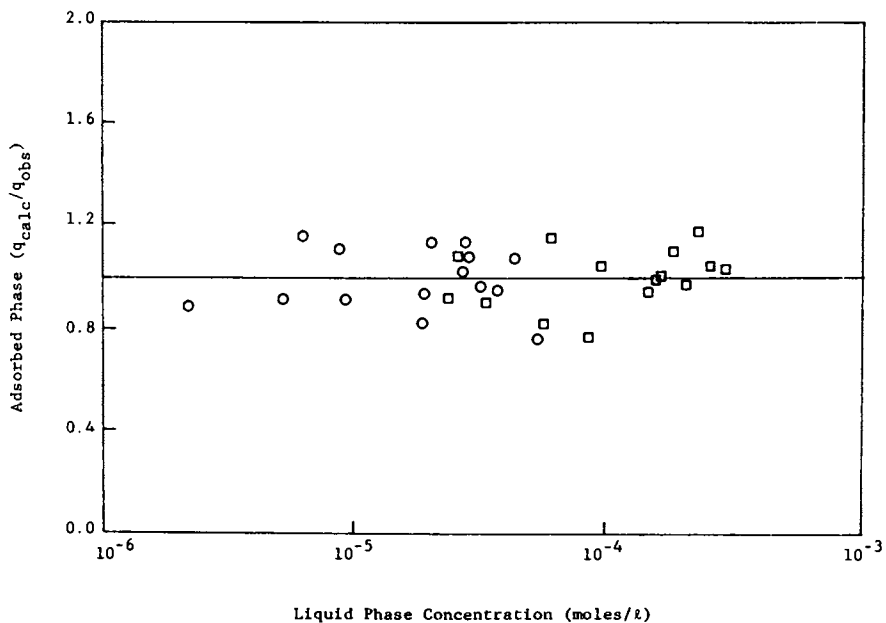
Figure 7. *Adsorption equilibria for phenol and dodecyl benzene sulfonate mixtures: (□) phenol, (○) dodecyl benzene sulfonate*

rates in excellent agreement with experimental data.

<div align="center">

TABLE 2

Mass Transfer and Surface
Diffusion Coefficients

</div>

Solute	k_f cm/sec	D cm^2/sec
Phenol	5.10×10^{-3}	1.38×10^{-8}
P-Bromophenol	5.40×10^{-3}	1.58×10^{-8}
p-Toluene Sulfonate	4.80×10^{-3}	1.70×10^{-8}
Dodecyl Benzone Sulfonate	2.21×10^{-3}	9.86×10^{-10}

Method of Solution of Multicomponent Model Equations

The system of equations (1) to (10) cannot be solved analytically, and finite different techniques must be employed. These equations are simplified by the introduction of dimensionless variables $\tau = Dt/R^2$, $x = r/R$, and the change of variable $u_k = xq_{ik}$ to the set of equations (15) to (19).

$$\frac{\delta u_k}{\delta \tau} = \bar{v}_k \left(\frac{\delta^2 u_k}{\delta x^2}\right) \tag{15}$$

$$\bar{v}_k = \frac{D_k}{D_1} \tag{16}$$

$$u_k(0,\tau) = 0$$
$$u_k(x,0) = 0 \tag{17}$$

$$q_i = 3\int_0^1 u_k x \, dx \tag{18}$$

$$\int_0^1 \frac{\delta u_k}{\delta \tau} x \, dx = \frac{k_{f_k} R (C_k - C_{s_k})}{1000\rho (1-\epsilon)D_k} \tag{19}$$

Denoting the solute species in a binary system by subscripts 1 and 2, the Crank-Nicholson finite difference approximation for

equation (15) is:

$$-\lambda u_{1_{j+1}}^{n+1} + (1+2\lambda)u_{1_j}^{n+1} - \lambda u_{1_{j-1}}^{n+1} =$$

$$\lambda u_{1_{j+1}}^{n} + (1-2\lambda)u_{1_j}^{n} + \lambda u_{1_{j-1}}^{n}, \qquad \begin{array}{l} j = 1, M \\ n = 1, N \end{array} \qquad (20)$$

$$-\nu' u_{2_{j+1}}^{n+1} + (1+2\nu')u_{2_j}^{n+1} - \nu' u_{2_{j-1}}^{n+1} =$$

$$\nu' u_{2_{j+1}}^{n} + (1-2\nu')u_{2_j}^{n} + \nu' u_{2_{j-1}}^{n} \qquad \begin{array}{l} j = 1, M \\ n = 1, N \end{array} \qquad (21)$$

where, $\nu' = \lambda \bar{\nu}$.

The subscripts n and j in these equations refer to the time and distance steps $\Delta\tau$ and Δx, and $\lambda = \Delta\tau/2(\Delta x)^2$. N is the number of time steps and M+1 is the number of distance steps.

The integrals in equation (18) and (19) are evaluated using the Trapezoidal rule. These equations for each solute species are then:

$$q_1 = 3(\Delta x)^2 \; (\sum_{j=2}^{M} u_{1_j} \; (j-1) + u_{1_{M+1}} \frac{M}{2}) \qquad (22)$$

$$u_{1_{M+1}}^{n+1} + \frac{2}{M} \sum_{j=2}^{M} u_{1_j}^{n+1} \; (j-1) = \frac{(4\lambda/M)k_{f1}R}{1000\rho(1-\epsilon)D_1} \; (C_1 - C_{s1}) +$$

$$\frac{2}{M} \sum_{j=2}^{M} u_{1_j}^{n} \; (j-1) + u_{1_{M+1}}^{n} \qquad (23)$$

The corresponding equations for solute 2 are,

$$q_2 = 3(\Delta x)^2 \; (\sum_{j=2}^{M} u_{2_j} \; (j-1) + u_{2_{M+1}} \frac{M}{2}) \qquad (24)$$

$$u_{2_{M+1}}^{n+1} + \frac{2}{M} \sum_{j=2}^{M} u_{2_j}^{n+1} \; (j-1) = \frac{(4\lambda/M)k_{f2}R}{1000\rho(1-\epsilon)D_1} \; (C_2 - C_{s2}) +$$

$$\frac{2}{M} \sum_{j=2}^{M} u_{2_j}^{n} \; (j-1) + u_{2_{M+1}}^{n} \qquad (25)$$

The initial and boundary conditions for each solute are:

$$u_{1_1}^n = u_{2_1}^n = 0 \tag{26}$$

$$u_1^1 = u_2^1 = 0 \tag{27}$$

$$C_1(o) = C_{1_o}$$

$$\tag{28}$$

$$C_2(o) = C_{2_o}$$

The finite difference equations for the fluid phase are:

$$C_1^{n+1} = C_1^n - \frac{W}{V}(q_1^{n+1} - q_1^n) \tag{29}$$

$$C_2^{n+1} = C_2^n - \frac{W}{V}(q_2^{n+1} - q_2^n) \tag{30}$$

The equilibrium surface concentrations on the solid phase q_{s1} and q_{s2} are given by equation (3). To obtain the concentrations C_{s1} and C_{s2} in the fluid phase, the two equations in equation (3) must be solved at each time step. This was done using the Newton-Raphson Method for solving nonlinear equations.

The equations (20) to (30) provide the basis for predicting the adsorption rate profiles for the binary system. The input parameters required for the model are the single-solute film transfer and surface diffusion coefficients, the single-solute isotherm constants and the mixture equilibria coefficients. The rate parameters were obtained from single solute rate data (20), and the equilibrium parameters were obtained from single and multi-solute equilibrium data.

Experimental Methods

The adsorbent used in this study is Filtrasorb 400 activated carbon obtained from Calgon Corporation, Pittsburg, Pennsylvania. The adsorbent was sieved and the size fraction 30/35 mesh – particles passing 30 mesh sieve and retained on a 35 mesh sieve – was used in all rate studies. Adsorption equilibrium is independent of particle size, and equilibrium data were obtained with both 30/35 and 60/100 mesh size fractions. The carbon was washed in distilled water to remove fines and leachable material and dried to constant weight at 105°C prior to use.

Crystalline p-bromophenol and p-toluene sulfonate were obtained in reagent grade form from Eastman Kodak Company. Reagent grade phenol was obtained from Mallinckrodt Chemical Works.

Sodium dodecyl benzene sulfonate was obtained from K & K Labora-
tories, Cleveland, Ohio, and consisted of a mixture of isomers.

All the solutes investigated show peak absorption in the
ultraviolet region, and were analyzed using ultraviolet absorp-
tion spectrophotometry. The absorbance-concentration calibration
curve followed Beer's law for single solutes. Calibration curves
were prepared for each solute at the two wavelengths correspond-
ing to the peak absorption wavelength for each solute in the
mixture. Two equations satisfying Beer's law can be set up for
a binary system at the two wavelengths, and these equations can
be solved to obtain concentration of each solute in the mixture.

Single and multicomponent equilibrium data were obtained
using the bottle-point method. A series of 100-ml aliquots of
known adsorbate concentration were added to 120 ml glass bottles
containing carefully weighed amounts of the adsorbent. The
bottles were tightly sealed with polyethylene caps and placed in
a tumbler to provide agitation. Blanks containing solution with-
out carbon were included, and served as a check on degradation
of organic material or adsorption on glass.

After equilibrium was attained over a period of several
days, the carbon was allowed to settle, and the supernatant
analyzed to determine the decrease on concentration ΔC by ad-
sorption. For dilute solutions, a Radke and Prausnitz (11) have
shown that the equilibrium adsorbent phase concentration are
given by

$$q_e = \frac{V}{W} \Delta C \qquad (31)$$

is equal to the invariant adsorption of the solute, independent
of the Gibbs dividing surface.

The rate experiments were carried out in 3.5 liter glass
jars covered with a plexiglass lid. Two baffles of 2 cm width
extended from the lid to 1 cm from the bottom of the reactor.
Agitation was provided by a stirring motor with polyethylene
stirrers, and the speed of the motor was controlled with a
variac. Three liters of solution without the adsorbent particles
was agitated, and allowed to reach equilibrium with the vessel
before withdrawing the initial sample for analysis. At time
t = 0, a measured quantity of activated carbon was introduced
into the reactor and agitated. Samples, 10 ml each were with-
drawn periodically, until equilibrium was reached, and analyzed
for the solute concentration in the liquid phase. The numerical
procedure developed earlier was adjusted to allow for the volume
reduction due to the withdrawal of samples at discrete time
intervals.

Experimental Results

The capability of the model to predict adsorption rates was

examined for the three solute mixture systems, phelol-p-toluene
sulfonate, phenol-P-bromophenol, and phenol-dodecyl benzene
sulfonate. The solutes exhibit a wide range of adsorption
behavior, and allow testing of the ability of the model to pre-
dict adsorption rates when: (1) the solute species have compar-
able single solute equilibrium and rate characteristics; (2)
comparable diffusion rates, but differing equilibrium character-
istics; and (3) differing diffusion rates and equilibria.
     As seen from Table 2, phenol, p-toluene sulfonate and
p-bromophenol have similar adsorption rate characteristics. The
equilibrium data for these solutes indicate that phenol and
p-toluene sulfonate have similar energies of adsorption (24),
as indicated by the constant b in the component isotherm
($q_e = Qb_Lc_e/(1 + b_Lc_e)$). p-bromophenol and dodecyl benzene
sulfonate are adsorbed more strongly than phenol (22).
     The experimental data for adsorption rates of phenol and
p-toluene sulfonate from a equimolar mixture of concentration
10^{-4} M are shown in Figure 8. The carbon dosage used in 0.67
gm/l. The solid and dotted lines are the model predictions for
phenol and p-toluene sulfonate, respectively. The experimental
and predicted profiles are in excellent agreement. The total
mixture concentration in the liquid phase is plotted in Figure
10 and shows good agreement with the predicted curve. The
results from a rate study with differing initial concentrations,
5×10^{-5} M for phenol and 2.5×10^{-5} M for p-toluene sulfonate
are shown in Figures 9 and 10. The predicted profiles are in
excellent agreement with the experimental curves. The model
verifications indicate that the representations of the rate
mechanisms are adequate. The introparticle diffusion rate is
characterized by the surface diffusion coefficient, and this
coefficient is invariant with particle diameter or initial
concentration of the solute. This obviates the necessity for
correlations between the internal diffusion rate and the vari-
ables initial concentration and particle diameter when using the
modeling approach of Hiester and Vermuelen (23) and Keinath and
Weber (24). Keinath and Weber (24) conducted a large number of
rate experiments to correlate particle size and initial solute
concentration with internal diffusion rates, and developed the
following correlating for the solute dintro-o-sec-butyl phenol.

$$\frac{d(q)^2}{dt} = 2.08 \ Co/d^{1.4} \tag{32}$$

Co is the initial solute concentration and d is the adsorbent
particle diameter. Such correlations, particularly for the
initial concentrations are restricted to the solutes being
studied.
     Thus, for solutes with comparable rate and equilibrium
characteristics, the model predictions are in excellent agree-
ment with the experimental data. The effect of assuming
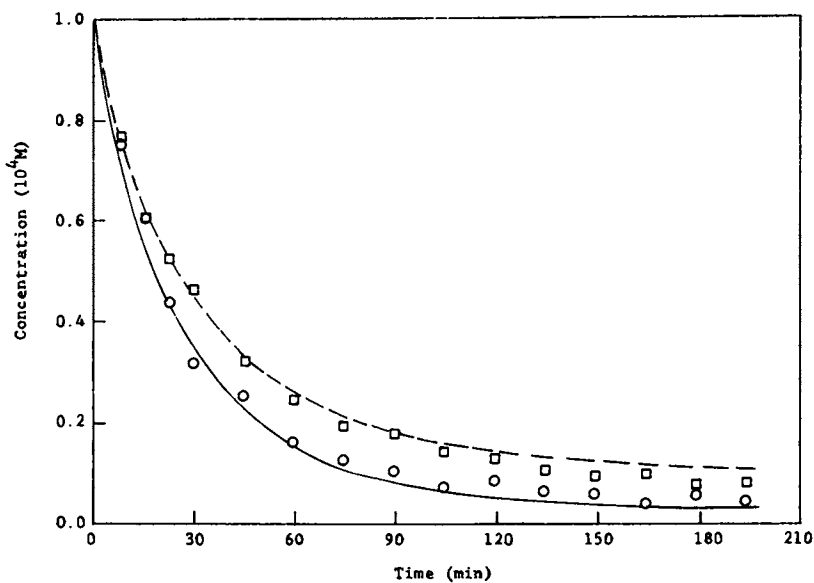
Figure 8. *Adsorption rates from phenol and p-toluene sulfonate mixtures:* (○) *experimental data, and* (———) *predicted rate for phenol;* (□) *experimental data and* (— —) *predicted rate for p-toluene sulfonate* ($C_{10} = C_{20} = 10^{-4}M$, *carbon =* 0.67 g/L)

Figure 9. Adsorption rates from phenol and p-toluene sulfonate mixtures: (O) experimental data and (——) predicted rate for phenol; (□) experimental data and (— —) predicted rate for p-toluene sulfonate ($C_{10} = 5 \times 10^{-5}$M, $C_{20} = 2.5 \times 10^{-5}$M, carbon = 0.33 g/L)

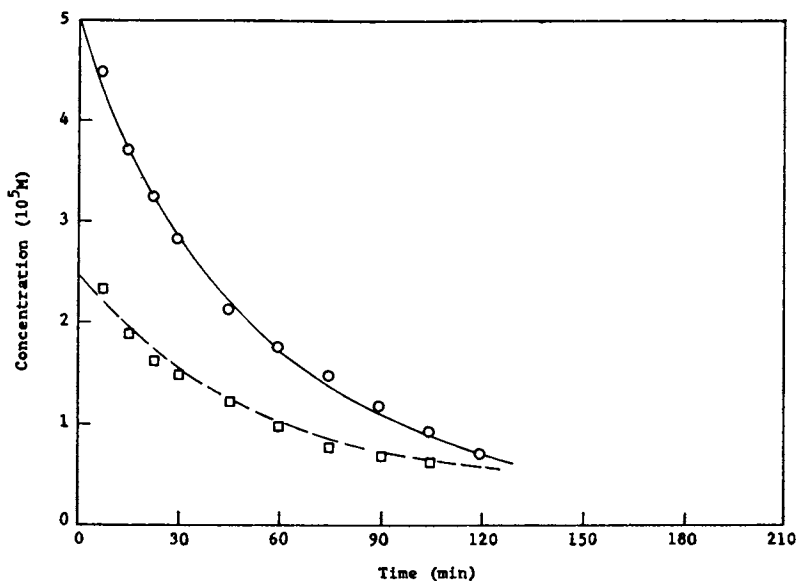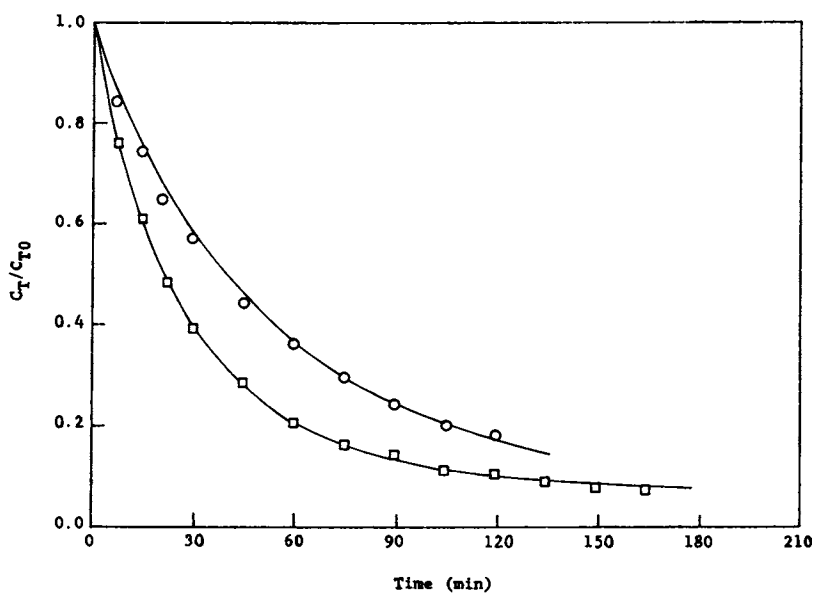Figure 10. Total concentration rate profile for adsorption from phenol and p-toluene sulfonate mixtures: (□) experimental data of Figure 8, (O) experimental data of Figure 9, (——) predicted rate

negligible internal diffusion resistance, is shown for the
phenol-p-toluene mixture in Figure 11. The solid lines represent
the predicted concentrations using the two-resistance model, and
the dotted lines represent film-diffusion controlled adsorption.
It is seen that the curves agree only up to the initial 15 min-
utes of the study. The two-resistance model thus provides a
much better representation of the adsorption rates. Furusawa
and Smith (25) have found this to be true for even small particle
sizes, ranging from 200 to 900 microns in diameter.

The experimental and predicted profiles for the adsorption
rates of phenol and p-bromophenol from an equimolar mixture of
concentration 5×10^{-4} M are shown in Figure 12. The predicted
profile for p-bromophenol is in excellent agreement with the
experimental data. However, for phenol there is some deviation
after the initial time period. The experimental adsorption rate
for phenol appears to be faster than predicted for about 60
minutes after the first 15 minutes. Thereafter, the rate is
slightly slower than predicted. From an examination of the
binary equilibrium data, this deviation may be attributed to the
inadequate correlation of the mixture equilibrium data in this
region. The predicted and experimental total concentration pro-
files are shown in Figure 13. Initial concentrations of 2.5 x
10^{-4} M for phenol, and 5×10^{-4} M for p-bromphenol were used in
another rate study, the data from which are shown in Figures 13
and 14. The experimental and predicted curves are in fair
agreement.

Phenol and dodecyl benzene sulfonate are two solutes that
have markedly different adsorption characteristics. The surface
diffusion coefficient of phenol is about fourteen times greater
than that for dodecyl benzene sulfonate. The equilibrium ad-
sorption constants indicate that dodecyl benzene sulfonate has
a much higher energy of adsorption than phenol (20,22). The
adsorption rates from a mixture of these solutes can be predicted
accurately, if (1) an adequate representation is obtained for the
mixture equilibria, and (2) the diffusion rates in the solid and
fluid phases are not affected by solute-solute interactions.

The experimental and predicted profiles for adsorption from
a mixture 5×10^{-5} M phenol and 5×10^{-5} M dodecyl benzene sul-
fonate are shown in Figure 15. The rate of adsorption of dodecyl
benzene sulfonate is faster than predicted, and for phenol, the
rate is slower than predicted. However, the shape of the pre-
dicted profiles for both solutes closely parallel the experi-
mental curves. Similar trends may be noted in Figure 16 for the
adsorption rates from a 10^{-4} M phenol and 10^{-4} M dodecyl benzene
sulfonate mixture. The mixture equilibrium data for these sol-
utes have been correlated satisfactorily. Thus, it would appear
that solute-solute interactions are affecting the diffusional
flux of each solute. Moreover, from Figure 17 for the total con-
centrations, it may be seen that the interaction effects are
mutually compensating. The total concentration profiles for both
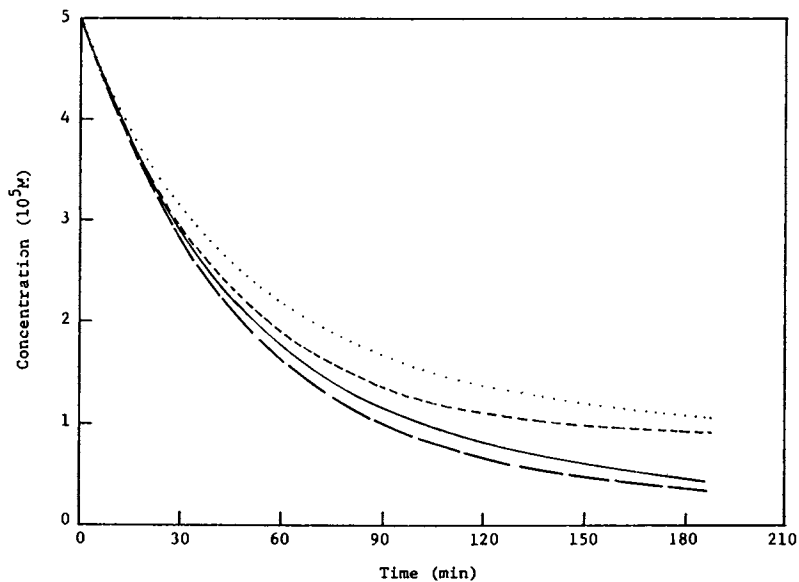
Figure 11. Effect of intraparticle diffusion on adsorption rates from mixtures: 2-resistance model, (———) phenol ($k_f = 5.1 \times 10^{-3}$ cm/sec, $D = 1.38 \times 10^{-8}$ cm²/sec) and (. . .) p-toluene sulfonate ($k_f = 4.8 \times 10^{-3}$ cm/sec, $D = 1.7 \times 10^{-8}$ cm²/sec); negligible intraparticle diffusion, (— —) phenol ($k_f = 5.1 \times 10^{-3}$ cm/sec) and (— — —) p-toluene sulfonate ($k_f = 4.8 \times 10^{-3}$ cm/sec)
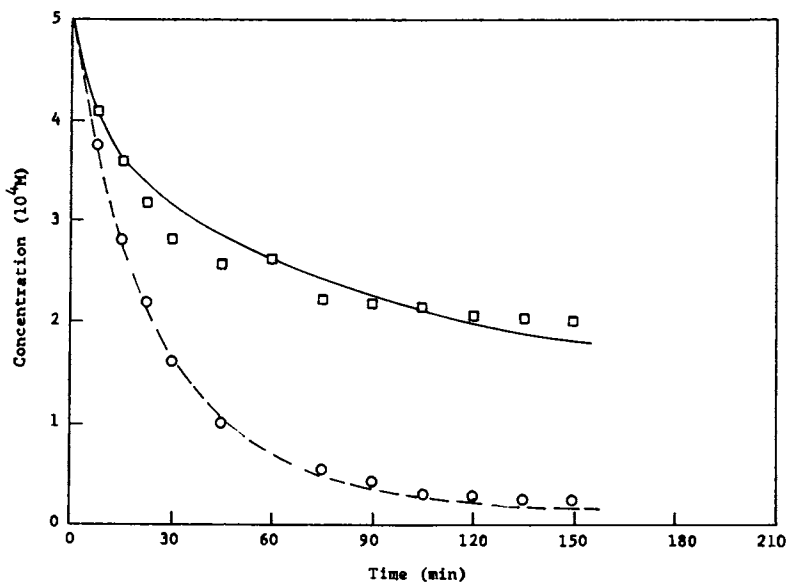
Figure 12. Adsorption rates from phenol and p-bromophenol mixtures: (□) experimental data and (———) predicted rate for phenol; (○) experimental data and (— —) predicted rate for p-bromophenol ($C_{10} = C_{20} = 5 \times 10^{-4}$M, carbon = 0.67 g/L)
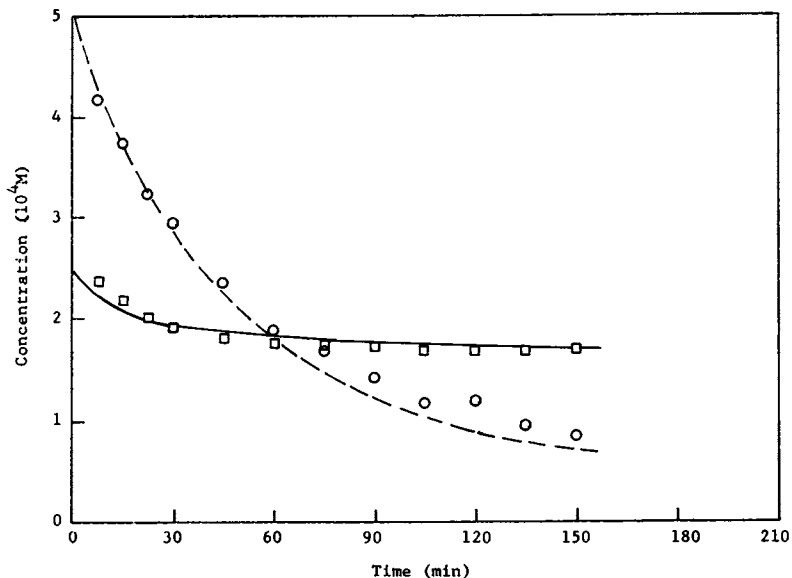
Figure 13.   Adsorption rates from phenol and p-bromophenol mixtures: (□) experimental data and (——) predicted rate for phenol; (○) experimental data and (— —) predicted rate for p-bromophenol ($C_{10} = 2.5 \times 10^{-4}M$, $C_{20} = 5 \times 10^{-4}M$, carbon = 0.33 g/L)
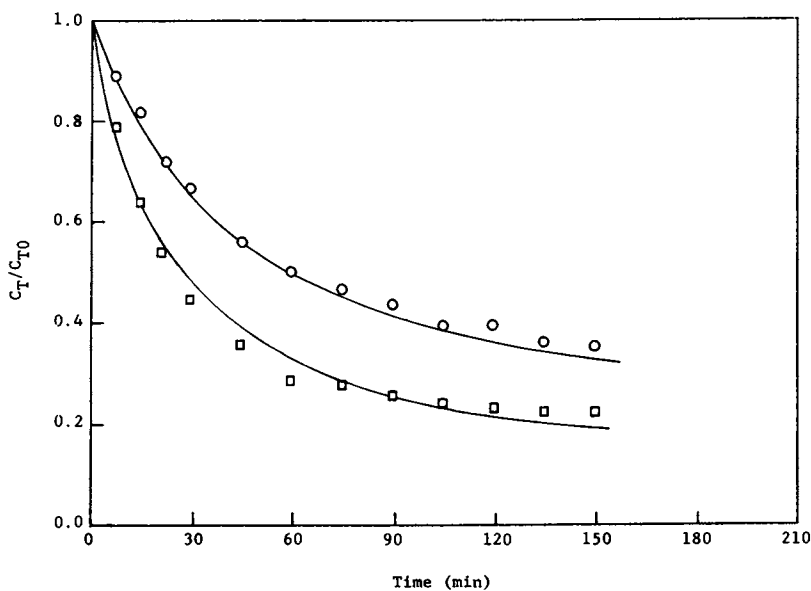
Figure 14.   Total concentration rate profile for adsorption from phenol and p-bromophenol mixtures: (□ and ○ respectively) data of Figure 13, (——) predicted
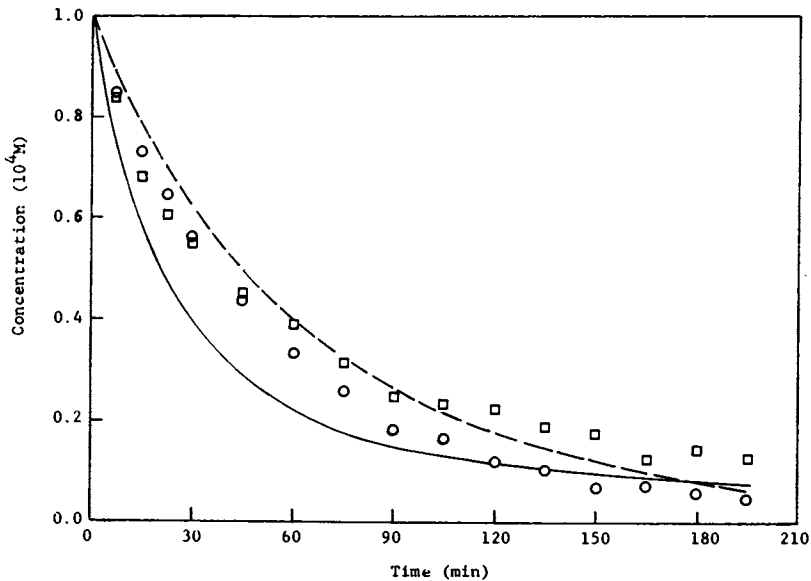
*Figure 15. Adsorption rates from phenol and dodecyl benzene sulfonate mixtures:
(□) experimental data and (———) predicted rate for phenol; (○) experimental data
and (— —) predicted rate for dodecyl benzene sulfonate ($C_{10} = C_{20} = 10^{-4}M$,
carbon = 0.67 g/L)*
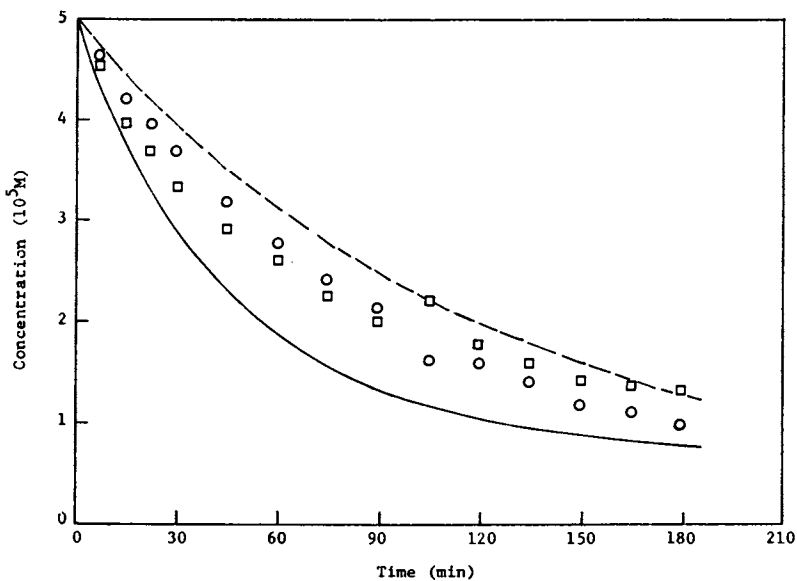
*Figure 16. Adsorption rates from phenol and dodecyl benzene sulfonate mixtures:
(□) experimental data and (———) predicted rate for phenol; (○) experimental
data and (— —) predicted rate for dodecyl benzene sulfonate ($C_{10} = C_{20} = 10^{-5}M$,
carbon = 0.33 g/L)*

experimental runs agree well with the predicted profiles.

Solute-solute interactions may affect the diffusion rates in the fluid phase, the solid phase, or both. Toor (26) has used the Stefan-Maxwell equations for steady state mass transfer in multicomponent systems to show that, in the extreme, four differ-ent types of diffusion may occur: (1) diffusion barrier, where the rate of diffusion of a component is zero even though its gradient is not zero; (2) osmotic diffusion, where the diffusion rate of a component is not zero even though the gradient is zero; (3) reverse diffusion, where diffusion occurs against the concen-tration gradient; and, (4) normal diffusion, where diffusion occurs in the direction of the gradient. While such extreme effects are not apparent in this system, it is evident that the adsorption rate of phenol is decreased by dodecyl benzene sul-fonate, and that of dodecyl benzene sulfonate increased by phenol.

The diffusional flux of each species in a multicomponent system may be derived from nonequilibrium thermodynamics (27), and may be represented by the expression:

$$J_i = \sum_i D_{ij} \, \nabla C_j \tag{33}$$

J_i is the flux of each component in the mixture, and is a func-tion of the gradients ∇C_j of all other components. D_{ii} are the main diffusion coefficients and D_{ij} representing interaction, are the cross diffusion coefficients. There are three independ-ent diffusion coefficients for a binary system and these, in general, vary with the concentration of the components. Kinetic theory of gases may be used to estimate these coefficients for ideal gas mixtures. However, no reliable methods are available for liquid mixtures.

Thus, it is apparent that the inclusion of interaction effects in a multicomponent adsorption model would pose formid-able problems in mathematical analysis, and in the application of the model. The phenol-dodecyl benzene sulfonate system may be analyzed qualitatively by examining the initial rates of the components in Figures 15 and 16. From the two rate studies, an average mass transfer coefficient of 2.97×10^{-3} cm/sec for phenol, and 2.9×10^{-3} cm/sec for dodecyl benzene sulfonate are estimated. When these values are used for the mass transfer coefficients in the multicomponent rate model, the predicted profiles are in much better agreement with the experimental data. This is shown in Figure 18. It appears thus, that some solute-solute interactions affecting diffusion of each solute is occurring in the boundary layer. Diffusional interactions may be expected to occur in the adsorbed phase also, when the adsorb-ed phase loading becomes substantial.
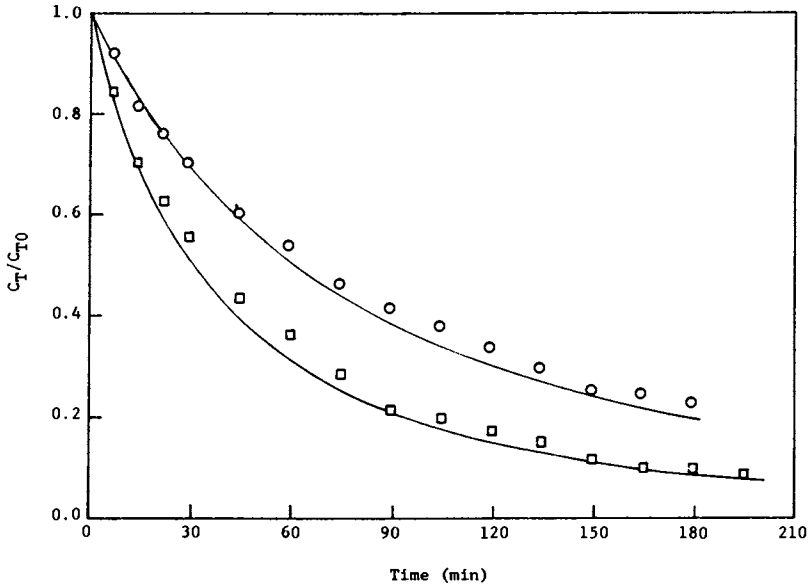
Figure 17.   Total concentration rate profile for adsorption from phenol and dodecyl benzene sulfonate mixtures: (□) data of Figure 15, (○) data of Figure 16, (———) predicted
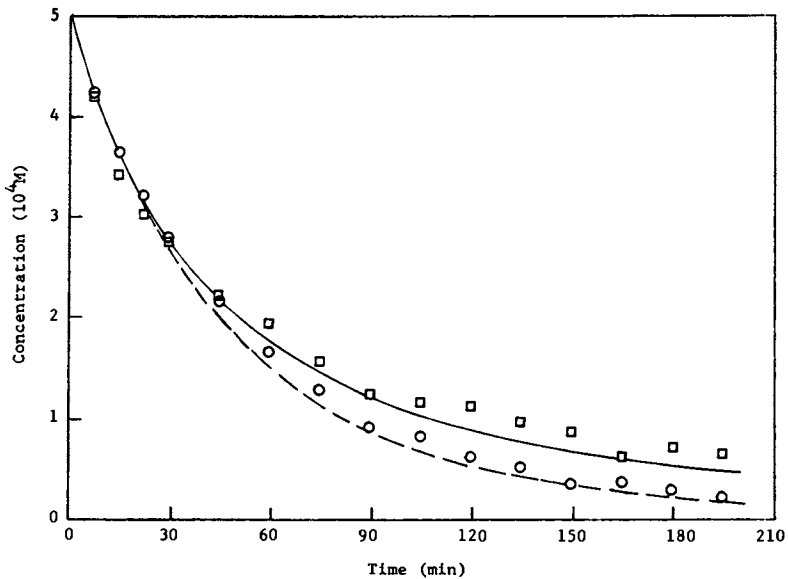
Figure 18.   Adsorption rates from phenol and dodecyl benzene sulfonate mixtures: (□) experimental data and (———) predicted rate using $k_f = 2.97 \times 10^{-3}$ cm/sec for phenol; (○) experimental data and (— —) predicted rate using $k_f = 2.9 \times 10^{-3}$ cm/sec for dodecyl benzene sulfonate

Summary and Conclusions

     A mathematical model has been developed to describe the
kinetics of multicomponent adsorption. The model takes into
account diffusional processes in both the solid and fluid phases,
and nonlinear adsorption equilibrium. Comparison of model pre-
dictions with binary rate data indicates that the model predic-
tions are in excellent for solutes with comparable diffusion rate
characteristics. For solutes with markedly different diffusion
rate constants, solute-solute interactions appear to affect the
diffusional flows. In all cases, the total mixture concentra-
tion profiles predicted compares well with experimental data.
     The basic developments reported herein can be used to pre-
dict multicomponent adsorption rates in different types of con-
tacting units, such as slurry adsorbers, moving bed units and
columnar operation. The adsorption rate and equilibrium equa-
tions would remain the same, but the reactor material balance
equation would be different depending on the reactor type and
geometry. Thus, the multicomponent adsorption model can be
utilized in practical processing applications in the chemical
industry, air pollution control, and water and wastewater treat-
ment.

List of Symbols

a =   three parameter isotherm constant

b =   three parameter isotherm constant

b_L =   Langmuir isotherm constant

C =   concentration of solute in liquid phase, moles/liter

C_s =   equilibrium concentration at the surface in liquid
        phase moles/liter

C_e =   equilibrium concentration in the liquid phase, moles/liter

D =   surface diffusion coefficient cm^2/sec.

k_f =   liquid phase mass transfer coefficient cm/sec.

k_f' =   liquid phase mass transfer coefficient liter/sec.

q =   concentration of solute on the solid phase moles/gm.

q_e =   equilibrium concentration on the solid phase moles/gm.

q_i =   concentration at any point in the particle, moles/gm.

q_s =   equilibrium concentration at the surface on the solid
        phase moles/gm.

Q =   monolayer capacity in Langmuir isotherm

R =   radius of particle

r =   radial coordinate

t   =   time

u   =   transformed solid phase concentration

V   =   reactor volume, liter

V_p =   volume of adsorbent particle

W   =   weight of adsorbent in reactor

x   =   dimensionless distance

Greek Letters

β =   three parameter isotherm constant

ρ =   particle density

ϵ =   particle porosity

η =   interaction parameters for mixture equilibria

τ =   dimensionless time

Literature Cited

1. Collins, H. W., Jr.; Chao, K.; AIChE Symp. Ser., 1973, 69 (134), 10.

2. Zwiebel, I.; Gariepy, R. L.; Schnitzer, J. J.; AIChE J., 1972, 18, 1139.

3. Zwiebel, I.; Kralik, C. M.; Schnitzer, J. J.; AIChE J., 1974, 20, 915.

4. Gariepy, R. L.; Zwiebel, I.; AIChE Symp. Ser., 1971, 67 (117), 17.

5. Usinowicz, P. J.; Weber, W. J., Jr.; Paper presented at the 46th Annual Conference of the Water Pollution Control Federation, October 1972.

6. de Boer, J. H.; "The Dynamical Character of Physical Adsorption," Oxford University Press, London, 1953.

7. Ross, S.; Olivier, J. P.; "On Physical Adsorption," John Wiley & Sons, Inc., New York, 1964.

8. Ruthven, D. M., AIChE J., 1976, 22, 753.

9. Butler, J. A. V.; Ockrent, C.; J. Phys. Chem., 1930, 34, 2841.

10. Jain, J. S.; Snoeyink, V. L.; J. Water Poll. Control Fed., 1972, 45, 2463.

11. Radke, C. J.; Prausnitz, J. M.; AIChE J., 1972, 18, 761.

12. Schay, G. J.; Fejes, F. P.; Szethemary, J.; Acta. Chem. Acad. Sci. Hungary, 1957, 12, 299.

13. Yon, C. M.; Turnock, P. H.; AIChE Symp. Ser., 1971, 67, 75.

14. Mathews, A. P.; Weber, W. J., Jr.; AIChE Symp. Ser., 1977, 73, 91.

15. Brian, P. L. T.; Hales, H. B.; AIChE J., 1969, 15, 419.

16. Calderbank, P. H.; Moo-Young, M. B.; Chem. Eng. Sci., 1961, 16, 39.

17. Harriott, P., AIChE J., 1962, 8, 93.

18. Levins, D. M., ; Gastonbury, J. R.; Chem. Eng. Sci., 1972, 27, 537.

19. Marangozis, J.; Johnson, A. I.; Can. J. Chem. Eng., 1962, 40, 231.

20. Mathews, A. P.; Ph.D. Thesis, University of Michigan, Ann Arbor, Michigan, 1975.

21. Brent, R. P.; "Algorithm for Finding Zeros and Extrema of a Function Without Calculating Derivatives," Stanford University Technical Report CS-198, Stanford, California, 1971.

22. Weber, W. J., Jr.; Morris, J. C.; ASCE, J. Sanit. Eng. Div., 1964, SA3, 79.

23. Hiester, N. K.; Vermuelen, T.; Chem. Eng. Prog., 1952, 48, 505.

24. Keinath, T. M.; Weber, W. J., Jr.; "A Mathematical Model for Prediction of Concentration-Time Profiles for Design of Fluid-Bed Adsorbers," Tech. Publ., Res. Project No. WP-00706, Fed. Water Poll. Control Admin., U.S. Dept. of Interior, April 1968.

25. Furusawa, T.; Smith, J. M.; AIChE J., 1974, 20, 88.

26. Toor, H. L.; AIChE J., 1957, 3, 198.

27. Fitts, D. D.; "Nonequilibrium Thermodynamics," McGraw Hill, New York, 1962.

Study of Mixture Equilibria of Methane and Krypton on 5A Zeolite

K. F. LOUGHLIN

University of Petroleum and Minerals, P.O. Box 144, UPM Box 25, Dhahran, Saudi Arabia

G. D. ROBERTS

Department of Chemical Engineering, The University of New Brunswick, P.O. Box 4400, Fredricton, N.B., Canada, E3B 5L1

Mixture equilibria models, derived from pure component models, inherit the primary assumptions on which the original isotherm is based, augmented by further additions. Limitations applicable to the original pure component models also generally apply to the multicomponent models. For instance isotherms derived based on localized behaviour in the pure state have this same premise in the multicomponent state. Among the simple adsorption theories for both pure and multicomponent systems, the Langmuir models envisage localized behaviour, the B.E.T. isotherms multilayered behaviour, the Polyani theory the potential theory, and among isotherms specifically applicable to molecular sieves, the Ruthven isotherm models (1, 2) assume non-localized sorption within the cavities.

A mixture equilibria model which is not based on any specific isotherm model does not have the limitations expressed in the derivation of such a model. The Ideal Adsorbed Solution Theory of Myers et al. (3) is based on the equivalence of the spreading pressures and does not presuppose any isotherm model. In fact, in the original papers, Glessner and Myers (4) stipulated that the model should only be applied using raw equilibrium data to calculate the spreading pressures. This is a very restrictive covenant and does not permit the use of the model for predictive purposes other than that for which data are available. However various authors have applied the Ideal Adsorbed Solution Theory (IAST) model using isotherm models (5, 6) quite satisfactorily.

The isotherm model of Schirmer et al. (7) for sorption in molecular sieves is based on statistical thermodynamics in which the configuration integrals describing the sorption behaviour are extracted from the available data. The model does not presuppose any specific kind of sorption mechanism. The multicomponent form of this isotherm derived by Loughlin and Roberts (8) is also not limited to any particular sorption mechanism,

and may be used, analogously to IAST, to calculate the multi-component equilibria for different sorption mechanisms.

In this paper we report experimental and theoretical results on the sorption of methane and krypton on 5A zeolite. The sorption of methane in the 5A cavity is reported to be non-localized (9), whereas that of krypton is localized at a cavity site and window site (10). The multicomponent form of the isotherm of Schirmer et al. is used to interpret the experimental data and to predict mixture equilibria at other concentrations.

Theory

In the model of Schirmer et al. (7) for sorption in zeolites, the canonical partition function q(i) is expressed as

$$q(i)\lambda^i = (P/RT)^i q_{i,conf} \tag{1}$$

assuming the residual contributions of moments, rotations and internal motions are unchanged in moving from the gas to the sorbed phase. They replace the integral expressions for $q_{i,conf}$ by finite sums as

$$q(i)\lambda^i = \left(\frac{P/P_o}{T/T_o}\right)^i \sum_{j=1}^{k} \exp\left\{i\left[\frac{S_{ij}T - E_{ij}}{RT}\right]\right\} \tag{2}$$

where the S_{ij} are constants representing the (T, V_o) standard difference of entropy, and the E_{ij} are energy constants for corresponding levels.

The resulting isotherm is

$$C = \frac{\sum_{i=1}^{m} i\left(\frac{P/P_o}{T/T_o}\right)^i \sum_{j=1}^{k} \exp\left\{i\left[\frac{S_{ij}T - E_{ij}}{RT}\right]\right\}}{1 + \sum_{i=1}^{m} \left(\frac{P/P_o}{T/T_o}\right)^i \sum_{j=1}^{k} \exp\left\{i\left[\frac{S_{ij}T - E_{ij}}{RT}\right]\right\}} \tag{3}$$

For a cavity which is energetically homogeneous the isotherm reduces to

$$C = \frac{\sum_{i=1}^{m} i\left(\frac{P/P_o}{T/T_o}\right)^i \exp\left\{i\left[\frac{S_i T - E_i}{RT}\right]\right\}}{1 + \sum_{i=1}^{m} \left(\frac{P/P_o}{T/T_o}\right)^i \exp\left\{i\left[\frac{S_i T - E_i}{RT}\right]\right\}} \tag{4}$$

The index m, representing the maximum sorption in the cavity, may be derived from considerations of the zeolitic cavity volume and molar volume of the sorbate, as $m \leq v/\beta$. However Schirmer et al. ($\underline{7}$) state that a maximum of 6 terms has been used in their work.

The extension of this model to a multicomponent sorbate is straightforward, and presented elsewhere by the authors ($\underline{8}$). The binary isotherm equation is

$$C_A = \frac{\displaystyle\sum_{j=o}^{n}\sum_{i=o}^{m} i\left(\frac{P_A/P_o}{T/T_o}\right)^i \left(\frac{P_B/P_o}{T/T_o}\right)^j \exp\left\{\ell\left[\frac{S_\ell T - E_\ell}{RT}\right]\right\}}{\displaystyle\sum_{j=o}^{n}\sum_{i=o}^{m} \left(\frac{P_A/P_o}{T/T_o}\right)^i \left(\frac{P_B/P_o}{T/T_o}\right)^j \exp\left\{\ell\left[\frac{S_\ell T - E_\ell}{RT}\right]\right\}} \tag{5}$$

$$S_\ell = \frac{1}{\ell}\left[iS_{A\ell} + jS_{B\ell} + R\ell n\,\frac{\ell!}{i!j!}\right] \tag{6}$$

$$E_\ell = \frac{1}{\ell}\left[iE_{A\ell} + jE_{B\ell} + E_M\right] \tag{7}$$

and the summations are now carried out over all values satisfying the restriction $i\beta_A + j\beta_B \leq v$ with a similar expression for C_B. E_m, the excess energy due to heat of mixing, is equal to zero for an ideal solution.

Schirmer et al. ($\underline{7}$) indicate that the constants S_{ij} and E_{ij} may be derived from physical or statistical thermodynamic considerations but do not advise this procedure since theoretical calculations of molecules occluded in zeolites are, at present, at least only approximate, and it is in practice generally more convenient to determine the constants by matching the theoretical equations to experimental isotherms. We have determined the constants in the model by a method of parameter determination using the measured equilibrium data. Defining the entropy constants and energy constants as vectors

$$\underline{S} = (S_1, S_2 \ldots \ldots \ldots S_m)^T \tag{8}$$

$$\underline{E} = (E_1, E_2 \ldots \ldots \ldots E_m)^T \tag{9}$$

the energy and entropy vectors may be optimized using the available pure component data and any suitable optimization technique. In this procedure, the components of the entropy vector should be restricted to have an order $S_1 > S_2 > S_3 \ldots > S_m$ on the basis of thermodynamic considerations. In our optimization

we initially specified the energy vector components equal
(E_1 = E_2 = E_3 = ...E_m) and equivalent to the negative of
the heat of sorption where known.

Apparatus, Materials and Procedure

     The apparatus, which is shown diagrammatically in
Figure 1, is similar to that discussed in the paper by Loughlin
et al. (11) with two modifications. Chambers E and C are
connected by a second path containing an impeller pump, which
is magnetically stirred, and the Barocel pressure transducer
has been removed. A 100 cm Eberbach cathetometer, subdivided to
1 mm, and having a vernier capable of being read to 0.1 mm, is
used to read a manometer for pressure measurement. The remaining
equipment is the same as reported previously (11).
     The sorbent was Linde 5A powder and the sorbates were
Matheson research grade methane (purity 99% +) and Matheson
research grade krypton (purity 99.99% +).
     The procedure adopted was similar to that reported
earlier (11) except that the mixture measurements were all
performed at 97.36 kPa and the gas phase was continuously
circulated between chambers E and C during runs to ensure
uniformity of composition. The pressure was recorded using the
manometer in chamber A, opened to chamber C; to ensure uniformity
of gas phase composition, the mercury reservoir R was period-
ically raised and lowered, exchanging the gas in the top of
chamber A with that in chamber C.

Results and Discussion

     Mixture equilibria isotherms were obtained for the
methane-krypton Linde 5A system at 238,255 and 271K at a total
pressure of 97.36 kPa. At each experimental point, the gas phase
composition (Y_A, Y_B) and the number of moles of each component
adsorbed were recorded.
     By reversing the order in which the gases are introduced
a very sensitive test of reproducibility is provided. The
experimental data are shown in Figures 2a to 2f. The order of
contacting, whether starting with krypton or methane, is
indicated by a O, ● or X, ✶ symbol. The experimental data shown
are independent of the order of contacting, demonstrating the
consistency of the data.
     The range of sorbate coverage is from 15% at the highest
temperature (271K) to 40% at the lowest temperature (238K). For
this system saturation coverage is 12 molecules/cavity for
either component. At 271 and 255K the total amount adsorbed
increases continuously with increasing mole fraction of methane,
whereas at 238K the total amount adsorbed passes through a
maximum at 60% methane in the adsorbed phase. This difference
is also reflected in the X, Y diagram which is symmetric at 271
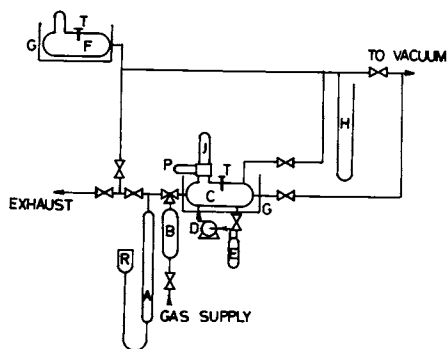
Figure 1.   Schematic of apparatus: A, calibrated variable-volume mercury burette; B, reference volume; C, main chamber; D, mixing pump; E, adsorption chamber; F, reference chamber; G, constant temperature baths; H, mercury manometer; J, cold-cathode gauge; P, Pirani vacuum gauge; R, mercury reservoir
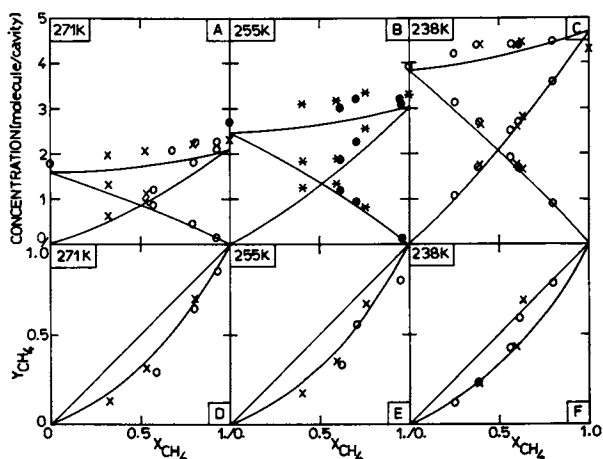
Figure 2.   Mixture equilibria diagrams for sorption of CH₄ and Kr on linde 5A sieve at 730 torr; (○, ●, x, *) data of Roberts, (————) theoretical curves calculated using Equation 5

and 255K but distinctly asymmetric at 238K (see Figures 2d, 2e
and 2f). It appears that at the lowest temperature no separation
is obtained above 60% sorbate concentration of methane in the
adsorbed phase.

   Roberts (18) indicates that each experimental point took
3 or 4 days to attain equilibrium in this portion of Figure 2f,
whereas for the other experimental data equilibrium was achieved
in under six hours. He postulates that during this time there
may have been a zero drift in the thermistor for measuring
composition.

   The system methane-krypton 5A was selected for study
because previous pure component studies for each of these
sorbates on Linde 5A zeolite indicate that the sorption mechanisms
are significantly different.

   According to the experimental and theoretical studies of
Ruthven and Loughlin (9), the sorption of methane is non-
localized within the 5A cavity, whereas the studies of Ruthven
and Derrah (12) indicate that the sorption of krypton appears
to be localized at either of two sites, the window sites capable
of sustaining 3 molecules per cavity or the cavity site capable
of sustaining 9 molecules per cavity. As both molecules have
similar molecular volumes, and as the Henry constants are not
too dissimilar, it was anticipated that the effect of the
localized non-localized behaviour would reveal some interesting
facets of the sorption mechanisms. Unfortunately, most of the
experimental data is at a low concentration, due to apparatus
limitations, being lower than 3 molecules/cavity at 271K,
approximately 3 molecules/cavity at 255K, and only being greater
than 3 molecules/cavity at 238K. The first two systems (271 and
255K) apparently show no effect of the interaction, whereas the
latter system at 238K appears to show significant interaction,
and this is the only system where krypton will apparently occupy
both sites significantly. More data at a higher concentration
are desirable to elucidate the effects of localized non-localized
interaction.

   Pure component experimental data for sorption of methane
and krypton on 5A zeolite at 238, 255, and 271K, and in the
pressure range of 0 to 97.36 kPa were also obtained during this
work (shown in Figures 3 and 4). Further sorption data for
methane on 5A zeolite (10, 13, 14), and for krypton on 5A zeolite
(10, 15) are also plotted for other temperatures, all of which
appear to be consistent. These experimental data were used to
derive the energy and entropy parameters in equation 4 for the
isotherm model of Schirmer et al. by a minimization of a sum of
squares optimization procedure.

   The resulting optimized parameters S_i and E_i for sorption
of methane and krypton on 5A zeolite are shown in Figure 5 and
are presented in Table 1. The calculated energy parameters –
22000 joules/mole for methane and – 16,725.0 joules/mole for
krypton were independent of the amount adsorbed and agree with
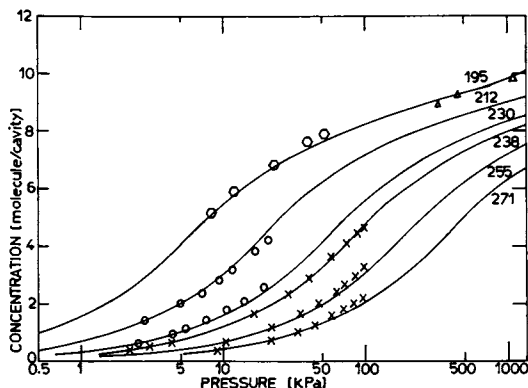
Figure 3. Equilibrium sorption data for CH₄ on pure 5A zeolite; parameter is temperature; data of (x) Roberts, (O) Derrah, (◇) Loughlin, (△) Lederman; (——) theoretical curves calculated using Equation 4 and data in Table I
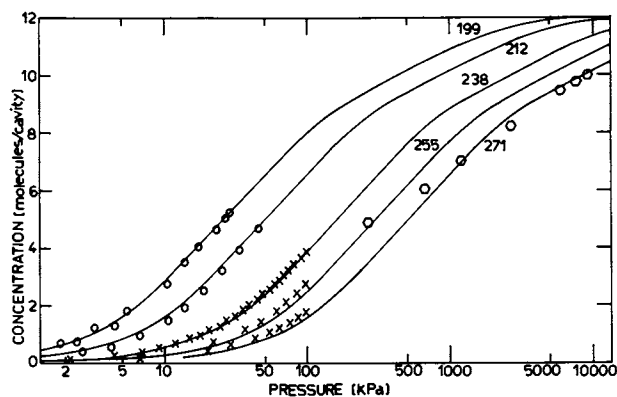
Figure 4. Equilibrium sorption data for Kr on pure 5A zeolite; parameter is temperature; data of (x) Roberts, (O) Derrah, (◇, at 271 K) Barrer et al.; (——) theoretical curves calculated using Equation 4 and data in Table I
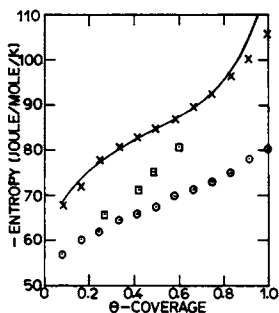
Figure 5. Variation of integral molar energy of sorption with coverage for (x) methane and (⊙) Kr on 5A zeolite; (▣) data of Rolniak for CH₄; (——) theoretical curve for CH₄ calculated using Equation 10 for Ruthven model

reported literatures values for these systems ($\underline{7}$, $\underline{9}$, $\underline{12}$, $\underline{15}$) with
one exception, that for methane reported by Rolniak ($\underline{16}$), which
appears to be substantially lower. The shape of the entropy
coverage plots (Figure 5) indicates that the incremental change
in energy of adsorption from the first to the last molecule is
much greater for methane than for krypton, favouring the
hypothesis that the molecules of methane appear to be non-
localized, whereas those of krypton appear localized ($\underline{17}$),
supporting conclusions of Ruthven and coworkers ($\underline{9}$, $\underline{12}$). Rolniak
($\underline{16}$) also calculated the entropy of adsorption for methane on
5A zeolite, and his experimental results are also shown in
Figure 5, after being reduced to the same standard state employed
in the isotherm derivation. His experimental values are
approximately 10 kjoules/mole K less than this work, which may
be attributed either to the high pressure aspects of their study,
or to a compensation effect due to interaction with heat of
sorption, as his value for the heat of adsorption on 5A zeolite

TABLE 1

Energy and Entropy of Adsorption Values employed in
Theoretical Studies with the isotherm of Schirmer et al.

Molecules/ Cavity	Entropy (joules/mole/K) Methane	Krypton	Hypothetical gases P	Q
1	− 67.8	− 57.0	− 67.8	− 57.0
2	− 73.5	− 60.3	− 71.1	− 62.7
3	− 73.3	− 62.0	− 72.8	− 66.5
4	− 80.8	− 64.6	− 75.4	− 70.0
5	− 83.0	− 66.0	− 76.8	− 72.2
6	− 84.8	− 67.5	− 78.3	− 74.0
7	− 87.0	− 70.2	− 81.0	− 76.2
8	− 89.6	− 71.4	− 82.2	− 78.8
9	− 92.4	− 73.2	− 84.0	− 81.6
10	− 96.7	− 75.1	− 85.9	− 85.9
11	− 100.3	− 78.2	− 89.0	− 89.5
12	− 106.0	− 80.1	− 90.9	− 95.2
Sum of Squares	0.235	1.285		
E_1 (Joules/mole)	−22000.	−16725.	−22000.	−16725.
Heat of Adsorption (Joules/mole)	−21350. ($\underline{9}$) −20520. to −22190. ($\underline{7}$) −15910. ($\underline{16}$)	−17250. ($\underline{10}$) − − −	− − − −	− − − −
Henry constant at 250K (molecules/ cavity/kPa)	0.0122	0.035	0.122	0.035

is significantly lower than others. Also shown in Figure 4 are
the calculated values of S_i derived from Ruthven's isotherm
using the equation (8)

$$S_i = R \ln(\frac{K_o P_o T}{T_o}) + \frac{R}{i} \frac{\ln(1-i\beta/v)^i}{i!} \tag{10}$$

Both models give substantially similar integral molar entropies
of sorption.

The fit of the theoretical isotherms calculated using
the S_i and E_i parameters in comparison with the experimental
data is satisfactory, as shown in Figures 2 and 3. The sum of
squares error calculated by the expression

$$[\sum_i (\frac{C_{theor}}{C_{exp}} - 1)^2]$$

as given in Table 1 is better for methane than for krypton for
approximately the same number of data points. A possible
explanation for this is the employment of only one energetic
site in modelling the krypton data, instead of using a two site
model as observed by Derrah (10).

Theoretical curves for the binary isotherm were calculated
from the pure component parameters given in Table 1 using
equation 5, and the resulting curves are shown in Figures 2a to
2f. There are some differences between the experimental and
theoretical curves but the theoretical curves give a qualita-
tively correct prediction of the form of the equilibrium diagrams.
The agreement between theory and experiment can only be as good
as the pure component prediction and in figures 2a to 2c, the
data most in error are those at X_{CH_4} of 0.0 and 1.0. As the
optimization of the S_i and E_i parameters of the model are based
on all the experimental data in Figures 3 and 4, a particular
experimental isotherm may differ by ± 5% from the theoretical
isotherm, giving rise to the discrepancy noted above. The shape
of the theoretical and experimental isotherms are qualitatively
similar in Figures 2a and 2b but differ in Figure 2c where a
maximum may be observed to occur in the experimental data. The
theoretical curve does not show any hint of a maximum although
qualitatively it is in good agreement with the experimental data.

The agreement is somewhat more satisfactory when the XY
curves are considered. In Figures 2d and 2e, experimental data
and theory are in substantial agreement and even in Figure 2f,
the agreement is excellent up to 60% mole fraction methane in
the adsorbed phase. At higher values, the experimental data
indicate that there appears to be no separation, whereas theory
indicates there is. The use of a two site binary form of the
Schirmer et al. model, may result in theoretical predictions in
better agreement with the experimental data. Further experimental
data at higher loadings are desirable to resolve this issue.

The IAST model of Myers and Prausnitz (3) was also used to calculate the mixture equilibria for this system using the theoretical isotherm of Schirmer et al. (equation 4) as the pure component model. The theoretical results for the two models were identical to three significant figures. This may indicate that the two models are equivalent, although this has not been proved.

Theoretical Studies

As the two sorbates methane and krypton on 5A appeared to have different mechanistic behaviour, further theoretical study appeared warranted. Two hypothetical gases P and Q whose properties are tabulated in Table 1 were used for comparison with the behaviour of methane and krypton. Hypothetical gas P was designed to have a Henry constant equal to methane, but to be a localized sorbate having entropy of sorption values decreasing incrementally as for krypton. Conversely, hypothetical gas Q had a Henry constant equal to that of krypton, but entropy of sorption values non-localized and decreasing incrementally as for methane.

XY diagrams on 5A zeolite were calculated for methane-krypton, methane-Q, P-krypton, and P-Q pairs at 250K at different pressures, and the results are plotted in Figure 6. In Figure 6a, the sorption of methane and krypton is favourable to methane, the higher Henry constant, at lower pressures. But as the pressure is increased, sorption becomes less favourable to methane, eventually becoming favourable to krypton at pressures of 1.33×10^4 kPa and above. Although having a lower Henry constant, krypton, being a localized sorbate, competes more strongly for sites as the pressure is increased, and eventually the localized behaviour dominates the Henry constant to alter the separability. Sorption of methane – Q pair, two non-localized sorbates, and of the P-krypton pair, two localized sorbates, is shown in Figure 6b for all pressures.

The separation is invariant with pressure, indicating that for non-localized pairs, or localized pairs, the predominant factor influencing the separation is the Henry constant. The sorption of the P-Q pair is shown in Figure 6c in which the higher Henry constant gas P is also the localized species; gas Q has the lower Henry constant and is non-localized. The figure indicates that for increasing pressures the separation is increased as localization augments the separation. Thus higher Henry constant and localization act to increase separation.

Typical amounts adsorbed versus Y_A, the gas phase mole fraction, for each of the four pairs are shown in Figure 7 for a total pressure of 133.37 kPa. These plots reinforce the conclusions revealed in the XY plots. In Figure 7a, the local-ization of krypton counteracts the higher Henry constant of methane to practically equalize the loadings. The loadings for
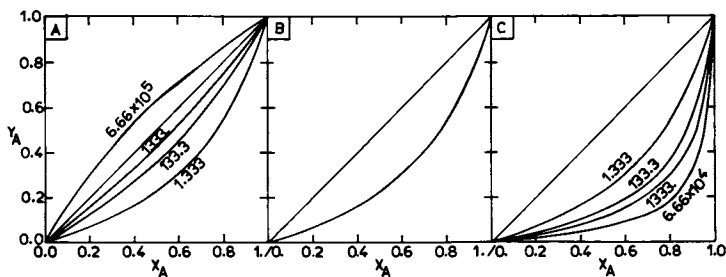
Figure 6.   XY diagrams for sorption on 5A zeolite at 250 K for various pressures. Gas pairs used were (left) CH₄–Kr, (center) CH₄–Q and P–Kr, and (right) P–Q. Mole fractions X and Y refer to the first component. Parameter is total pressure in kPa.
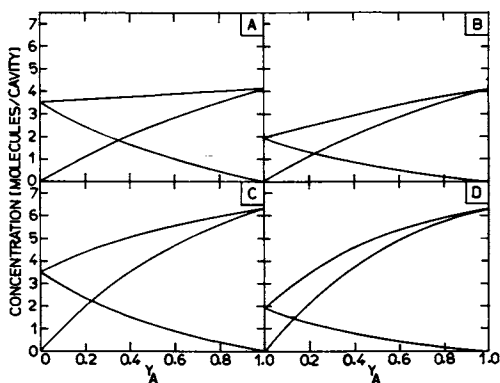

Figure 7.   Concentration–Y_A diagrams at 250 K and 1000 torr for (A) CH₄–Kr, (B) CH₄–Q, (C) P–Kr, and (D) P–Q pairs. Y_A is the gas-phase mole fraction of first component named.

the non-localized pair methane-Q in Figure 7b are less than that
for the localized pair P-krypton in Figure 7c but the ratio of
the loadings is unchanged for varying gas phase concentrations.
This fact is shown more clearly in Figure 8 where the total
pressure - Y_A diagram at 133.37 kPa for both species is the same,
indicating that the Henry constant is the dominating factor.
In Figure 7d the sorbate concentration of the higher Henry
constant localized species totally dominates, indicating the
reinforcement of the two factors.
      The separation factor, defined by

$$\alpha = \frac{X_A/X_A}{X_B/Y_B} \qquad (11)$$

was calculated for various permutations of temperature and
pressure. The binary model used in this work reduces to Langmuir's
binary model at low concentration, for which the separation
factor α is equal to the ratio of the Henry constants. The
variation of α with Θ (the loading) at 250K and gas phase
concentrations of 50% is shown in Figure 9 for the methane -
krypton and the P-Q pair system. The curves for this figure were
derived by varying the total system pressure. The dotted line
in the figure is for a separation of 3.45 applicable to the
binary Langmuir model invariant with loading. The separation
factor for methane-krypton is initially favourable to methane
at a 3.45 ratio, decreases as the loading increases, becomes
1.0 @ 84% loading decreasing to 0.54 at saturation where the
zeolite prefers krypton. Conversely for the P-Q pair the
separation factor increases from 3.45 at θ = 0 to 22.8 at
saturation. It should be noted that the percentage increase or
decrease is similar at equal loadings. Optimum separation for
the methane-krypton system is attained at the lowest coverage
possible and for the P-Q pair where localization reinforces the
Henry constant at the highest loading possible.
      These results are elaborated in further detail in Figure
10 where the separation factor for both pairs is plotted
against temperature for various isobars for a gas phase
composition of 50%. The dotted lines are the limiting separation
factors at Θ = 0. At low pressures the systems approach the
limiting separating factors (the low loading asymptote) and
diverge at higher pressures to a high loading asymptote at
maximum pressures.
      The difference between the two asymptotes is a decrease
by a factor of 6.5 for the methane krypton system and an
increase by a factor of 6.5 for the P-Q pair throughout the
temperature range. Decrease in both pressure and temperature
favour separation in the case of methane-krypton-5A except where
the favourability is altered where the converse is true, whereas
decrease in temperature but increase in pressure favour separation
in the case of the P-Q pair.
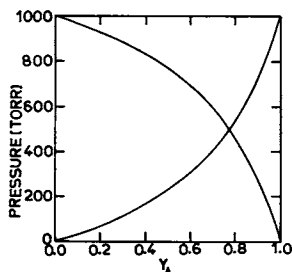
Figure 8. Pressure–Y_A diagram at 250 K for nonlocalized pair CH_4–P and localized pair Kr–Q at a total pressure of 1000 torr. Component A is the first specie named.
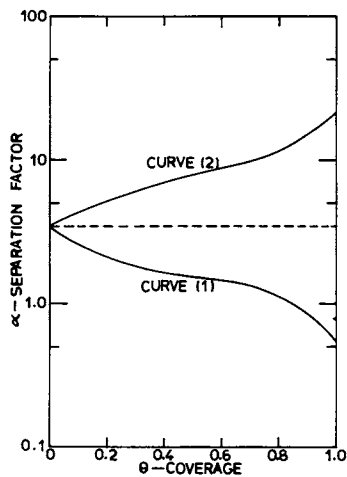
Figure 9. Variation of separation factor with coverage for (Curve 1) CH_4–Kr and (Curve 2) P–Q pair at 250 K and gasphase concentrations of 50% due to changing total system pressure. The firstnamed specie is component A in Equation 11; (– – –) limiting Langmuir separation.
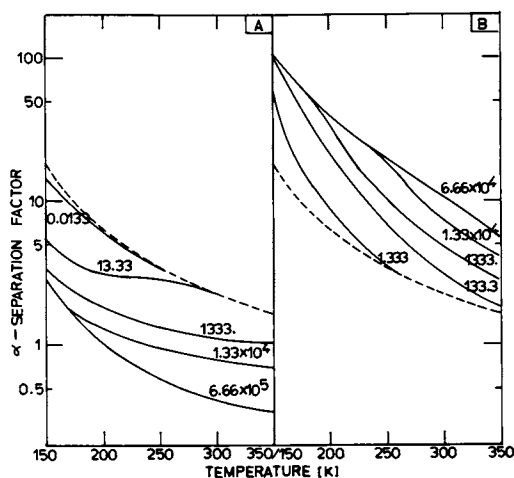
Figure 10. Variation of separation factor with temperature at different pressures for (A) CH₄–Kr and (B) P–Q pairs; (– – –) limiting Langmuir case; calculations performed for a gas-phase concentration of 50%. The first-named specie is Component A in Equation 11. Parameter is total pressure in kPa.

In summary, in operation of adsorption systems involving a localized and non-localized pair, selection of best separability is dependent both on the Henry constant and on the type of site interaction. Higher Henry constant combined with a localized site favours the employment of high pressure systems; conversely, higher Henry constant combined with a non-localized site favours low pressure systems. The choice of appropriate temperatures depends on whether the Henry constants diverge or converge as the temperature is altered.

Nomenclature

|	
C	Concentration, molecules/cavity
E_{ij}	Molar constant for energy (j^{th} level) for i molecules/cavity
E_i	Molar constant for energy for i molecules/cavity for one energy level only
E_m	Energy of mixing
$\underline{E}$	Vector of energy constants
k	Maximum number of energy levels
K	Henry's constant, molecules/cavity/kPa
ℓ	Sum of molecules A and B in a cavity = i + j
m	Maximum number of molecules of A a cavity will hold
n	Maximum number of molecules of B a cavity will hold
P	Pressure, kPa
P_o	Standard state for pressure = 101.36 kPa
q(i)	Canonical partition function for a cavity containing i molecules of the same type
$q_{i,conf}$	Contribution of configuration to q(i)
R	Gas constant
S_{ij}	Molar constants for (T,V_o) – standard difference of entropy for j^{th} level
S_i	Molar constants for (T,V_o) – standard difference of entropy for 1 energy level only
$\underline{S}$	Vector of entropy constants S_i
T	Temperature
T_o	Standard state for temperature = 273.1K
v	Cavity volume = 776 cubic angstoms
V_o	Standard volume = (RT_o/P_o)
X	Mole fraction sorbed phase
Y	Mole fraction gas phase

Greek

α	Separation factor
β	Molecular volume of sorbate
λ	Exp (μ/kT)
Θ	Fractional coverage

Subscripts/Superscripts

A   Component A
B   Component B
i   Number of molecules of component A in a cavity
j   Number of molecules of component B in a cavity

Acknowledgements

Literature Cited

1.   Ruthven, D.M., Nature, Phys. Sci., 1971, 232, 70.

2.   Ruthven, D.M., Loughlin, K.F., and Holborow, K.A., Chem.
        Eng. Sci., 1973, 28, 701.

3.   Myers, A.L., and Prausnitz, J.M., A.I.Ch.E.J., 1965,
        11, 121.

4.   Glessner, A.J., and Myers, A.L., C.E.P. Symposium Series,
        1969, 63, 73.

5.   Danner, R.P., and Wenzel, L.A., A.I.Ch.E.J., 1969, 15,
        515.

6.   Danner, R.P., and Choi, E.C.F., Ind. Eng. Chem. Fundam,
        1978, 17, 1978.

7.   Schirmer, W., Fiedler, K., and Stach. H., A.C.S. Symposium
        Series, 1977, 40, 305.

8.   Loughlin, K.F., and Roberts, G.D., A.I.Ch.E.J., accepted
        for publication.

9.   Ruthven, D.M., and Loughlin, K.F., Trans. Faraday Soc.,
        1972, 68, 696.

10.   Derrah, R.I., Ph.D. thesis, University of New Brunswick
        (1973).

11.   Loughlin, K.F., Holborow, K.A. and Ruthven, D.M., A.I.Ch.E.
        Symposium Series, 1974, 71 (152), 24.

12.   Ruthven, D.M., and Derrah, R.I., Can. J. Chem. 53(7), 996,
        1975.

13.   Loughlin, K.F., Ph.D. Thesis, University of New Brunswick
        1970.

14.   Lederman, P.B., Ph.D. Thesis, University of Michigan
        (1961).

15.   Barrer, R.M., Papadopovlos, R., and Ramsey, J.D.F.,
       Proc. Roy. Soc., A326, 333 (1972)

16.   Rolniak, P.D., Ph.D. Thesis, Rice University, Houston,
       Texas, (September 1976)

17.   Ross, S. and Oliver, J.P., "On Physical Adsorption",
       Interscience Publishers, 1964.

18.   Roberts, G.D., M.Sc. Thesis, University of New Brunswick
       (1978)

Apparent Surface Diffusion Effects for Carbon Dioxide/Air and Carbon Dioxide/Nitrogen Mixtures with Pelleted Zeolite Beds

RICHARD T. MAURER

Union Carbide Corporation, Engineering Products & Processes Department, Tarrytown Technical Center, Tarrytown, NY 10591

As knowledge concerning diffusion·processes in molecular sieve zeolites broadens, it becomes increasingly clear that development of a truly generalizable model for diffusivity prediction in such adsorbents is not likely in the immediate future. The complex electrical forces within and on the surface of the zeolitic crystals, the importance of geometric factors in adsorption of larger molecules, the possibility of diffusive resistances external to the crystals themselves, all conspire to make such a task extremely formidable, especially when it is realized that the predictive models ought to be applicable to adsorption processes involving heat transfer and multicomponent mixtures as well. When the sorbing (and/or desorbing) molecules are small, the situation becomes perhaps somewhat simpler from the standpoint of theoretical analysis, but more difficult experimentally because of the small time constants involved. Problems in analyzing such diffusion processes can arise due to limitations in the resolving ability of the timing device or when other diffusive resistances with larger time constants are present. Nonetheless, such systems can yield interesting information regarding certain features of zeolitic diffusion, and may perhaps be more amenable to successful correlation by means of theoretical or semi-empirical models.

In this work, we investigate the diffusion rate of carbon dioxide, from a carrier stream of air or nitrogen, into pelleted forms of Linde types 4A, 5A, and 13X Molecular Sieves. The data are derived from the measurement of breakthrough curves in a uniformly packed column of pellets initially loaded with carrier gas alone, with the feed mixture introduced at constant pressure and flowrate. In selected cases, breakthrough runs were made for identical feed conditions but with different sized pellets, to permit an estimation of the contribution of zeolitic resistances to the overall mass transfer resistances in the system. Using this information, along with information regarding equilibrium loadings and effects of heat transfer, an attempt is made to correlate the mass transfer data over a wide range of feed

conditions, based on standard diffusivity models (using constants derived from physical properties of the system), along with a model for correlating apparent effects due to surface diffusion within the particles (using a correlation constant of best fit for each sorbate-sorbent system).

Theoretical Considerations

The packed bed breakthrough method for investigation of mass transfer phenomena in sorbent systems can in many instances offer certain advantages not found in other experimental methods. The method is especially useful when the adsorption isotherms for the principal sorbate exhibit favorable curvature (convex toward loading axis). In such a case, there is the potential for a portion of the sorption front to approach a stable wave form (shape of the front invariant with time). Given the existence of a stable or "steady-state" mass transfer zone (MTZ) and a detailed knowledge of the equilibrium loading characteristics within that zone, one can extract local values of the effective mass transfer resistance at any concentration in the zone.

Another feature of the breakthrough method is that the uniform geometry of the packed column permits fairly straightforward analysis of the thermal waves produced due to heats of adsorption, and of their effect on the shape of the sorption fronts. The most obvious advantage of this method, however, is the fact that the results of the breakthrough experiments can be applied rather directly to the design of commercial adsorbers, with relatively little analysis of the data.

Except in very simple systems (e.g., nonadsorbable carrier and negligible thermal effects), the analysis of breakthrough data from the standpoint of mass transfer phenomena requires fairly sophisticated mathematical modeling techniques, as well as precise knowledge of the multicomponent loadings at equilibrium conditions over the ranges of pressure, temperature, and concentration encountered in the bed. The Linde Division of Union Carbide Corporation has spent many years developing the data and computer programs necessary for such analysis, and continues expanding its data base to provide the capability for accurate design in a wide range of adsorption systems. Among the models and mathematical tools used to analyze the breakthrough data discussed below are the following, which will be discussed briefly in this section.

(1) The loading ratio correlation (LRC) method for correlation of pure component sorption therms and prediction of multicomponent sorption therms.

(2) The MASC (for "multicomponent adsorption simulation calculations") computer program, which identifies the regions of stability and instability within the sorption fronts, the distance which the front must travel through the bed for the potentially stable regions to attain their ultimate steady-state

shapes, and the axial temperature and loading profiles within the bed under conditions of adiabatic operation (no heat loss through the walls of the packed column).

(3) The SSMTZ computer program, which uses the LRC coefficients and models for the various mass transfer resistances in the system to predict the shape of the stable portions of the breakthrough curves in the multicomponent system under isothermal conditions.

(4) The SSHTZ computer program, which is similar to the SSMTZ program, except that SSHTZ can predict the shape of the stable portions of the breakthrough curves for either isothermal or adiabatic operation. Due to the complexities involved in the solution, however, SSHTZ is limited to predictions for binary mixtures only.

The methods for correlating the breakthrough data using these tools will be described later. First, let us briefly discuss the tools and models themselves.

The Loading Ratio Correlation. The equilibrium sorption therms for the pure components are correlated to the LRC model ($\underline{1}$), which can be stated in the following manner:

$$\frac{X}{X_o} = \frac{(bP)^{1/n}}{1 + (bP)^{1/n}} \tag{1}$$

where

$$\ln b = A_1 + A_2/T \tag{2}$$

$$n = A_3 + A_4/T \tag{3}$$

Thus, five constants (A_1, A_2, A_3, A_4, and X_0) are used to model the pure component loadings within the ranges of pressure and temperature required. The LRC model, as extended by the method of Markham and Benton ($\underline{2}$), is also used to predict the loadings in the multicomponent system, based upon the correlation coefficients for the pure component loading data, viz.,

$$\frac{X_i}{X_{oi}} = \frac{\phi_i}{1 + \sum_j \phi_j} \tag{4}$$

where

$$\phi_i = (b_i p_i)^{1/n_i} = (b_i y_i P)^{1/n_i} \tag{5}$$

The differential heat of adsorption for each component in the mixture is estimated using the Clapeyron equation, extended to multicomponent mixtures and assuming ideal behavior of the gas phase (fugacity of i-th component $\simeq p_i$), that is,

$$\frac{\Delta H_i}{R} = \left[\frac{\partial (\ln p_i)}{\partial (I/T)}\right]_{X_j = Constant} \tag{6}$$

Combining (2), (3), (4), and (6) yields the following relation:

$$\frac{\Delta H_i}{R} = A_{2i} + A_{4i} \ln \frac{X_i/X_{oi}}{I - \sum_j (X_j/X_{oj})} \tag{7}$$

The Masc Program. The MASC computer program, developed by Dr. F. W. Leavitt of Union Carbide, simulates multicomponent adsorption processes in fixed beds through a finite difference solution of the partial differential equations for heat and mass transfer, using the LRC model to compute equilibrium sorption properties and assuming a gas phase driving force for mass transfer. The program is capable of solving these equations subject to a variety of initial and boundary conditions, including conditions in which the bed is exhausting to a lower pressure or being pressurized by a gas mixture. For a constant pressure adsorption process, as encountered in the breakthrough experiments described here, the following equations are employed:

Mass Balance:

$$-\frac{\partial}{\partial L} (G_M y_i) + D_{ax} \rho_{gm} \frac{\partial^2 y_i}{\partial L^2} = \frac{\partial}{\partial \theta} (\rho_b X_i + \varepsilon_T \rho_{gm} y_i) \tag{8}$$

Energy Balance:

$$-G_M C_{pg} \frac{\partial T}{\partial L} + k_{ax} \frac{\partial^2 T}{\partial L^2} = \rho_b C_{ps} \frac{\partial T}{\partial \theta} + \rho_b \sum_j (\Delta H_j \frac{\partial X_j}{\partial \theta}) \tag{9}$$

Rate Equation:

$$\rho_b \frac{\partial X_i}{\partial \theta} = \rho_{gm} (Ka)_{eff} (y_i - y_i^*) \tag{10}$$

Initial Condition:

$$y_i (0,L) = y_{r_i} (L) \tag{11}$$

Boundary Conditions:

$$y_i(\theta,0) = y_{f_i} \tag{12}$$

$$\left[\frac{dy_i'(\theta,L)}{dL}\right]_{L=L_b} = 0 \tag{13}$$

Similar initial and boundary conditions apply for the temperature profiles.

   The SSMTZ and SSHTZ Programs. Although MASC has the ability to simulate all the processes occurring in a constant pressure adsorption front, and as such can compute bed temperature profiles and concentration profiles, whether steady or unsteady in character, the finite difference solution requires the bed length to be divided into a large number of increments (requiring long run times and large computing costs) if one wishes to accurately simulate the relatively sharp fronts formed in the steady state portion of the sorption wave. For this reason, MASC is generally used only to obtain information related to the location of potential regions of stability or instability within the fronts, the length of bed required to form the fully stable fronts, and the temperature at points where the stable and unstable portions of the fronts intersect one another. Given the existence of a stable region, it is possible to reduce the differential heat and mass balances within that region to a simpler form, in order to study the mass transfer phenomena therein in greater detail. This is the purpose of the SSMTZ and SSHTZ programs.
   Both programs use Michaels' method (3) for determination of the steady-state values of MTZ length, using a gas phase driving force (with all system mass transfer resistances expressed in terms of an effective film resistance, $1/(Ka)_{eff}$), and including a correction term to account for the storage of gas in the void spaces within and between the sorbent particles, viz.,

$$[\text{LUB}]_{Y_1}^{Y_2} = u_f [\text{TUB}]_{Y_1}^{Y_2} = \frac{G_1'}{\rho_{gm}} \int_{Y_1}^{Y_2} \frac{dY}{(Ka)_{eff}(Y - Y^*)} \tag{14}$$

where

$$G_I' = y_I(G_M - \varepsilon_T \rho_{gm} u_f) \tag{15}$$

and

$$u_f = y_I G_M / (\rho_b \frac{\Delta X}{\Delta Y} + y_I \varepsilon_T \rho_{gm}) \tag{16}$$

where u_f is the speed of the steady-state portion of the front, and ΔX and ΔY are the changes in loadings and mole ratios (moles
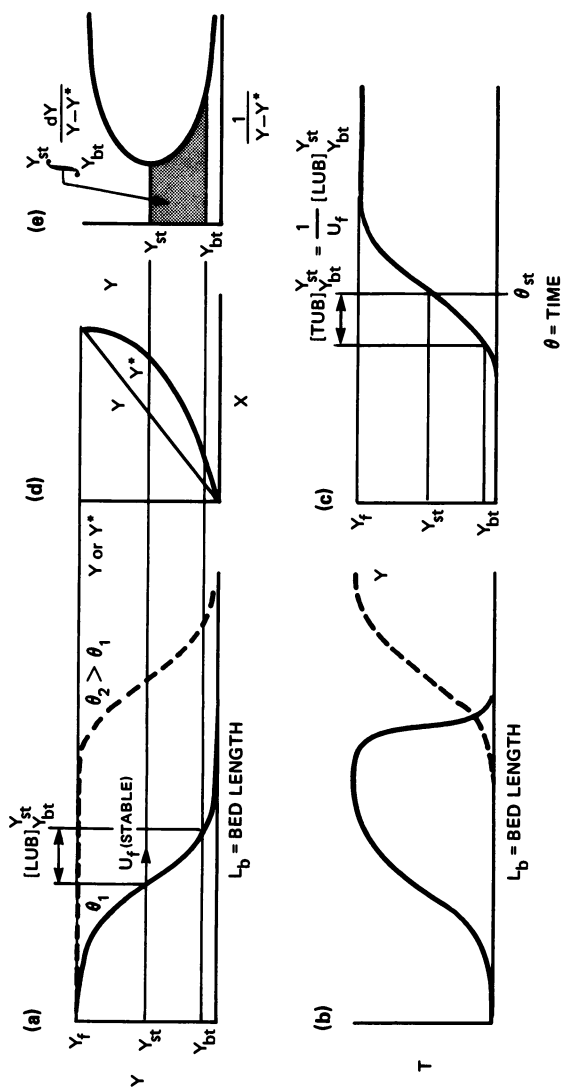
Figure 1. Case I (fully stable) profiles: (a) progression of concentration front, (b) progression of temperature front, (c) breakthrough curve, (d) equilibrium (Y) and operating (Y) lines for steady-state front, (e) graphical representation of the integral used in the prediction of steady-state LUB values*

per mole of inert), respectively, between the leading and trail-
ing edges of the steady-state front.

   If the entire sorption front is stable, as shown in Figure 1,
the length of the MTZ may be measured from any point within the
wave.   However, when sorptive heating effects become important
(generally at high sorbate concentrations), an unsteady wave may
form.   Generally, if the sorbate-sorbent system exhibits favor-
able adsorption isotherms, the lower portion of the sorption
front can still form a stable wave, but the upper portion of the
front (near the feed concentration) will be unstable, that is,
will expand indefinitely as feed gas continues to enter the bed,
as shown in Figure 2.   In many such cases, the stoichiometric
point of the overall (steady plus unsteady) front is found to be
within the unsteady portion of the front.   Thus, this point
should not be used as a reference from which to measure the
length of the steady-state MTZ.   If the point at half the feed
concentration $Y_{1/2}$, which for this type of front is always less
than the gas phase concentration at the stoichiometirc point, is
determined to fall within the steady state front, this point is a
convenient point of reference for such measurements.   In this
work, $Y_{1/2}$ is used as the point of reference for all cases
studied, since it was determined that this concentration was
always within the steady-state region.

   To determine the concentration at the "crossover" point
(where stable and unstable regions of the front intersect), the
method of Leavitt (4) can be used, provided the carrier gas is
essentially unadsorbed, and axial diffusion forces and thermal
conductivities are negligible (see the aforementioned reference
for the corrections for these latter effects).   For such a case,
an energy balance across the stable and unstable portions of the
front, along with relations to describe the equilibrium loadings
at the extrema of these fronts (for example, the LRC model) can
be combined to solve for the crossover concentration.   The energy
balance across each front takes the form:

$$\Delta t = \Delta H / (C_{pg}/\Delta Y - C_{ps}/\Delta X) \tag{17}$$

   As mentioned above, the SSMTZ program calculates the steady-
state MTZ lengths, taking into account the effects of multi-
component adsorption and diffusion, but assuming isothermal
conditions.   The SSHTZ program accounts for the effect of the
heat of sorption in an adiabatically operated column upon the
length of the steady-state MTZ, but is limited to systems of
binary mixtures only.   Together, these programs form a powerful
tool in the analysis of mass transfer phenomena in stable fronts,
as will be explained shortly.

   Diffusion Models for MTZ Length Correlation.   Figure 3 shows
the various diffusive resistances likely to occur in the packed
bed systems investigated, and the manner in which they are
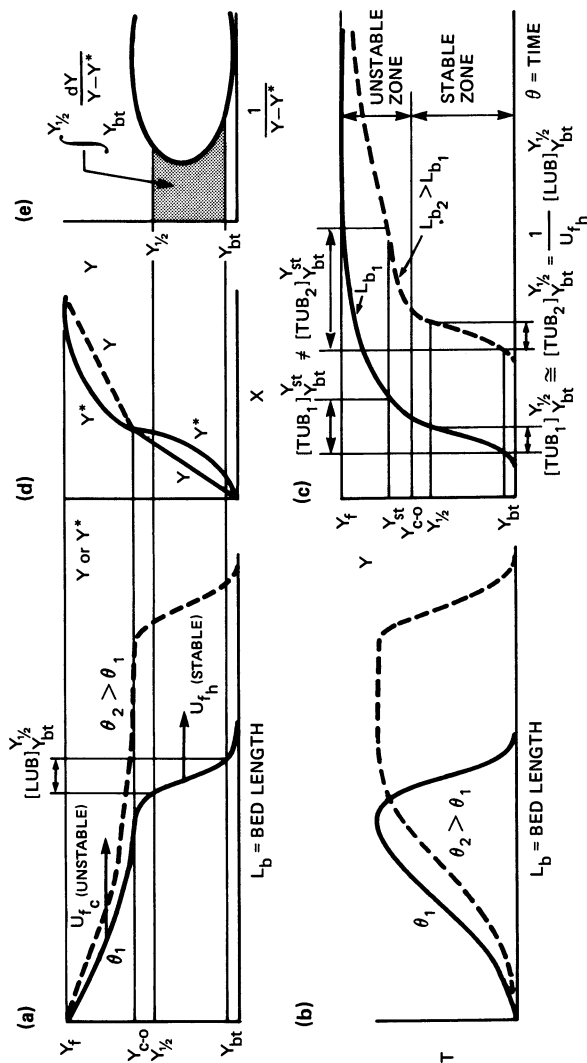
Figure 2. Case II (partially unstable) profiles: (a) progression of concentration front, (b) progression of temperature front, (c) breakthrough curves at two values of bed length, (d) equilibrium (Y*) and operating (Y) lines for stable and unstable portions of the front, (e) graphical representation of the integral used in the prediction of the steady-state LUB values in the stable zone
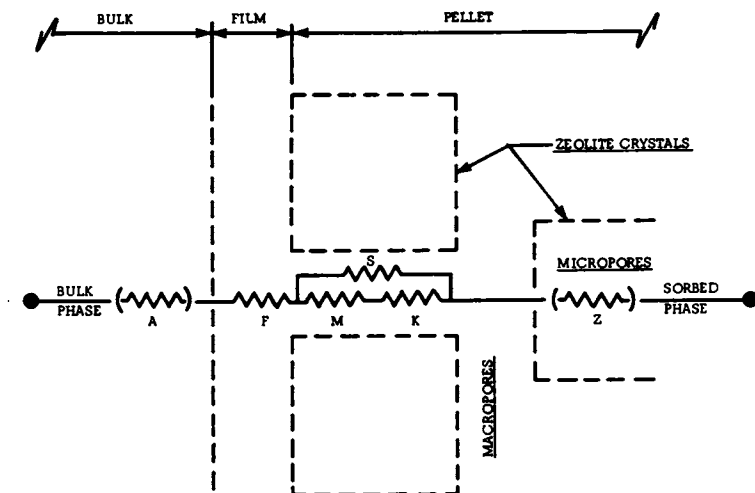
SYMBOL	TYPE OF DIFFUSION	REGION OF INFLUENCE	COMMENTS
A	Axial (Molecular + Eddy)	Extraparticulate (Bulk Phase)	Treatable as series resistance only in linearized model.
F	Film	Bulk/Pellet Interface	Function of particle Reynolds Number.
M	Maxwell	Particle Macropores (Intercrystalline)	Sorbate/sorbate collisions.
K	Knudsen	"	Sorbate/wall collisions.
S	Surface	"	Sorbate sliding or hopping along surface of crystals. Dependent on sorption isotherm, zeolite and sorbate geometry.
Z	Zeolitic	Particle Micropores	Actually acts as series-parallel resistance. Treatable as series resistance alone only if either macropore or micropore resistance dominates. Dependent on sorption isotherm, zeolite and sorbate geometry.

Figure 3. Schematic representation of the diffusion resistances considered for packed-bed MTZ analysis

combined to give an overall effective resistance value. Such
treatment applies strictly for systems in which the adsorption
isotherms are linear (5), but should be applicable with little
loss of accuracy to systems with favorable curvature of the
sorption therms, as long as concentration dependence of the
individual resistances is slight and intraparticle resistances
form the dominant resistance in the system (this is the case in
these investigations).

Axial, film, and macropore Maxwell and Knudsen diffusion
coefficients are estimated based on relatively standard formu-
lations (6, 7, 8, 9), using estimates of physical properties
shown in Table I to compute the diffusivity values for the
systems studied. The effect of errors in the estimated values
of these properties will be discussed later.

As seen below, the breakthrough runs investigated showed, in
addition to the above-mentioned resistances, indications of the
presence of surface diffusion effects (causing MTZ lengths to be
shorter than those predicted on the basis of the abovementioned
resistances) as well as effects due to intrazeolitic micropore
resistances (resulting in decreased dependence of MTZ length
upon particle diameter, after adjustment for extraparticulate
film and axial diffusion effects). Since both effects are
expected to be concentration-dependent, but would not necessarily
depend on concentration in identical ways, it was decided that
only the surface diffusion model would be used to correlate the
MTZ lengths within a given sorbate-sorbent system. For studies
involving breakthrough runs with different particle sizes but
identical feed conditions, the effective micropore (intra-
crystalline) resistance time-constant could be determined, allow-
ing one to estimate the amount of surface diffusion based on
measurements of the experimental MTZ length and knowledge of the
contributions of the other resistances to that length. For such
cases, the correlating parameter in the surface diffusion model
is reported along with estimated value of the micropore resist-
ance. However, in the correlation of all the values of MTZ
length measured within a given sorbate-sorbent system at differ-
ent feed conditions, effects of intracrystalline resistance are
not included; the correlating parameter in the surface diffusion
model is chosen to give the best fit of the MTZ data within a
given sorbate-sorbent system.

The model chosen to represent the effects of surface dif-
fusion along the walls of the macropores is a modification of the
Sladeck-Gilliland model (10, 11), which has the form:

$$D_s = \frac{D_{os} \rho_p S_g}{\tau_s} \left(\frac{dc_s}{dc_g} \right) \exp (\Delta H/mRT) \qquad (18)$$

In this form, the model invokes the concept of adsorption on
two-dimensional surface sites, a concept which is not particu-
larly relevant to adsorption on (or in) zeolite media. However,

TABLE I

Estimated Physical Properties of Adsorbent Pellets

Adsorbent	d_p (cm)	l_p/d_p	$d_{p_{eff}}$ (cm)	a (cm^{-1})	ρ_b (g/cm^3)	ρ_p (g/cm^3)	(1) ϵ_p	(2) r_{pore} (Å)	r_M	C_p (cal/g-K)
4A 1/16"	0.16	1.6	0.19	18	0.72	1.13	0.32	900	1.5	0.2
1/8"	0.32	1.6	0.36	9	0.72	1.13	0.32	900	1.5	0.2
5A 1/16"	0.16	1.6	0.19	18	0.69	1.15	0.32	900	1.5	0.2
1/8"	0.32	1.6	0.36	9	0.69	1.15	0.32	900	1.5	0.2
1/4"	0.64	1.6	0.71	4.5	0.69	1.15	0.32	900	1.5	0.2
13X 1/16"	0.16	1.6	0.19	18	0.61	1.01	0.32	900	1.5	0.2
1/8"	0.32	1.6	0.36	9	0.61	1.01	0.32	900	1.5	0.2

(1)   Excluding micropore (intracrystalline) void spaces

(2)   Assumes mean crystal diameter of about one micron

a similar model can be proposed for the case of zeolites, using the following transformation of variables:

$$c_s S_g = X \qquad\qquad (19)$$

$$c_g \cong \frac{yP}{RT} \qquad\qquad (20)$$

Using these relations in equation (18), and applying the LRC model to predict the loadings and heats of adsorption, the model for "surface" diffusion of the i-th component in a multicomponent mixture becomes:

$$D_{s_i} = (\frac{D_{os}}{\tau_s})(\frac{RT\, X_{oi}\rho_p}{n_i}) \frac{1 + \sum_j \phi_j - \phi_i}{(1 + \sum_j \phi_j)^2} \phi_i^{1-n_i} \cdot$$

$$\exp\,[-A_{1i} + (A_{2i}\,(1-2m) + A_{4i}\ln\phi_i)/2mT]\qquad (21)$$

This model actually contains two parameters of correlation, i.e., (D_{os}/τ_s) and m. However, the value of m in nonmicroporous media was found by Sladeck and Gilliland to be relatable to the type of interaction between sorbate and sorbent (11), and generally takes a value of 1, 2 or 3, depending on the interaction. For the case of CO_2 on molecular sieve zeolites, a value of m = 2 was chosen since, although CO_2 possesses no dipole moment (suggesting a value of m = 1), its quadrupole moment is not zero, and various physical properties (e.g., viscosity) suggest a fairly high degree of polar character, which would be expected to be exhibited to an even greater degree within the fields of the zeolite crystals. Based on this m value, the values of (D_{os}/τ_s) which gave the best fit of the experimental data in each sorbate-sorbent system are reported in Table III. Again, it should be noted that these values are based on the assumption that intracrystalline micropore resistances are negligible (which they generally are not), and should therefore be regarded as a lower limit on the actual (D_{os}/τ_s) values apparent in each system.

Correlation of Steady State MTZ Lengths to Theoretical Models. To properly relate the breakthrough data to fundamental mass transfer coefficients, a precise accounting for effects of multicomponent adsorption and heat transfer must be made. The following steps were taken to ensure that such effects were not misinterpreted as effects due to mass transfer. First, pure component data involving adsorption of oxygen, nitrogen and carbon dioxide on Linde type 4A, 5A and 13X pellets were correlated to the LRC model over the range of pressure and temperature investigated. Next, the CO_2 loadings predicted by the multicomponent form of the LRC model (based on LRC coefficients for the pure component sorption therms) were compared to the actual CO_2 loadings at full bed capacity, obtained by integration of the

experimental breakthrough curves. Although this comparison does
not permit evaluation of the multicomponent loadings at concen-
trations other than the feed concentration for a given experi-
mental breakthrough run, in most cases a number of runs were
made within each sorbate-sorbent system at different feed condi-
tions. The overlap in the loading data thus produced permits a
fairly high degree of confidence in the performance of the multi-
component predictions over the entire breakthrough front.

Although the pure component LRC coefficients, as applied in
the multicomponent model of equation (4), generally gave an
excellent fit of the breakthrough loadings, there was one series
of runs (the low concentration CO_2/air/5A system) for which the
pure component LRC's did not provide a satisfactory fit of the
data. For these cases, the A_3 and X_0 constants for the pure
component CO_2/5A LRC correlation were modified to provide a
better fit of the breakthrough loadings.

Since the columns used in the various breakthrough experi-
ments varied from run to run (see experimental section), certain
questions needed to be resolved with the help of the above-
mentioned computer programs, along with the LRC coefficients for
prediction of the multicomponent loadings and heats of sorption.
These questions included the following:

    (1) Which portion of the breakthrough wave has the poten-
        tial for formation of a thermally stable front?

    (2) For that potentially stable portion, was the column long
        enough for the front to have essentially attained its
        ultimate steady-state shape at breakthrough?

    (3) Was the column cross-sectional area sufficient to effect
        essentially adiabatic behavior of the sorption fronts,
        and, if not, how much would the steady-state MTZ lengths
        change between operation at fully adia- batic conditions
        and operation at fully isothermal conditions?

    (4) If both heat effects and effects of multicomponent ad-
        sorption are important, can the SSMTZ program (which can
        handle multicomponent effects but not effects of heat
        transfer) and the SSHTZ program (which can handle heat
        effects but is limited to binary mixtures) be used in
        tandem to extract mass transfer information in a
        quantitative manner?

To answer questions (1) and (2), MASC was run assuming ad-
iabatic conditions, using an effective mass transfer coefficient
value which gave the best fit for the breakthrough trace at a bed
length equivalent to that in the actual column. The computer
simulation was then repeated using larger values of bed length,
but the same feed conditions, LRC coefficients, and effective
mass transfer coefficient, to see whether the shape of the stable
portion of the front changed to any significant degree with
further progress along the bed. If not, it could be concluded
that the actual breakthrough trace represented, within the region
of potential stability, its ultimate steady-state shape.

For a resolution of question (3), either MASC or the simpler
SSHTZ program was run under both isothermal and adiabatic con-
ditions, with effective mass transfer coefficients chosen to
simulate the stable portion of the sorption fronts. Fortunately,
in most cases described below, the programs predicted that the
steady-state MTZ lengths did not change by more than 10% or so
between the two extremes. Thus, an extensive analysis of the
wall effects in the various columns was not required for proper
interpretation of MTZ data.
     Where both multicomponent and heat transfer effects appeared
important, it was necessary to compare the results of selected
runs via the MASC program under adiabatic conditions to the value
obtained by multiplying the MTZ length prediction via SSMTZ
(isothermal, multicomponent) by the ratio of MTZ lengths pre-
dicted by SSHTZ under adiabatic and isothermal conditions. If
the values are essentially equivalent, the SSMTZ and SSHTZ
programs could be used to analyze the MTZ data with a high degree
of confidence.

Experimental

     Pure component loadings for CO_2, N_2 and O_2 on com-
mercial pelleted forms of Linde type 4A, 5A and 13X molecular
sieve zeolites were derived from various gravimetric and volu-
metric measurements. The range of pressures and temperatures
over which these measurements were made were at least as broad
as those encountered in the breakthrough experiments described
here, to permit accurate estimations of heats of adsorption in
the manner described by equation (6) above. As mentioned above,
the pure component data were correlated to the LRC model, and the
CO_2 loadings predicted by the multicomponent LRC model compared
to actual loadings in the breakthrough runs at bed saturation.
     The breakthrough runs are drawn from past fixed-bed labor-
atory studies by several Linde investigators, comprising adsorp-
tion of CO_2 from a carrier of dry air or nitrogen on 4A, 5A and
13X pellets with diameters of 1/16" (0.16 cm), 1/8" (0.32 cm) and
1/4" (0.64 cm) and length-to-diameter ratio of about 1.6. The
range of feed concentrations investigated is shown in Table II.
Prior to each breakthrough run, the bed was regenerated by
flowing heated (200-300C) carrier gas through the column, then
cooling to ambient temperature using the same carrier. Air used
in the CO_2/air runs was passed over another bed of molecular
sieve prior to mixing with the CO_2 feed stream, to remove
moisture and additional CO_2 present in the air stream. CO_2
concentrations in the breakthrough fronts were continuously
monitored by means of a thermal conductivity cell. Values of bed
length and cross-sectional area varied from study to study. In
the low concentration CO_2 (<2 mole percent) studies, bed diam-
eters ranged from 5 to 10 cm (I.D.); in all cases, the ratio of
bed diameter to pellet diameter exceeded 25 to 1, so that

TABLE II

Conditions of Breakthrough Runs

System	No. Of Runs	G_M (gmol/hr./cm2)	P (Bar)	T (K)	y_f	$y_f P$ (Bar)	Range of 100 y_{bt}/y_f Analyzed
Low CO2 Concentrations:	34						
CO2/N2/4A 1/8" & 1/16"	5	9.8-17.1	6.2-32	290-298	0.0045-0.019	0.06-0.62	0.1-10
CO2/Air/4A 1/8" & 1/16"	4	7.3-11.7	6.2-103	297-299	0.00033-0.00034	0.002-0.034	0.1-10
CO2/Air/5A 1/8" & 1/16"	8	4.9-41	1.0-70	202-306	0.00033-0.01	0.002-0.021	0.7-10
CO2/Air/13X 1/8" & 1/16"	17	7.8-21	2.4-70	201-325	0.00003-0.0026	0.0002-0.21	0.7-10
High CO2 Concentrations:	2						
CO2/Air/5A 1/8"	1	1.82	1.43	313	0.132	0.19	15-80
CO2/N2/5A 1/4"	1	1.64	1.43	307	0.098	0.14	5-80

reasonably uniform radial velocity profiles could be expected.
Two runs at high CO_2 concentrations (9.8 mole percent CO_2/
N_2/5A 1/4" and 13.2 mole percent CO_2/air/5A 1/8" LMS pellets),
for which it was determined that effects of heat transfer could
be very important, were run in a special column designed by
F. W. Leavitt (developer of the MASC program) to simulate essen-
tially adiabatic behavior. The column was constructed of thin-
walled sheet metal and was 24.8 cm in diameter. Electric heating
jackets placed in sections along the wall of the column and con-
trolled by thermocouples placed at corresponding intervals along
the centerline of the bed were used to maintain the wall at es-
sentially the same temperature as the bed interior.

Results and Discussion

A comparison between the CO_2 loadings at bed saturation and
those predicted using equation (4) with the LRC coefficients
derived from pure component loading data is shown in Figure 4.
Loadings for the high concentration CO_2/5A runs shown in Table II
are not illustrated in Figure 4, as these cases will be treated
separately below. It can be seen from Figure 4 that the pre-
dictions correspond very well to the actual data, except in the
CO_2/5A cases, for which loadings were overpredicted at lower
concentrations and underpredicted at higher concentrations of
CO_2. For this reason, the LRC coefficients for CO_2 on 5A were
altered in the manner described above. Results of these modifi-
cations are illustrated in Figure 5.
Figure 6(a) shows experimental LUB/G_M values at two values
of breakthrough concentration for breakthrough runs involving
CO_2/air on 4A, 5A and 13X 1/16" and 1/8" pellets at identical
feed conditions. When effects due to extraparticulate (film and
axial) resistance (accounting for 15% or less of the overall
resistance) are subtracted, and the resulting LUB/G_M values are
divided by the square of the pellet diameter, as shown in Figure
6(b), three interesting features can be observed. First of all,
within each zeolite system, it is seen that the value of
$(LUB/G_M d_p^2)_{intraparticle}$ is higher for the case of 1/16" pellets
than it is for the 1/8" pellets, suggesting the presence of
micropore (intracrystalline) resistance. Assuming that macropore
and micropore resistances act approximately as resistances in
series, the data indicate that in all three cases, micropore re-
sistance accounts for about twenty percent and fifty percent of
the overall intraparticle resistance in the 1/8" and 1/16"
pellets, respectively. Secondly, it can be seen from Figure 6(b)
that, although micropore resistances appear to exist in addition
to macropore resistances, the actual values of
$(LUB/G_M d_p^2)_{intraparticle}$ are _less_ than those predicted on
the basis of macropore Maxwell and Knudsen diffusion alone
(dashed lines in Figure 6(b)). In fact, for the case of 13X 1/8"
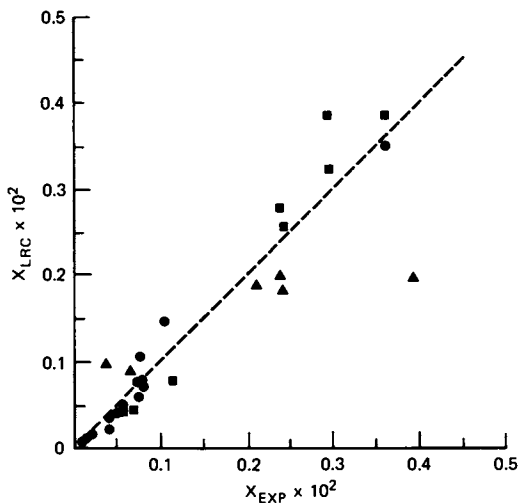pellets, the actual MTZ lengths are only one-fifth of those

Figure 4.   Experimentally determined stoichiometric loadings vs. those calculated via the LRC equations for the CO_2 breakthrough runs on (■) 4A, (▲) 5A, and (●) 13X LMS pellets
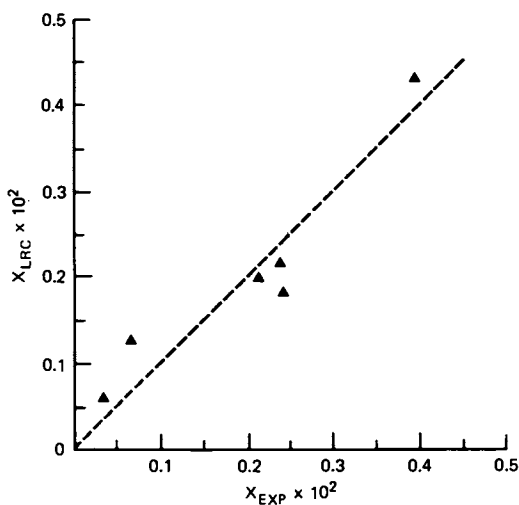

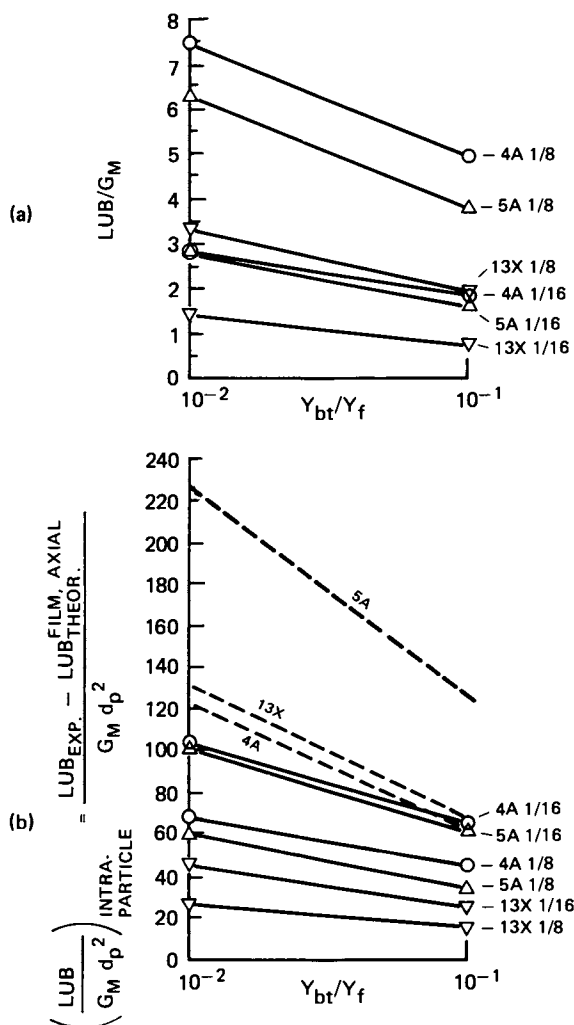*Figure 5.   Fit of adjusted LRC equation for low concentration CO_2/air/5A LMS breakthrough data*

Figure 6.(a)Experimental $[LUB]_{Y_{bt}}^{Y_{1/2}}/G_M$ *values for 330 ppm* CO_2/air break-through runs at 6.2 bar, 25°C, and* $G_M = 11.7$ gmol/hr/cm² on (○) 4A, (△) 5A, and (▽) 13X 1/16″ and 1/8″ LMS pellets; (b) Estimated intraparticle contribution to experimental* $LUB/G_M d_p^2)$ values of Figure 6(a) vs. (– – –) predicted contribution from intraparticle Maxwell and Knudsen resistances alone.*

predicted by these macropore resistances.

The third feature of interest, though more subtle, deserves perhaps the greatest attention. As mentioned above, the ratios of micropore-to-macropore resistance as inferred from Figure 6(b) are approximately identical for the 4A, 5A, and 13X systems shown. Furthermore, since the intrapellet structure and geometry for the three products are roughly the same (except, of course, for the intracrystalline portions), the contributions of Maxwell and Knudsen diffusion to the macropore resistance would be expected to be roughly similar as well (the predicted LUB differences between the 5A product and the 4A and 13X products shown in Figure 6(b) for Maxwell and Knudsen diffusion are due to differences in the equilibrium sorption therms rather than to differences in particle geometry). Based on these assumptions, one of two different hypotheses may be inferred: either the micropore resistances for all three products are approximately identical for these conditions, or there is some additional diffusional mode present which can reduce the overall macropore resistance in such a way as to maintain the same micropore-to-macropore resistance ratio in all three products.

The first hypothesis seems unlikely to be true in view of the rather wide variation in the ratio of carbon dioxide's kinetic diameter to the diameter of the intracrystalline pores (about 0.87, 0.77 and 0.39 for 4A, 5A and 13X, respectively (12)). The alternative hypothesis, however, (additional diffusional modes through the macropore spaces) could be interpreted in terms of transport along the crystal surfaces comprising the "walls" of the macropore spaces. This surface diffusion would act in an additive manner to the effective Maxwell-Knudsen diffusion coefficient, thus reducing the overall resistance to mass transfer within the macropores.

Incidentally, these features cannot be accounted for by assuming different values of macropore radius or tortosity factor in the predictive equations. Even with the assumptions of negligible Knudsen resistance ($r_{pore} \rightarrow \infty$) and no tortuosity ($\tau_M = 1$), the predicted macropore resistances (excluding surface effects) would be lowered by only forty percent, which is still insufficient to account for the low LUB values, at least in the 5A and 13X systems. There appears, therefore, to be a fairly strong case for the presence of a surface diffusion effect in these systems, with the possibility of such an effect in the CO_2/air/4A system as well.

Based upon the results shown in Figure 6 and the surface diffusion model given by equation (21), the values of (D_{os}/τ_s) which best fit the three systems were computed, both from the standpoint of assuming complete macropore control and from that of assuming the existence of micropore resistance as well, in the amount predicted from Figure 6. These values are given in Table III.
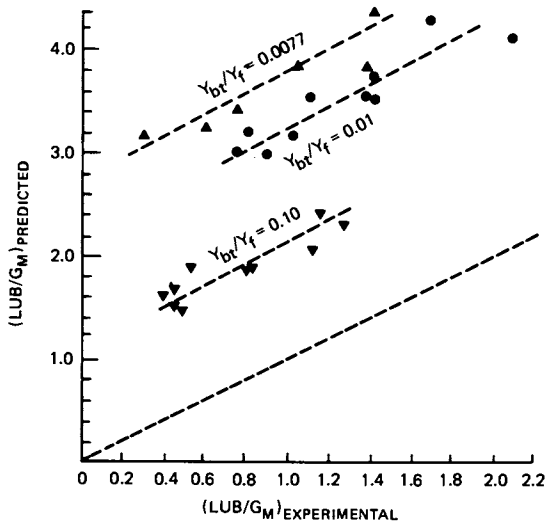
Figure 7.   Experimental vs. predicted $[LUB]_{Y_{bt}}^{Y_{1/2}}/G_M$ *for* $CO_2/air/13X$ *1/16" LMS pellets, assuming* $(\overline{D}_{os}/\tau_s) = 0$
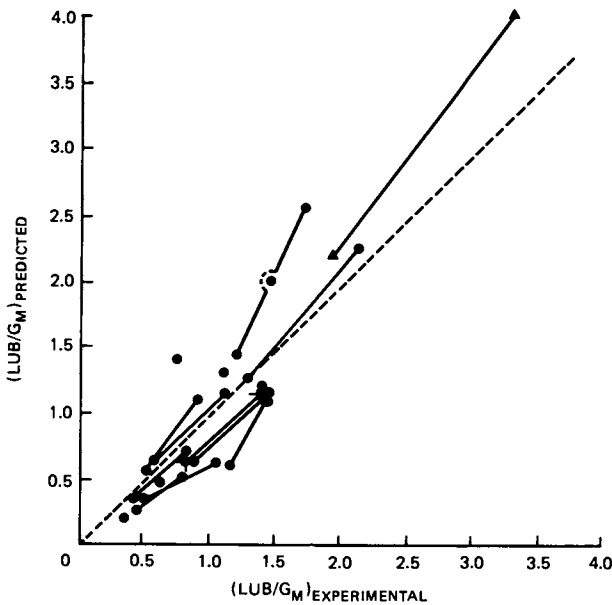

Figure 8.   Experimental vs. predicted $[LUB]_{Y_{bt}}^{Y_{1/2}}/G_M$ *for* $CO_2/air/13X$ (●) *1/16" and* (▲) *1/8" LMS pellets, assuming* $(\overline{D}_{os}/\tau_s) = 1.76$ cm^2/hr

TABLE III

Correlation Parameters for Fits of CO_2 Breakthrough Data

Adsorbent	Excluding Effects of Micropore Resistance	*Including Effects of Micropore Resistance	
	D_{os}/τ_s (cm^2/Hr.)	D_{os}/τ_s (cm^2/Hr.)	**$(Ka)^{-1}_{Zeolitic}$ (Hr.)
4A LMS	0.37	1.39	2.5×10^{-5}
5A LMS	0.84	2.32	1.9×10^{-5}
13X LMS	1.76	4.27	1.2×10^{-5}

* Strictly applicable only to runs shown in Figure 6
** Film coefficient basis.

Using the values of (D_{os}/τ_s) derived on the assumption of complete macropore control (to avoid the problem of correlations involving two concentration-dependent models, as explained above), the rest of the breakthrough data were also correlated within each of the three (4A, 5A and 13X) systems. Figure 7 shows the results of the attempted correlation of MTZ length data in the 13X system before the surface diffusion model was included. Not only are all of the predicted values greater than the actual ones, they also tend to deviate further from the actual values as the value of breakthrough concentration decreases, a trend which would be expected on the basis of the surface diffusion model for the case of favorably curved sorption therms. Figure 8 shows the same MTZ data correlated to predictions in which the surface diffusion model has been included, using the (D_{os}/τ_s) value given in Table III (micropore resistance excluded). Lines connecting the points in Figure 8, as well as those in Figure 9 and 10, indicate that these points were all taken from a single breakthrough run at different values of breakthrough concentration. Comparison between Figures 7 and 8 shows a remarkable improvement in the correlation when the surface diffusion model is added. That the predictions for the case involving 1/8" pellets lie somewhat above the 45 degree line is fully expected, since micropore (intracrystalline) resistances were not accounted for in the correlation.
Though the improvements in correlation were not quite so dramatic in the 4A and 5A systems as they were for the 13X system, the values of (D_{os}/τ_s) of Table III still gave fairly reasonable fits of the MTZ lengths for these cases as well, as indicated in Figures 9 and 10. The MTZ lengths for the high concentration CO_2 runs on 5A (see Table II) are not included in Figure 10, but will be treated in greater detail below.
In addition to improvement in the fit of the data to the predictive models over a wide range of feed and breakthrough
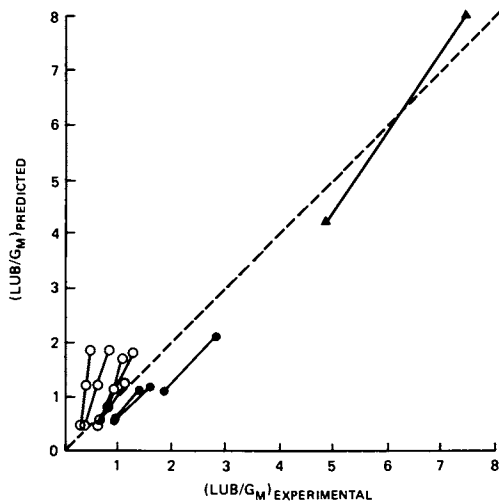
Figure 9. Experimental vs. predicted $[LUB]_{Y_{bt}}^{Y_{1/2}}/G_M$ for $CO_2/N_2/4A$ (○) 1/16", $CO_2/air/4A$ (●) 1/16" and (▲) 1/8" LMS pellets, assuming $(D_{os}/\tau_s = 0.37$ cm^2/hr

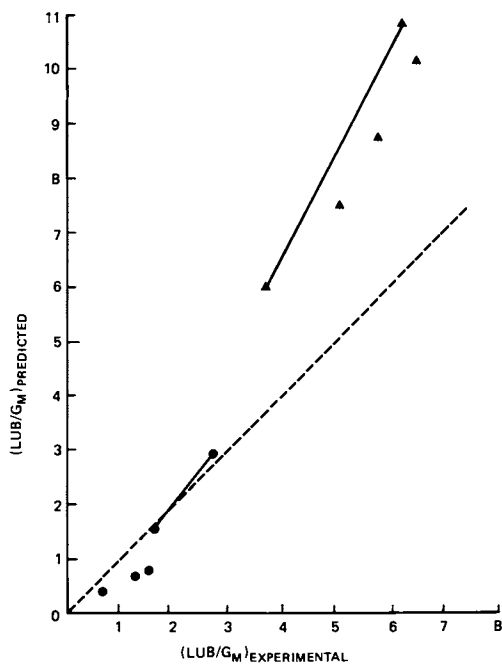*Figure 10. Experimental vs. predicted $[LUB]_{Y_{bt}}^{Y_{1/2}}/G_M$ for $CO_2/air/5A$ (●) 1/16" and (▲) 1/8" pellets, assuming $(D_{os}/\tau_s) = 0.84$ cm^2/hr*

conditions, inclusion of the surface diffusion model gave
significant improvements in predictions of the dependence of MTZ
length upon specific parameters such as feed temperature and
feed pressure. Figure 11 shows three data points taken from
three breakthrough runs involving CO_2/air/13X 1/16" pellets,
in which feed pressure was varied, but all other feed conditions
(as well as the breakthrough concentrations at which the LUB was
measured) remained constant. Although the predictions without
the surface model correctly predicted a decrease in MTZ length
with increasing pressure, addition of the surface diffusion
model improved the predictions substantially, from both the
standpoint of the average LUB values over the entire pressure
range and the ratio of LUB at low pressures to those at high
pressures.

    Figure 12 shows a similar degree of improvement of the de-
pendence of MTZ length of feed temperature. Again derived from
CO_2/air/13X 1/16" pellet systems, the runs consisted of two
sets of three breakthrough runs, with feed temperature being the
only parameter varied in the set, but with slightly different
conditions for either set.

    In Figure 13, three breakthrough runs involving CO_2/air/4A
1/16" pellets with variations in feed pressure alone are shown.
Although the predictions using the surface diffusion model are
slightly low, the fit is again much better than that without
this model, especially in the ratios of MTZ lengths at high and
low pressures. Incidentally, not enough data were taken to
permit similar evaluations of the dependence on temperature in
the 4A system or on pressure or temperature in the 5A system.

    Figure 14 shows a portion of the breakthrough fronts for the
high-concentration CO_2/5A 1/8" and 1/4" runs. As mentioned
above, these cases required extensive computer analysis to
identify the potentially stable portion of the front and the
degree to which steady-state behavior of the fronts was
approached. It was found that the original pure-component LRC's
provided a good fit of the breakthrough loadings and were
therefore used in their unmodified form in the multicomponent
loading predictions. This good fit is not suprising, since at
the high feed concentrations used, the LRC's predicted that N_2
and O_2 account for less than five percent of the overall
loadings at bed saturation. Based on the above-mentioned
computer programs, it was determined that the stable portion of
the fronts had attained, at breakthrough, between eighty-five
and ninety percent of their ultimate steady-state MTZ lengths,
and that extraparticulate (film and axial) resistances con-
tributed less than twenty percent of the overall mass transfer
resistance in either run.

    Also presented in Figure 14 are the computer predictions of
the breakthrough fronts based on three separate assumptions.
Curve 1 is based on the assumption that the sole intraparticle
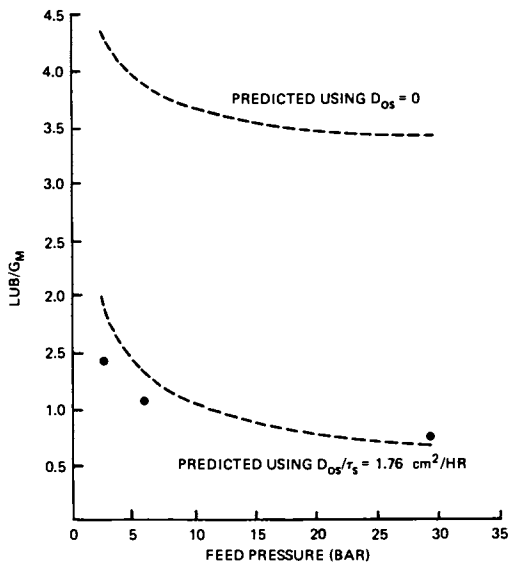resistances are due to Maxwell and Knudsen diffusion. It is seen

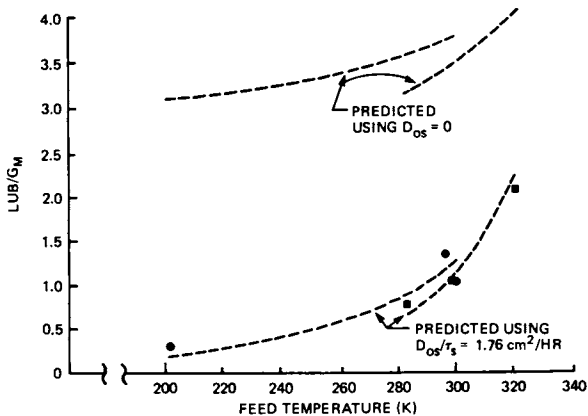*Figure 11. Experimental (●) vs. predicted (– – –) variation of LUB/G$_M$ with feed pressure for selected CO$_2$/air/13X 1/16" runs*

Figure 12. Experimental (●, ■) vs. predicted (– – –) variation of LUB/G$_M$ with feed temperature for selected CO$_2$/air/13X 1/16" runs
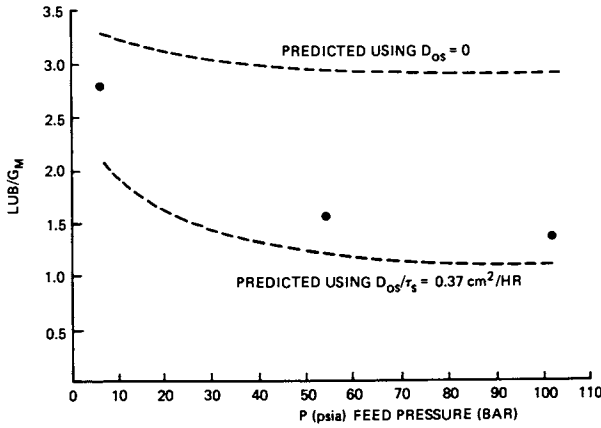
Figure 13. Experimental (●) vs. predicted (–––) variation of LUB/G$_M$ with feed pressure for selected CO$_2$/air/4A 1/16" runs
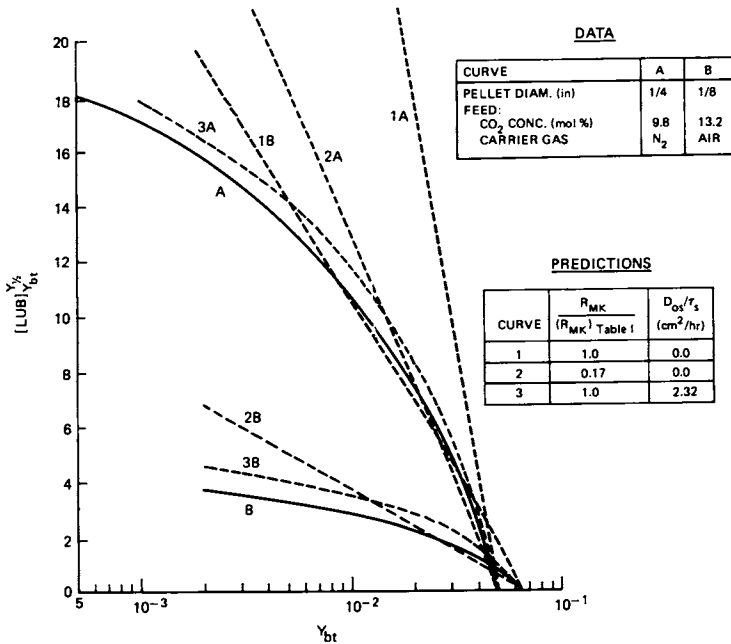

Figure 14. Experimental vs. predicted values of [LUB]$_{Ybt}$$^{Y_{1/2}}$ for high concentration CO/5A breakthrough runs

that, as with the previous series of runs, this assumption tends
to overestimate the size of the MTZ. Curve 2 assumes that intra-
particle resistance is still via the Knudsen and Maxwell diffu-
sional modes, but that the effective resistance due to these
modes is only seventeen percent of that predicted by the dif-
fusion models. Such an assumption gives fairly reasonable MTZ
length predictions down to about ten percent of the feed concen-
tration, but tends to overpredict these lengths at lower concen-
trations. Curve 3 assumes that surface diffusion is present; the
value of (D_{os}/τ_s) assumed in the model is that derived from the
runs shown in Figure 6 for the case where micropore resistances
are accounted for. However, since the results of Figure 6 sug-
gest almost full macropore control for the case of 1/8" and 1/4"
pellets, the effects of the micropore resistances were neglected
for the current predictions. It can be seen that curves 3A and
3B, for the $CO_2/N_2/5A$ 1/4" and $CO_2/air/5A$ 1/8" cases, respec-
tively, yield very good fits of the breakthrough curves over the
entire range of measurements shown in Figure 14.

    Using the computer programs discussed above, it is possible
to extract from these breakthrough curves the effective local
mass transfer coefficients as a function of CO_2 concentration
within the stable portion of the wave. These mass transfer
coefficients are shown in Figure 15, along with the predicted
values with and without the inclusion of the surface diffusion
model. It is seen that without the surface diffusion model, very
little change in the local mass transfer coefficient is pre-
dicted, whereas with surface diffusion effects included, a more
than six-fold increase in diffusion rates is predicted over the
concentrations measured and the predictions correspond very
closely to those actually encountered in the breakthrough runs.
Further, the experimentally derived results indicate that, for
these runs, the assumption that micropore (intracrystalline)
resistances are small relative to overall mass transfer resist-
ance is justified, since the effective mass transfer coeffi-
cients for the two (1/8" and 1/4" pellets) runs scale approxi-
mately to the inverse of the square of the particle diameter, as
would be expected when diffusive resistances in the particle
macropores predominate.

Conclusions

    The preceding analyses of fixed bed breakthrough curves
involving CO_2/air or $N_2/4A$, 5A or 13X Linde Molecular Sieve
pellets strongly suggest the presence of some beneficiating mode
of mass transport, which appears to effect a reduction in the re-
sistances to mass transfer within the macropore spaces of the ze-
olite pellets. The author attributes these effects to the pres-
ence of surface diffusion along the faces of the zeolite crys-
tals, which form the walls of the macropores. Equation (21) of
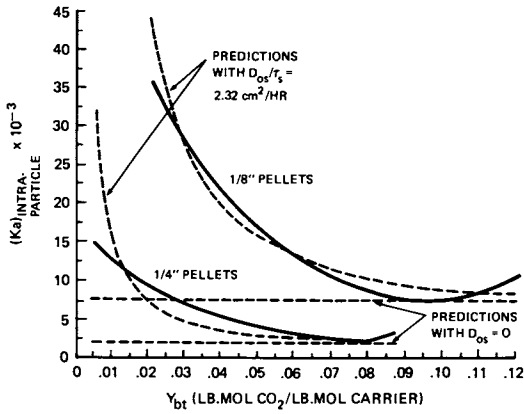the text, based on the Sladeck-Gilliland model for surface

Figure 15. Predicted vs. experimentally obtained mass transfer coefficients as functions of breakthrough concentration for the high concentration $CO_2/5A$ runs of Figure 14.

diffusion on nonporous or solely macroporous sorbent media, appears to provide an excellent means for correlating this effect, at least within a given sorbate-sorbent system. Although the systems investigated here exhibited predominantly macropore control (at least those with pellet diameters exceeding 1/8" or 0.32 cm), there is no reason to believe that surface diffusion effects would not be exhibited in systems in which micropore (intracrystalline) resistances are important as well. In fact, this apparent surface diffusion effect may be responsible for the differences in zeolitic diffusion coefficients obtained by different methods of analysis (13). However, due to the complex interaction of various factors in the anlaysis of mass transport in zeolitic media, including instabilities due to heat effects, the presence of multimodal pore size distribution in pelleted media, and the uncertainties involved in the measurement of diffusion coefficients in multi-component systems, further research is necessary to effect a resolution of these discrepancies.

Nomenclature

a	=	Outer particle surface area per volume of column, cm^2/cm^3
A_b	=	Cross-sectional area of packed column, cm^2
A_1, A_2, A_3, A_4	=	Coefficients in loading ratio correlation (LRC), defined by equations (2) and (3)
b	=	Parameter in LRC equation, equal to $\exp(-A_1-A_2/T)$
c_g	=	Gas phase concentration, $gmol/cm^3$
c_s	=	Sorbed phase concentration, $gmol/cm^2$
C_{pg}	=	Heat capacity of gas phase, $cal/gmol$-K
C_{ps}	=	Heat capacity of solid phase, cal/g-K
d_p	=	Particle diameter, cm
D_{ax}	=	Axial diffusivity, cm^2/hr
D_S	=	Surface diffusivity along the walls of the particle macropores, cm^2/hr
D_{os}	=	Preexponential factor in Gilliland-Sladeck model for surface diffusion, cm^2/hr

Nomenclature (Cont'd)

G_I' =   Molar velocity of fluid phase in moving bed analysis of steady-state wave, defined by equation (15), gmol/hr/cm^2

G_M =   Molar velocity of feed gas, gmol/hr/cm^2

ΔH =   Differential heat of adsorption, cal/gmol

k_{ax} =   Effective bed thermal conductivity in axial direction, cal/hr/cm/K

K =   Mass transfer coefficient, expressed as equivalent film coefficient, cm/hr

l_p =   Particle length, cm

L =   Axial distance measured from feed end of bed, cm

L_b =   Overall length of bed, cm

LUB =   Length of unused bed in sorption front, ft.

m =   Parameter in activation energy term of Gilliland-Sladeck model for surface diffusion = 1, 2 or 3 depending on type of sorbate-sorbent interaction

n =   Parameter in LRC equation = $A_3 + A_4/T$

P =   Pressure, Bar (1 Bar = 100 kPa)

P_i =   Partial pressure of component i in mixture, Bar

r_{pore} =   Mean radius of macropore channels, $\overset{\circ}{A}$

R =   Gas constant

S_g =   Intraparticle specific surface area, cm^2/g of sorbent

t =   Temperature in mass transfer front, °C

T =   Temperature, K

TUB =   Time of unused bed, hr = $(LUB)/u_f$

Nomenclature (Cont'd)

u_f = Mass transfer front speed, defined by equation (16), cm/hr

V_o = Superficial velocity through unpacked column = G_M/ρ_{gm}

X = Loading of sorbate, gmol/g of sorbent

X_o = Maximum achievable loading, gmol/g of sorbent

y = Gas phase mole fraction

y_I = Mole fraction of inert carrier gas

Y = Gas phase molar ratio, gmol/gmol carrier

Greek Letters

ε_p = Void fraction of particle macropores, cm^3/cm^3 particle

ε_T = Total void fraction of bed, excluding intracrystalline (micropore) voids = $1 - (\rho_b/\rho_p)(1-\varepsilon_p)$

θ = Time, hr

ρ_b = Particle bulk (packed) density, g/cm^3

ρ_{gm} = Molar density of gas phase, $gmol/cm^3$

ρ_p = Particle piece density, g/cm^3

τ_M, τ_S = Tortuosity factor for Maxwell and surface diffusion, respectively

ϕ_i = $(b_i p_i)^{1/n_i}$ in LRC equation

Subscripts

bt = Conditions at breakthrough concentration

eff = Effective value

f = Conditions at feed concentration

r = Residual bed conditions (at beginning of each sorption run)

Nomenclature (Cont'd)

1/2   =   Conditions at the point at half the
                    sorbate feed concentration

i   =   1, 2, ... n component

Superscript

*   =   Equilibrium value

Abstract

     Breakthrough runs for CO_2/N_2 and CO_2/Air mixtures on
Linde 4A, 5A, and 13X pellets of three different diameters were
carried out in fixed bed columns designed to simulate nearly
adiabatic behavior. The sorption fronts were analyzed to sepa-
rate effects of intraparticle mass transfer from those due to
heat transfer and extraparticle (film and axial) mass transfer
phenomena. Although the dependence of mass transfer zone (MTZ)
length upon pellet size indicated that mass transfer rates for
pellets with diameters of 1/8" and larger are essentially con-
trolled by macropore resistances, the observed MTZ lengths were
consistently less (sometimes by nearly an order of magnitude)
than those predicted by macropore Maxwell and Knudsen dif-
fusional modes alone. Such predictions were also unable to
account for variations in MTZ length with different feed con-
ditions. Inclusion of a surface diffusion model, however, gave
excellent correlations of the data over wide ranges of pressure,
temperature, and concentration. The author suggests that such a
surface effect and/or heat transfer effects discussed in the
paper could conceivably account for past discrepancies in the
values of zeolitic (micropore) diffusion coefficients as ob-
served through different experimental techniques.

Literature Cited

1. Yon, C.M.; Turnock, P.H. AICHE Symposium Ser. No. 117, 1971, 67, 75.
2. Markham, E.D.; Benton, A.F. J. Am. Chem. Soc., 1931, 53, 497.
3. Michaels, A.S. Ind. Eng. Chem., 1952, 44, 1922.
4. Leavitt, F.W. Chem. Engr. Progr., 1962, 58, 54.
5. Lightfoot, E.N.; Sanchez-Palma, R.J.; Edwards, D.O., in "New Chemical Engineering Separation Techniques" (Schoen, H.M., Ed.); Interscience: New York, 1962, p. 99.
6. Perry, R.H.; Chilton, C.H.; Kirkpatrick, S.D. "Chemical Engineers' Handbook", 4th ed.; McGraw-Hill: New York, 1962; pp. 13-16.
7. Treybal, R.E. "Mass Transfer Operations"; McGraw-Hill: New York, 1955; pp. 54-55.
8. Hirschfelder, J.O.; Curtiss, C.F.; Bird, R.B. "Molecular Theory of Grases and Liquids"; John Wiley & Sons: New York, 1954.
9. Satterfield, C.N. "Mass Transfer in Heterogeneous Catalysis"; MIT Press: Cambridge, Mass., 1970; pp. 33-42.
10. Gilliland, E.R.; Baddour, R.F.; Perkinson, G.P.; Sladeck, K.J. Ind. Eng. Chem. Fundamentals, 1974, 13, 95.
11. Sladeck, K.J.; Gilliland, E.R.; Baddour, R.F. Ind. Eng. Chem. Fundamentals, 1974, 13, 100.
12. Breck, D.W. "Zeolite Molecular Sieves"; John Wiley & Sons: New York, 1974; p. 384.
13. Ruthven, D.M., in "Molecular Sieves - II" (Katzer, J.R., Ed.); ACS Symposium Ser. No. 40; American Chemical Society: Washington, D.C., 1977; p. 330.

Influence of Presorbed Water on the Sorption of Nitrogen by Zeolites at Ambient Temperatures

DONALD PETERSON

Department of Chemistry, California State University, Hayward, Hayward, CA 94542

Zeolites (1, 2) are well known as extraordinary desiccants and, in the absence of sorbed water, as unique sorbents for even highly volatile nonpolar substances, including permanent gases (3). Of the nonpolar permanent gases, nitrogen is most strongly sorbed, owing to its large quadrupole moment (4). Thus, even at room temperature, zeolite NaA in the active, dehydrated form, sorbs over one percent by weight nitrogen at atmospheric pressure (5). Because nitrogen is selectively sorbed from mixtures with oxygen (6), a zeolite equilibrated with air will contain (apart from water) nearly pure nitrogen. Indeed, a one-gallon can of active NaA zeolite in pellet or bead form in contact with air at 25°C contains over twenty liters of nitrogen gas. Any experimenter who has attempted sorption measurements on liquid solutions is well aware of this property, and has had to make due allowance for the release of the sorbed gas upon contact with the solution.

It is well known that sorption of nonpolar substances is strongly influenced by the presence of sorbed water or other hydrogen-bonding or polar substance (7, 8). The nonpolar molecules simply cannot compete with polar ones for the strongest sorption sites. For fairly nonvolatile compounds like, for example, n-butane (sorbed in zeolite CaA) presorption of water means simply a roughly proportionate decrease in sorption capacity. But for oxygen (sorbed in zeolite NaA), it means a disproportionate reduction to near zero capacity (8). This latter measurement with oxygen was made at 90 K; it is of interest to know if the same behavior applies to nitrogen at ambient temperature.

Because of these, and other mainly practical implications, an exploratory study was recently undertaken (9) to provide somewhat more detailed information about nitrogen uptake from air by zeolite NaA in a range of ambient temperatures than was currently available (5, 10, 11, 12, 13), and to assess the influ-

ence of presorbed water under these conditions. The present
study amplifies that work and extends it to three other zeolites
in common use.

Experimental

     The sorbents used in this study were standard Union Carbide
products, molecular sieves types 4A (zeolite NaA), 5A (zeolite
CaA), 13X (NaX), and Sk-40 (NaY) in the pure, "powder" form. The
only chemical analyses performed were those needed to establish
the extent of Ca^{++}-ion exchange of Na^+ in zeolite CaA (70%), and
the Si/Al ratios in zeolite NaX (1.25) and NaY (2.40). The pow-
der was pressed into pellets of ca. 12 mm diameter and 5 mm
thickness by applying a pressure of 25 K psi for one minute. The
pellets were then crushed, screen-graded and 14-28 mesh fractions
collected for measurement. Nitrogen gas, containing a maximum
5 ppm impurities, was supplied by Airco Industrial Gases. It was
passed through a liquid-nitrogen trap packed with Ottawa sand to
ensure removal of condensibles.
     Sorption measurements were made in conventional McBain
quartz-helix balances mounted in a water bath with a Plexiglass
face; the temperature of the bath was constant to within ±
0.01°C. Extensions of helices having sensitivities of ca. 2 mg
mm^{-1} were read to 0.01 mm with a precision of ± 0.02 g sorbate
per 100 g sorbent. However, because of experimental uncer-
tainties described later, the precision of uptakes is seldom
better than ± 0.1 g/100 g, and sometimes worse. The helices were
calibrated at five-degree temperature intervals between 5 and
50°C, and at 100-mg mass intervals up to 400 mg; calibration
formulae comprising functions of both independent variables were
found by a polynominal least-squares fit of all the data. Pres-
sures were measured with large-bore mercury manometers.
     Prior to sorption measurements, zeolite samples were acti-
vated by evacuation at elevated temperatures. There is fre-
quently some question as to how precisely one can establish the
mass of a zeolite sample from which all zeolitic water, but no
water arising from collapse of structural hydroxyl groups, has
been removed (14). In order to establish that the (zeolitic-
water-free) masses of the activated zeolite samples used here are
well defined, the following stepwise activation procedure was
used. Each sample was first heated in vacuo at 300°C. When the
pressure had dropped to below about 10^{-4} torr, the balance was
isolated from the pumps, the rate of pressure increase measured,
and evacuation resumed. This process was repeated until the rate
of pressure increase fell to below 5×10^{-4} torr min^{-1}, a dura-
tion of time which was from 15 to 30 minutes. This is a rate
such that were the increase due to water vapor alone, and were
the rate to remain constant, the weight loss would still be un-
detectable after 24 hrs., a duration seldom exceeded in acti-
vating zeolites.

This procedure was repeated, first evacuating at 350°C, and finally, at 400°C. The results are expressed in Table I as residual masses of (presumed) water present after activation at 300 and 350°C presuming none to be present after activation at 400°C. They show that 1) retention of water by these zeolites at high temperature increases in the sequence CaA≃NaY<NaX<NaA, and 2) the 400°C activation procedure is expected to have produced well defined reference masses in every case except that of NaX, where the indefiniteness is of the order of experimental uncertainties.

Table I.   Residual Water After Activation at Lower
Temperatures Relative to Activation at 400°C

Zeolite	Residual Water, g/100 g Zeolite	
	300° Activation	350° Activation
NaA	0.31	0
CaA	0	0
NaX	0.13	0.10
NaY	0.01	0

Nitrogen uptakes were measured at between 10 and 16 pressures of from 50 to 760 torr, and at 10, 25, and 40°C; at each temperature the first half were taken with increasing nitrogen pressures, the second half with decreasing pressures. This was done using each of the four zeolites activated as described above, and on each sample after the successive presorption of increments of water; in each case, sufficient water was eventually presorbed so as to reduce the uptake of nitrogen to near zero.

During the presorption of water, care was taken not to exceed the equilibrium pressure for the loading desired. Presorption was carried out at 50°C, at which the equilibrium pressure for the lowest loading of 1.5 g/100 g zeolite is ca. 2×10^{-4} torr (15). The reason for this precaution is the extreme tenacity with which zeolites hold water molecules, particularly in the sites of lowest potential (16). While water molecules within the pores of zeolites at high loadings are known to be quite mobile (17), there is reason to believe that this mobility may well not pertain to water molecules occupying these sites of lowest potential. In taking care not to exceed the equilibrium pressure for a given loading, it is hoped that the presorbed water molecules are truly in an equilibrium distribution, and not unevenly distributed preferentially into energetic sites near crystal surfaces. Whether or not water molecules at low loadings are mobile within the zeolite, they certainly are not with respect to escape from the crystal surface: at a loading of 1.5 g H_2O/100 g zeolite, no weight loss is observable after days of exposure to a vacuum of 10^{-5} torr at 50°C.

The sorption of nitrogen occurs instantaneously on intro-

duction of the gas, and appears to be essentially complete within
a few seconds. A gradual, continued mass increase extending over
the ensuing few minutes is undoubtedly due to thermal equilibra-
tion of the zeolite sample after being warmed by the heat re-
leased during sorption. The reverse effects were observed when
approaching equilibrium by desorption. At least ten minutes were
allowed for each equilibration. The generally close agreement
between sorption and desorption points as shown for the dehy-
drated zeolites in Figure 1 indicates that an equilibrium was
being closely approached in each instance. However, on evacua-
tion after completion of measurements for some isotherms, there
remained a small residual mass of approximately the limiting pre-
cision of 0.03 g/100 g zeolite or less. This effect was ob-
served to be most pronounced with zeolite 13X, and at 10°C, was
twice the limiting precision; these residues are shown as the
filled symbols at zero pressure in Figure 1. In the latter case,
the desorption points can be seen to lie above the sorption
points in the lower portion of the isotherm. The residual masses
were consistently ca. 0.03 g/100 g NaA zeolite, but varied be-
tween ± 0.03 g/100 g for zeolites NaY and CaA. These residual
masses persisted even after subsequent evacuation at 50°C for
several hours, indicating a component of irreversible sorption of
nitrogen with respect to the temperatures in the range of
measurement.
     In the hydrated zeolites, the residual masses after isotherm
measurements were in general slightly greater in zeolites NaA and
NaX, but again mostly negligible in zeolites CaA and NaY. In
order to characterize this implied irreversible sorption further,
the uptake of nitrogen at 25°C and 600 torr by zeolites NaA and
NaX containing 3 g presorbed water per 100 g zeolite was followed
for one month. The nitrogen uptakes at the end of this period
are compared to those after 10 minutes' contact in Table II.

Table II. Long-term Nitrogen Uptake at 25°C and 600 torr

	Nitrogen Uptake, g/100 g Zeolite	
Zeolite	After 10 Minutes	After one Month
NaA	0.18	0.58
NaX	0.40	0.51

At the end of one month, the rate of increase was approximately
0.1 g/100 g per month; thus, the slow sorption process appears
to be near completion, at least in zeolite NaA. Again, these
mass increases persisted after prolonged evacuation at 50°C.
     That these increases are due to uptake of nitrogen and not
traces of water or other nonvolatile impurities within the
vacuum system is supported by 1) the variability of the magni-
tude of the effect among the four zeolites studied, 2) the in-
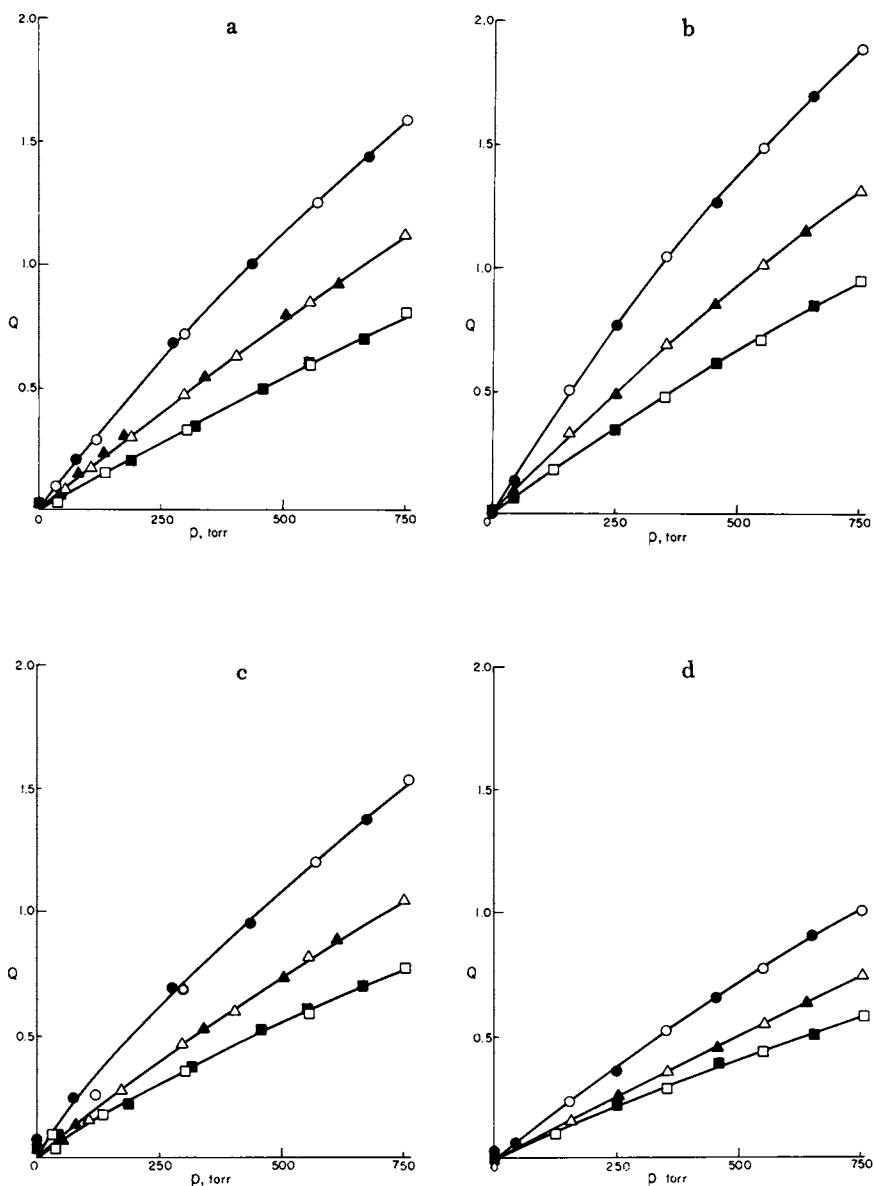crease of the size of the residues with increasing content of

Figure 1. Isotherms for sorption of nitrogen on zeolites (a) NaA, (b) CaA, (c) NaX, and (d) NaY at (○) 10°C, (△) 25°C, and (□) 40°C. The ordinate is in units of g nitrogen/100 g dehydrated zeolite. Sorption data are shown as open symbols, desorption data, as filled symbols.

presorbed water, and 3) the care taken to preclude nonvolatiles
from the system. However, the effect is only marginally larger
than limiting experimental uncertainties and must be regarded as
only tentatively established. The central purpose of this work
was to study the primary, rapid sorption of nitrogen, with re-
spect to which the implied irreversible component is to be re-
garded as a further source of experimental uncertainty.

Interpretations of results using hydrated zeolites are also
subject to uncertainty arising out of the need of assuming that
true equilibria are reached in spite of the stepwise addition of
water and nitrogen. In view of the vastly different sorbabili-
ties of these two substances, this is certainly a reasonable
approximation: water molecules occupying sites at very low equi-
librium pressure are not likely to be displaced by nitrogen
molecules. That the above implied irreversible uptake of nitro-
gen in zeolites NaA and NaX is not evidence for such a displace-
ment process is inferred from its occurrence also in the dehy-
drated forms. This assumption of site independence is most
valid at the lowest water loading of 1.5 g/100 g zeolite, but may
be questioned in instances where appreciable nitrogen sorption
occurs at high water loadings. A further complication is that
at these higher water loadings, some sorbed water will escape
from the zeolite. However, care was taken to minimize the ex-
posure of hydrated zeolites to dynamic vacua; once nitrogen gas
had been admitted, the rate of escape of water from zeolite
crystals can be presumed negligible in the time-frame of the
isotherm measurements. In any event, uncertainty in the mass of
water present affects nitrogen loadings very little, since the
latter are based on the helix extension immediately prior to in-
troduction of nitrogen gas, leading to an uncertainty in nitro-
gen loadings ranging from 0 to 0.03 g/100 g zeolite. Recorded
mass losses prior to nitrogen introduction cannot be definitely
attributed solely to loss of sorbed water at these high water
loadings, as loss of the implied irreversibly sorbed nitrogen
under these conditions might contribute. Uncertainty in water
loadings due to this effect is estimated at ca. 0.2 g/100 g
zeolite; the lowest water loading at which this applies is shown
in Table III.

Table III. Lowest Loading at which Appreciable Desorption
           of Water Occurs

| Zeolite | Water Loading, g/100 g Zeolite | |
	Lowest Applicable	Maximum Reported
NaA	> 6	6
CaA	4.5	18
NaX	4.5	18
NaY	3	18

In an additional experiment, it was verified that under the conditions employed here, the uptake of nitrogen by molecular sieve type 3A (KA) is negligible.

Results

The observed sorption capacity Q for nitrogen is shown as a function of pressure p, for the dehydrated zeolites in Figure 1. Here, and throughout this paper, sorption capacities are expressed as one-hundred times the mass sorbate x per unit mass of dehydrated sorbent m,

$$Q = 100x/m$$

This is also true of nitrogen sorption in hydrated zeolites.

The observed variation of nitrogen sorption capacity at atmospheric pressure with content of presorbed water is shown in Figure 2. In all cases, the nitrogen capacity is seen to fall off regularly with increasing amounts of presorbed water, the rate of fall being highest in zeolite NaA and lowest in zeolite NaY.

As a means of identifying divergent data, as well as providing an analytic basis of reporting all the observed data, use was made of the simple Langmuir model, which experience shows (18) frequently applies quite well in the region of very low relative coverages when characterized by isotherms of very little curvature like those encountered here. A linear regression was made of the data for each isotherm according to the customary linear form of Langmuir's equation,

$$\frac{p}{Q} = \frac{1}{a} + \frac{b}{a} \, p, \tag{1}$$

with $a = Q_m b$ and (19)

$$b = \frac{h^3 N_A}{(2\pi m k T)^{3/2} \, R'T} \, e^{q_{st}/RT} \tag{2}$$

Here Q_m is the monolayer capacity (expressed in units of Q), q_{st} is the isosteric heat of sorption, h is Planck's constant, k is Boltzmann's constant, N_A is Avogadro's number, m is the mass of a nitrogen molecule, T is the absolute temperature, and R and R' are molar gas constants (units of q_{st}/T and $h^3 N_A/(2\pi m k)^{3/2} T^{5/2}$, respectively). Expressed as p/Q, some data were observed to deviate substantially from the others. One or two of these values from each such set of data and in a few cases, three, were then subjected to the statistical "4d" test and rejected if they qualified. The rejected data were invariably those corresponding to the lowest pressures, which contribute disproportionately owing to the form of Equation 1. A second linear regression was made of the remaining data, and its results used in lieu of the
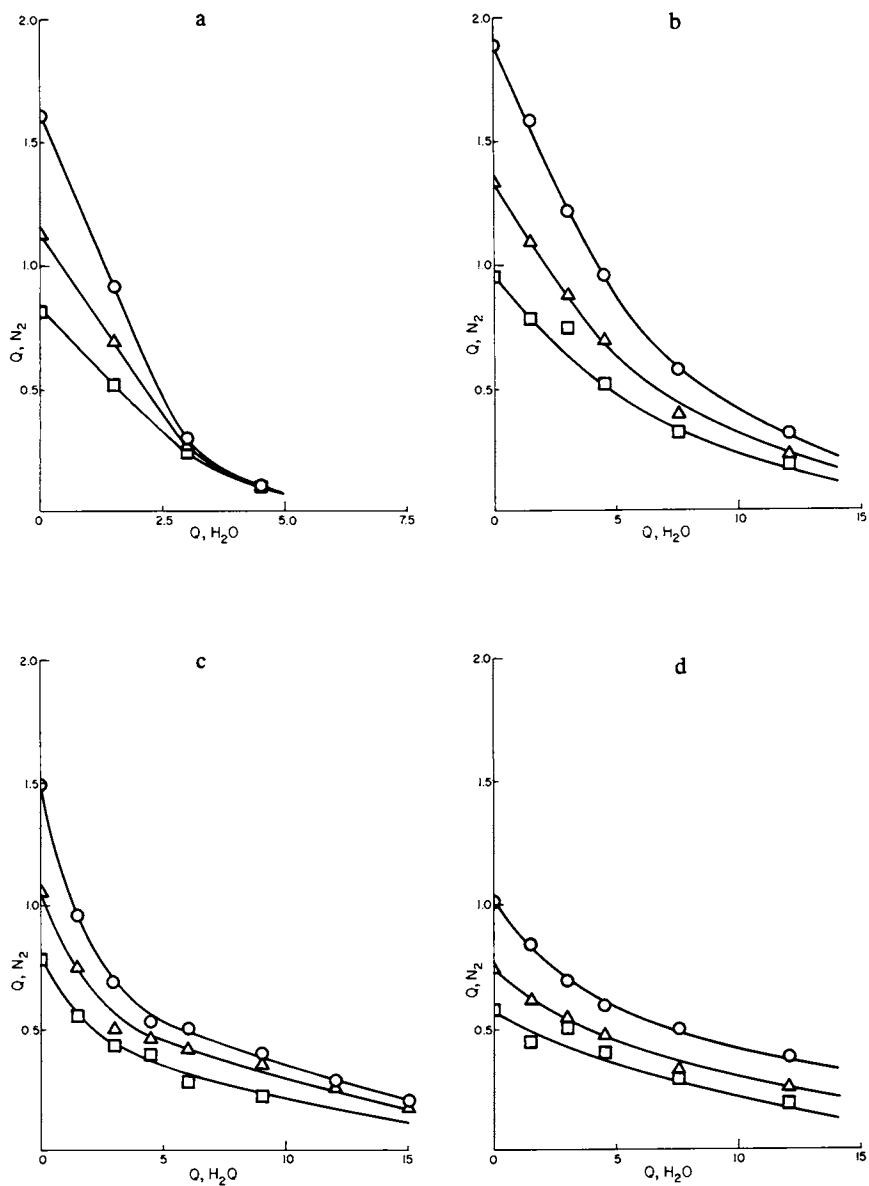
Figure 2.   Sorption capacity for nitrogen at 1 atm pressure vs. content of presorbed water on zeolites (a) NaA, (b) CaA, (c) NaX, and (d) NaY at (○) 10°C, (△) 25°C, and (□) 40°C.   Both ordinate and abscissa are in units of g sorbate/100 g dehydrated zeolite.

Table IV. Values of Langmuir Parameters
(Q in g/100 g zeolite, p in torr)

$Q(H_2O)$	T, °C	NaA			CaA			NaX			NaY		
		Q_m	$10^5 a$	$10^5 b$	Q_m	$10^5 a$	$10^5 b$	Q_m	$10^5 a$	$10^5 b$	Q_m	$10^5 a$	$10^5 b$
0	40	10.5	111	11	5.7	151	26	3.3	130	39	5.3	86	16
	25	7.2	172	24	5.8	223	38	8.4	159	19	6.4	108	17
	10	6.3	275	44	7.7	337	44	6.0	262	44	7.5	156	21
1.5	40	11.4	75	7	8.0	115	14	6.4	81	13	2.0	82	41
	25	6.4	102	16	5.7	180	32	2.4	134	56	7.1	85	6
	10	3.8	151	40	6.2	284	46	4.5	159	35	7.1	127	18
3	40		–		5.2	115	22	2.2	70	32		–	
	25		–		6.4	135	21	8.9	70	8		–	
	10		–		11.4	189	17	4.9	107	22		–	
4.5	40		–		5.9	75	13	0.8	100	125		–	
	25		–		5.6	103	18	1.8	82	46		–	
	10		–		11.8	140	12	5.7	71	12		–	

Zeolite

original regression. Values of the Langmuir isotherm parameters
so obtained are summarized for regions of relatively higher
coverage in Table IV. Isotherms for higher presorbed water con-
tents than those contained in Table IV are at relatively lower
coverage and are adequately represented as linear; nitrogen
capacities in this region may be approximated with the aid of
those contained in Figure 2 for atmospheric pressure.

    While the values in Table IV, when substituted into Equa-
tion 1, represent the observed results to within experimental
error, their practical utility probably ends there. To begin
with, values do not exhibit consistent trends, and thus do not
readily admit a general correlation at all water contents and
temperatures for any of the four zeolites. Most consistency and
breadth is observed in the CaA parameters and least, in those of
NaY, in which the greatest and lowest relative precision, re-
spectively, was obtained. Because of the poor experimental pre-
cision and near linearity of the isotherms, the parameters gen-
erally are quite poorly determined. Standard errors in the
values of Q_m in Table IV are such that for each set of isotherms
at the three temperatures reported, corresponding values of Q_m,
within the limits of experimental error, are the same, as is
indeed required by the Langmuir model. Weighted averages of Q_m
values and their standard errors for each trio of isotherms con-
tained in Table IV are shown in Table V.

Table V. Average Monolayer Coverages of Nitrogen

      (g/100 g zeolite)

Presorbed Water,	Zeolite			
g/100 g zeolite	NaA	CaA	NaX	NaY
0	7.8±2.0	6.4±0.6	5.9±8.2	6.4±1.9
1.5	6.4±7.8	6.5±1.9	4.1±2.1	7.1±4.3
3	–	7.8±3.1	4.8±2.4	–
4.5	–	7.9±2.4	3.8±1.8	–

The monolayer values are roughly one-fourth those reported at far
lower temperatures, save that for NaA, from which nitrogen is
excluded at low temperatures ([8]).

    Lack of consistency is also seen in the values of b.
According to Equation 2, values of b at 10°C would be expected
to be ca. 2.2 times those pertaining to 40°C. While some of the
data reflect this trend, many do not. Further, nearly all the
fitted values of b lead, through Equation 2, to values of q_{st}
which are in the range of 8 to 9 kcal mol^{-1} compared to re-
ported values in the range of 4 to 6 kcal mol^{-1} ([3], [13], [20]). It
can be seen through Equation 2 that values of b are over 100
times too large to be consistent with these values.

    Isosteric heats were obtained using the fitted curves with
the aid of the Clausius-Clapeyron equation:

$$\left[\frac{d \ln p}{dT^{-1}}\right]_Q = \frac{-q_{st}}{R} \quad .$$

Within experimental error, heats were not observed to vary with coverage; values obtained for the dehydrated zeolites and most hydrated ones of Table IV are shown in Table VI.

Table VI.   Isosteric Heats of Sorption
(kcal mol^{-1}, ± 0.5 kcal mol^{-1})

Presorbed Water g/100 g zeolite	NaA	CaA	NaX	NaY
0	4.5	5.0	4.5	4.2
1.5	3.7	–	–	3.7
4.5	–	3.8	3.0	–

Discussion

Uptake of nitrogen is seen to vary markedly among the zeolites studied, being in zeolite CaA twice what it is in NaY in the temperature range studied. Values for dehydrated zeolites compare well with findings of the few sorption studies found in the literature at such high relative temperatures. A comparison at 25°C and at a nitrogen equilibrium pressure of one atmosphere is shown in Table VII. The value of 1.32 g/100 g under the same conditions reported here for zeolite CaA is in reasonable agreement with a previously reported one of 1.52 (10), as is the present value of 1.06 g/100 g for zeolite NaX with an extrapolation of data (13) at somewhat lower temperatures and pressures. Somewhat lower values are reported (12) for European zeolite NaA and NaX products. Uptakes by hydrated NaA zeolite are in as close agreement with values reported (9) for the sorbent in bead form as can be expected in view of the relatively large experimental uncertainties in both studies, and the presence of an imprecisely known amount of binder in the latter case.

Table VII.   Reported Sorption Capacities for Nitrogen on
Zeolite NaA at 25°C and Atmospheric Pressure

Capacity, g/100 g zeolite	Reference	Comment
1.11	This work	
(0.92)	9	Contains approximately 20% binder
1.15	3	Interpolated from data at 0 and 30°C
1.15	5	Interpolated from data at -78 to 30°C
1.00	10	Extrapolated from data at -78 to 0°C

The isosteric heats of sorption reported in Table VI are also in acceptable agreement with values based on sorption measurements made near ambient temperature by other investigators, as the comparisons in Table VIII show.

Table VIII. Reported Isosteric Heats of Sorption
(kcal mol^{-1})

Zeolite				Reference	Method
NaA	CaA	NaX	NaY		
4.5	5.0	4.5	4.2	This work	
4.5				9	Static Equilibrium
4.4				21	Gas Chromatography
	5.2			20	Static Equilibrium
	5.5			12	Static Equilibrium
		4.5	4.3	3	Gas Chromatography
		4.5		13	Static Equilibrium
			3.8	22	Gas Chromatography

The declines in nitrogen sorption capacity contained in Figure 2 afford several interesting comparisons. First, the persistence of nitrogen sorption in zeolites CaA, NaX, and NaY with presorbed water levels at which uptake in NaA has all but vanished supports the proposal (8) that the reduction of nitrogen capacity by sorbed water involves a blockage to an appreciable fraction of the zeolite interstices as opposed to a simple covering of active sites, which would appear to be the mechanism of nitrogen exclusion common to the three larger-pore zeolites. From the decline in nitrogen sorption on anhydrous NaA at low temperatures (below -80°C) (8), uptake at higher temperatures may be expected to be sensitively dependent on the positions of the first water molecules sorbed. In dehydrated NaA, three of the twelve sodium ions occupy positions partially blocking the six eight-membered rings of oxygen atoms giving access to the sorption cavity within each unit cell (S_{II} sites); eight, nearby positions on the periphery of the cavity walls (S_I sites); and one, a more distant position on the cavity wall (23). The first water molecules to enter a cavity would more likely be sorbed in positions in closer proximity to S_I ions. However, S_I and S_{II} sites are only 400 pm apart (22), so that the positive end of the dipole of a water molecule sorbed near a Na_I cation may be supposed to repulse a nearby Na_{II} ion so that it is displace far enough into the 8-ring as to preclude the rapid passage of nitrogen molecules. On the other hand, it can be argued that the more likely sites for initial sorption of water molecules are those within the smaller sodalite cages (23), adjacent

to the Na_I ions, owing to the stronger attractive dispersion interaction with the oxygen atoms of the framework existing there. The net anionic charge on the framework may then permit sufficient movement of Na_{II} ions toward the 8-ring centers to inhibit passage of nitrogen molecules.

Evenly distributed, three sorbed water molecules per unit cell would in either event then become sufficient to reduce rapid nitrogen uptake appreciably. This corresponds to a loading of presorbed water equal to 3.2 g/100 g zeolite. This value is in close agreement with what was observed, some allowance being made for unevenness of distribution of sorbed water molecules. If this is the mechanism for exclusion of nitrogen from sorption sites in zeolite NaA, then uptake of nitrogen in hydrated NaA is to be regarded as consisting of rapid equilibration in as yet unblocked cavities, followed by a highly activated penetration of blocked cavities. A very gradual uptake of nitrogen was indeed observed with 3 g presorbed water per 100 g zeolite in an amount approximating the volume of these cavities. (See Experimental section and Table II.)

The curves of Figure 2 may be thought of as "titration" curves for the sites involved, those in zeolite NaA equalling the number of 8-rings. That sites of similar nature are involved is also shown by the observed constancy of isosteric heats of sorption with coverage. It is then clear that the initial, steep fall of the CaA zeolite curves corresponds to sites of greater number in the A structure. These curves have the appearance of being the sum of two lines of different slope. Lines drawn through the first three points (first two at 40°C) are all found to intercept the horizontal axis at Q = 8.4 g water per 100 g zeolite, which corresponds to 7.8 water molecules per unit cell. This admits the very direct interpretation that in CaA, it is the total S_I sites which are being titrated. The remaining more gradual drop then describes the filling of sites of appreciably higher sorption potential. The curves have essentially reached zero at Q = 17 g/100 g zeolite, which may be noted to be just beyond the loading at which the isosteric heat of sorption becomes essentially constant at ca. 17.5 kcal mol^{-1} after falling from at least 30 kcal mol^{-1} near zero coverage ($\underline{8}$).

Results on the X and Y zeolites do not allow as clear an analysis. Less well defined extrapolations of the early portions of the curves of Figure 2c lead to a value of 4.3 g/100 g zeolite for type NaX. This corresponds to about 35 water molecules per unit cell, or 4.4 per supercage (or per sodalite unit). It is tempting to identify the sites being titrated here as those within the sodalite units, which will accommodate four each ($\underline{24}$). The titration curves for NaY show evidence of a less steep decline at low water loadings, but do not permit an estimate of the number of sites being titrated. A reasonable interpretation of this difference is that while the same sites are being occupied, the degree of filling is reduced by the lower cation density in

NaY relative to NaX, particularly in sites within sodalite units
(25). Proton magnetic relaxation studies show that in both types
NaX and NaY zeolites, up to about 5% of the total sorption sites
for water, or ca. 1.3 g/100 g zeolite, the range covered in the
present study, are distinguished by the fact that the residence
time of individual water molecules retained on them is one-hun-
dred times larger than that of molecules occupying all other
sites (26); this observation was interpreted, however, as being
due to sorption at crystal imperfections.

Conclusion

        The above observations show that measurement of the influ-
ence of a strongly bound polar sorbate on the uptake of a weakly
bound nonpolar one are a useful source of corroborative infor-
mation concerning the character of sorption sites in zeolites.
The utility of this approach can be broadened by the choice of
alternate sorbates or series of either polar or nonpolar sor-
bates. It is limited by the need to select sorbate pairs whose
relative sorbabilities are such that the polar sorbate is not
appreciably desorbed during the measurement of uptake of the non-
polar sorbate.
        Of particular interest in the present study is the apparent
existence of an activated sorption mechanism for nitrogen in
partially hydrated zeolite NaA, a further study of which is
planned. The less definitely established irreversibly sorbed
nitrogen on dehydrated zeolites NaA and NaX, but not on CaA and
NaY, is in need of confirmation, and of further characterization.
A practical utility of the results is the quantifying of nitrogen
uptake from air, which persists even with appreciable sorbed
water. This amount can be approximated from the isotherms as the
capacity at 0.8 atm. inasmuch as the contribution due to oxygen
is very small. Conversely, the isotherms can be used to assess
the state of hydration of a zeolite, with the aid of a measure-
ment of the amount of sorbed nitrogen, either by mass loss on
evacuation at room temperature in a balance, or by collection of
gas evolved on immersion of a sample in water.

Literature Cited

1. Barrer, R.M., British Chem. Eng., 1959, 4, 267.
2. Breck, D.W., "Zeolite Molecular Sieves," John Wiley & Sons,
    New York, NY, 1974.
3. Neddenriep, R.J., J. Colloid Interface Sci., 1968, 28, 293.
4. Kington, G.L.; Macleod, A.C., Trans. Faraday Soc., 1959, 55,
    1799.
5. Harper, R.J.; Stifel, G.R.; Anderson, R.B., Can. J. Chem.,
    1969, 47, 4661.
6. Danner, R.P.; Wenzel, L.A., A.I.Ch.E. Journal, 1969, 15, 515.
7. Barrer, R.M.; Rees, L.V., Trans. Faraday Soc., 1954, 50, 1.
8. Breck, D.W.; Eversole, W.G.; Milton, R.M.; Reed, T.B.;
    Thomas, T.L., J. Am. Chem. Soc., 1956, 78, 5963.
9. Peterson, D.L., J. Colloid Interface Sci., in press.
10. Ruthven, D.M., A.I.Ch.E. Journal, 1976, 22, 753.
11. Ruthven, D.M.; Derrah, R.I., J. Chem. Soc. Faraday Trans. I.,
    1975, 71, 2031.
12. Gnauck, G.; Rosner, E.; Eichhorst, E., Chemische Tech., 1970,
    22, 680.
13. Barrer, R.M.; Stuart, W.I., Proc. R. Soc. London, Ser.A,
    1959, 49, 464.
14. Barrer, R.M.; Denny, A.F., J. Chem. Soc., 1964, 4684.
15. Data Sheets, Union Carbide Corp., Tarrytown, NY.
16. Barrer, R.M.; Bratt, G.C., Phys. Chem. Solids, 1960, 12,
    146.
17. Parravano, C.; Baldeschwieler, J.D.; Boudart, M., Science,
    1967, 155, 1535.
18. Brunauer, S.; Emmett, P.H.; Teller, E., J. Am. Chem. Soc.,
    1938, 60, 309.
19. Fowler, R.H., Proc. Camb. Phil. Soc., 1935, 31, 260.
20. Rouquerol, R.; Partyka, S.; Rouquerol, J., Coll. Int.
    C.R.N.S., No. 21, Marseille (19-1), Thermochimie, C.N.R.S.,
    Paris, 1972.
21. Habgood, H.W., Can. J. Chem., 1964, 42, 2340.
22. Egerton, T.A.; Stone, F.S., J. Colloid Interface Sci., 1972,
    38, 195.
23. Reed, T.B.; Breck, D.W., J. Am. Chem. Soc., 1956, 78, 5972.
24. Yanagida, R.Y.; Amaro, A.A.; Seff, K., J. Phys. Chem., 1973,
    77, 805.
25. Mortier, W.J.; Bosmans, H.J.; Uytterhoeven, J.B., J. Phys.
    Chem., 1972, 76, 650.
26. Pfeifer, H.; Gutsze, A.; Zhdanov, S.P., Z. Phys. Chem.
    (Leipzig), 1976, 257, 735.

Selective Sorption Properties of Zeolites

R. M. DESSAU

Central Research Division, Mobil Technical Center, Princeton, NJ 08540

Zeolites are highly porous crystalline adsorbents
with pore openings of fixed and uniform dimension.
The surface for adsorption is essentially entirely
internal due to the channels and cavities which
uniformly penetrate the entire volume of the adsorbent.
The molecular sieving properties of the zeolites are
uniquely determined by their pore diameters, the magni-
tude of which determines what size molecules are
totally excluded from the interior of the zeolite.
Quite apart from this molecular sieving effect,
zeolites are also effective in selectively sorbing
particular components from a mixture of molecules all
individually capable of penetrating the entire zeolite.
Some liquid phase sorption equilibria studies have
been reported for both the small-pore 5A molecular
sieve (1) and the large-pore faujasite NaY zeolite
(2). With the recent synthesis of intermediate pore
size zeolites such as ZSM-5 and ZSM-11(3), a study of
the selective sorption properties of these zeolites
was initiated.

The high silica/alumina ratio zeolites ZSM-5 and
ZSM-11 both contain two intersecting channel systems
composed of 10-membered oxygen rings. The channels
in these zeolites are elliptical, with a free cross-
section of 5.5 x 5.1 for the linear channels, and a
cross-section of 5.6 x 5.4 for the sinusoidal channels
in ZSM-5. The channel structures of these two zeolites
are shown in Figure 1.

EXPERIMENTAL

Materials

The hydrogen forms of the ZSM-5 and ZSM-11
samples were prepared from the parent as-synthesized
zeolites (4) by drying at 125°C, calcining in nitrogen
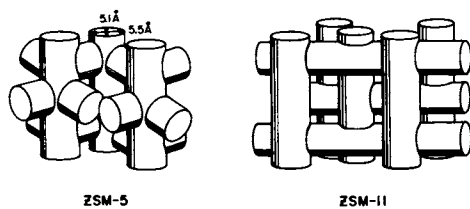
Figure 1. The channel structure in ZSM-5 and ZSM-11

at 538°, and ion-exchanging with ammonium chloride
solution, followed by programmed air calcination at
2°/min. from 25°-538°, with the temperature held at
538° for 10 hours. The dealuminized mordenite sample
was prepared by refluxing Zeolon Type 100H (Norton Co.)
in 0.5N aqueous hydrochloric acid for 16 hours. The
high silica/alumina ratio ZSM-5 sample (SiO_2/Al_2O_3 =
 1670) was obtained according to the procedure given
in the patent literature (5).

The silica/alumina mole ratios of the zeolites
studied were as follows: ZSM-5, 62; large crystal
ZSM-5, 75; high silica ZSM-5, 1670; ZSM-11, 78; and
dealuminized mordenite, 61. Aluminum analysis was
by atomic absorption spectroscopy. Zeolite crystal-
lite sizes were generally less than 0.1μ, except for
the large crystal ZSM-5 sample which was larger than
1μ.

Due to the high hydrophobicity of these zeolites,
no pretreatment to remove sorbed water was required
immediately prior to their use in the sorption experi-
ments.

The organic sorbates used were the purest (>99%)
available commercially, as were the non-sorbable
solvents and internal standards: 1,3,5-tri-iso-
propylbenzene, 1,3-di(trifluoromethyl)benzene,
mesitylene, tetramethylsilane, and cis- and trans-
decalin.

Competitive Sorption Studies

In a typical experiment, 2 grams of a solution
containing two sorbates (2.5% by weight each) in an
inert solvent was added directly to 1g of a zeolite
contained in a vial. An internal standard such as
mesitylene was used in some cases. This mixture,
which occasionally was shaken at room temperature,
was sampled periodically for changes in substrate
concentrations. Microliter size samples were analyzed
by vapor phase chromatography and were compared to the
original solution analyzed in the identical manner.
The selectivity factor observed was defined as:

$$S_{A,B} = \frac{\text{(A adsorbed on zeolite)}}{\text{(B adsorbed on zeolite)}} \times \frac{\text{(B in solution)}}{\text{(A in solution)}}$$

Sorption was generally rapid and complete within a few
hours. Establishment of equilibrium was assumed when
no significant changes were observed after 24 hours.

Counterdiffusion Studies

In a typical experiment, two solutions were pre-
pared: A - contained 0.3g p-xylene, 0.3g 1,3-di(tri-
fluoromethylbenzene, and 11.4g 1,3,5-tri-isopropyl-
benzene; B - contained 1.0g n-nonane, 1.0g mesitylene
and 6.0g 1,3,5-tri-isopropylbenzene.   3.0g of solution
A was added to 1.0g H-ZSM-5 at room temperature; the
sorption of p-xylene was monitored over a period of
several hours by gas chromatography. When the sorption
had reached a constant value, 0.6g of solution B was
added. The resulting desorption of p-xylene and the
adsorption of n-nonane was monitored by gas chromato-
graphy. In these experiments, the 1,3-di(trifluoro-
methyl)benzene and mesitylene behaved exclusively as
non-sorbing internal standards.
A similar experiment was performed with a large
crystal (>1µ) H-ZSM-5 of 75 silica/alumina ratio, and
also with a sample of 1670:1 silica/alumina ratio
H-ZSM-5.

Relative Sorption in Binary n-Paraffin Systems

Two grams of a solution containing 5% each of two
linear paraffins and an internal standard 1,3,5-tri-
tert-butylbenzene dissolved in 1,3,5-tri-isopropyl-
benzene was added to 1g H-ZSM-5. Equilibrium sorption
was established within a few hours and remained con-
stant for 24 hours.

Separation of Functionally Substituted Hydrocarbons

Two grams of a solution containing 5% each of two
functionally substituted hydrocarbons and an internal
standard mesitylene dissolved in tetramethylsilane was
added to 1g H-ZSM-5. Microliter samples were with-
drawn periodically and analyzed by vapor phase chroma-
tography.

Selective Sorption of Alcohols from Aqueous Solution

Two grams of an aqueous solution containing 3.2%
each n-butyl alcohol, iso-butyl alcohol, and tert-
butyl alcohol was added to 1g high silica/alumina ratio
H-ZSM-5 (SiO_2/Al_2O_3 = 1670). Sorption of tert-butyl
alcohol appeared negligible, and sorption of the other
two isomers was calculated relative to tert-butyl
alcohol.

<center>RESULTS</center>

Sorption Properties of ZSM-5

At room temperature ZSM-5 readily sorbs linear and monomethyl-substituted paraffins as well as monocyclic hydrocarbons such as cyclohexane, and aromatics including benzene, toluene, and p-xylene. Sorption of slightly larger molecules, such as 2,2-dimethyl butane and o-xylene, occurs at a substantially slower rate, which is especially noticeable when zeolitic crystallites larger than 1μ in size are used. Still somewhat larger compounds such as cis- and trans-decalin, m-di(trifluoromethyl) benzene, tetramethylsilane, and 1,3,5-trimethylbenzene, do not sorb to any significant extent at room temperature. On the basis of the sorption data available, it appears that molecules having minimum elliptical cross-sections greater than 6.4 x 6.9Å (as measured on molecular scale models) would be excluded from the interior of these zeolites. (See Table I.)

<center>Table I
Sorption in ZSM-5 and Molecular Size</center>

Compound	Sorption in ZSM-5[a]	Molecular Size[b] in Å
Neopentane	Yes	6.2 x 6.2
Benzene	Yes	6.2 x 3.4
1-methylbutylbenzene	Yes	6.4 x 6.2
o-xylene	Yes	6.8 x 3.4
Cis-decalin	No	7.0 x 5.2
Tetramethylsilane	No	7.0 x 7.0
1,3-di(trifluoromethyl) benzene	No	7.0 x 5.1
Cyclooctane	No	7.1 x 4.9
1-ethylpropylbenzene	No	7.1 x 6.4
1,3,5-trimethylbenzene	No	7.6 x 3.4

(a) At room temperature in the liquid phase.
(b) Elliptical cross-section as determined from Courtauld molecular models.

Selective Sorption Properties of ZSM-5 and ZSM-11

In view of the large number of new zeolites recently synthesized, considerable effort has been expended in their physical characterization, in particular, via their sorption capacities for various organic substrates. The molecular exclusion properties of these zeolites have been used to estimate their pore-opening catacteristics and shape-selective properties (6). In contrast to the molecular sieving

effect, the selective sorption of one component from a sorbable mixture has received much less attention. Limited liquid phase equilibrium sorption data have been reported on binary hydrocarbon systems for A- and Y-type zeolites. The present studies on the novel intermediate-pore zeolites ZSM-5 and ZSM-11 have revealed some significant differences, emphasizing the uniqueness of these zeolites.

Separation of Paraffins from Aromatics

Highly selective sorption of aromatic compounds from paraffin-containing solutions has been reported for the faujasites NaX, NaY, and HY under equilibrium conditions (2). Thus, benzene is preferentially adsorbed relative to n-hexane or n-decane, p-xylene relative to n-octane, and naphthalene relative to n-decane. The measured separation factors in these systems are so large (K>700) that essentially only one species exclusively occupies the internal volume of the zeolites.

In distinct contrast to the faujasites, the intermediate-pore zeolites ZSM-5 and ZSM-11 exhibited a marked preference for n-paraffins relative to aromatics. As can be seen from Table II, both H-ZSM-5 and H-ZSM-11 preferentially sorbed n-nonane from mixtures of nonane and p-xylene dissolved in an inert, non-sorbable solvent, 1,3,5-tri-isopropylbenzene. Selectivity factors greater than 40 were observed, despite the fact that both compounds were readily sorbed when higher zeolite/sorbate ratios were used. Highly selective sorption of n-heptane relative to naphthalene, and n-tetradecane relative to 1-phenyloctane, was also observed with H-ZSM-5.

Counterdiffusion Studies

The very high affinity of these zeolites for n-paraffins was confirmed by counterdiffusion studies, in which p-xylene was initially sorbed into the zeolite prior to n-nonane addition. The n-paraffin rapidly displaced virtually all of the sorbed p-xylene, as shown schematically in Figure 2. Similar results were obtained with both small (∿0.02μ) and large (>1μ) crystal forms of H-ZSM-5, as well as with a very high silica/alumina ratio (1670:1) form of H-ZSM-5.
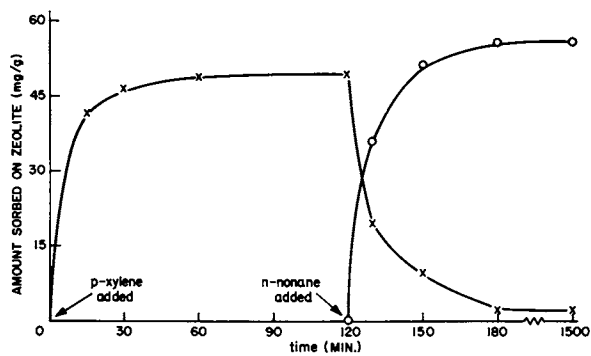
Figure 2.   Counterdiffusion of (x) p-xylene and (○) n-nonane in ZSM-5

Table II
Selective Sorption of Paraffins from Solution

Zeolite	Solv.[a]	Si/ Al$_2$	Time Hrs.	% n-Nonane Sorbed	% p-Xylene Sorbed	Total Sorbed mg/g	Select. Nonane/ Xylene
H-ZSM-5	T	62	4	72	3	56	82
"	"	"	27	74	5	59	57
H-ZSM-5	T	"	20	83	10	73	43
H-ZSM-5	D	"	20	63	4	66	45
H-ZSM-5	H	"	70	47	3	50	30
H-ZSM-11	T	78	6	98	34	66	99
H-ZSM-11	T	"	5	77	3	60	116
"	"	"	24	78	4	61	83
H-Mordenite	T	61	1	46	42	22	1.2
"	"	"	70	64	50	29	1.8

(a) Solvents used were: T = 1,3,5-tri-isopropyl-
    benzene; D = 1,3-di(trifluoromethyl)benzene;
    H = hexamethyldisiloxane.

The high equilibrium selectivity for normal
paraffins relative to aromatics observed for H-ZSM-5
and H-ZSM-11, so contrary to that reported for the
lower silica/alumina ratio zeolites, may in part be
due to the much higher silica/alumina ratio of these
relatively hydrophobic zeolites, resulting in reduced
polarity and ability to interact with polarizable
molecules. However, other zeolites of comparable
silica/alumina ratio, such as dealuminized H-morde-
nite, exhibited no such enhanced preference for n-
paraffins (7) (see Table II). Clearly, silica/alumina
ratio alone is insufficient to account for these
differences. The structure of these zeolites, there-
fore, must play some role in the observed selectivity.
Iso-paraffins too can be separated from aromatics
on H-ZSM-5, a process that cannot be accomplished with
either the small-pore or large-pore zeolites, such as
A and Y. While the selectivity is not nearly as large
as it is for n-paraffins, selective sorption of 2-
methylheptane relative to p-xylene (selectivity
factor = 6.7) was nevertheless observed.

Effect of n-Paraffin Chain Length

Only a few studies have been reported on the
effect of molecular size on the adsorption of normal
paraffins in zeolites. For both small- and large-pore
low silica/alumina zeolites, in liquid phase

equilibrium sorption experiments, the lower molecular
weight normal paraffin (in the C_6-C_{14} range) was
always sorbed preferentially (see Table III) (1,2).
    In contrast, the present work shows that with
H-ZSM-5, the higher molecular weight normal paraffin
was preferentially sorbed from tri-isopropylbenzene
solution at room temperature (see Table III), under
equilibrium liquid phase conditions. The different
behavior of ZSM-5 may be due to the fact that, unlike
A and Y zeolites, it contains no large cavities in
which n-paraffins can coil around themselves. The
coiling of high molecular weight paraffins inside A
and Y zeolites results in additional entropy loss
upon sorption, thereby reversing the normal order of
preferential sorption of the higher molecular weight
component. The relatively narrow and uniform channels
in ZSM-5 prevent the n-paraffins from coiling about
themselves, thereby re-establishing the expected pre-
ferential sorption of the higher molecular weight
component.

Table III
Relative Adsorptivities for Binary
n-Paraffin Systems over Various Zeolites

5A (1)		NaY (2)		H-ZSM-5	
C_6/C_{10}	5.2	C_8/C_{10}	2.0	C_6/C_9	0.29
C_6/C_{12}	4.3	C_8/C_{12}	1.7	C_8/C_{10}	0.23
C_6/C_{14}	10	C_8/C_{14}	2.9	C_8/C_{12}	0.11
C_{10}/C_{12}	3.0			C_8/C_{16}	0.09
C_{10}/C_{14}	7.1			C_{12}/C_{14}	0.77
C_{12}/C_{14}	6.2				

Preferential Sorption of n-Paraffins Relative to Branched Cyclic Hydrocarbons

    Despite the fact that both normal and monomethyl-
substituted paraffins readily enter the pores of ZSM-5
and ZSM-11, preferential sorption of the normal isomer
is observed under thermodynamic equilibrium, non-
kinetically controlled conditions. Whereas small-pore
zeolites, such as 5A and erionite, totally exclude
branched hydrocarbons, and large-pore zeolites exhibit
little preference, the intermediate pore-size zeolites
ZSM-5 and ZSM-11 show a marked preference for sorption
of the linear paraffin, even under equilibrium condi-
tions. Competitive liquid phase sorption studies at
room temperature indicated selectivity factors greater
than ten in favor of n-hexane relative to

3-methylpentane (see Table IV). A dealuminized morde-
nite of similar silica/alumina ratio failed to exhibit
any such selectivity.

Table IV
n-Paraffin Sorption Selectivity

Zeolite	Solvent	n/iso Selectivity[a]
H-ZSM-5	Mesitylene	17
H-ZSM-11	1,3,5-tri-isopropylbenzene	14
H-Mordenite (dealum.)	"	0.7

(a) Relative equilibrium adsorptivity of n-hexane
    to 3-methyl pentane from solution phase at
    room temperature.

The intermediate pore-size ZSM-5 is also effec-
tive in selectively sorbing paraffins from cycloparaf-
fins. Certain cycloparaffins such as decalin and
cyclooctane appear to be totally excluded from the
interior of the zeolite at room temperature. Selec-
tivity factors for n-hexane relative to cyclohexane
and for n-heptane relative to cycloheptane, all of
which are capable of being sorbed individually, were
about 100 in favor of the normal paraffin. Even iso-
paraffins such as 3-methylpentane were selectively
sorbed relative to their cyclic isomers (selectivity
factor = 4).
This behavior of ZSM-5 differs considerably from
that reported for the large-pore zeolites, mordenite
(8) and faujasite (2). With those zeolites, prefer-
ential sorption of the cycloparaffin was generally
observed.

Separation of Aromatic Isomers

The use of various zeolites for the separation of
xylene isomers has received a considerable amount of
attention. Numerous patents have been issued for
such separations; however, equilibrium selectivity
factors tend to be relatively low (9). We found
virtually no p-xylene selectivity for a dealuminized
H-mordenite under equilibrium conditions. H-ZSM-5,
however, did exhibit a distinct preference for
p-xylene sorption even at equilibrium (Table V).
The high isomer selectivity observed for ZSM-5
can be further enhanced by imposing kinetic diffusion-
al effects upon the thermodynamic selectivity, thereby
magnifying the preference for p-xylene sorption (10).

Thus, by increasing the ZSM-5 crystal size from .02μ
to 2μ, very high selectivities were obtained even
after several days stirring in a batch reactor.   A
similar increase was observed upon cesium ion exchange,
which served to accentuate the diffusional rate dif-
ferences between the two xylene isomers.

<div align="center">
Table V
Selective Sorption of Xylene
Isomers from Solution
</div>

Zeolite	Solv.[a]	Time Hr.	% para-xylene Sorbed	% ortho-xylene Sorbed	Total Sorbed Mg/g	Select. para/ortho
H-ZSM-5	D	0.1	86	8	56	71
"	M	1	84	11	42	43
"	M	24	63	25	42	5.1
"	M	96	68	28	45	5.3
Cs-ZSM-5	D	0.1	98	10	51	∿400
"	D	24	89	20	52	31
H-ZSM-5 (large crystal)	M	120	94	8	48	>200
H-Mordenite (dealuminized)	T	0.5	34	31	15	1.16
"	T	70	65	63	29	1.06

(a) Solvents: D = 1,3-di(trifluoromethyl)benzene;
              M = mesitylene;
              T = 1,3,5-tri-isopropylbenzene.

The unique intermediate pore size channel struc-
ture of ZSM-5 is ideally suited for accomplishing
separations unobtainable by other means.   Thus, ZSM-5
effectively separated the pentylbenzene isomers, in
that n-pentylbenzene was preferentially sorbed rela-
tive to 1-methylbutylbenzene with a selectivity factor
of 50, while the slightly larger isomer, 1-ethylpropyl
benzene was totally excluded from the zeolite at room
temperature.   Similarly, 1-methylnaphthalene was
separated from 2-methylnaphthalene by selective sorp-
tion of the 2-methyl isomer.

Separation of Functionally Substituted Hydrocarbons

The separations achievable by use of ZSM-5 are
not limited to simple hydrocarbons, as many function-
ally substituted hydrocarbon isomers can now be
readily separated from each other.   Many of these
separations are unachievable by other means, and

should prove of interest in the specialty chemical and
pharmaceutical industry. A few typical examples are
shown below in Table VI.

Table VI
Separation of Functionally Substituted
Hydrocarbons Over H-ZSM-5

Type of Separation	A	B	% A Sorbed	% B Sorbed	Selectivity, A/B
Paraffinic from aromatics	1-chloro-heptane	chloro-benzene	76	2.5	100
Linear from branched	n-butyl-acetate	iso-butyl-acetate	86	14	39
Para from ortho	p-cresol	o-cresol	73	49	2.8

Selective Sorption from Aqueous Solution

The high hydrophobicity of ZSM-5 permits the
selective sorption of organic compounds dissolved in
water. A high (1670:1) silica/alumina ratio ZSM-5
preferentially sorbed n-butyl alcohol (90.7% sorbed)
from iso-butyl alcohol (17.3% sorbed) and tert-butyl
alcohol (∿0% sorbed), all dissolved in water.

CONCLUSIONS

The unique selective sorption properties described
above for the intermediate pore-size, high silica/alumina
ratio zeolites, ZSM-5 and ZSM-11, suggest great poten-
tial for their use as selective adsorbents achieving
seprations unobtainable by other means. The work
described herein also demonstrates the value of compe-
titive sorption tests in characterizing the physical
and catalytic properties of various zeolites. A
knowledge of relative adsorptivities under both
kinetic- and thermodynamic-controlled conditions is
essential for interpreting and predicting catalytic
reaction phenomena.

ACKNOWLEDGEMENTS

LITERATURE CITED

1. Sundstrom, D. W. and Krant , F. G., J.Chem.Eng. Data, 1968, 13, 223.
2. Satterfield, C. N. and Chen, C. S., AIChE, 1972, 18, 720; Satterfield, C. N. and Smeets, J. K., AIChE, 1974, 20, 618.
3. Kokotailo, G. T., Lawton, S. L., Olson, D. H., Meier, W. M., Nature, 1978, 272, 437; Kokotailo, G. T., Chu, P., Lawton, S. L., Meier, W. M., Nature, 1978, 275, 119.
4. Argauer, R. J. and Landolt, G. R., U.S. Patent 3,702,886,1972; Chu, P., U. S. Patent 3,709,979, 1972.
5. Dwyer, F. G. and Jenkins, E.E., U.S. Patent 3,941,871, 1976.
6. Breck, D. W., "Zeolite Molecular Sieves"; J.Wiley and Sons, New York, 1974, 593-724.
7. A high selectivity for paraffins has been reported for a dealuminized mordenite (SiO_2/Al_2O_3 = 93), under dynamic conditions, however; Eberly, P.E.Jr., Ind. Eng. Chem., Prod. Res. Develop., 1971, 10, 433.
8. Voorhies, A. Jr., Hatcher, W. J. Jr., Ind. Eng. Chem., Prod. Res. Develop., 1969, 8, 361.
9. Seko, M., Miyake, T., Inada, K., Ind. Eng. Chem., Prod. Res. Develop., 1979, 18, 263.
10. Chen, N. Y., Kaeding, W. W., Dwyer, F. G., J. Amer. Chem. Soc., 1979, 101, 6783.

Four Crystal Structures of Ba$_x$Na$_{12-2x}$–A (1 ≤ x ≤ 6) Relating to the Instability of Barium-Exchanged Zeolite A Toward Dehydration

YANG KIM, V. SUBRAMANIAN, ROGER L. FIROR, and KARL SEFF

Chemistry Department, University of Hawaii, Honolulu, HI 96822

Even in the very first announcement (1) of the discovery and properties of zeolite A, it was stated that the zeolite framework decomposed upon ion exchange with Ba^{2+}. Later work (2,3) showed that Ba^{2+}-exchange could be carried to near completion at room temperature, but that the zeolite structure was lost when evacuation at higher temperatures was attempted. Similar instability was not noted with Ca^{2+} and Sr^{2+}, and indeed the crystal structures of fully dehydrated Ca$_6$–A and Sr$_6$–A were determined (4). (The nomenclature refers to the contents of the Pm3m unit cell. For example, Ca$_6$–A represents Ca$_6$Si$_{12}$Al$_{12}$O$_{48}$, exclusive of water molecules if a hydrated crystal is considered.) Instability upon ion-exchange is common for zeolite 4A when aqueous solutions of Cr^{2+}, Fe^{2+}, Ni^{2+}, Cu^{2+}, Pb^{2+}, or Hg^{2+}, for example, are used (at moderate concentrations, ca 0.1 M), probably because cation hydrolysis leads to substantial proton concentrations within the zeolite. However, only with Ba^{2+} is zeolite A entirely stable when hydrated at 25°C, and yet unstable to dehydration at higher temperatures.

An explanation for this unique behavior can be found in barium's ionic size and charge. With a crystal ionic radius (5) of about 1.34 Å, Ba^{2+} is the largest dipositive ion except for Ra^{2+}. Accordingly, it might have been anticipated that the sites selected by Ba^{2+} would be different from, and apparently less stabilizing to the zeolite framework than, those occupied by Sr^{2+} or Ca^{2+} in their dehydrated structures (3). The calculations of Nitta et al. (6,7) fully support these expectations, and show 1) that Ba^{2+} ions are less suited to 6-ring sites than are the smaller Group II ions, and 2) that Ba^{2+} ions prefer to occupy 8-rings at some compositions, possibly at all compositions.

Because fully dehydrated Ba$_6$–A is not crystalline (3,4), it cannot be studied crystallographically, so the structural basis for the instability must be learned less directly. Accordingly, the 4 structures described in Table I were determined. That

Table I. Summary of Experimental Results

Composition	Dehydration Conditions T°(C)	P(Torr)	t(days)	a (Å) at 24°C	No. of Ba²⁺ ions near 6-rings large cavity	sodalite cavity	8-rings	Number of reflections (m) I > 3σ(I)	Number of parameters (s) in least-squares	R_1 [a]	R_2 [b]	Goodness-of-fit [c]
Ba₆-A	hydrated			12.288(1)	2½	1½	2	330	57	0.105	0.091	4.46
Ba₆-A	50	10⁻⁵	2	12.189(2)	2	1	3	160	37	0.123	0.084	4.49
Ba₃.₅Na₅-A	100	2x10⁻⁵	2	12.267(2)	2½	0	1	104	30	0.065	0.042	2.02
Ba₁Na₁₀-A	400	10⁻⁶	1	12.262(3)	½	0	½	246	31	0.061	0.042	2.03

[a] $R_1 = \Sigma(F_o - |F_c|)/\Sigma F_o$

[b] $R_2 = [\Sigma w(F_o - |F_c|)^2/\Sigma wF_o^2]^{\frac{1}{2}}$

[c] Goodness-of-fit $= [\Sigma w(F_o - |F_c|)^2/(m-s)]^{\frac{1}{2}}$

these crystals did not decompose indicates something about the thermal stability of Ba_xNa_{12-2x}–A at the several compositions, as does the work of Dyer et al. (3).

Experimental Section

Crystals of zeolite 4A were prepared by Charnell's method (8).

A single crystal, a cube 0.09 mm on an edge, was lodged in a fine glass capillary. Ion exchange to give Ba_6–A was performed using flow methods: 0.1 M $Ba(OH)_2$ solution was allowed to flow past the crystal at a velocity of approximately 1.0 cm/s for 4 days at 25°C.

This same crystal, after it was used to determine the structure of hydrated Ba_6–A, was evacuated at 10^{-5} Torr for 2 days at 50°C. While still in vacuum, it was sealed in its capillary with a torch.

Another crystal, 0.08 mm on an edge, was exchanged as before but for a shorter time to yield $Ba_{3.5}Na_5$–A. It was dehydrated at 100°C and 2×10^{-6} Torr for 2 days after which, while still in vacuum, it was sealed in its capillary.

The Ba_1Na_{10}–A crystal was prepared by ion-exchange under static conditions. To 10 mg of zeolite 4A powder containing some large crystals, 2.4 mg of $Ba(NO_3)_2$ (J. T. Baker Chemical Co.) and enough water to submerge all solid particles, was added so that at equilibrium a zeolite of composition Ba_2Na_8–A might result (2). (It may be (vide infra) that the largest crystals exchanged less completely than the smaller ones, or that some Ba^{2+} was precipitated.) After 2 days, the supernatant solution was decanted and a fresh aliquot of water added; this was repeated twice. Finally the crystals were rinsed with water and dried in air. An 80 μm single crystal was selected and evacuated at 10^{-6} Torr and 400°C for 1 day, after which it was sealed off under vacuum.

Microscopic examination showed that the exchange and dehydration procedures had little effect on the appearances of the crystals, all of which remained clear and colorless.

The cubic space group Pm3m (no systematic absences) was chosen for X-ray diffraction studies for reasons previously cited (9). Preliminary crystallographic experiments and subsequent data collection were performed at 24°C with an automated, four-circle Syntex P1 diffractometer, equipped with a graphite monochromator and a pulse-height analyzer. Molybdenum radiation was used for all experiments ($K\alpha_1$, $\lambda = 0.70930$ Å; $K\alpha_2$, $\lambda = 0.71359$ Å). In each case, the cell constant was determined by a least-squares treatment of 15 intense reflections for which $18° < 2\theta < 24°$ (see Table I).

For each crystal, reflections from two intensity-equivalent regions of reciprocal space ($hk\ell$, $h \leq k \leq \ell$, and khl, $k \leq h \leq \ell$) were examined using the θ-2θ scan technique. (For Ba_1Na_{10}–A, the two regions examined were $hk\ell$ and $h\ell k$.) Each reflection was

scanned at a constant rate of 1.0 deg min^{-1} from 1° (in 2θ) below
the calculated $\underline{K}\alpha_1$ peak to 1° above the $\underline{K}\alpha_2$ maximum. Background
intensity was counted at each end of a scan range for a time equal
to half the scan time. The intensities of 3 reflections in
diverse regions of reciprocal space were recorded after every 100
reflections to monitor crystal and instrument stability. Only
small random fluctuations of these check reflections were noted
during the course of data collection. All unique reciprocal
lattice points for which 2θ < 70° were examined for hydrated
Ba$_6$-A, partially dehydrated Ba$_6$-A, and dehydrated Ba$_1$Na$_{10}$-A. For
dehydrated Ba$_{3.5}$Na$_5$-A, 2θ < 45° was used because of the paucity
of data at higher angles.

The raw data for each region were corrected for Lorentz and
polarization effects including that due to incident beam mono-
chromatization; the reduced intensities were merged; and the
resultant estimated standard deviations were assigned to each
averaged reflection by the computer program COMPARE (10). Other
details regarding data reduction have been discussed previously
(11). An absorption correction was expected to be unimportant
and was not applied (12,13,14). Only those reflections in each
merged data set for which the net count exceeded 3 times its
corresponding esd were used in structure solution and refinement.

Structure Determination

Hydrated Ba$_6$-A. Full-matrix least-squares refinement was
initiated using atomic coordinates from the structure of
dehydrated Ca$_6$-A (4). The model consisted of all framework
positions ((Si,Al), O(1), O(2), and O(3)), 4 6-ring Ba^{2+} ions (3
in the large cavity and 1 in the sodalite unit), and 1 Ba^{2+} ion
at an 8-ring site. Convergence occurred with $\underline{R}_1$ = 0.20 and $\underline{R}_2$ =
0.23. A difference function at this stage revealed 3 peaks at
(0.2, 0.32, 0.5), (0.156, 0.42, 0.42), and (0.135, 0.135, 0.155).
The first 2 were identified as oxygens at O(5) and Ba^{2+} ions at
Ba(3), respectively, and the last peak was unstable in least-
squares refinement. A subsequent isotropic refinement of these
atoms with framework atoms varying anisotropically converged with
$\underline{R}_1$ = 0.169 and $\underline{R}_2$ = 0.153.

A difference Fourier synthesis revealed 4 peaks (0.7 to
1.7 eÅ^{-3} in height, esd = 0.134 eÅ^{-3}) at (0.125, 0.125, 0.15),
(0.257, 0.257, 0.468), (0.31, 0.31, 0.31) and (0.085, 0.085,
0.085). Only the last peak, O(4), was stable in least-squares
refinement, reducing $\underline{R}_1$ to 0.138 and $\underline{R}_2$ to 0.131. The aniso-
tropic refinement of all positions except O(5), which was refined
isotropically, converged quickly at $\underline{R}_1$ = 0.119 and $\underline{R}_2$ = 0.104.
Moving O(4) off its threefold axis and O(5) off its mirror plane,
to correspond better with the local symmetry, reduced $\underline{R}_1$ by
0.014 and $\underline{R}_2$ by 0.009 to their final values (see Tables I and
IIa).

Instability & Crystal Structure

Table II. Positional, Thermal,[a] and Occupancy Parameters

a. Hydrated Ba_6-A

	Wyckoff Position	x	y	z	β_{11}[b] or B	β_{22}	β_{33}	β_{12}	β_{13}	β_{23}	Fixed Occupancy
(Si,Al)	24(k)	0	1841(3)	3731(3)	25(3)	19(2)	11(3)	0	0	0(4)	24[c]
O(1)	12(h)	0	2272(11)	5000	97(18)	38(13)	17(11)	0	0	0	12
O(2)	12(i)	0	2913(8)	2913(8)	48(13)	18(7)	18(7)	0	0	22(17)	12
O(3)	24(m)	1125(6)	1125(6)	3476(9)	58(7)	58(7)	97(12)	72(17)	70(13)	70(13)	24
Ba(1)	8(g)	2487(4)	2487(4)	2487(4)	67(3)	67(3)	67(3)	83(8)	83(8)	83(8)	2.5
Ba(2)	8(g)	1333(22)	1333(22)	1333(22)	320(32)	320(32)	320(32)	189(85)	189(85)	189(85)	1.5
Ba(3)	24(m)	1407(29)	4284(11)	4284(11)	362(59)	74(13)	74(13)	-150(38)	-150(38)	-86(34)	1.5
Ba(4)	12(i)	0	4668(25)	4668(25)	189(66)	76(38)	76(38)	0	0	-123(179)	0.5
O(4)	24(m)	435(72)	1007(76)	1007(76)	167(231)	170(75)	170(75)	-715(218)	-715(218)	203(159)	4.5
O(5)	48(n)	2359(35)	3002(36)	4669(39)	5(2)						7.5

In Adsorption and Ion Exchange with Synthetic Zeolites; Flank, W.;
ACS Symposium Series; American Chemical Society: Washington, DC, 1980.

b. Partially Dehydrated Ba$_6$-A

	Wyckoff Position	x	y	z	β_{11}ᵇ or B	β_{22}	β_{33}	β_{12}	β_{13}	β_{23}	Fixed Occupancy
(Si,Al)	24(k)	0	1834(7)	3734(6)	48(8)	50(7)	21(6)	0	0	24(12)	24ᶜ
O(1)	12(h)	0	2307(25)	5000	82(29)	103(31)	31(23)	0	0	0	12
O(2)	12(i)	0	2930(12)	2930(12)	75(26)	49(15)	49(15)	0	0	55(41)	12
O(3)	24(m)	1099(10)	1099(10)	3441(15)	75(10)	75(10)	107(20)	87(32)	4(25)	4(25)	24
Ba(1)	8(g)	2570(12)	2570(12)	2570(12)	125(10)	125(10)	125(10)	144(25)	144(25)	144(25)	2
Ba(2)	8(g)	1319(70)	1319(70)	1319(70)	451(76)	451(76)	451(76)	422(182)	422(182)	422(182)	1
Ba(3)	24(m)	599(44)	4499(14)	4499(14)	1117(105)	228(23)	228(23)	-770(124)	-770(124)	51(53)	3
O(5)	48(n)	2527(169)	3743(111)	4756(436)	18(11)						6

c. Dehydrated Ba$_{3.5}$Na$_5$-A

	Wyckoff Position	x	y	z	β_{11}ᵇ or B	β_{22}	β_{33}	β_{12}	β_{13}	β_{23}	Fixed Occupancy
(Si,Al)	24(k)	0	1828(5)	3724(4)	67(7)	35(6)	26(6)	0	0	-1(10)	24
O(1)	12(h)	0	2280(16)	5000	96(24)	50(22)	61(22)	0	0	0	12
O(2)	12(i)	0	2909(9)	2909(9)	80(24)	45(13)	45(13)	0	0	30(34)	12
O(3)	24(m)	1119(7)	1119(7)	3444(10)	50(7)	50(7)	98(17)	40(27)	17(19)	17(19)	24
Ba(1)	8(g)	2345(8)	2345(8)	2345(8)	120(6)	120(6)	120(6)	185(19)	185(19)	185(19)	2.5
Ba(4)	12(i)	0	4597(33)	4597(33)	421(93)	213(68)	213(68)	0	0	54(118)	1
Na	8(g)	1837(67)	1837(67)	1837(67)	50(8)						5

d. Dehydrated Ba$_1$Na$_{10}$-A

	Wyckoff Position	$\underline{x}$	$\underline{y}$	$\underline{z}$	β_{11} or $\underline{B}_{iso}$	β_{22}	β_{33}	β_{12}	β_{13}	β_{23}	Occupancy fixed	Occupancy varied
(Si,Al)	24($\underline{k}$)	0	1839(2)	3729(2)	30(2)	27(2)	20(2)	0	0	9(3)	24	--
O(1)	12($\underline{h}$)	0	2289(7)	5000	53(8)	64(8)	32(6)	0	0	0	12	--
O(2)	12($\underline{i}$)	0	2902(4)	2902(4)	83(9)	37(5)	37(5)	0	0	44(12)	12	--
O(3)	24($\underline{m}$)	1127(3)	1127(3)	1127(3)	51(3)	51(3)	45(5)	20(9)	13(6)	13(6)	24	--
Ba(1)	8($\underline{g}$)	2545(20)	2545(20)	2545(20)	49(7)	49(7)	49(7)	52(17)	52(17)	52(17)	½	0.47(2)
Na(1)	8($\underline{g}$)	2009(4)	2009(4)	2009(4)	58(4)	58(4)	58(4)	58(8)	58(8)	58(8)	7½	--
Ba(4)	12($\underline{i}$)	0	4720(116)	4720(116)	30(6)						½	--
Na(2)	12($\underline{i}$)	0	4339(31)	4339(31)	8(1)						2½	--

[a] Positional and anisotropic parameters are given x 10^4. Numbers in parentheses are the estimated standard deviations in the units of the least significant figure given for the corresponding parameter. The anisotropic temperature factor is $\exp[-(\beta_{11}\underline{h}^2 + \beta_{22}\underline{k}^2 + \beta_{33}\underline{\ell}^2 + \beta_{12}\underline{hk} + \beta_{13}\underline{h\ell} + \beta_{23}\underline{k\ell})]$.

[b] R.m.s. displacements can be calculated from β_{11} values using the formula, $\mu_1 = 0.225 \ \underline{a} \ (\beta_{11})^{\frac{1}{2}}$, where $\underline{a}$ is the cell constant (Table I).

[c] Occupancy for (Si) = 12; occupancy for (Al) = 12. Occupancies are given as the number of atoms or ions per unit cell.

The final difference function showed no significant peaks: a broad peak at $(\frac{1}{2},\frac{1}{2},\frac{1}{2})$ was 2.7 $e\text{Å}^{-3}$ in height but with an esd of 0.12 $e\text{Å}^{-3}$ at a general position, the esd is $(0.12 \times 48) = 5.8$ $e\text{Å}^{-3}$ at this special position (15). All shifts in the final cycle of least-squares refinement were less than 0.1% of their corresponding esd's.

The final structural parameters are presented in Table IIa. Interatomic distances and angles are given in Table III.

Partially Dehydrated Ba$_6$-A. Full-matrix least-squares refinement was initiated using the atomic parameters of the framework atoms and of the barium ions (Ba(1), Ba(2), Ba(3), and Ba(4)) in fully hydrated Ba^{2+}-exchanged zeolite A. Full anisotropic refinement converged to the error indices $R_1 = 0.113$ and $R_2 = 0.088$. Simultaneously, the occupancy numbers at Ba(1), Ba(2), Ba(3), and Ba(4) refined to 1.9(1), 1.2(1), 2.0(5) and 0.8(5), respectively. Because the Ba(3) and Ba(4) positions had nearly become coincident, they were represented as 3 Ba^{2+} ions at an intermediate position, designated Ba(3). The occupancies at Ba(1) and Ba(2) were fixed at 2 and 1 in further refinement. A subsequent difference Fourier synthesis served to locate the water molecules at O(5). Numerous attempts to locate additional water molecules failed.

The final refinement used anisotropic thermal parameters for all positions except O(5), for which only isotropic values were used. The largest peak ($\underline{x} = 0.21$, $\underline{y} = \underline{z} = \frac{1}{2}$, height 1.6 $e\text{Å}^{-3}$) on the final difference Fourier function (esd = 0.13 $e\text{Å}^{-3}$ at a general position) was unstable in least-squares refinement. The structure of partially dehydrated Ba$_6$-A is shown in Figure 1.

Dehydrated Ba$_{3.5}$Na$_5$-A. Full-matrix least-squares refinement began using coordinates for the zeolite framework atoms and for the Ba^{2+} position at Ba(1) found in hydrated Ba$_6$-A. Anisotropic refinement converged to $R_1 = 0.238$ and $R_2 = 0.215$ as the number of Ba^{2+} ions at Ba(1) refined to 2.5(3). A subsequent difference Fourier function revealed 3 peaks at (0.0, 0.469, 0.469), (0.109, 0.109, 0.109), and (0.203, 0.203, 0.203), the second of which was unstable in later least-squares refinement. Simultaneous occupancy and positional refinement showed that the first peak refined as 1.1(1) Ba^{2+} ions, and the third as 5.4 (1.8) Na^+ ions, to $R_1 = 0.066$ and $R_2 = 0.042$.

It is easy to distinguish Ba^{2+} ions from Na^+ for several reasons. Firstly, their atomic scattering factors are quite different, 54 e^- for Ba^{2+} vs 10 e^- for Na^+. Secondly, their ionic radii are quite different, $Ba^{2+} = 1.34$ Å and $Na^+ = 0.97$ Å (5). Also, the approach distances between these ions and zeolite oxide ions in dehydrated Na$_{12}$-A (16) and hydrated Ba$_6$-A are known (see Table III). Finally, the requirement that 12 cationic charges be placed per unit cell does not allow the major positions to refine to acceptable occupancies with an alternative assignment of ionic identities.

Table III. Selected Interatomic Distances (Å) and Angles (Deg)[a]

	Hydrated Ba$_6$-A	Partially Dehydrated Ba$_6$-A	Ba$_{3.5}$Na$_5$-A	Ba$_1$Na$_{10}$-A
(Si,Al)-O(1)	1.645(6)	1.65(1)	1.66(1)	1.653(4)
(Si,Al)-O(2)	1.659(11)	1.66(2)	1.66(1)	1.651(3)
(Si,Al)-O(3)	1.668(8)	1.65(1)	1.66(1)	1.675(2)
Ba(1)-O(3)	2.66(1)	2.74(2)	2.51(1)	2.69(2)
Ba(2)-O(3)	2.66(3)	2.61(8)		
Ba(2)-O(4)	2.25(10)	--		
Ba(3)-O(1)	3.14(3)	2.84(4)		
Ba(3)-O(2)	2.94(3)	2.80(3)		
Ba(3)-O(5)	--	2.54(3)		
Ba(1)-O(5)	2.76(5)	3.0(5)		
Ba(4)-O(1)	2.98(3)	--	2.88(4)	3.0(1)
Ba(4)-O(2)	3.07(3)	--	2.92(8)	3.1(2)
Na(1)-O(3)		--	2.33(8)	2.33(8)
Na(2)-O(2)				2.49(5)
O(4)-O(4)	2.7(1)	--		
O(4)-O(4)	2.5(1)	--		
O(5)-O(5)	3.58(1)	--		
O(1)-(Si,Al)-O(2)	108.6(6)	105.8(12)	107.4(8)	108.4(4)
O(1)-(Si,Al)-O(3)	110.4(5)	113.1(9)	111.7(7)	112.3(3)
O(2)-(Si,Al)-O(3)	107.8(5)	107.7(9)	107.1(6)	106.2(3)
O(3)-(Si,Al)-O(3)	111.8(8)	108.8(13)	111.5(9)	111.2(4)
(Si,Al)-O(1)-(Si,Al)	142.4(10)	139.0(20)	140.9(13)	141.0(6)
(Si,Al)-O(2)-(Si,Al)	165.0(7)	162.5(11)	164.0(8)	165.8(5)
(Si,Al)-O(3)-(Si,Al)	147.0(8)	146.1(13)	145.3(8)	144.5(4)
O(3)-Ba(1)-O(3)	100.2(5)	94.6(8)	106.4(6)	96(1)
O(3)-Ba(2)-O(3)	100.5(10)	100.8(29)		
O(4)-Ba(2)-O(4)	68(5)	--		
O(1)-Ba(3)-O(2)	52.2(4)	55.7(10)		
O(1)-Ba(4)-O(2)	52.6(4)		54.8(7)	52(3)
O(3)-Na-O(3)			120(14)	118.9(4)

[a] The numbers in parentheses are the estimated standard deviations in the units of the least significant digit given for the corresponding parameter.
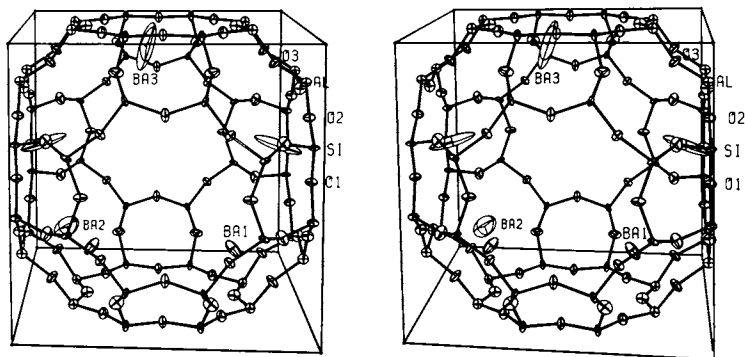
Figure 1. A stereoview of partially dehydrated Ba₆-A. Ellipsoids of 20% probability are shown. Water molecules are not shown in this figure.
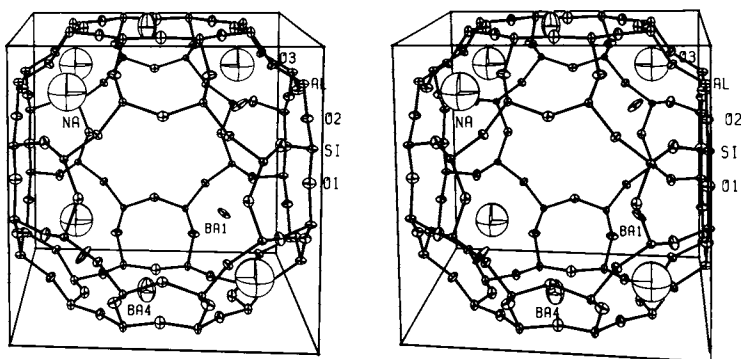
Figure 2. A stereoview of dehydrated Ba₃.₅Na₅-A. Ellipsoids of 20% probability are shown.

The isotropic thermal ellipsoid at Na was very large, indicating the presence of 2 or more nonequivalent Na^+ ions at this position. Attempts to separate it into 2 nonequivalent Na^+ ion positions failed. The final model (see Table IIc) is the result of anisotropic refinement of all positions, except Na which was refined isotropically, with occupancies fixed. The final difference Fourier function, whose estimated standard deviation is 0.06 $e\text{Å}^{-3}$, was featureless. See Tables IIc and III, and Figure 2, for additional information.

$Ba_1Na_{10}-A$. Least-squares refinement was initiated using the coordinates of dehydrated 4A for framework atoms and 6- and 8-ring Na^+ ions. Initially, a single data set of 130 unique reflections for which $3° < 2\theta < 55°$ was used in refinement. After 3 cycles, the thermal parameters at Na(1) and Na(2) became elongated, suggesting the presence of non-equivalent ions at each site; $\underline{R}_1$ and $\underline{R}_2$ were 0.079 and 0.069, respectively. A subsequent difference Fourier function showed a large peak at $\underline{x} = \underline{y} = \underline{z} = 0.26$ (peak height = 1.6 $e\text{Å}^{-3}$, esd = 0.07). Occupancy refinement at this site using a larger merged data set converged at 0.47(2) Ba^{2+} ions; at the same time the occupancy at Na(1) refined to 7.9(2) ions. In subsequent refinement, the occupancies at Na(1) and Ba(1) were fixed at 7.5 and 0.5 respectively (see Table IId). Treating the 8-ring density as Ba^{2+} ions, the occupancy converged at 0.85(3). With this value set at 1.0, a difference function was generated which was essentially flat. This model, with 2 of the 3 8-rings empty, has only 10.5 Na^+ and Ba^{2+} charges instead of 12.0 as required for charge neutrality. It was therefore inferred that the 8-ring Ba^{2+} position was an average over a Na^+ and a nearby Ba^{2+} position. Careful refinements of Na(2) and Ba(4) ensued; although simultaneous refinement of all positional, occupancy, and thermal parameters could not be done, refinements were successful when one parameter on each atom was fixed. (Initially positions for Na(2) and Ba(4) were obtained from the structures of dehydrated 4A and $Ba_{3.5}Na_5-A$.) In successive cycles, parameters were varied in pairs, and in the final cycles of refinement, positional and thermal parameters were varied at the fixed occupancies given in Table IId. The largest correlation coefficient in least-squares (0.73) was between the $\underline{y}$ parameter of Ba(4) and its thermal parameter; the correlation coefficient between the $\underline{y}$ (=$\underline{z}$) parameter of Na(2) and that of Ba(4) was not large (-0.36).

The full-matrix least-squares program used in all structure determinations minimized $\Sigma\underline{w}(\Delta|\underline{F}|)^2$; the weight ($\underline{w}$) of an observation was the reciprocal square of $\sigma(F)$, its standard deviation. Atomic scattering factors (17,18) for Ba^{2+}, Na^+, O^-, O^0, and $(Si,Al)^{1.75+}$ were used. The function describing $(Si,Al)^{1.75+}$ is the mean of the Si^0, Si^{4+}, Al^0, and Al^{3+} functions. All scattering factors were modified to account for the real component (f')

of the anomalous dispersion correction ($\underline{19},\underline{20}$).

A listing of observed and calculated structure factors is available for all 4 crystals by interlibrary loan from Hamilton Library at this university; see your librarian.

Description of the Structures

Hydrated Ba_6-A. In the structure of hydrated Ba_6-A, 4 Ba^{2+} ions are distributed over 2 nonequivalent 6-ring sites: 2.5 of these are recessed 1.23 Å into the large cavity from the (111) plane of the oxygen 6-rings and 1.5 ions are 1.22 Å into the sodalite unit (see Table IV). The 2 remaining Ba^{2+} ions are found at 2 nonequivalent 8-ring sites: 0.5 are in the planes of 8-rings and 1.5 are off such planes. See Table IIa and Figures 3 and 4.

The ions at Ba(1) and Ba(2) have distorted octahedral coordination: 3 of the ligands in each case are framework oxide ions at O(3), and the 3 others are water molecules at O(5) and O(4), respectively. Each Ba^{2+} ion is 2.66 Å from 3 O(3) framework oxide ions, but the Ba(1)-O(5) and Ba(2)-O(4) distances, 2.76(5) Å and 2.3(1) Å respectively, are quite different. However, these distances are comparable to Ba-O distances observed in Ba^{2+}-containing minerals ($\underline{21}$).

The remaining Ba^{2+} ions at Ba(3) and Ba(4) are associated with 8-ring oxide ions. The 1.5 Ba^{2+} ions at Ba(3) are located off 8-ring planes where each Ba^{2+} approaches 3 oxide ions, 1 at O(2) at 2.98 Å and 2 at O(1), 3.14 Å away. The 0.5 Ba^{2+} ions at Ba(4) are located in 8-ring planes, but off their centers. They also approach 3 oxide ions, 1 at O(2) at 3.07 Å and 2 at O(1), 2.98 Å away. The half-integral occupancy numbers of the Ba^{2+} ions in all of their positions indicate the presence of a superstructure.

Figures 3 and 4 show plausible sodalite unit and large cavity structures which are consistent with the structural parameters determined for hydrated Ba_6-A.

Partially Dehydrated Ba_6-A. After the very same crystal used to determine the structure of hydrated Ba_6-A was evacuated at 50°C and 10^{-5} Torr for 2 days, the Ba^{2+} ions are found redistributed in the unit cell: 3 Ba^{2+} ions are associated with 6-rings, 2 in the large cavity and 1 in the sodalite unit, and 3 (the maximum number) are associated with 8-rings, but do not lie in the 8-ring planes. The number of Ba^{2+} ions associated with 6-rings (at Ba(1) and Ba(2)) has decreased by 1, and the number associated with 8-rings (at Ba(3) and Ba(4)) has increased correspondingly. This indicates that Ba^{2+} ions, once some of their water molecules are removed and they must look more to the zeolite framework for ligand atoms, locate in the larger 8-rings to the maximum extent possible, perhaps because they do not fit as well into 6-rings because of the relatively large ionic radius of Ba^{2+}, 1.34 Å ($\underline{5}$). The same preference for 8-rings by

Table IV. Deviation of Atoms (Å) from the (111) Plane at O(3)

	Hydrated Ba$_6$-A	Partially Dehydrated Ba$_6$-A	Ba$_{3.5}$Na$_5$-A	Ba$_1$Na$_{10}$-A
O(2)	0.07	0.14	0.09	0.08
Ba(1)	1.23	1.45	0.95	1.38
Ba(2)	-1.22	-1.19	--	--
Ba(3)	3.01	2.77	--	--
Na or Na(1)	--	--	-0.12	0.24
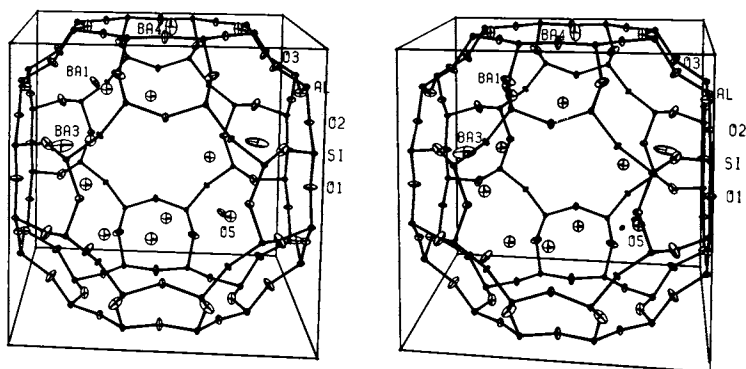
Figure 3. A stereoview of the large cavity of hydrated Ba$_6$-A. Ellipsoids of 20% probability are shown. Ba^{2+} ions are arranged within their equipoints of partial occupancy in a chemically plausible manner.
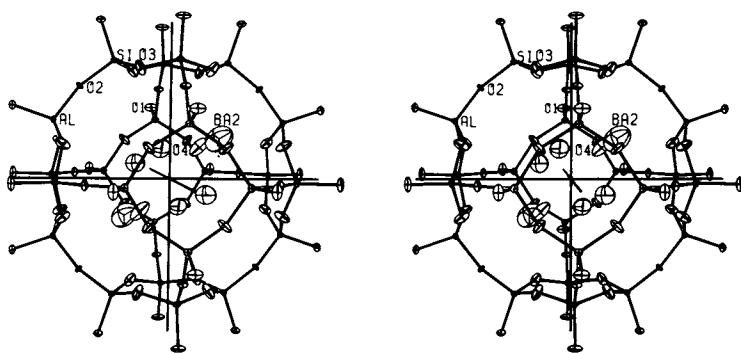
Figure 4. A stereoview of the sodalite unit of hydrated Ba$_6$-A. Ba^{2+} ions are coordinated to 3 framework oxide ions, O(3), and probably to some unlocated water molecules. Ellipsoids of 20% probability are used.

the larger alkali metal ions K^+ (radius = 1.33 Å) (22), Rb^+
(1.47 Å) (13), and Cs^+ (1.69 Å) (23) as compared to Na^+ (0.97 Å)
has been noted.

The 2 ions at Ba(1) extend 1.45 Å into the large cavity from
the O(3) planes of the oxygen 6-rings, and the ion at Ba(2) is in
the sodalite unit, 1.19 Å from such (111) planes. Each ion at
Ba(1) is coordinated by a distorted octahedron of oxygen atoms:
it is 2.74(2) Å from 3 O(3) framework oxide ions and 3.0(5) Å
from 3 water molecules at O(5). (Some of the water molecules at
O(5), an averaged position, are associated with Ba(3) ions,
hence the low precision of geometry involving O(5).) The ion at
Ba(2) is coordinated to 3 O(3) framework oxide ions at 2.61(8) Å.
This Ba^{2+} ion has a large anisotropic thermal parameter and the
O(3)-Ba(2)-O(3) angle is 101(3)° (cf. the O(3)-Ba(1)-O(3) angle
is 95(1)°). This suggests that the ion at Ba(2) is also asso-
ciated with some water molecules, but these could not be located.

The remaining 3 Ba^{2+} ions are at Ba(3), which is near but
off the 8-ring planes. Each ion approaches 3 framework oxide
ions at approximately equal distances--2.84 Å to 2 O(1) and
2.80 Å to 1 O(2). These have very high thermal motion normal
to the 8-ring plane as did one Ca^{2+} ion in dehydrated Ca_6-A and
one Sr^{2+} ion in dehydrated Sr_6-A (4). With such thermal motion,
these 3 Ba^{2+} ions are certainly not firmly held by the zeolite;
this may be a source of instability.

Dehydrated $Ba_{3.5}Na_5$-A. In the structure of $Ba_{3.5}Na_5$-A, the
5 Na^+ ions are distributed amongst the 8 equivalent positions of
its equipoint, each position being on a threefold axis and near a
6-ring plane. Each Na^+ ion approaches 3 O(3) oxide ions of the
zeolite framework with usual Na-O contact distances of 2.33(8) Å
(16). The large isotropic thermal ellipsoids of the Na^+ ions
suggest that this position is an average of 2 or more nonequi-
valent positions.

The 2.5 Ba^{2+} ions at Ba(2) are located in the large cavity,
0.95 Å from the (111) plane at O(3). The Ba-O contact distance,
2.51(1) Å, is 0.15 Å less than the corresponding distance in
hydrated Ba_6-A. This difference is likely to be meaningful even
though refinements in Pm3m yield only the conformations of
averaged 6-rings, so that the environment of an ion associated
with a particular 6-ring is inaccurately described by the
present data.

The ion at Ba(4) is associated with 8-ring oxygens. This
position is located on the plane of an 8-ring but is off its
center to enable more favorable approaches to framework oxide
ions (Ba(4)-O(1) = 2.88 Å, and Ba(4)-O(2) = 2.92 Å). These Ba-O
contact distances are again shorter than those in hydrated Ba_6-A
(see Table III). The final R_2 value, 0.042, and the unusually
featureless final difference Fourier function suggest that little
or no water is present in this crystal.

Dehydrated Ba_1Na_{10}-A. The 11 ions in the structure of $Ba_1\overline{Na_{10}$-A fill all of the} 6-ring sites (8 per unit cell) and all of the 8-ring sites (3 per unit cell). The 10 Na^+ ions are located at 2 crystallographically distinct sites: $7\frac{1}{2}$ of them at Na(1) are at 6-ring sites 0.24 Å from the (111) plane at O(3); the remaining $2\frac{1}{2}$ at Na(2) are at 8-ring sites. The Na(1)-O(3) distance, 2.321(6) Å, and the Na(2)-O(3) distance, 2.49(5) Å, correspond nicely to distances observed in dehydrated zeolite 4A (16).

The Ba^{2+} ion is distributed over 2 sites: the $\frac{1}{2}$ at Ba(1) is near a 6-ring, and the other $\frac{1}{2}$ at Ba(4) is in the plane of an 8-ring. This distribution indicates the presence of a super-structure in which the Ba^{2+} and Na^+ ions are ordered.

Discussion

Crystal stability is related to the amount of barium and water in the zeolite. Single crystal data by their number tend to indicate a decrease in the crystal quality of zeolite A at higher Ba^{2+} and lower H_2O contents. Although hydrated Ba_6-A had a large diffraction pattern (330 reflections at the 3σ level), the same crystal upon partial dehydration at 50°C had many fewer reflections, only 160. No single crystal pattern at all remains after evacuation at 100°C. The two partially Ba^{2+}-exchanged structures, $Ba_{3.5}Na_5$-A and Ba_1Na_{10}-A, appear to be completely dehydrated; the $\underline{R}$ values and goodness-of-fits are supportive of this (see Table I). The diffraction pattern of $Ba_{3.5}Na_5$-A is very weak (105 reflections) compared with Ba_1Na_{10}-A (242), indicating decreasing crystal quality and stability with increasing Ba^{2+} content in the dehydrated zeolite.

The structural basis for the instability may be found in the inability of Ba^{2+} to adjust to low coordination numbers. Barium ions in naturally occurring minerals and oxides have coordination numbers ranging from 6 to 10 (21). Some Ba^{2+} ions in hydrated Ba_6-A have a coordination number of 6, which, upon dehydration, would be reduced to 3, the partially Ba^{2+}-exchanged structures indicate, if dehydrated Ba_6-A were to form.

The structural basis for the instability may be found in the greater tendency of Ba^{2+}, compared to Ca^{2+} or Sr^{2+} (4), to occupy 8-ring sites. Even evacuation of hydrated Ba_6-A at 50°C results in a Ba^{2+} ion in every 8-ring. Simultaneously, of course, fewer Ba^{2+} ions are available to occupy 6-ring sites, which are too small to accommodate such large cations anyway.

According to the theoretical calculations of Nitta et al., the Ba^{2+} ion in dehydrated Ba_1Na_{10}-A should be at an 8-ring site (7), in contrast to the distribution over 2 sites found here. Their calculation on dehydrated Ba_6-A (6) indicates that 3 barium ions (the maximum number) should be associated with 8-rings and 3 with 6-rings, and that the 8-ring sites are lower in energy. This distribution is indeed observed in partially dehydrated

Ba_6-A, with the minor difference that the 8-ring ions are found off the plane at sites of (m) symmetry (see Fig. 1) instead of on the plane with site symmetry mm as the calculations assume. Although it is possible that water molecules at O(5) are responsible for the lower symmetry observed, a Sr^{2+} ion in dehydrated Sr_6-A was also located off the plane at a site of symmetry m. (A calcium ion in dehydrated Ca_6-A was found in the plane.)

Acknowledgements

Abstract

    The crystal structures of hydrated (a = 12.288(1) Å) and partially dehydrated (a = 12.189(2) Å) fully Ba^{2+}-exchanged zeolite A, and two crystal structures of partially Ba^{2+}-exchanged, fully dehydrated zeolite A, stoichiometries $Ba_{3.5}Na_5$-A (a = 12.267(7) Å) and Ba_1Na_{10}-A (a = 12.262(3) Å) per unit cell, have been determined from 3-dimensional X-ray diffraction data gathered by counter methods. All structures were solved and refined in the cubic space group Pm3m at 24°C. In the fully hydrated structure, 4 of the 6 Ba^{2+} ions per unit cell are located on threefold axes near 6-rings: 2.5 of these are recessed 1.23 Å into the large cavity, and 1.5 ions are 1.22 Å into the sodalite unit. The remaining 2 Ba^{2+} ions are found at 2 non-equivalent 8-ring sites, ½ on and 1½ off the plane. The final weighted R value, R_2, based on 330 observed reflections for which $I_o > 3\sigma(I_o)$ is 0.091. This crystal was then evacuated at 10^{-5} Torr for 2 days at 50°C, and the resulting structure was refined to R_2 = 0.084 using 160 reflections. Three Ba^{2+} ions are associated with 6-rings, 2 in the large cavity and 1 in the sodalite unit, and 3 (the maximum number) are associated with 8-rings but do not lie in the 8-ring planes. The structure of $Ba_{3.5}Na_5$-A (104 reflections, R_2 = 0.042) evacuated at $2x10^{-6}$ Torr for 2 days at 100°C showed 2.5 Ba^{2+} ions in the large cavity at 6-ring sites and 1 in an 8-ring plane. The 5 Na^+ ions occupy 6-ring sites. The structure of Ba_1Na_{10}-A evacuated at 400°C (242 reflections, R_2 = 0.043) has ½ Ba^{2+} ion at a threefold-axis site in the large cavity and the remaining ½ Ba^{2+} in the plane of an oxygen 8-ring. Of the 10 Na^+ ions, 7.5 are at 6-ring sites and 2.5 are in 8-rings. The relatively large Ba^{2+} ions cannot approach oxide ions as closely as smaller cations can. As a result, they do not fit into conventional sites near 6-ring centers, and 8-ring sites are occupied more than they are in those corresponding structures involving smaller cations (such as Ca^{2+}) which have been determined. Low coordinate Ba^{2+} (such as 3-coordinate Ba^{2+} which appears to form upon dehydration) may

seek to increase its coordination number by disrupting the
zeolite framework. These considerations should provide the
structural basis for the instability of Ba_6-A toward dehydration.

Literature Cited

1. Breck, D. W.; Eversole, W. G.; Milton, R. M.; Thomas, T. L.
   J. Am. Chem. Soc. 1956, 78, 5963.
2. Sherry, H. S.; Walton, H. F. J. Phys. Chem. 1967, 71, 1457.
3. Dyer, A.; Celler, W. Z.; Shute, M. Adv. Chem. Ser. 1971, 101,
   436.
4. Firor, R. L.; Seff, K. J. Am. Chem. Soc. 1978, 100, 3091.
5. "Handbook of Chemistry and Physics," 55th ed. CRC Press:
   Cleveland, Ohio, 1974: pF-198.
6. Ogawa, K.; Nitta, M.; Aomura, K. J. Phys. Chem. 1979, 83,
   1235.
7. Nitta, M.; Ogawa, K.; Aomura, K. "Proceedings of Symposium
   on Zeolites," Szeged, Hungary; 1978, pp. 227-231.
8. Charnell, J. F. J. Cryst. Growth 1971, 8, 291.
9. Cruz, W. V.; Leung, P. C. W.; Seff, K. J. Am. Chem. Soc.
   1978, 100, 6997.
10. Principal computer programs used in this study: T. Ottersen,
    COMPARE data reduction program, University of Hawaii, 1973;
    full-matrix least-squares, P. K. Gantzel, R. A. Sparks, and
    K. N. Trueblood, UCLALS4, American Crystallographic Asso-
    ciation Program Library (old) No. 317 (revised 1976);
    Fourier program, C. R. Hubbard, C. O. Quicksall, and
    R. A. Jacobson, Ames Laboratory Fast Fourier, Iowa State
    University, 1971; C. K. Johnson, ORTEP, Report No. ORNL-
    3794, Oak Ridge National Laboratory, Oak Ridge, Tennessee,
    1965.
11. Kim, Y.; Seff, K. J. Am. Chem. Soc. 1978, 100, 175.
12. Kim, Y.; Seff, K. J. Phys. Chem. 1978, 82, 925.
13. Firor, R. L.; Seff, K. J. Am. Chem. Soc. 1977, 99, 1112.
14. Vance, Jr., T. B.; Seff, K. J. Phys. Chem. 1975, 79, 2163.
15. Cruickshank, D. W. J. Acta Crystallogr. 1949, 2, 65.
16. Subramanian, V.; Seff, K. J. Phys. Chem. 1977, 81, 2249.
17. Doyle, P. A.; Turner, P. S. Acta Crystallogr., Sect. A 1968,
    24, 390.
18. "International Tables for X-ray Crystallography," Vol. IV,
    Kynoch Press: Birmingham, England, 1974; pp. 73-87.
19. Cromer, D. T. Acta Crystallogr. 1965, 18, 17.
20. Reference 18, pp. 149-150.
21. Barium ions in many minerals and other oxide materials are
    6 to 10 coordinate with Ba-O bonds in the range 2.6 to
    3.2 Å. See, for example, "Structure Reports, Metals and
    Inorganic Sections," 1978, 42A, p 411.
22. Raghavan, N. V.; Seff, K. J. Phys. Chem. 1976, 80, 2133.
23. Firor, R. L.; Seff, K. J. Am. Chem. Soc. 1977, 99, 6249.

The Effect of Oxygen of Photoluminescence and Resonance Energy Transfer in Copper (I) Y Zeolite

D. H. STROME and K. KLIER

Lehigh University, Bethlehem, PA 18015

Electronic properties of intrazeolitic complexes of transition metal ions with oxygen are of interest for elucidation of oxygen binding and its activation for oxidation reactions. In an earlier study, dioxygen and monooxygen chromium species were reported to be formed by specific interactions between the oxygen molecules and the Cr^{II} ions planted in the Type A zeolite (1). The Cr^{II}A and several other zeolites containing transition metal ions, which may exist in two or more valence states, were also found to be oxidation catalysts. One such system of note is the copper containing Type Y zeolite, the redox chemistry of which was studied in several recent investigations (2, 3, 4, 5). These studies established the range of conditions at which copper exists in divalent, monovalent, or zerovalent state and in particular determined the reduction conditions in hydrogen and carbon monoxide atmospheres for a complete conversion of $Cu^{II}Y$ to $Cu^{I}Y$ but no further to $Cu°$. The Cu^{I} ions in type Y zeolite were reported to be specific adsorption centers for carbon monoxide (6), ethylene (7), and to catalyze the oxidation of CO (8). In the present work the Cu^{I} ions were also found to be specific adsorption centers for oxygen.

The Cu^{I} centers in Type Y zeolite display a characteristic photoluminescence (3, 4, 9) of a wavelength 540 nm and decay time 100-120 µs which do not depend upon whether the $Cu^{I}Y$ zeolite was prepared by direct ion exchange of the zeolite with a Cu^{I} solution or by an exchange with a Cu^{II} solution followed by reduction in hydrogen (4). The 540 nm (100-120 µs) photoemission was identified as the $^3E^-(^3D_3\ 3d^94s) \rightarrow {}^1A(^1S_0\ 3d^{10})$ transition of Cu^{I} in the C_{3v} field of the oxygen six-ring windows (4); a subsequent investigation of the effects of carbon monoxide on the $Cu^{I}Y$ photoluminescence established that the 540 nm emission corresponds to hidden sites SI' or SI and new emissions were observed at 560 nm (125 µs) and 470 nm (75 µs) when the Cu^{I} ions were pulled out to the SII and SII' sites, respectively (10).
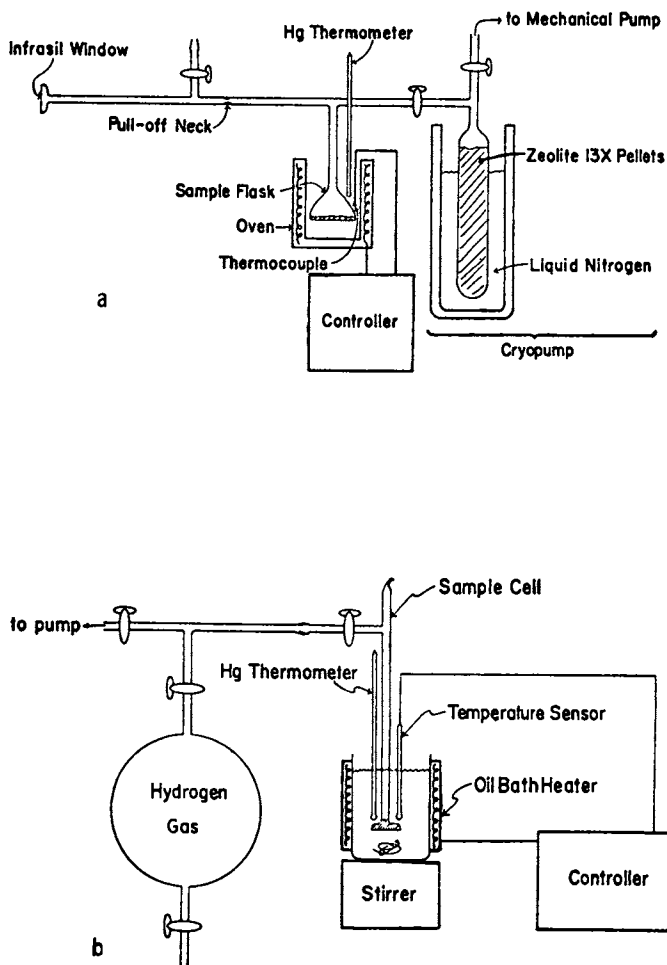
Figure 1.   (a) The zeolite dehydration apparatus; (b) the zeolite reduction apparatus

This study examines the oxygen-Cu^IY system. Evidence is presented for the excitation energy transfer between the Cu^I emitting centers and their oxidation products across distances exceeding that between the nearest sodalite units. The absorption spectra of the Cu^{II} species are also interpreted theoretically, using a model of the Cu^{II}-SI' site for the bare Cu^{II}Y zeolite and of the O_2^--Cu^{II}-SII complexes of various geometries for the oxidation product of Cu^IY. As a result, a fairly complete description of the electronic properties and interactions of the species formed in the oxygen-Cu^IY system is given.

Experimental

Sample Preparation. Copper Y zeolite was prepared by ion exchange of sodium Y (Linde SK-40) zeolite with aqueous $Cu(NO_3)_2$ solution. $Cu_{16}Na_{24}Y(Cu^{II}Y)$ (11) was obtained by stirring a slurry of 50g of NaY in 1 dm^3 of 0.1 M $Cu(NO_3)_2$ at 25° for 4 h. The copper content was determined by spectrophotometry of Cu^{2+} after dissolution of exchanged sieve. The Cu^{II}Y zeolite was washed, air dried, and 2g samples were dehydrated in an apparatus (Fig. 1a) under vacuum first at room temperature and then at 100°C, 200°C, 300°C, and 400°C, being held at each temperature for one hour. The constricted part of the tube (Fig. 1a) was then sealed off, sample transferred *in vacuo* into the Infrasil cell and reduced by hydrogen (Ultra-high purity, Air Products) at 1 atm and 200°C for 14 h in an apparatus (Fig. 1b). The temperature of 200°C gives rise to almost complete reduction of the Cu^{II}Y to Cu^IY without reducing further to $Cu°$ (4).

Spectroscopy. Diffuse reflectance spectra were recorded in the Infrasil cell (Fig. 1) on a Cary 14R spectrophotometer with digital output; the data were processed according to Schuster-Kubelka-Munk theory as has been previously described (12). Undispersed illumination (mode 2) was used for taking the spectra of luminescent samples between 5000 and 45000 cm^{-1}. Emission and excitation spectra were recorded using a Spex 1702 monochromator (slits set for 1 nm bandpass) with an EMI 9635 QBM photomultiplier to measure emission and an Oriel 7244 double monochromator (Oriel 7270 gratings, slits set for 5 nm bandpass) with 150 W Xe and 45 W D_2 lamps used for excitation. The Cu^IY sample was in the same Infrasil cell as that used for reflectance spectroscopy in a geometry shown in Fig. 2. Block diagram of the luminescence spectrometer is shown in Fig. 3. Mirrors 1, 2, and 3 (3 is the "polished aluminum" surface in Fig. 2) focus an image of the exit slit of the excitation monochromator onto the surface of the powder in the Infrasil cell, and any emitted light is collected by mirror 4 (after reflecting off 3) and focused onto the entrance slit of the emission monochromator. Mirrors 2 and 4 are toroidal, with an aluminized front surface and MgF_2 overcoating. Mirror 1 is front-surface-aluminized with SiO overcoating. Mirror 3 was made by
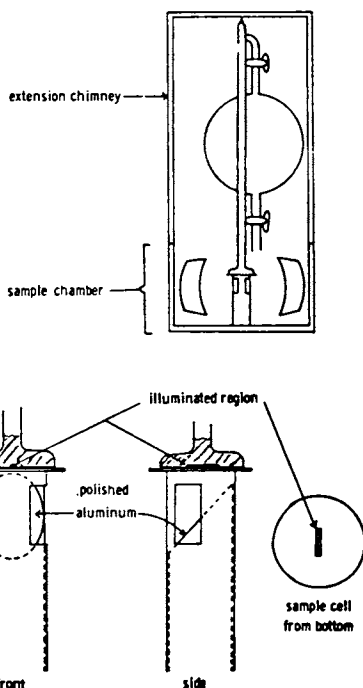
Figure 2. Sample chamber details for photoluminescence measurements: top, side view of sample chamber; bottom, detail at Mirror 3
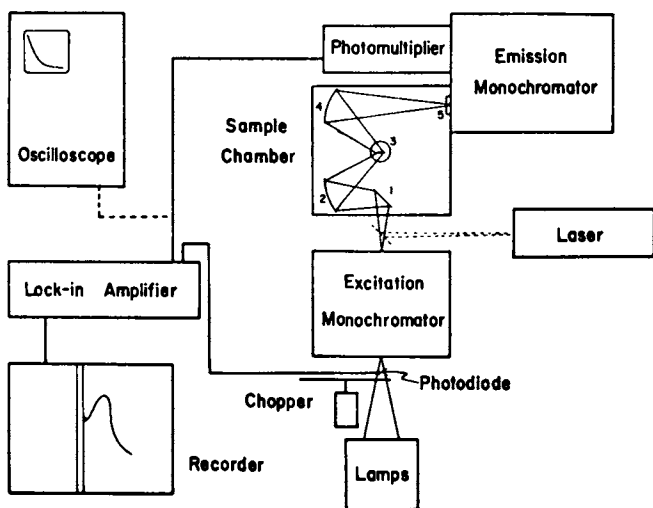
Figure 3. Block diagram of the photoluminescence spectrometer

polishing the machined (45°) surface of an aluminum rod. The optical filter (numbered 5 in Figure 3)-Schott KV370 plus Schott KV389- was used to remove scattered excitation light from the emission beam. A pulsed nitrogen laser (13) was used as a source for decay lifetime measurements. The laser wavelength was 337 nm, the output pulse duration about 1 ns, and the repetition rate typically 5 to 10 pulses per second.

The photomultiplier signal was fed by a one-meter coaxial cable to a 10^4 ohm load resistor at the oscilloscope vertical input. The observed risetime was about 1.6 μs, agreeing well with the estimated theoretical value of about 2 μs, at 180 pF total distributed capacitance plus 20 pF at the scope input. The scope was triggered by the RF pulse generated by the laser trigger spark gap by using a short antenna. The oscilloscope was a Tektronix 3100 digital processing oscilloscope equipped with a 4K memory and a hardwire signal averager which permitted the shot noise of the photomultiplier to be almost completely removed from the data. Photoluminescence decay curve after 2^{12} averages is shown for the Cu^IY sample in Fig. 4 as the solid line. The dashed line represents a semilogarithmic transform of the decay curve showing that the decay is exponential. The error in decay time measurement was found to be ±5% from a comparison of many measurements on a number of Cu^IY samples.

Results

$Cu^{II}Y$. The absorption spectra of hydrated and dehydrated $Cu^{II}Y$ zeolites are shown in Figs. 5 and 6, respectively. The dehydrated $Cu^{II}Y$ zeolite also displayed a weak photoluminescence at 540 nm, in qualitative accord with the reports of partial autoreduction of Cu^{II} to Cu^I upon dehydration, which amounts to approximately 20% of Cu^{II} converted to Cu^I at the dehydration temperature of 400°C (3). The sharp peaks at 5200 and 7000 cm^{-1} in Fig. 5 are the (ν+δ) and (2ν) vibrational bands of water (14). Their absence in Fig. 6 demonstrates that the dehydration of $Cu^{II}Y$ is complete. Also, absence of the silanol (2ν) band at 7300 cm^{-1} (15) shows that hydroxyl groups are absent in the dehydrated $Cu^{II}Y$ as well as in all subsequently treated copper zeolites. The broader bands between 9000 and 16000 cm^{-1} and above 30000 cm^{-1} are electronic absorption spectra of the copper species in the hydrated and dehydrated $Cu^{II}Y$, as follows from their comparison with the spectra of NaY and Cu^IY.

Cu^IY. The absorption, excitation, and emission spectra of the Cu^IY specimen were reported earlier (4, 10). The emission line is a perfect Gaussian centered at 18400 cm^{-1} (543 nm) of half-width 2900 cm^{-1}. The decay time of this luminescence was 112 μs on the present sample.

Cu^IY with oxygen. When the Cu^IY sample was exposed to dry
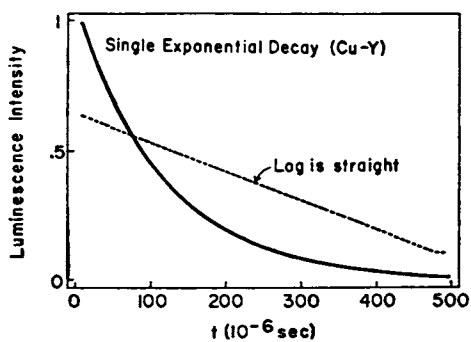
Figure 4.   Luminescence decay curve and its semilogarithmic representation for Cu(I)Y
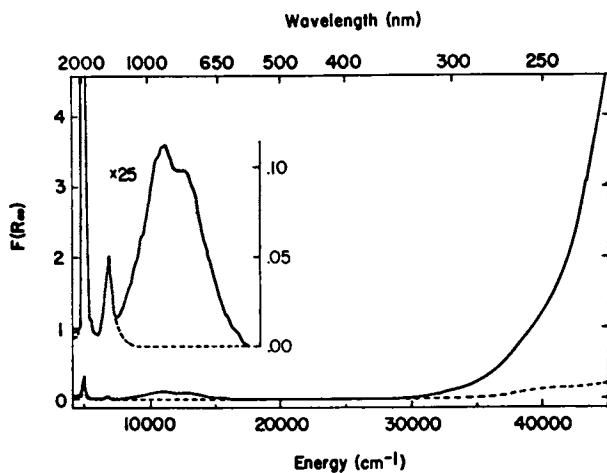
Figure 5. Diffuse reflectance of (———) hydrated Cu-exchanged and (– – –) unexchanged Y zeolite; $F(R_x)$ is proportional to the absorption coefficient.
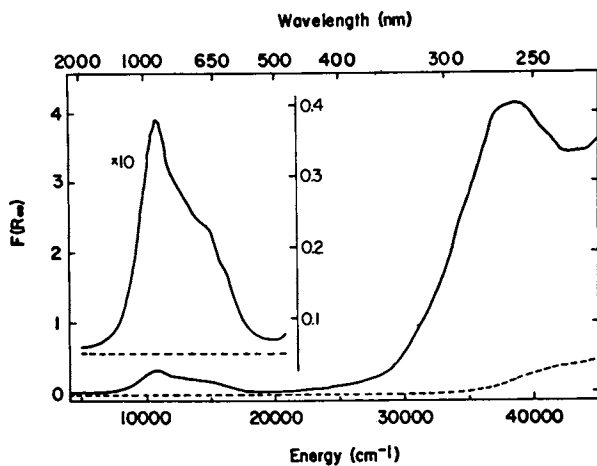
Figure 6. Diffuse reflectance of (———) dehydrated Cu-exchanged and (– – –) unexchanged Y zeolite

oxygen at 25°C and atmospheric pressure, a very slow process of luminescence quenching took place which resulted in the decrease of intensity and, although the spectral shape or position of the residual Cu^IY emission band did not change, in a reduction of the decay time. The latter observation is in contrast with the effect of adsorbed CO which quenches the luminescence intensity but leaves the decay time of the residual emission unchanged (10). The changes of the intensity and decay time during the exposure of Cu^IY to oxygen are shown in Fig. 7. In the presence of oxygen the decay time deviated from single exponential in an increasing measure with increasing time of exposure; the bar over the symbol τ denotes an average decay time except for the last point ($>10^7$s) at which two distinct lifetimes were determined from the photoluminescence decay, 28 μs shown in Fig. 7, and 6 μs. The reflectance spectrum of the Cu^IY exposed to oxygen was taken after the last data point and is displayed in Fig. 8. This spectrum of reoxidized Cu^IY is different from the spectrum of the bare $Cu^{II}Y$ zeolite, as follows from the comparison of Figs. 6 and 8.

Discussion

The electronic properties and location of the Cu^{II} ions in Type Y zeolite. (i) Hydrated $Cu^{II}Y$. The spectrum in Fig. 5 essentially agrees with earlier reported spectra of hydrated $Cu^{II}Y$ zeolites (16, 17, 18), although some more structure is noted here. The near-infrared band system at 11000-15000 cm^{-1} has been discussed by de Wilde, Schoonheydt, and Uytterhoeven (18). Their spectrum of hydrated $Cu^{II}Y$ is shown as a single band at 12150 cm^{-1} with width 5700 cm^{-1}, and for comparison they give analogous values for Cu^{II} in aqueous solution of 12300 cm^{-1} and 5000 cm^{-1}. Their conclusion is that in the hydrated $Cu^{II}Y$ zeolite the copper ions are present mainly as the hexaquo complexes. Spectra reported by Holmes and McClure (19) for six-coordinated Cu^{II} in the $CuSO_4 \cdot 5H_2O$ lattice are also very similar, although two of the ligands are sulfate oxygens and not water molecules. The near infrared band has been resolved into 10500 cm^{-1}, 13000 cm^{-1}, and 14500 cm^{-1} components with a total half-width of 5500 cm^{-1}. The hydrated $Cu^{II}Y$ bands in Fig. 5 show components at 11200 cm^{-1}, 13000 cm^{-1}, and a small shoulder at 15000 cm^{-1} with a total half-width of 5500 cm^{-1}. More important than a close agreement of the band maxima frequencies of the various hexacoordinated $Cu^{II}Y$ complexes, the intensities of the hydrated $Cu^{II}Y$ are much lower than those of dehydrated $Cu^{II}Y$ or oxidized $Cu^{II}Y$ (Fig. 9), which indicates the presence of an inversion center in the hydrated $Cu^{II}Y$ and its absence in dehydrated $Cu^{II}Y$ or oxidized Cu^IY. The inversion center in Cu^{II} complexes implies a D_{4h} or Jahn-Teller distorted O_h symmetry and the conclusion that the divalent copper is present in hydrated $Cu^{II}Y$ as a hexaquocomplex is well supported.

(ii) Dehydrated $Cu^{II}Y$. The total absence of water and hydroxyl vibrational peaks in Fig. 6 shows that the Cu^{II} ions are
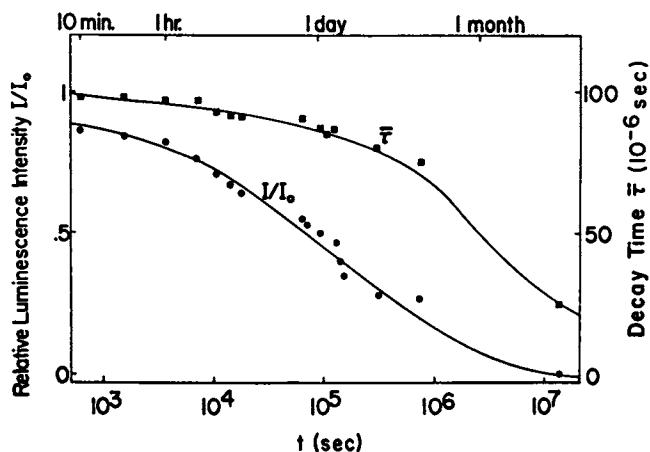
Figure 7. Relative luminescence intensity and decay lifetime of Cu(I)Y during exposure to oxygen at 25°C and 1 atm. The decay times are average lifetimes except for the last point at which two distinct lifetimes, $\tau = 28$ μsec and $\tau = 6$ μsec (not shown here), were determined.
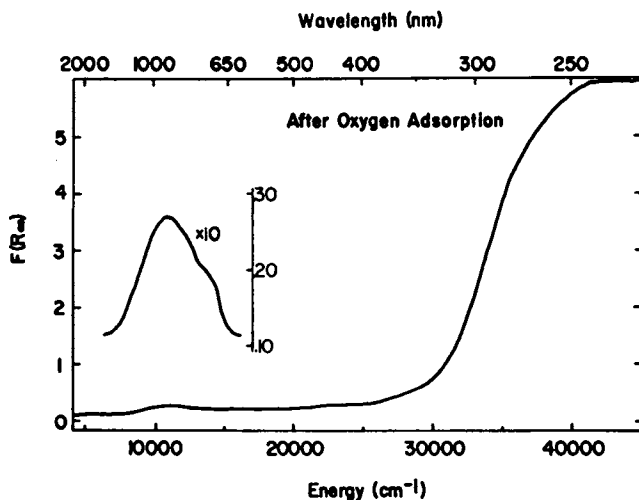
Figure 8. Diffuse reflectance of reduced CuY zeolite after long exposure to oxygen

Figure 9. The near-IR bands of (a) hydrated Cu(II)Y, (b) dehydrated Cu(II)Y, and (c) oxidized Cu(I)Y. The 540-nm photoemission of Cu(I)Y is shown as Curve d.
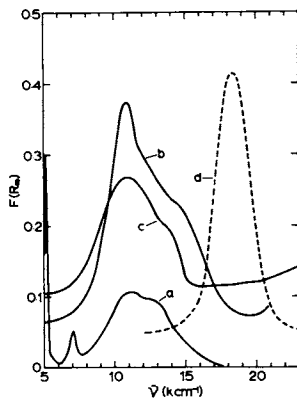
Figure 10. Term splitting diagrams for the Cu(II) ion in a C_{3v} site with Jahn–Teller and spin orbit splitting and band assignments for experimentally observed transitions (Figure 9b) drawn to scale.
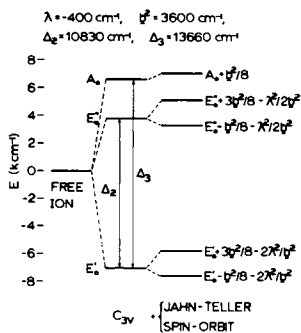
coordinated to the framework in the dehydrated $Cu^{II}Y$ zeolite. In-
deed an X-ray structural analysis of the dehydrated $Cu_{16}^{II}Na_{24}Y$
zeolite, a composition identical with that used in the present
work, located 78% of the copper ions in SI' and 22% in SI position
(20). Considering that the SI site is an inversion center, the
fraction of copper ions therein contributes little to the intensi-
ty of optical absorption and the electronic spectrum in Fig. 6 is
almost entirely that of the Cu^{II} ions in the SI' position. The
near infrared electronic band is composed of a narrow peak cen-
tered at 10900 cm^{-1} and two broader bands centered at 12700 and
14650 cm^{-1}. This spectrum is identical with that reported by de
Wilde, Schoonheydt, and Uytterhoeven (18), and therefore merits
an interpretation which is given below.

The C_{3v} symmetry at the SI' site imposes on the Cu^{II} ion term
splitting (21) shown in Fig. 10. The relative separations Δ_2 be-
tween the E-states and Δ_3 between the lower E-state and the A-
state depend on the angle β between the Cu-O bond and the three-
fold symmetry axis (22) and, conversely, from measured Δ_2 and Δ_3
one can determine β. The E-states are split further by the Jahn-
Teller effect and spin orbit coupling into E^+ and E^- components,
the energies of which are given by (21)

$$E^{\pm} = R^2 \pm \sqrt{\frac{1}{2} \underset{\sim}{b}^2 R^2 + \lambda^2 M_L^2 M_S^2} + BR^3 \cos 3\phi$$

where $R^2 = \frac{1}{2} k(q_x^2 + q_y^2)$, k is the vibrational force constant of a
degenerate $\tilde{E}$-vibration mode of the C_{3v} complex, q_x and q_y are the
normal coordinates, b is the Jahn-Teller coupling constant, λ is
the term spin-orbit coupling constant, M_L and M_S are the orbital
and spin z-component quantum numbers for the hole in the d-system
of the Cu^{II} ion, B is the anharmonicity constant and ϕ is the
angle between $\vec{R}$ and the x-coordinate. The anharmonicity contrib-
utes little to determining the energy minimum which is approxi-
mately at

$$E_{min}^- = - \frac{\underset{\sim}{b}^2}{8} - \frac{2\lambda^2 M_L^2 M_S^2}{\underset{\sim}{b}^2}$$

with

$$R_{eq} = R(E_{min}^-) = \sqrt{\frac{\underset{\sim}{b}^2}{8} - 2\lambda^2 M_L^2 M_S^2 / \underset{\sim}{b}^2}.$$ Expressions for the

remaining energies at $R = R_{eq}$ are given at the term levels in Fig.
10, in which the lower-lying E-states are labeled as E' and the
higher-lying E-states are denoted as E". The E" orbitals are
nearly in the xy plane, and so their $M_L = \pm 2$, the E' orbitals have
$M_L = \pm 1$, and the A orbital has $M_L = 0$. $M_S = \pm\frac{1}{2}$ for all states.
With these values of M_L and M_S the energies of the four possible
transitions in this system are

$$(E'^+ - E'^-) = \frac{1}{4} \underset{\sim}{b}^2 \qquad\qquad [1]$$

$$(E^{"+} - E^{'-}) = E_o^{"} + \frac{3}{2} \frac{\lambda^2}{\underset{\sim}{b}^2} \qquad\qquad [2]$$

$$(E^{"+} - E^{'-}) = E_o^{"} + \frac{\underset{\sim}{b}^2}{2} + \frac{3}{2} \frac{\lambda^2}{\underset{\sim}{b}^2} \qquad\qquad [3]$$

$$(A - E^{'-}) = A_o + \frac{\underset{\sim}{b}^2}{4} + 2 \frac{\lambda^2}{\underset{\sim}{b}^2} \qquad\qquad [4]$$

Here the constant $\underset{\sim}{b}$ was assumed to have the same value for both the E' and E" states. This assumption is consistent with transition [2] being a narrow peak while transitions [3] and [4] are broader bands, as the structure of the near-infrared absorption of $Cu^{II}Y$ demonstrates (Fig. 9). Transitions [2], [3], and [4] are assigned the observed frequencies 10900, 12700, and 14650 cm^{-1}, and transition [1] will be shown to be below 1000 cm^{-1}. The energy difference between transitions [2] and [3] depends only on the Jahn-Teller coupling constant, which is determined to be $\underset{\sim}{b}^2 = 3600$ cm^{-1} from the observed frequencies. The spin-orbit coupling constant λ is equal to 829 cm^{-1} for the free Cu^{II} ion (23), but in Cu^{II} complexes assumes the value close to 400 cm^{-1}. In the present analysis the band centers are insensitive to various choices of λ. With $\lambda = 400$ cm^{-1} and $\underset{\sim}{b}^2 = 3600$ cm^{-1}, the energies of the $E'^{\pm}$, $E"^{\pm}$, A, $E_o^{"}$, and A_o are given in the term diagram Fig. 10. The energy $E_o^{"}$ was set equal to zero.

The desired ratio $\frac{\Delta_2}{\Delta_3} = \frac{E_o^{"}}{A}$ is found to be equal to 0.793 which is consistent with the angle $\beta = 100°$ and with the O-Cu^{II}-O angle of 117°. This is in excellent agreement with the O-Cu^{II}-O angle of 115.9° found by X-ray diffraction (20). Both the structural determination and the present analysis of optical data thus demonstrate conclusively that the Cu^{II} ions are located close to the plane of the oxygen six-ring base of the SI' position, much more so than the Ni^{II} ions with the O-Ni^{II}-O angle of 100° (24).

The size of the Jahn-Teller distortion is estimated from the value of R_{eq} determined from $\underset{\sim}{b}^2$ and λ for the ground state, $R_{eq} = 19$ $cm^{-\frac{1}{2}}$. The quadratic potential R_{eq}^2 can be expressed in terms of displacements along the bonds,

$$R_{eq}^2 = \frac{1}{2} a_1 (Q_{12}^2 + Q_{13}^2 + Q_{14}^2) + \frac{1}{2} a_2 (Q_{23}^2 + Q_{34}^2 + Q_{42}^2) \quad ,$$

where Q_{12}, Q_{13}, and Q_{14} are displacements along the Cu-O bonds, Q_{23}, Q_{34}, and Q_{42} are displacements along the O-O links, and a_1 and a_2 are the central force constants (25). These force constants have close values for C_{3v} molecules with close reduced mass, and we have chosen, in the absence of known vibrational spectra of $Cu^{II}Y$, $a_1 = 3.23 \times 10^5$ dyn/cm and $a_2 = 0.88 \times 10^5$ dyn/cm of AsF_3 to approximate the vibrations of the $Cu^{II}O_3(SI')$ site.

That these force constants are not far from a reasonable estimate
is apparent from the assignment of a force constant 1.22×10^5 dyn/
cm for the symmetric vibration in Ca^{2+}-zeolite in the far infrared
study by Butler et al ($\underline{26}$). However, less than fully symmetric
modes must be used in the analysis of Jahn-Teller distortions,
and so the AsF_3 analogy will have to suffice. With these values,
the distortion R_{eq} is represented by $-Q_{12} = 0.05$-0.06 Å and
$Q_{34} = 0.08$-0.04Å for the ratio of symmetry coordinates $S_{4a}:S_{3a}$
($\underline{25}$) ranging from 0 to ∞. Two other equivalent distortions of
the $Cu^{II}O_3(SI')$ site are obtained by rotation through $\pm 120°$ in
the xy plane. The vibronic interactions causing the site dis-
tortion were already considered to be the cause of large g-factor
anisotropy and broadening of EPR lines in $Cu^{II}Y$ dehydrated at
400°C when the zeolite loses the last amount of water and all
copper becomes coordinated to the framework oxygens ($\underline{16}$). Hence
the present theory, which quantitatively interprets the optical
spectrum, is also in a quantitative accord with structural param-
eters, particularly the O-Cu^{II}-O angle, and in a qualitative
agreement with the EPR observations.

  *The photoluminescence of Cu^IY with adsorbed oxygen-evidence
for and quantitative analysis of resonance energy transfer.* The
Cu^IY zeolite used in this study was prepared by reduction of the
dehydrated $Cu^{II}Na$ Y zeolite in hydrogen. The reduction reaction
may be written as

$$Cu^{II}_{16}Na_{24}Y + 8H_2 \rightarrow Cu^I_{16}H^I_{16-x} \, \square_{O \, \frac{x}{2}} \, Na_{24}Y + \frac{x}{2} H_2O \quad,$$
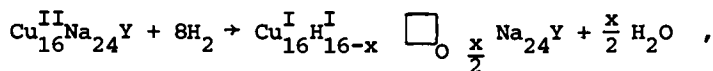
where $\square_O$ is a symbol for oxygen vacancy. While Rickert in his
pioneering study of the redox chemistry of CuY zeolite ($\underline{2}$) implied
that x = 0, the autoreduction study of Jacobs et al. ($\underline{3}$) put for-
ward evidence that some oxygen vacancies are formed even before
hydrogen is admitted. Thus in Cu^IY reduced by hydrogen there are
at least two kinds of defects, the proton and the oxygen vacancy.
These defects are not coordinated to the Cu^I ions, however, be-
cause the photoemission of Cu^IY, which is characteristic of the
local environment ($\underline{10}$), is identical for samples prepared by the
reduction of $Cu^{II}Y$ and by direct ion exchange from Cu^I solution
which does not produce such defects ($\underline{4}$).
  The photoluminescence parameters of the Cu^IY 540 nm emission
and their interpretation were reported in detail earlier ($\underline{4}$). The
emission line is redrawn here in Fig. 9 to show its partial over-
lap with the absorption spectra of the Cu^{II} species. Upon expo-
sure to oxygen the intensity of this line is gradually reduced
without changing the line-shape or frequency at maximum, but with
a change in the emission decay time, as shown in Fig. 7. The de-
creasing lifetime indicates that the excitation energy is chan-
neled away by a radiationless process which competes with photo-
emission to reach the ground state.

A theory containing such a mechanism has been put forward by Förster (27) for the case of fluorescent solutions and later augmented by Dexter (28) for the case of sensitized luminescence in solids. It involves the resonant transfer of energy between an emitting center and a perturbing center based on the electrostatic interaction between them. This Förster-Dexter theory provides a good framework for interpreting effects in which quenching and decay acceleration occur without change in the spectral character of the emission. Dexter's discussion (28) is formulated for the case in which energy absorbed by a sensitizer (S) undergoes a resonance transfer to an activator (A). In the initial state ψ_i(S*A) the atom S is excited and A is not, and in the final state ψ_f(SA*) atom A is excited and S is not. These states are coupled by the Coulomb interaction V between S and A, and the result of time-dependent perturbation theory is that there is a probability

$$P_{SA} = \frac{2\pi}{h} \left| <\psi_f|V|\psi_i> \right|^2 \rho E$$

of a transition between the two states, where ρE is the density of final states, and h is Planck's constant. Dexter expresses P_{SA}, for the case where S*→S and A→A* are both dipole transitions, in terms of experimentally measurable quantities:

$$P_{SA} = \tau^{-1} R_{SA}^{-6} 3h^4 (4\pi)^{-1} Q_A \int f_S(E) F_A(E) E^{-4} dE = \tau_s^{-1}(R_o^6/R_{SA}^6) \ .$$

Here Q_A in the integrated (over energy E) absorption cross section due to the A→A* transition, and F_A is its normalized line-shape; τ_S is the decay lifetime of the (unpeturbed) S*→S transition, and f_S is its normalized lineshape; R_{SA} is the distance between S and A, and R_o may be termed the critical transfer radius. The transfer probability thus depends on (i) the strengths of the S*→S and A→A* transitions individually (as measured by τ_S and Q_A); (ii) the separation of the two centers; and (iii) the special overlap of the emission S with the absorption of A.

For the present case, S will be identified with the Cu^I emitting center, and A with the product of its oxidation by oxygen. There is indeed an overlap between the absorption spectrum F_A of oxidized Cu^IY and the emission line f_S of Cu^IY, as is apparent from Fig. 9. The overlap integrals of F_A and f_S were determined by normalizing both lines to unit area and integrating numerically. The absorption cross-section Q_A was determined from the reflectance curve of Fig. 9c, in which the concentration was assumed to be equal to the original Cu^{II} concentration. Using the initial $\tau_S = 112\times10^{-6}$s, and inserting values for fundamental constants, the value obtained for the critical transfer radius R_o is

$$\left(R_o^6 \right)_{Cu^I Cu^{II}} = 5.66 \times 10^{-42} cm^6 \quad .$$

The Cu^I emitting centers thus undergo a radiative transition with a probability $P_{radiative} = \tau_s^{-1}$ and a non-radiative transition with a probability $P_{SA} = \tau_s^{-1} R_o^6 / R_{SA}^6$. The total transition rate $P_{total} = P_{radiative} + P_{SA}$ determines the measured decay lifetime, $\tau_{measured} = \tau$. From these definitions follows the fundamental relation for decay lifetimes in resonance transfer,

$$\frac{\tau_s}{\tau} = 1 + \left(\frac{R_o}{R_{SA}} \right)^6 \quad ,$$

from which R_{SA} can be calculated from measured quantities τ_s, τ, and R_o above with no adjustable parameters. The above equation holds for resonance transfer from one sensitizer to a single activator. In a geometric situation such as existing in doubly exchanged zeolites, each sensitizer has a certain probability to transfer energy to many activator centers and the equation has to be modified to read

$$\frac{\tau_s}{\tau} = 1 + \sum_{k=1}^{N} \left(\frac{R_o}{R_{SA,k}} \right)^6$$

where k indexes the different A atoms near a particular S, in order of increasing R_{SA}, and N is large enough so that $(R_o/R_{SA,N})^6$ becomes negligible. In order to interpret the observed lifetimes, therefore, the knowledge of the distribution of the distances $R_{SA,k}$ is desirable. The model ensuing from such a distribution will be discussed in our future work. In this paper we shall confine ourselves to the determination of an average distance $\overline{R}_{SA}$ defined as

$$\overline{R}_{SA}^{\;6} = 1 \Big/ \sum_{k=1}^{N} \left(\frac{1}{R_{SA,k}} \right)^6$$

which can be determined directly from the observed lifetimes.

In addition to determining the distances $\overline{R}_{SA}$ from lifetimes, the concentration [S] of the sensitizer centers can be obtained from the measured intensities and lifetimes. Denoting the illumination intensity as I_{inc}, at a steady state there is a balance between the rate of $S \to S^*$ excitation, $\eta\, I_{inc}[S]$, where η is the quantum efficiency of the excitation, and the rate of

deexcitation, $[S^*] P_{total}$,

$$I_{inc}[S] = P_{total}[S^*] = \tau^{-1}_{measured}[S^*] \quad .$$

The emission intensity I is given by $P_{radiative}[S^*] = \tau^{-1}_s[S^*]$, and thus

$$[S] = (\tau_s/\tau) I/(\eta I_{inc}) \quad .$$

For the oxygen adsorption proceeding with time as shown in Fig. 7 the sensitizer concentration $[S_o]$ at time zero is associated with the initial lifetime $\tau = \tau_s$, and it follows that

$$\frac{[S]}{[S_o]} = \left(\frac{\tau_s}{\tau}\right)\frac{I}{I_o} \quad .$$

Because the activator is formed in this system at the expense of the sensitizer (the activator centers are oxidized sensitizer centers), its relative concentration is equal to $1 - [S]/[S]_o$. The distances $\overline{R}_{SA}$ calculated from the measured lifetimes depicted in Fig. 7 and from R_o determined above are plotted in Fig. 11 against the relative activator concentration determined from lifetimes and intensities of Fig. 7. For all except the last point, $\overline{R}_{SA}$ are average S-A distances. The two distinct lifetimes of 28 μs and 6 μs at the right hand end of the graph (Fig. 7) result in $\overline{R}_{SA}$ = 11.1 Å and 8.3 Å at 95% activator concentration in Fig. 11. At this point each emitting center is completely surrounded by the activator centers and so 11.1 Å and 8.3 Å represent the shortest S-A distances attainable in the $Cu_{16}Na_{24}Y$ zeolite. It is noted that 11.1 Å is comparable with the distance between two neighboring sodalite cages, 10.7 Å, which indicates that the excitation energy is transferred from S in one sodalite unit to A in another. The distance 8.3 Å indicates transfer around a single sodalite cage. Since there are in average two copper atoms in one sodalite unit, 8.3 Å is the closest distance between the Cu^I emitting center and an oxidized Cu^{II} activator center. At lower activator concentrations between 15% and 55%, the $\overline{R}_{SA}$ distances are between 16.4 and 17.3 Å (Fig. 11), extending beyond the distance between the centers of the nearest sodalites.

The electronic properties of the activator center: the Cu^{II}*-O_2^- complex.* The absorption spectrum of the oxidized Cu^IY is different from that of the dehydrated $Cu^{II}Y$ (compare Figs. 6, 8, and 9) in the following respects: (i) the near-infrared band has only two identifiable components, each of which is broader than those of dehydrated $Cu^{II}Y$ but with the total bandwidth less than that of dehydrated $Cu^{II}Y$; (ii) the UV absorption of oxidized Cu^IY is at higher energies and has a much higher intensity than that
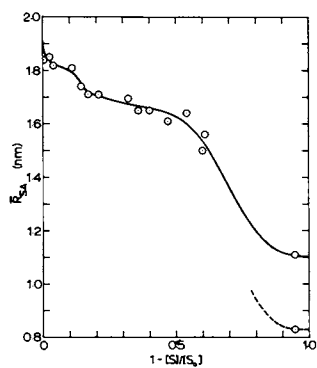
Figure 11. The average sensitizer–activator distances $\overline{R}_{SA}$ vs. the concentration of the activator $1-[S]/[S_o]$ for $Cu(I)Y$ exposed to oxygen. $\overline{R}_{SA}$ and $[S]/[S_o]$ were calculated from lifetimes and intensities in Figure 7 and from $R_o{}^6 = 5.66 \times 10^{-42}$ cm^6.

of dehydrated $Cu^{II}Y$. The absorption spectrum of the oxidized $Cu^{I}Y$
is also different from that of the hydrated $Cu^{II}Y$: (i) it has no
water or OH vibrational maxima; (ii) it has 3-4 times higher in-
tensity of the near-infrared electronic band and different fre-
quencies at maxima; (iii) its UV absorption is at lower energies
than that of hydrated $Cu^{II}Y$. It is concluded that the oxidized
$Cu^{I}Y$ complex is a different moiety than either dehydrated or hy-
drated $Cu^{II}Y$, and that the copper ions are not coordinated to
water or OH groups. The near-infrared absorption shows, however,
that copper is bivalent. The intensity of the near-infrared elec-
tronic band excludes the SI site for this Cu^{II} ion, because the
center of symmetry is retained in SI site even upon Jahn-Teller
distortion. Oxygen was taken up but did not react with the hydro-
gen from previous reduction for form OH or H_2O, and it is there-
fore concluded that oxygen is coordinated to the copper ions.
Were the product of oxidation a Cu^{++}-O^- complex in the SII site,
the coordination would be near tetrahedral with expected absorp-
tion band at 5800 cm^{-1} (29) and not at the observed frequencies
of 11000-14000 cm^{-1}. It is therefore assumed that the oxidized
complex is Cu^{II}-O_2^-. The subsequent analysis supports this propo-
sition and, in addition, assists in determining the structure of
this complex.

The geometric model adopted here is one in which the O_2^- mole-
cule provides a C_{2v} component to the crystal field potential a-
round the Cu^{II} ion, and together with the three framework oxygens
of the SII site makes an additional tetrahedral (T_d) component.
This model has been theoretically analyzed earlier (30) and the
one-d-electron matrix of the potential (V_{T_d}+$V_{C_{2v}}$) given therein
needs only to change sign to describe the one-d-hole complex of
Cu^{II}. The matrix elements of the (V_{T_d}+$V_{C_{2v}}$) potential depend on
structural and crystal field parameters which are: the angles Θ_0
and Φ_0 defined in the upper drawing in Fig. 12, the T_d field
strength parameter G_4, and the C_{2v} parameters G_2' and G_4'. G_4 is
set here equal to 1800 cm^{-1}, which is the value derived from the
analysis of the spectrum of dehydrated $Cu^{II}Y$, since the same type
framework oxygens are at the base of the Cu^{II} (SI') site as well as
at the base of the Cu^{II}-O_2^- complex. Further, G_2' = 10 G_4' proved
to be universally valid for the first transition series ions in
zeolites (22). Figure 12 shows the $3d^9$ Cu^{II} ion energies obtained
by the diagonalization of the (V_{T_d}+$V_{C_{2v}}$) matrix for various values
of the angles Θ_0 and Φ_0 with G_4' adjusted to best fit the observed
spectrum as shown in Fig. 13. It is seen from the right-hand sec-
tion of Fig. 12 that good fits are obtained only for Θ_0 close to
45°; at lower Θ_0 an absorption band is predicted between 10,000
cm^{-1} and 5000 cm^{-1} which is not observed. Θ_0 = 0° and G_4' = 1000
cm^{-1} may be taken to represent trigonal Cu^{II}-O_2^- complex in which
the O_2^- axis is aligned with the trigonal axis and O_2^- is a much
stronger ligand than the framework oxygens, or a Cu^{II}-O^- com-
plex with a strong O^- ligand. On the other hand, the term
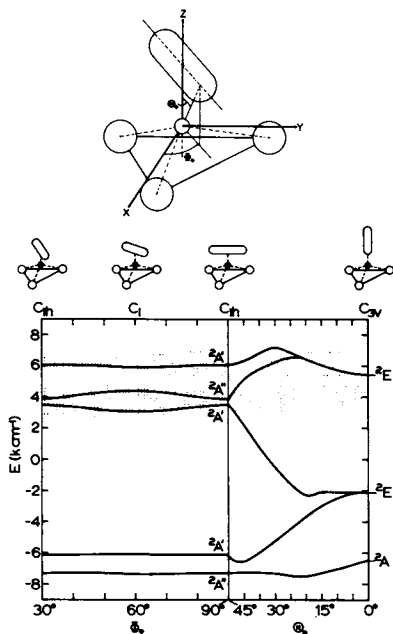
Figure 12. The term diagrams for the $Cu(II)$–O_2^- complex of various configurations determined by the angles Θ_0 and Φ_0 defined in the top drawing. The symmetry labels A' and A" denote orbitals symmetric and antisymmetric with respect to the reflection plane of the C_{1h} group at $\Phi_o = 30°$ and $\Phi_o = 90°$. The individual orbitals at $\Phi_o = 90°$, $\Theta_o = 44°$, $G_4' = 2300$ cm^{-1}, and $G_4 = 1800$ cm^{-1} have the following form:

$$|1> = 0.998 \, d_{yz} + 0.056 \, d_{xy}$$
$$|2> = 0.889 \, d_{z^2} - 0.029 \, d_{zx} + 0.457 \, d_{x^2-y^2}$$
$$|3> = 0.130 \, d_{z^2} + 0.973 \, d_{zx} - 0.190 \, d_{x^2-y^2}$$
$$|4> = 0.056 \, d_{yz} - 0.998 \, d_{xy}$$
$$|5> = 0.439 \, d_{z^2} - 0.228 \, d_{zx} - 0.869 \, d_{x^2-y^2}$$

Shaded areas indicate the positions of experimentally observed bands of Figure 9c.
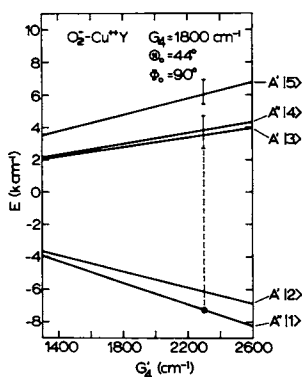
Figure 13. The term diagram of the $Cu(II)$–O_2^- complex at $\Phi_0 = 90°$, $\Theta_0 = 44°$, and varying O_2^- ligand strength G_4'. Vertical bars indicate the positions of experimentally observed bands of Figure 9c.

diagram is little dependent on the angle Φ_O in the xy plane, and
all Φ_O configurations with $\Theta_O = 44°$ and $G_4' = 2300$ cm^{-1} fit the
observed transitions well. It is concluded that the O_2^- species
is a π-bonded ligand with a strong C_{2v} potential. The wide angle
Θ_O indicates that the major source of this potential is the
$\pi^*(2p_z)$ orbital of O_2^-, where indeed the excess electron resides.
Eigenvector calculations show that the ground state of copper for
$\Phi_O = 90°$ is one with the d-hole in the orbital $\Psi_{A"} = 0.998$ d_{yz} +
0.056 d_{xy}; thus the ground state of the Cu^{II}-O_2^- complex originates
from the attraction of a hole in the Cu^{II}-d_{yz} orbital to the
electron in the O_2^--$\pi^*(2p_z)$ orbital.

Summary

The present results and their interpretation, along with
earlier studies of copper faujasite structural and spectroscopic
properties, provide a consistent picture of the CuY zeolite
chemistry. After dehydration of Cu^{II}Y, the Cu^{II} ions are lo-
cated in the SI' sites in a close, near planar coordination to
framework oxygens. A strong Jahn-Teller coupling distorts this
site to three equivalent geometries with one Cu-O distance dif-
ferent from the other two. Upon reduction by hydrogen, Cu^I ions
are produced in the SI' or SI positions, which are also sites for
Cu^I ions directly introduced by ion exchange. Sites SI' are pre-
ferred by a distribution derived from resonance energy transfer
data. The reactions of the Cu^I ions with adsorbing molecules
are slow and involve their migration to the SII sites. The com-
plex with oxygen formed therein has an absorption spectrum that
is consistent with π-bonded O_2^- to Cu^{II}(SII) but not with "head-
on" bonded O_2^- or an O^--Cu^{II} complex.
The most remarkable result reported here is the evidence for
an efficient resonance energy transfer between the Cu^I emitters
and the Cu^{II}-O_2^- acceptors of excitation energy from one sodalite
cage to another, and from inside the sodalite cage to complexes
in the supercage.

Acknowledgment

<div align="center">ABSTRACT</div>

The decay time of the green (540 nm) photoluminescence of
the dehydrated $Cu^I_{16}Na_{24}$ Y zeolite was found to gradually change
from 112 to 28 and 6 μs upon exposure to oxygen. Simultaneously

a near-infrared electronic absorption band of a Cu^{II}-oxygen complex developed which partially overlapped with the Cu^{I} photoemission peak. The observed decay times, emission intensities, and absorption intensities were quantitatively treated by Förster-Dexter resonance transfer theory from which the sensitizer (S = Cu^{I})-activator (A = Cu^{II}-oxygen complex) distances were determined at various stages of oxygen adsorption. A very efficient excitation energy transfer occurs between S and A in neighboring sodalite units across distances of 11-12 Å.

The absorption spectrum of the Cu^{II}-oxygen complex was in good agreement with that theoretically predicted for an O_2^{-}-Cu^{II}-O_3 species (O_3 are the three proximal oxygens in the six-ring window) wherein the O_2^{-} anion axis is parallel to the O_3 plane. A wide O_2^{-}-Cu^{II} angle indicates bonding of the $Cu^{II}d_{yz}$ orbital with the $\pi_g^{*}(z)$ orbital of O_2^{-}. A "head-on" oxygen-Cu^{II} model was found incompatible with the observed spectrum.

The absorption spectrum of the bare $Cu^{II}Y$ zeolite was also measured and interpreted using a model of a Cu^{II}-O(SI') site. The O-Cu^{II}-O angle was determined to be 117° from optical spectra, in excellent agreement with 115.9° found by X-ray crystallography (20). Based upon the observed spectral splitting of 1800 cm^{-1} of the ^2E states of Cu^{II}-O_3, first order vibronic theory predicted a Jahn-Teller distortion of 0.05-0.06 Å along the Cu^{II}-O bonds.

Literature Cited

1. Kellerman, R.; Klier, K. ACS Symposium Series, 1977, 40, 120.
2. Rickert, L. Ber. Bunsenges. phys. Chem., 1969, 73, 331.
3. Jacobs, P. A.; de Wilde, W.; Schoonheydt, R. A.; Uytterhoeven, J. B.; Beyer, H. J. Chem. Soc. Faraday I, 1976, 72, 1221.
4. Texter, J.; Strome, D. H.; Herman, R. G.; Klier, K. J. Phys. Chem., 1977, 81, 333.
5. Huang, Y. Y.; Mainwaring, D. E. J. Chem. Soc. Chem. Commun., 1974, 584.
6. Huang, Y. Y. J. Catalysis, 1973, 30, 187.
7. Huang, Y. Y. J. Am. Chem. Soc., 1973, 95, 6636.
8. Kubo, T.; Tominaga, H.; Kunugi, T. Bull. Chem. Soc. Japan, 1973, 46, 3549.
9. Maxwell, I. E.; Drent, E. J. Catalysis, 1976, 41, 412.
10. Strome, D. H.; Klier, K. J. Phys. Chem., in press.
11. The subscripts at Cu and Na denote the number of the respective Cu^{II} and Na^{I} ions per unit cell of the Type Y zeolite. The copper content corresponds to 2 Cu^{II} ions per sodalite unit.
12. Klier, K. Catal. Rev., 1967, 1, 207.
13. Bergmann,E. E. Appl. Phys. Lett., 1976, 28, 84.
14. Luck, W. A. P. Ber. Bunsenges. phys. Chem., 1965, 69, 626.
15. Shen, J. H.; Zettlemoyer, A. C.; Klier, K. J. Phys. Chem., in press.

16. Mikheikin, I. D.; Shvets, V. A.; Kazanskii, V. B. Kinet. Catal., 1970, 11, 609.
17. Kiselev, A. V.; Kuzmenko, N. M.; Lygin, V. I. Russian J. Phys. Chem., 1973, 47 (1), 88.
18. De Wilde, W.; Schoonheydt, R. A.; Utterhoeven, J. B. ACS Symp. Ser., 1977, 40, 132.
19. Holmes, O. G.; McClure, D. S. J. Chem. Phys., 1957, 26, 1686.
20. Gallezot, P.; Taarit, Y. Ben; Imelik, B. J. Catalysis, 1972, 26, 295.
21. Klier, K.; Hutta, P. J.; Kellerman, R. ACS Symp. Ser., 1977, 40, 108.
22. Kellerman, R.; Klier, K. Surface and Defect Properties of Solids (Chem. Soc. London), 1975, 4, 1.
23. Griffith, J. S., The Theory of Transition-Metal Ions, Cambridge University Press 1964, p. 437.
24. Olson, D. H. J. Phys. Chem., 1968, 72, 4366.
25. Herzberg, G., Molecular Spectra and Molecular Structure II. Infrared and Raman Spectra of Polyatomic Molecules, Van Nostrand Reinhold Co. 1945.
26. Butler, W. N.; Angell, C. L.; McAllister, W.; Risen, W. M. J. Phys. Chem., 1977, 81, 2061.
27. Förster, Th. Ann. Phys., 1948, 2, 55.
28. Dexter, D. L. J. Chem. Phys., 1953, 21, 836.
29. Pappalardo, R. Mol. Spectroscopy, 1961, 6, 554.
30. Klier, K.; Kellerman, R.; Hutta, P. J. J. Chem. Phys., 1974, 61, 4224, Appendix.

Preparation of Copper(II)-Exchanged Y Zeolites from Sodium and Ammonium Y Zeolites

RICHARD G. HERMAN and JOHN B. BULKO

Center for Surface and Coatings Research, Sinclair Laboratory, Building #7, Lehigh University, Bethlehem, PA 18015

The preparation of ammonium ion exchanged Y zeolites has long been known to be a precursor step in the preparation of H Y zeolites. The former materials have been characterized by thermogravimetric experiments, while the latter zeolites that contain the H atoms as hydroxyl groups have been intensively examined by infrared spectroscopy ($\underline{1},\underline{2},\underline{3},\underline{4}$). A systematic description of the preparation of NH_4 Y zeolites has apparently not been reported, although an ion exchange isotherm for the Na-NH_4 exchange at 25°C has been given ($\underline{5}$).

Divalent copper Y zeolites have been widely prepared and the Cu(II)-Na exchange process has been described by ion exchange isotherms ($\underline{5},\underline{6}$). It was clearly shown that Y zeolite exhibited a strong preference for Cu(II) over Na^+. Similar behavior might be expected for the Cu(II)-NH_4^+ ion exchange, although hydrogen bonding by the ammonium ion in the hydrated zeolite lattice might influence the ion exchange process. Clarification of the practical preparative relationships involved in the Cu(II)-NH_4-Na Y zeolite system is desired because of developing industrial application of these materials. For example, Cu-H-Na Y zeolites ($\underline{7}$) and Cu-H-RE Y zeolites ($\underline{8}$), where RE = rare earth, have been found to be excellent cracking catalysts that produce high octane gasoline having enhanced aromatic and olefinic content. In addition, it has been observed recently that Cu-H Y zeolites efficiently adsorb NH_3 from gas streams containing low concentrations of this impurity ($\underline{9}$).

Experimental

Ammonium Ion Exchange. Linde anhydrous Na Y zeolite was used as received to prepare NH_4^+ ion exchanged samples. The general procedure was to add the zeolite to 1.0 M NH_4NO_3 solution at a designated temperature (23, 50, 65, 85, or 100°C) such that the ratio of solution volume to solid mass (v/m) was 20 cm^3/g. The mixture was stirred continuously for 4 h, allowed to stand for 5 min, and then the supernatant was decanted and the solid

was filtered onto Whatman #2 filter paper with the aid of suction.
The zeolite was washed with 10 cm^3 portions of water, where total
v/m = 20 cm^3/g, and added to a fresh aliquot of ammonium nitrate
solution. After this procedure was once again repeated, the re-
sultant zeolite was dried at ambient temperature in an open vessel
placed in a fume hood.

Copper(II) Ion Exchange. Starting with anhydrous Na Y and
hydrated NH$_4$ Y zeolites, ion exchange was carried out with fil-
tered Cu(NO$_3$)$_2$·3H$_2$O solutions of different concentrations in
order to obtain samples with different Cu(II) contents. The
equilibrations were carried out for 4 h at ambient temperature
with v/m = 20 or 200 cm^3/g.
       An additional series of samples of Na Y was equilibrated
with 0.01 M Cu(II) solutions, v/m = 20 cm^3/g, in which the pH
was artificially adjusted to 3.0, 5.0, or 9.0. For the acid
solution equilibrations, the copper(II) nitrate solutions were
adjusted to the desired pH by the addition of 1.0 M HNO$_3$ or 0.1 M
NaOH. After the addition of the zeolite, which had been slur-
ried in a small amount of water, the solution was continuously
stirred for 4 h at ambient temperature. The pH was monitored
and maintained at the required values. For the preparation of
the sample at pH = 9.0, the Na Y zeolite was added to water
(v/m = 10 cm^3/g) and the pH was decreased to 6.0 by the addition
of 1.0 M HNO$_3$. Following the addition of the Cu(II) solution,
the pH was increased to pH 9 by means of 0.1 M NaOH over a period
of 0.5 h. Stirring was continued for 3.5 h, during which time
the pH was maintained at 9.0.

Analyses. Ammonium ion-containing samples were analyzed
commercially for N, H, and Na content. The copper(II) concen-
trations were determined commercially and by atomic absorption
or spectrophotometric measurements a) on the preparative fil-
trates, b) following back-exchange of the zeolites by Ag^{+}, and/
or c) following complete dissolution of the zeolites.

Results

Ammonium Ion Exchanged Y Zeolites. The effect that equili-
bration temperature exerted upon the degree of NH$_4^+$ ion exchange
of Na Y zeolite was studied in this part of the investigation.
The results of two of the five triple equilibrations are shown
in Figure 1. Sample C was found to correspond to Na$_6$(NH$_4$)$_{50}$
(AlO$_2$)$_{56}$(SiO$_2$)$_{136}$·200H$_2$O [Found: 0.81 wt % Na, 4.32 wt % N, 3.62
wt % H; Calculated: 0.86 wt % Na. 4.35 wt % N, 3.73 wt % H],
while sample F was determined to be Na$_{14}$(NH$_4$)$_{42}$(AlO$_2$)$_{56}$(SiO$_2$)$_{136}$
·200H$_2$O [Found: 1.95 wt % Na, 3.59 wt % N, 3.57 wt % H; Calcu-
lated: 1.99 wt % Na, 3.64 wt % N, 3.52 wt % H]. After a single
4 h equilibration, the samples prepared at the five designated
temperatures were observed to be 68-71 % exchanged by NH$_4^+$, and

this can be illustrated by the analytical data for sample D
[Found: 2.58 wt % Na, 3.32 wt % N, 3.43 wt % H; Calculated: 2.56
wt % Na, 3.29 wt % N, 3.42 wt % H], which is typical of these
samples and corresponds to $Na_{18}(NH_4)_{38}(AlO_2)_{56}(SiO_2)_{136} \cdot 200H_2O$.
The extent of NH_4^+ ion exchange after triple equilibrations is
shown in Figure 2 to correspond directly with the temperature.
The supernatant pH for these samples was 5.3 ± 0.2, while the pH
after a single equilibration, e.g. samples A and D in Figure 1,
was 6.5 ± 0.2.

Copper(II) Ion Exchanged Y Zeolites. The zeolites utilized
were the parent anhydrous Na Y zeolite [$Na_{56}(AlO_2)_{56}(SiO_2)_{136}$ and
the hydrated NH_4 Y zeolites designated as samples C and F in the
previous section. Upon Cu(II) ion exchange of Na Y zeolite at
ambient temperature with the constraint of v/m = 20 cm^3/g, the
final pH was found to be proportional to the initial copper(II)
concentration in solution as shown by the semi-log plot in Fig-
ure 3. The initial pH of the exchange solution was, in each case,
the value expected for the designated copper(II) nitrate concen-
tration. Increasing v/m by a factor of 10 resulted in a curve
that appeared to consist of two linear regions. At low copper(II)
concentrations, it is apparent in Figure 3 that one of the linear
portions of the curve is parallel to the straight line obtained
when v/m = 20 cm^3/g.
      Using hydrated NH_4 Y zeolites as starting materials, similar
behavior was observed. Most of the data points in Figure 3 for
the Cu(II) + NH_4 Y exchange were obtained using Sample C, which
was depicted in Figures 1 and 2 (89% NH_4^+ exchanged). However,
the three data points for v/m = 20 cm^3/g designated by triangles
in Figure 3 were obtained with Sample F (75% NH_4^+ exchanged).
Identical exchange behavior for these two samples is demonstrated
by the single curve drawn through the two sets of data points for
v/m = 20 cm^3/g. Although the final pH was always acidic, vibra-
tional studies showed that the unexchanged NH_4^+ ions remained in
the zeolites instead of being replaced by H^+ ions (9).
      Following analyses of most of the samples indicated in Fig-
ure 3, the curves shown in Figure 4 were constructed. Additional
points corresponding to equilibration of Na Y samples in distilled
water for 4 h are included in the plot at pH = 10.32(v/m =
20 cm^3/g) and at pH = 9.21(v/m = 200 cm^3/g). It is evident from
this figure that, under the conditions that these experiments
were carried out, a maximum of 71% copper(II) exchange was
achieved with the NH_4 Y zeolites. A lower exchange level was
attained by the Na Y zeolites when equilibrated with the same
copper-containing solutions. Higher copper(II) ion exchange was
observed with the two v/m = 200 cm^3/g series than with the v/m =
20 cm^3/g series, as would be expected since the quantity of cop-
per is 10 times greater with respect to the zeolite in the former
as compared with the latter.
      The analytical results for the Na Y samples that had been

Figure 1. The extent of ammonium ion exchange of Na Y zeolite (△) at 23°C and at (○) 85°C. Equilibrations of the solutions with v/m = 20 cm³/g were carried out for 4 hr each.
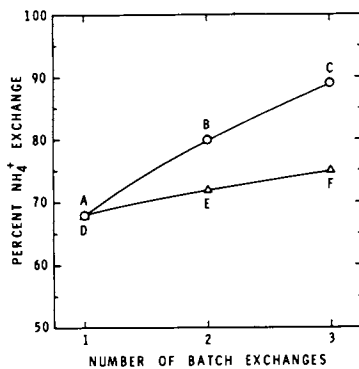
Figure 2. The degree of ammonium ion exchange of Na Y zeolite following triple equilibrations at selected temperatures. Points C and F correspond to the designated data points in Figure 1.
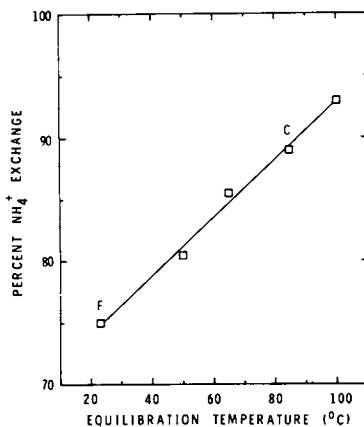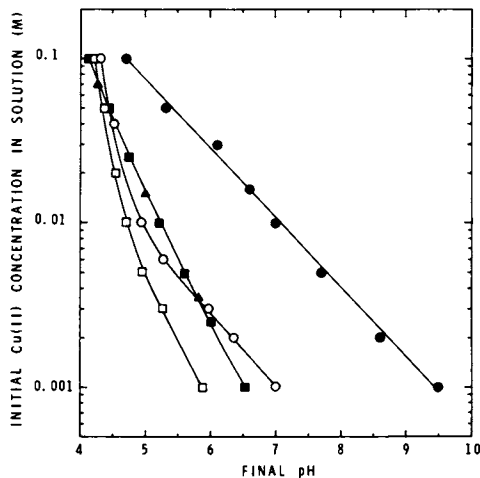
Figure 3.   The final pH of the solutions following ion exchange of (●, ○) Na Y, (■, □) NH₄ Y—89% exchanged, and (▲) NH₄ Y—75% exchanged zeolites by Cu(II) solutions of various concentrations at ambient temperature.   The curves correspond to series of samples prepared with v/m = 20 cm³/g (filled symbols) or 200 cm³/g (open symbols).
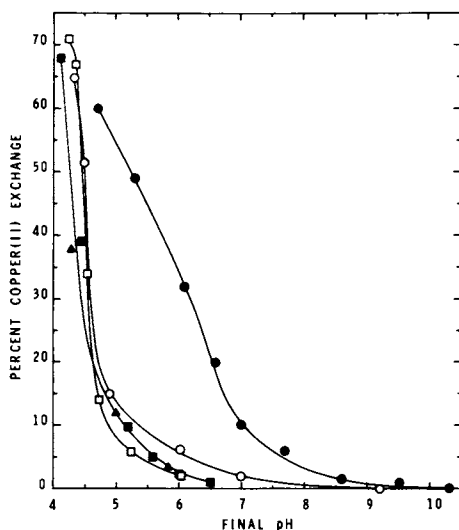
Figure 4.   The percent Cu(II) exchange of (●, ○) Na Y, (■, □) NH₄ Y—89% exchanged, and (▲) NH₄ Y—75% exchanged zeolites as a function of the final solution pH, which was altered by varying v/m from 20 cm³/g (filled symbols) to 200 cm³/g (open symbols) and by varying the Cu(II) solution concentration.

equilibrated with 0.01 M Cu(II) solutions at certain controlled
pH values are presented in Figure 5. The copper and sodium ion
concentrations were determined by atomic absorption following
back-exchange with Ag^+, while the hydrogen cation contents were
calculated by difference, assuming a constant total cation con-
tent of 3.2 meq/g of hydrated Y zeolite. The % copper(II) ex-
change of these samples, given in the order of increasing pH,
are 3.8, 13, 9.8, and 2.1%. Analyses by X-ray powder diffraction
indicated that none of these samples suffered a loss of crystal-
line during the ion exchange treatments.

Discussion

    Ion Exchange. It is evident from Figure 1 and the data pre-
sented in the Results Section that NH_4^+ was easily ion exchanged
into Na Y zeolite. During the short equilibration times used in
this study, the NH_4^+ ions entered the zeolite lattice and were
preferred over Na^+ by the supercage sites. However, these mono-
valent cations did not displace the sodium ions from the sodalite
cages nor from the hexagonal prisms during a single equilibration
at ambient temperature since 18 Na^+ ions per unit cell were not
exchanged. Although it was shown that a dehydrated Na Y zeolite
contained 48% of the cations in the small cages (10), a single
crystal X-ray study of hydrated [Na,Ca] faujasite indicated the
presence of 17 cations in the sodalite cages (11). The present
observations are in agreement with other ion exchange studies,
which showed that equilibration of Na Y with NH_4^+ (12), La^{3+} (13),
and Ca^{2+} (14) at 25°C for 24 h or less did not exchange 16 Na^+
ions per unit cell. Repeated equilibrations with fresh ammonium
nitrate solution did lead to migration of some of the Na^+ ions
out of the small cages and replacement by NH_4^+ ions, and this
process was enhanced by elevated temperatures, as shown by Fig-
ures 1 and 2. All of these highly exchanged NH_4^+ samples were
observed to contain about 200 water molecules per unit cell, in
agreement with a previous report (3), although a higher degree
of hydration was reported elsewhere (4). For comparison, Na Y
zeolites (15) and Cu-Na Y zeolites (16) contain approximately
260 H_2O/unit cell when fully hydrated.
    In comparison with the 68% exchange level achieved by equili-
brating Na Y with 1.0 M NH_4^+, Figure 4 correlated with Figure 3
demonstrates that about the same degree of ion exchange was ob-
tained when Na Y and NH_4 Y-89 zeolites were equilibrated with 0.1
M Cu(II) solutions. The 71% copper(II) exchanged sample corre-
sponds to $Na_6(NH_4)_{10}Cu_{20}$ Y zeolite, while $Na_6(NH_4)_{16}Cu_{17}$ Y repre-
sents the Cu Y-60 zeolite. These results support the proposal
that Cu(II) ion exchange carried out at ambient temperature for
short equilibration periods (less than 24 h) displaces only the
univalent cations in the supercages (16,17). A kinetically con-
trolled slow step follows in which the hydrated ions, where the
hydrated radius of Cu(II) is 0.419 nm (18) and the hydrated
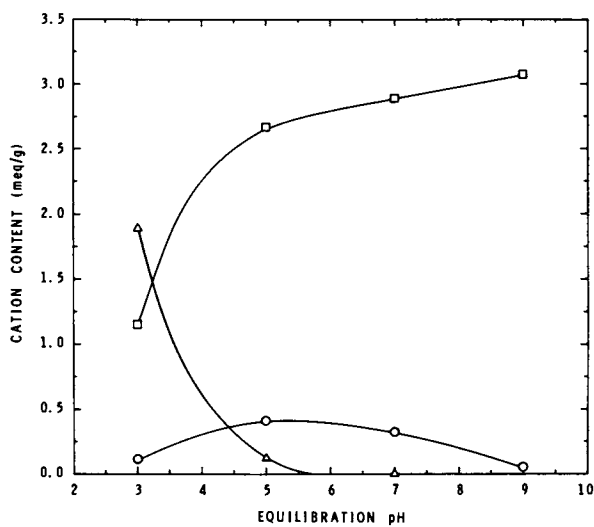
Figure 5.   The exchangeable (□) sodium ion, (○) divalent copper ion, and (△) hydrogen ion content vs pH for Na Y zeolite equilibrated with 0.01M copper(II) nitrate solutions for 4 hr at ambient temperature with v/m = 20 cm³/g.

radius of NH_4^+ is 0.331 nm (19), shed water molecules and pass
through 0.26 nm windows (maximum effective diameter) into the
sodalite cages. This process is enhanced by increasing the equil-
ibration temperature, which yields higher ion exchange levels.

   After the copper(II) ion exchange treatments, the final pH
was observed to be lower, especially at low Cu(II) concentrations,
for the Cu-NH_4 Y exchanges than for the Cu-Na Y exchanges, as
shown in Figure 4. This is due to the prior preparation of the
NH_4 Y zeolites, during which they were in effect prewashed prior
to the Cu(II) ion exchange. The effect was much less noticeable
with v/m = 200 cm^3/g than with v/m = 20 cm^3/g, as would be ex-
pected. This difference in final pH apparently did not influence
the resultant degree of ion exchange at low copper concentration.
This is illustrated by the exchanges carried out using 0.01 M
Cu(II) solution. With v/m = 20 cm^3/g, both the Na Y and the
NH_4 Y zeolites were 10% ion exchanged with Cu(II), while with
v/m = 200 cm^3/g the two zeolites attained 15 and 14% exchange
levels, respectively.

   Copper(II) Exchange at Controlled pH Values. The cation
concentrations displayed in Figure 5 for pH 7 were obtained fol-
lowing an equilibration with 0.01 M Cu(II) solution to which no
acid or base had been added. Therefore, this pH was "naturally"
determined by the balance between copper nitrate concentration
and amount of Na Y zeolite mixed with the solution, as was the
case for the samples that yielded the data in Figure 3. This
balance was altered by the addition of acid or base during the
preparation of the three other samples depicted in Figure 5. As
the acid concentration was increased, the quantity of H^+ ions in
the zeolite also increased.

   The exchange in alkaline medium was achieved by mixing the
two reagents and then gradually increasing the pH to 9. Un-
doubtedly some ion exchange occurred during this process. Fol-
lowing equilibration and filtration, the filtrate was observed
to be clear and colorless while the dried solid was a light tan,
as described previously (16). The cation concentrations de-
picted in Figure 5 were determined by back-exchange with Ag^+. A
quantity of copper was not removed from the zeolite by the Ag^+
back-exchange and was probably present on the zeolite in the form
of CuO, which would be present in the amount of 0.012 g/g of
anhydrous zeolite.

   Routine Preparations. From the discussion of Figure 5, it
can be deduced that it is preferable to carry out ion exchange
of Y zeolite with copper(II) without altering the resultant pH.
The ion exchange process can be controlled by the Cu(II) con-
centration in the equilibration solution, as Figures 3 and 4
demonstrate. Therefore, for a 10% Cu(II) exchanged Na Y zeolite,
a 0.01 M Cu(II) solution can be used with v/m = 20 cm^3/g. The
resultant pH, which connects Figure 3 with Figure 4, is 7.

Similarly, a 0.10 M Cu(II) solution with NH_4 Y (at v/m = 20 cm^3/g) yielded a 68% Cu (II) exchanged sample in a pH 4.15 supernatant.

The volume of solution used per g of zeolite also plays a part in determining the ion exchange level achieved. As pointed out in a previous section, in 0.01 M Cu(II) solution with v/m = 20 cm^3/g, both Na and NH_4 Y zeolites attained a 10% Cu(II) exchange level. Increasing the v/m ratio by a factor of 10 and decreasing the copper concentration to 0.005 M yielded 9% exchanged samples for both Y zeolites. Thus, Figures 3 and 4 can be utilized to prepare Na or NH_4 Y zeolites having a predetermined Cu(II) content by varying a number of experimental parameters.

The approximate linearity of the v/m = 20 cm^3/g plots in Figure 3 is of interest. These data points represent samples that had rather large amounts of zeolite present in comparison to the volume of the solution. In these preparations, the solution pH was determined by the Na Y zeolite but was moderated by the quantity of copper salt initially present. Increasing the solution volume by a factor of 10 yielded curves having an inflection point near a copper concentration of 0.01 M. Below this concentration, the curves are parallel to the corresponding v/m = 20 cm^3/g curves and again reflect the presence of the zeolite. For the more concentrated copper(II) reagent solutions, however, the final pH is determined directly by the salt concentration and not by the zeolite.

Conclusions

The preparative relationships between the degree of ion exchange of Na Y and NH_4 Y zeolites with copper(II) ions as a function of the initial copper(II) solution concentration and the resultant pH after equilibration have been determined. Copper and ammonium ions readily replace sodium ions in the supercages, where the selectivity is Cu(II) > NH_4^+ > Na^+ in the hydrated zeolite. Repeated equilibration of Na Y with NH_4^+ results in some of the Na^+ ions in the small cages being exchanged, and elevated temperatures enhance this replacement. Graphs have been presented that allow the preparation of Cu(II) ion exchanged Na Y or NH_4 Y zeolites having predetermined copper(II) contents.

Literature Cited

1. Uytterhoeven, J. B.; Christner, L. G.; Hall, W. K., *J. Phys. Chem.*, (1965), 69, 2117.
2. Ward, J. W., *J. Catal.*, (1967), 9, 225.
3. Cattanach, J.; Wu, E. L.; Venuto, P. B., *J. Catal.*, (1968), 11, 342.
4. Kerr, G. T., *J. Catal.*, (1969), 15, 200.
5. Lai, P. P.; Rees, L. V. C., *J. Chem. Soc., Faraday Trans. I*, (1976), 72, 1809.

6. Maes, A.; Cremers, A., J. Chem. Soc., Faraday Trans. I, (1975) 71, 265.
7. Lussier, R. J.; Magee, J. S., Jr.; Albers, E. W., U.S. Patent 3.929,621, (Dec. 30, 1975); assigned to W. R. Grace & Co.
8. Dolbear, G. E.; Magee, J.S., U.S. Patent 3.835,032, Sept. 10, 1974); assigned to W. R. Grace & Co.
9. Herman, R. G.; Bulko, J. B., 14th Middle Atlantic Regional Meeting of the American Chemical Society, King of Prussia, PA, April 23-25, 1980, Abstr. No. CSC-9.
10. Eulenberger, G. R.; Shoemaker, D. P.; Keil, J. G., J. Phys. Chem., (1967), 71, 1812.
11. Baur, W. H., Am. Mineralogist, (1964), 49, 697.
12. Sherry, H. S., J. Phys. Chem., (1966), 70, 1158.
13. Sherry, H. S., J. Colloid Interface Sci., (1968), 28, 288.
14. Barrer, R. M.; Davies, J. A.; Rees, L. V. C., J. Inorg. Nucl. Chem., (1968), 30, 3333.
15. Breck, D. W., "Zeolite Molecular Sieves", Wiley, New York, 1974.
16. Herman, R. G.; Flentge, D. R., J. Phys. Chem., (1978), 82, 720.
17. Lai, P. P.; Rees, L. V. C., J. Chem. Soc., Faraday Trans. I, (1976), 72, 1809.
18. Nightingale, E. R., Jr., J. Phys. Chem., (1959), 63, 1381.
19. Chu, P.; Dwyer, F. G., J. Catal., (1980), 61, 454.

Lead and Cadmium Ion Exchange of Zeolite NaA

ELLIOT P. HERTZENBERG and HOWARD S. SHERRY

The PQ Corporation, Research and Development Division, P.O. Box 258,
Lafayette Hill, PA 19444

In recent years the necessity of controlling the heavy metal
content of waste water has become more apparent. This need has
prompted us to study Pb^{2+} and Cd^{2+} ion exchange in the synthetic
zeolite Na-A. There has been no work published on Pb^{2+} ion
exchange in this zeolite and we are only aware of the work of
Gal and coworkers on Cd^{2+} ion exchange of Na-A (1). Gal and
Radovanov (2) and Maes and Cremers (3,4) have also reported work
on Cd^{2+} ion exchange of zeolites Na-X and Na-Y.

A large body of information has been published on polyvalent
ion exchange in zeolites. Examples of alkaline earth ion exchange
in zeolites include studies on ion exchange of Na-A (5),
Na-X (6,7), Na-Y (7,8), zeolite T (9), and erionite (10).
Examples of Ni^{2+}, Co^{2+} and Zn^{2+} ion exchange for Na^+ in zeolites
include exchange of Na-A (1), Na-X (2,3). The work cited above
provides a sampling of the variety of ion exchange behavior
exhibited in these systems.

Also of relevance is trivalent ion exchange typified by the
work done on La^{3+} ion exchange of Na-X and Na-Y (11).

It is the purpose of the work reported herein to compare the
ion exchange of Pb^{2+} and Cd^{2+} for Na^+ in zeolite A to that of
other ions in the same and other zeolites. To further this end,
we have studied these ion exchange reactions as a function of
temperature and different anions.

Experimental Section

All metal salts were reagent grade. Doubly deionized water
was used to prepare the solutions of 0.1N metal ion. The lead
acetate solutions were filtered through a Millipore filter in
order to remove a slight turbidity.

Zeolite Na-A was synthesized in our laboratory. After
crystallization from the sodium aluminosilicate gel, the zeolite
was carefully washed with deionized water in order to remove
occluded impurities without causing H_3O^+ ion exchange. It was
then stored in a desiccator containing saturated NH_4Cl solution.

The zeolite was highly crystalline and contained negligible amounts of crystalline impurities or amorphous material.

Table 1 lists the chemical analysis of the Na-A used in this work.

<u>Table 1</u>

<u>Chemical Analysis of Zeolites Na-A</u>

	% Wt.	Moles/Mole Al_2O_3
Na_2O	17.2	0.98
SiO_2	32.9	1.94
Al_2O_3	28.9	1
H_2O	<u>21.8</u>	
Total	100.8	

The atom ratio of Na/Al in the Na-A was 0.98 and the Si/Al ratio was 0.97. The calculated exchange capacity is 7.0 milliequivalent per gram (meq/g) of anhydrous zeolite.

Phase equilibrium was accomplished by weighing suitable quantities of the sodium form of the zeolite into 125 ml polycarbonate bottles which contained 50 ml of the salt solution. The total salt concentration was 0.100 ($\pm$0.010) N, known to three significant figures. At the high end of the isotherm, the starting solution contained only the ingoing cation; at the low end, the solution contained both of the exchanging cations. The equilibrations were carried out for a minimum of three days in a New Brunswick Scientific Company AQUATHERM Water Bath Shaker at 5°, 25°, and 50°C, with temperature control to $\pm$0.5°C. Prior to analysis of the equilibrium solutions, the solid and solution phases were rapidly separated by filtration through a Millipore filter immediately after removal from the constant temperature bath. Lead and sodium analyses of the filtrate were obtained by atomic absorption spectroscopy. The cadmium analyses of the filtrate were obtained by plasma emission spectroscopy. These analyses showed that two Na^+ ions entered the solution for every Cd^{2+} or Pb^{2+} that left ($\pm$2%).

Results and Discussion

Lead ion-exchange isotherms are plotted in Figures 1 and 2. The data in Figure 1 for the $Pb(NO_3)_2$-Na-A system show that Na-A is extremely selective for Pb^{2+} and that this selectivity increases with temperature over the range of 50°C. Comparison of this system with the $Pb(CH_3COO)_2$-Na-A system (Figure 2) shows
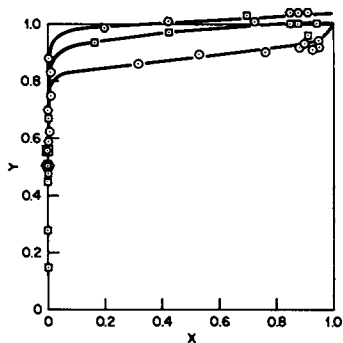
Figure 1. Pb–Na–A system at 0.1 normality: (⊙) NO_3^- at 5°C, (⊡) NO_3^- at 25°C, (⊙) NO_3^- at 50°C
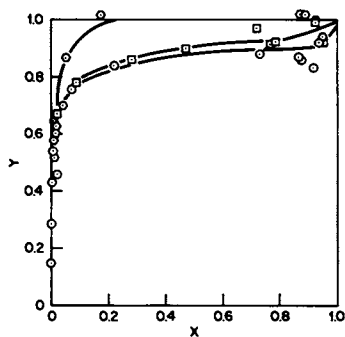
Figure 2. $Pb(CH_3COO)_2$–Na-A system at 0.1 total normality: (⊙) 5°C, (⊡) 25°C, (⊙) 50°C

that the selectivity of Na-A for Pb is greater from nitrate
solution than from acetate solution and that the temperature
effect is similar.

Cadmium ion-exchange isotherms are plotted in Figures 3 and
4. Zeolite Na-A is selective for Cd^{2+} over Na^+ ion but Pb^{2+} ion
is preferred to an even greater degree. Just as in the case of
Pb^{2+} exchange, Na-A removes more Cd^{2+} from a nitrate solution
than from the corresponding acetate solution. The temperature
dependence of Cd^{2+}-Na^+ ion exchange is negligible within the
precision of our experimental data.

We have used the phase distribution data shown in Figures
1-4 to calculate the standard free energies of the ion exchange
reaction using a simplified version of the equation of Gaines
and Thomas (12).

$$logK = -\frac{1}{2.303} + \int_0^1 logK_c' \, dY \qquad (1)$$

This equation states that the logarithm of the equilibrium
constant, K, can be determined by integrating the area under a
plot of the corrected selectivity coefficient, K_c, versus
loading of the heavy metal ion, Y. The selectivity coefficient
is defined as follows:

$$K_c = \frac{Y(1-X)^2}{(1-Y)^2 X} \cdot 2N_T = \frac{Y \cdot M_{Na}^2}{(1-Y)^2 M_{M^{2+}}} \qquad (2)$$

where K_c = the selectivity coefficient

Y = equivalent fraction of the
heavy metal in the zeolite

X = normality of the heavy metal
ion in solution/total normality

N_T = total normality of the solution

M = molality of the ions in solution

This selectivity coefficient is related to the equilibrium
constant, K, by the equation

$$K = K_c \cdot \frac{f_{M^{2+}}}{f_{Na}^2} \cdot \frac{\gamma_{Na}^2}{\gamma_{M^{2+}}} \qquad (3)$$
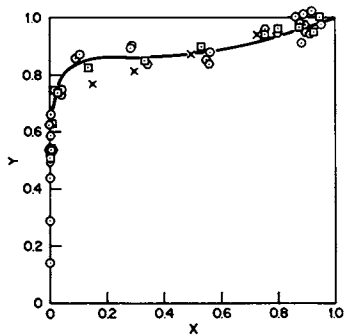
Figure 3.   Cd(NO₃)₂–Na-A system at 0.1 total normality: (⊙) 5°C, (▣) 25°C, (⬡) 50°C, x–x Cl⁻ at 25°C
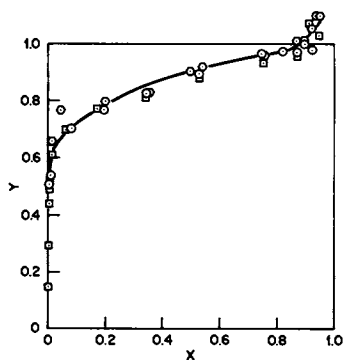
Figure 4.   Cd(CH₃COO)₂–Na-A system at 0.1 total normality: (⊙) 5°C, (▣) 25°C, (⊙) 50°C

The corrected selectivity coefficient is related to the equilibrium constant and the selectivity coefficient by:

$$K = K_c' \cdot \frac{f_{M^{2+}}}{f_{Na}^2} \tag{4}$$

$$K_c' = K_c \cdot \frac{\gamma_{Na}^2}{\gamma_{M^{2+}}} \tag{5}$$

$$K_c = K_c \cdot \frac{\gamma_{NaX_\pm}^4}{\gamma_{MX_{2\pm}}^3} \tag{6}$$

In equation 3 the terms of f_{Na^+} and $f_{M^{2+}}$ are the rational activity coefficients of exchanging cations in the zeolite phase and the terms γ_{Na^+} and $\gamma_{M^{2+}}$ are the molal single ion activity coefficients in the solution phase. Equation 4 can be rewritten as equation 5 when the two salts, NaX and MX_2 have a common anion. The mean molal activity coefficients usually can be estimated from literature data. The corrected selectivity coefficient includes a term that corrects for the non-ideality of the solution phase. Thus any variation in the corrected selectivity coefficient is due to non-ideality in the zeolite phase (see equation 3).

We have plotted in Figures 5-8 the rational selectivity coefficient, $K_{R.C.}$, vs. heavy metal ion loading, Y. The rational selectivity coefficient for di-univalent ion exchange is defined as

$$K_{R.C.} = \frac{Y(1-X)^2}{(1-Y)^2 X} = K_c' \cdot \frac{1}{2N_T} \cdot \frac{\gamma_{MX_{2\pm}}^3}{\gamma_{NaX_\pm}^4} \tag{7-a}$$

$$K_c' = K_{R.C.} \cdot 2N_T \cdot \frac{\gamma_{NaX_\pm}^4}{\gamma_{MX_{2\pm}}^3} \tag{7-b}$$
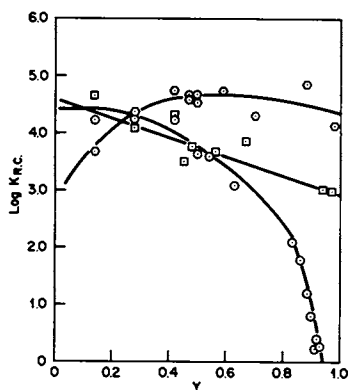
Figure 5.   *Rational selectivity coefficient vs. Pb²⁺ ion exchange from NO₃⁻ solution: (⊙) 5°C, (□) 25°C, (⟡) 50°C*
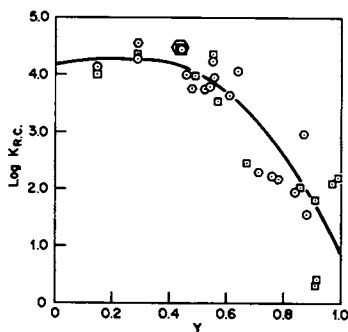
Figure 6.   *Rational selectivity coefficient vs. Pb²⁺ ion exchange from CH₃COO⁻ solution: (⊙) 5°C, (□) 25°C, (⟡) 50°C*

Figure 7. Rational selectivity coefficient vs. Cd²⁺ ion exchange from NO₃⁻ solution: (⊙) 5°C, (□) 25°C, (◇) 50°C
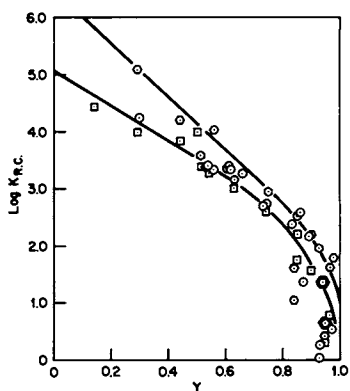
Figure 8. Rational selectivity coefficient vs. Cd²⁺ ion exchange from CH₃COO⁻ solution: (⊙) 5°C, (□) 25°C, (◇) 50°C
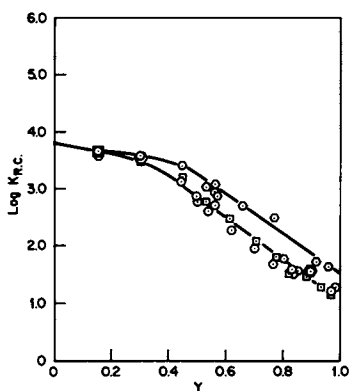
Substituting equation 7-b into equation 1 gives

$$\log K = -\frac{1}{2.303} + \log 2N_T \frac{\gamma_{NaX^+}^4}{\gamma_{MX_{2+}}^3} + \int_0^1 K_{R.C.} \, dY \qquad (8)$$

where the solution phase activity coefficient term is assumed independent of Y. The plots in Figures 5-8 have been used to evaluate the integral in equation 8 where a reasonable estimate of the activity coefficient term for the solution phase could be made. Standard free energies have been calculated from the equations

$$\Delta_{G^\circ_T} = -2.303RT \log K \text{ kilojoules/equiv}$$

These data are shown in Table 2.

Table 2

Standard Free Energies of Reaction

Reaction	ΔG_T, Kj/equiv		
	278°K	298°K	323°K
Cd^{2+} + 2Na-A	-10.4	-6.86	-6.40

Enthalpies of reaction have not been calculated because in most cases our data are not sufficiently accurate to differentiate between 5° and 25°C. However, the data clearly show that Na-A becomes more selective for Pb^{2+} and Cd^{2+} with increasing temperature.

Our isotherms also show that Na-A removes more Pb^{2+} and Cd^{2+} from nitrate solutions than from acetate solutions. If the data of Gal and coworkers (1) for the $CdCl_2$ + Na-A reaction is also used, the selectivity of Na-A for Cd as a function of coion exhibits the series

$$NO_3^- > CH_3COO^- > Cl^-$$
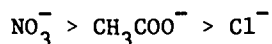
This sequence follows the inverse of the sequence of the degree of complexation of Cd^{2+} by the coions (13) as shown in Table 3.

<p align="center">Table 3</p>

<p align="center">Complexation of Lead and Cadmium</p>

		Formation Constant	
Metal	Anion	$\log\beta_1$ *	$\log\beta_2$ **
Pb	OH^-	7.82	10.85
	CH_3COO^-	2.52	4.00
	Cl^-	1.62	2.44
	NO_3^-	1.18	–
Cd	OH^-	4.17	8.33
	Cl^-	1.95	2.50
	CH_3COO^-	1.5	2.3
	NO_3	0.40	–

$$\text{* } M^{2+} + A^- = MA^+ \qquad \beta_1$$

$$\text{** } M^{2+} + 2A^- = MA_2 \qquad \beta_2$$
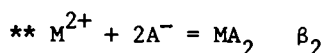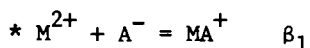
We have obtained part of a $CdCl_2$–Na-A ion-exchange isotherm in 0.1N solution at 25°C to check the results obtained by Gal and coworkers (1). These data, shown in Figure 3 as crosses, indicate that the preference of Na-A for Cd^{2+} ions varies with coion according to the series

$$NO_3^- > CH_3COO^- \cong Cl^-.$$
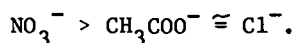
We cannot explain why we find that Na-A exhibits a higher selectivity for Cd^{2+} in the Cl^- system than Gal (1) found. Perhaps this difference relates to the difference in our batches of zeolite.

The standard free energies measured for the reaction

$$M^{2+}(sol) + 2Na^+(zeol) = M^{2+}(zeol) + 2Na^+(sol)$$
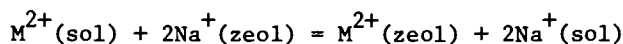
should be the same no matter which heavy metal salt is used, because in the Gaines & Thomas approach (12) corrected selectivity coefficients are used. We are not able to demonstrate that we obtain the same standard free energies in the nitrate and acetate system because no data are available on the mean molal activity coefficients of $Cd(CH_3COO)_2$ and $Pb(CH_3COO)_2$. We expected that Gal and coworkers (1) would obtain the same value for the standard free energy for Cd^{2+} exchange of Na-A at 298°K as we did. Our value is -6.86Kj/equiv and theirs is 4.56Kj/equiv. We cannot rationalize this difference. However, it is clear that our values for the standard free energies of exchange and those of Gal (1) are quite uncertain because of complexation.

It is not likely that acetato or nitrato complexes of Cd^{2+} and Pb^{2+} will diffuse into zeolite A, because CH_3COO^- and NO_3^- are too large. Barrer and Meier (14) have shown that zeolite A does not occlude salt molecules during aqueous ion exchange. They had to use a fused salt system to enable $AgNO_3$ to diffuse into Na-A. Furthermore, even on a selectivity basis it is likely that simple divalent cations are strongly preferred to the complex monovalent cations. Thus the exchange reaction can be thought of as a competition for Cd^{2+} and Pb^{2+} ions between the fixed negative charges in the zeolite phase and the mobile, negatively charged ligands in the solution phase.

It is worth noting that, although we show points on our ion exchange isotherms indicating greater than 100% Pb^{2+} and Cd^{2+} ion exchange, we believe that within our experimental error two Na^+ ions were replaced with one Cd^{2+} or Pb^{2+} ion. We are aware that McCusker and Seff (15) have reported considerable "over-ion exchange." However, they used crystals of Na-A prepared by Charnell's method (16) and did not chemically analyze them. Basler and Malwald (17) have recently shown that Na-A crystals prepared by Charnell's method have considerable amounts of aluminum occluded in the supercages of the zeolite as well as in the sodalite cages, probably as sodium aluminate (they found Si/Al atom ratios as low as 0.88). This excess aluminum could give rise to considerable excess ion-exchange capacity. Basler and Malwald also showed that Na-A, synthesized by the standard method, contained only small amounts of excess aluminum in the sodalite cages and that this material had an Si/Al ratio of 0.98-0.97. Thus we feel that only a small amount of over-exchange could occur in our case.

Abstract

Lead and cadmium ion exchange of zeolite Na-A has been studied as a function of coion and temperature. It is found that the zeolite is very selective for these ions and that this selectivity is greater in nitrate solutions than in acetate solutions. The temperature dependence of the ion exchange reaction is small but distinguishable in the case of Pb^{2+} and too small to observe in the case of Cd^{2+}.

Literature Cited

1. Gal, I. J., Jankovic, O., Malcic, S., Radovanov, P., and Fodorovic, M., J. Chem. Soc., Far. Trans., 1971, 67, 999.
2. Gal, I. J., and Radovanov, P., J. Chem. Soc., Far. Trans., 1975, 71, 1671.
3. Maes, A., and Cremers, A., J. Chem. Soc., Far. I, 1975, 71, 265.
4. Rosolovskaza, E. N., Topchieva, K. V., and Dorozkho, S. P., Zhur. Fiz. Khimii, 1977, 51, 1469.
5. Sherry, H. S., and Walton, H. F., J. Phys. Chem., 1967, 71, 1457.
6. Barrer, R. M., Rees, L. V. C., and Shamsuzzoho, J. Inorg. Nucl. Chem., 1966, 28, 629.
7. Sherry, H. S., J. Phys. Chem., 1968, 77, 4086.
8. Barrer, R. M., Davies, J. A., and Rees, L. V. C., J. Inorg. Nucl. Chem., 1968, 30, 3333.
9. Sherry, H. S., "Proc. Intern. Conf. Ion Exchange in the Process Industries," London, July 1969, 1970, 329.
10. Sherry, H. S., Clays and Clay Minerals, 1979, 27, 231.
11. Sherry, H. S., J. Col. and Inter. Sci., 1968, 28, 288.
12. Gaines, G. L. Jr., and Thomas, H. C., J. Chem. Phys., 1953, 21, 714.
13. "Langes' Handbook of Chemistry," twelfth ed., J. A. Dean, Ed., McGraw-Hill, Co., N.Y., 1972.
14. Barrer, R. M., and Meier, W. M., J. Chem. Soc., 1958, 299.
15. McCusker, L. B., and Seff, K., J. Am. Chem. Soc., 1978, 100, 5052.
16. Charnell, J. F., J. Cryst. Growth, 1971, 8, 291.
17. Basler, W. D., and Malwald, W., J. Phys. Chem., 1979, 83, 2148.

Liquid Phase Drying Applications of Zeolites

GEORGE W. YOUNG, JOSEPH R. KIOVSKY, and PRAMOD B. KORADIA

Norton Company, P.O. Box 350, Akron, Ohio 44309

A major application of synthetic and natural zeo-
lites is in dehydration processes. However, much of
the published work has been concentrated on the drying
of either gases or liquid paraffinic hydrocarbons,
while relatively little published information exists
on commercial application of zeolites for dehydration
of other liquid feedstocks.

Hales (1) mentions some of the non-paraffinic
organic fluids that may be dried with zeolitic desic-
cants but he gives few qualitative details. Dexant
(2) provides some information on co-adsorbing species
for dehydration of alcohols and aldehydes over small-
port zeolites (3A, 4A, 5A). Although most liquid dry-
ing studies have used the small-port zeolites to pre-
vent co-adsorption, Koradia and Kiovsky (3) have
reported on the drying of some chlorinated hydrocarbons
using mordenite and have found commercially acceptable
adsorption capacities.

In many processes (e.g. polymerizations, catalytic
reactions) even trace amounts (< 50 ppm) of water can
cause problems and the only practical solution for de-
hydration of these liquids is the use of an appropriate
zeolite. For example, Stannet et al. (4) report on
the use of molecular sieves to dehydrate liquid vinyl
monomers prior to radiation-induced ionic polymeriza-
tion.

Very often the liquids to be processed may be con-
taminated with substances detrimental to some types of
zeolites; consequently a complete knowledge of the
process stream composition and physical properties must
be available before preliminary sieve selection can
be made. In the absence of prior knowledge of sep-
aration factors, competitive co-adsorption, environ-
mental stability, regeneration techniques, or irre-
versible zeolite contamination, zeolite contamination,
zeolite specification must be proceded by time-con-

suming experimental work. In only a few cases is it
possible to extrapolate from different liquid types
to make engineering estimates, but detailed specific
designs must be based on experimental verification.
    In this paper we intend to demonstrate the process
of zeolite selection for the dehydration of two dif-
ferent liquids of significant commercial importance,
80 ppm water in benzene contaminated by HCl, and 1200
ppm of water in 1,4 butanediol. We will present the
experimental data obtained from both static feasibility
and dynamic design testing and make a comparison among
these systems and earlier work on the liquid phase
drying of chlorinated hydrocarbons.

Experimental

    The experimental work can conveniently be classi-
fied into four major categories: (a) Static equi-
librium Testing; (b) Dynamic Equilibrium Testing;
(c) Regeneration Technique Investigation; (d) Oper-
ational Stability.
    The static testing served primarily as a feasi-
bility study to determine if the proposed dehydration
could in fact be carried out as a practical process.
Static tests were performed by putting preweighed
amounts (0.1-5 gm) of freshly activated zeolite into
sealed vessels containing approximately 50 ml of the
test liquid. A vessel containing only the test liquid
was also prepared for use as an experimental blank.
The sealed vessels were allowed to sit for approxi-
mately five days to attain equilibrium and the rate
of dehydration observed by monitoring the liquid phase
water concentration as a function of time.
    In this manner, it was possible to investigate the
efficiency of various types of zeolite with a partic-
ular liquid system and also to investigate the effect
of equilibrium water concentration on static adsorp-
tion capacity.
    For the benzene test program, three primary benzene
solutions were prepared: one was fully saturated with
water, another was saturated with water and hydro-
chloric acid, and the third solution was only partially
saturated. These primary solutions were mixed in
various proportions to provide a wide range of concen-
trations for the static tests.
    The butanediol-water solutions were much easier to
prepare because of complete miscibility; due to the
hygroscopic nature of butanediol it was necessary to
keep all solutions under a dry nitrogen blanket.

The water analyses were carried out using an automatic Karl Fischer titrator (Aquatest II) and normally no problems were encountered. However, for the benzene-water-hydrochloric acid system, the acid strongly interfered with the water analyses. With a slight modification of operating procedure, reasonably satisfactory, but low precision, results were obtained. For these analyses, the sample was introduced into the analyzer by injection with the syringe needle below the surface of the vessel solution and every benzene injection was preceded by a 100 μl methanol sample. In addition to this procedure, the reagent solutions were replaced every ten to twelve hours.

Dynamic testing was carried out using the equipment shown schematically in Figure 1. The test liquid was pumped from the reservoir R1 using a peristaltic pump and passed through the adsorption bed contained in a stainless steel tube. For each of the initial dynamic runs, the bed was loaded with freshly activated zeolite (0.16 cm pellets) and when operational stability was being investigated, regeneration could be accomplished in situ.

The adsorption bed could be operated vertically or horizontally and was surrounded by a muffle furnace for the regeneration studies. Various lengths of bed were employed and the adsorbent in the bed was supported at both ends with porcelain saddles.

When operated in a horizontal mode, inlet and outlet risers were located at S1 and S2 to insure complete flooding of the adsorption bed. Septa at S1 and S2 also provided access for inlet or outlet liquid samples that could be analyzed. When regeneration studies were being performed, an internal thermocouple was used to monitor the adsorption bed temperature and the dry nitrogen regeneration gas was passed through the bed by switching valve V1.

For preliminary regeneration studies, differential thermal analyses (DTA) were carried out using a duPont 990 instrument. The temperature rise rate was usually $10°C$/minute and the sample was purged with dry nitrogen at 10 sccm. Gas chromatographic studies performed on the benzene system employed a Hewlett Packard 5840A instrument equipped with a 1/8" x 6' column packed with Chromosorb 101 at $180°C$ and with 25 sccm helium flow; detection was by thermal conductivity and the gas sample (from nitrogen regeneration) was introduced by a heated automatic gas sample valve. For these studies, some zeolite that been saturated with the benzene-water mixture, was loaded into a micro-desorption bed (0.6 cm diameter) contained within a heated valve compartment of the
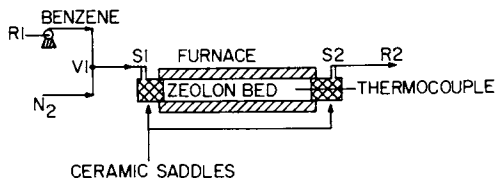
Figure 1.   Schematic of dynamic adsorption test equipment
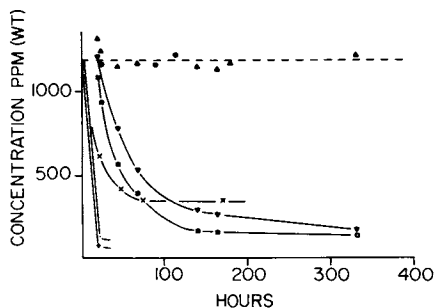
Figure 2.   Static adsorption test for preliminary Zeolon screening for butanediol–water system: (▲) blanks, (⊙) 5 g Z200H, (▣) 5 g Z500, (▼) 5 g Z900Na, (•) 5 g Z500 powder with agitation, (+) 5 g Z500 pellets with agitation,(X) 1 g Z500 with agitation

chromatograph and a nitrogen purge (< 100 sccm) was
used for desorption.

Static Testing.

The dehydration of the water-butanediol system
was investigated using three different zeolites:
Zeolon   200H (Z200H), Zeolon 900 Na (Z900Na) (both
synthetic large port mordenites), and Zeolon 500 (Z500)
(a natural chabazite-erionite). The approach to
static equilibrium for these zeolites is shown in
Figure 2.
A surprising result from this test was the behav-
ior of Z200H, which showed essentially no dehydration
effect. This was surprising since Z900Na, which is
also a large port mordenite, demonstrated good selec-
tivity for water adsorption. Gehrhardt and Kyle (5)
claim that the effectiveness of natural zeolites as
drying agents is due to a sieving effect as well as a
strong affinity for water. While this may be true
for small-port zeolites (3A or 4A) in a system where
the organic component has a large effective molecular
diameter compared to the sieve port size, we cannot
claim such a sieving effect with the butanediol-water
system over any of the tested zeolites. Rather, we
are most likely dealing with relative adsorption
affinities of the organics and water for the particular
zeolite structure as commented on by Satterfield and
Cheng (6).
In light of this argument, the completely dif-
ferent behavior of Z200H and Z900Na with butanediol-
water can readily be explained by the presence of
strong hydrogen bonding forces between the diol oxygen
atoms and the zeolitic hydrogen of Z200H; consequently
there is no preferential adsorption of water. On the
other hand there would be no hydrogen bonding with
Z900Na and the natural preference of zeolites for
water results in the desired dehydration.
As might be expected, static tests are severely
hindered by diffusional resistances; thus, when the
test is carried out with agitation, the approach to
equilibrium is much more rapid. No attempt was made
to obtain static equilibrium capacity data. However,
it was apparent from the data in Figure 2 that either
Z900Na or Z500 could be used to commercially dehydrate
butanediol. From the practical viewpoint, Z500, be-
ing much less expensive than Z900Na, was selected for
regeneration and dynamic equilibrium testing.
For the benzene-hydrochloric acid-water system
there was no point in screening several zeolites for

TABLE I

BUTANEDIOL (BDO) WATER (H_2O)

DIFFERENTIAL THERMAL ANALYSES RESULTS

Zeolon	Adsorbates	Peak 1 Temp, °C	Peak 2 Temp, °C	Peak 3 Temp, °C	Peak 4 Temp, °C
Z500	Water	160 (L ENDO)	-	-	-
Z500	BDO-H_2O	175 (L ENDO)	240 (S ENDO)	330–400 (L EXO)	-
Z500	BDO-H_2O Regenerated at 400°C for 2 hrs	160 (S ENDO)	-	-	-
Z500	BDO-H_2O Regeneration 316°C for 2 hrs	170 (S ENDO)	-	470 (M EXO)	-
Z500	BDO-H_2O Regenerated by H_2O Wash followed by 200°C for 2 hrs	160 (M ENDO)	-	350 (L EXO)	-
Z500	BDO-H_2O Regenerated H_2O wash followed by 400°C for 2 hrs	180 (S ENDO)	-	-	-
Z500	BDO-H_2O Regenerated at 200°C for 2 hrs	160 (S ENDO)	240 (S ENDO)	350 (L EXO)	-
Z200H	BDO-H_2O	80 (S ENDO) 160–180 (L ENDO)	230 (S ENDO)	310 (L EXO)	520 (M EXO)
Z200H	BDO-H_2O Regenerated at 400°C for 2 hrs	120 (S ENDO)	-	280 (S EXO)	550 (M EXO)
Z200H	BDO-H_2O Regenerated at 200°C for 2 hrs	150 (S ENDO)	300 (L EXO)	300 (L EXO)	520 (M EXO)

L = Large Peak   ENDO = Endothermic
M = Medium Peak   EXO = Exothermic
S = Small Peak

process suitability, since the presence of the acid
environment demanded the use of highly acid-resistant
zeolite Z200H.

Since benzene is not likely to undergo hydrogen
bonding, it was expected that Z200H would be suitable.
There was, however, some uncertainty about the selec-
tive adsorption of the water over the acid, so some
very preliminary static equilibrium capacity data
were generated.

Figure 3 shows the results obtained for the ben-
zene-water system and compares these with the results
from the benzene-water-hydrochloric acid system. The
acid-free system exhibited the almost linear adsorp-
tion isotherm expected at low water concentrations,
while the data from the acid system, although some-
what scattered, suggest that the adsorption capacity
was increased when some HCl was present. In any case,
the feasibility of using Z200H to dehydrate the ben-
zene-hydrochloric acid system was demonstrated, and
justified embarking on regeneration and dynamic
equilibrium test studies.

Regeneration Testing.

To investigate the desorption characteristics of
water and butanediol several differential thermal
analyses (DTA) were performed on samples of Z500 and
Z200H that had been previously saturated with water,
butanediol, or both. Other samples that had been re-
generated by a variety of techniques were also studied.
Table I summarizes the results obtained from this
work. Z200H was examined, in part, to determine if,
in fact, there was significant adsorption of both
components.

The water desorption from Z500 was characterized
by a large endotherm appearing at approximately 160°C.
With butanediol and water present (Figure 4), this
endotherm was shifted slightly to 175°C and a second
small endotherm was observed at 240°C. Also, a large
exotherm appeared at about 330-400°C. Since the de-
sorption of a physically adsorbed species should
produce an endotherm, it is apparent that the exotherm
must be associated with some molecular rearrangement.
The most likely explanation is the cyclization
reaction of butanediol to produce tetrahydrofuran.

Figure 4 also shows the DTA curve from water and
butanediol adsorbed on Z200H. In addition to the
water endotherm at approximately 160-170°C, the small
endotherm at 230°C and the exotherm at 310°C, there
is also a second endotherm at 520°C and a small endo-

Figure 3. Static adsorption equilibrium tests on Z200H: (⊙) benzene–water system, (⊡) benzene–water–HCl system
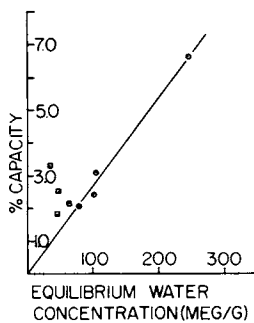
Figure 4. Differential thermal analysis results: (1) benzene–water–HCl on Z200H, (2) butanediol–water on Z500, (3) butanediol–water on Z200H
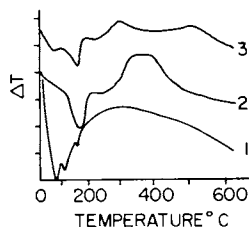
Figure 5. Desorption rates from Z200H during regeneration: (⊙) water, (⊡) benzene
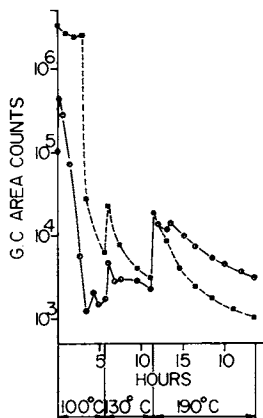
thermic shoulder at 80°C. The increased complexity
of this DTA curve, while not yet fully understood,
gives some qualitative evidence for the greatly en-
hanced adsorption of butanediol on Z200H in compari-
son to Z500.

Several regeneration schemes were investigated and
DTA analyses were run on the regenerated samples. In
all cases, regeneration was carried out by passing dry
nitrogen through the heated bed for a specified time.
In some cases, this nitrogen stripping was preceded
by washing the spent sieve at room temperature with
water. Regeneration at 200°C was ineffective in that
although some water was removed, the organic was not
desorbed, while using the normally recommended re-
generation temperature of 316°C produced only slight
removal of the organic. However, after two hours at
400°C, either with or without prior water washing, the
sample of Z500 seemed to be completely regenerated.
This suggests that steam stripping prior to nitrogen
stripping may not be necessary. In contrast to these
results with Z500, regeneration of Z200H at 400°C was
not effective.

The DTA results for the benzene-water-hydrogen
chloride system are summarized in Table II and appear
to be much less complex than the butanediol results.
HCl desorbs at approximately 65°C, water desorbs at
approximately 120°C and benzene desorbs from 150-220°C.
A typical DTA curve is shown in Figure 4. These re-
sults suggest that it should be possible to regenerate
at low temperature (<200°C) and so help minimize any
of the zeolite-catalyzed reactions of benzene. Goto
et al. (7) report a regeneration scheme of three hours
at 500°C for their study of the benzene-water system.
However, they used a small-port (4A) zeolite which
may have excluded the benzene from adsorption.

To further investigate the regeneration, a micro-
regeneration system was set up. A sample of Z200H
with adsorbed benzene, HCl, and water was purged with
dry nitrogen and the effluent periodically analyzed.
Initially the system was maintained at 100°C for five
and one half hours, then the temperature was raised
in two stages to 190°C. Figure 5 shows how the con-
centration of benzene and water in the purge gas
changed with time during this regeneration. The free
liquid is quickly removed and then adsorbed benzene
and water desorb, the amount desorbing showing expo-
nential decay at constant temperature. This figure
clearly shows that benzene is the major adsorbate on
the Z900H.

TABLE II

BENZENE HCl WATER DIFFERENTIAL THERMAL ANALYSIS RESULTS

ON Z200H

Adsorbate	Peak 1 Temp, °C	Peak 2 Temp, °C	Peak 3 Temp, °C
Water	-	125 (ENDO)	-
HCl	60 (ENDO)	-	-
Benzene-Water	-	120-220 (Broad ENDO)	-
HCl-Water-Benzene	75 (ENDO)	110 (ENDO)	160 (ENDO)

A typical chromatogram showed five or six peaks in addition to those produced by nitrogen, water and benzene. Although these other peaks were not identified, but were not a result of contamination from either the liquid or zeolite, they illustrated that zeolite-catalyzed reactions of benzene were occurring.

Dynamic Testing.

The pioneering work of Michaels (8) in developing the concept of a mass transfer zone (MTZ) for ion exchange processes has led to the simplified design techniques currently employed for molecular sieve driers. Michaels suggested that during the initial period of an ion exchange process, a zone was established in the bed wherein all of the ion exchange between the fluid and solid phases occurred.

He considered this zone to show characteristic concentration profiles in both phases, and subsequently suggested that once the zone was fully established, it would move at a uniform velocity along the bed, provided the fluid velocity and inlet concentration were constant.

In dynamic testing, by monitoring the effluent fluid for the adsorbing components, the concentration profile in the mass transfer zone (known as the breakthrough curve) and the MTZ length can be determined. Also, the equilibrium adsorption capacity of the adsorbent can be determined under the proposed operating conditions. These data, obtained from small-scale laboratory units, can then be used to design commercial-size driers. Typically, the breakthrough curve is an almost symmetrical sigmoid, indicating that in the mass transfer zone only about 50% or less of the equilibrium adsorption capacity of the sieve, based on the initial adsorbent concentration, is used.

The results of the dynamic testing with the butanediol-water-Z500 are given in Table III. The majority of the runs were made with a 23 cm bed length and at a superficial linear velocity of 0.5 cm/minute. The equilibrium capacity was found to be approximately 8.5 grams of water/100 grams of fresh Z500, and this capacity seemed independent of the water concentration in the range of 480-1200 ppm water. However, the MTZ was determined to be in the range of 100-165 cm, indicating that the mass transfer zone was much larger than the entire adsorption bed. Figure 6 shows a typical breakthrough curve obtained during these dynamic tests. This curve shows significant

TABLE III

DYNAMIC TEST RESULTS

BUTANEDIOL-Z500

Run	Zeolon 500, gms	Bed Length cm	Flow Rate cc/min	SLV cc/min	Inlet Water ppm	Equilibrium Capacity, %	MTZ cm	Equilibrium Time, min
1	68.0	61	1.0	0.51	1207	8.2	115	10200
2	66.0	58	2.3	1.17	1080	8.6	107	2390
3	24.8	23	1.0	0.51	1090	7.8	165	12500
4	24.0	23	1.0	0.51	480	9.1	85	15000
5	24.8	23	1.0	0.51	1240	8.7	99	7350

departure from the classical sigmoid curve normally
encountered in drying studies with zeolites,even under
laminar flow (5), In this present case, after an
initial rapid rise, the curve flattens out and the
outlet water concentration very slowly approaches the
inlet value.

Similar results, summarized in Table IV, were
obtained from the dynamic tests on the benzene-water-
hydrochloric acid system. This time, the bed length
was 0.3 cm/min (Reynolds Number, Re_p = 0.003), the
water concentration was approximately 80 ppm and the
superficial linear velocity was 15.3 cm/min (Re_p =
12.5). The acid concentration varied from 600-3000
ppm and at higher concentrations of HCl, the equilib-
rium capacity for water may be reduced. The estimat-
ed water capacity for 80 ppm water in benzene with
approximately 2000 ppm HCl is 7.8 grams of water/100
grams of Z200H. There may be a slight decline in
adsorption capacity after four regeneration cycles,
but these data are confounded with the HCl concen-
tration. The MTZ length was determined to be in the
range of 60-170 cm, again substantially greater than
the entire adsorption bed. Even though these experi-
ments were conducted at high Re_p, the typical break-
through profile, Figure 7, was similar in shape to
that observed during the butanediol tests. Thus,
after the initial rapid increase, the effluent water
concentration leveled out and only slowly progressed
to equilibrium. The greater scatter of the data
shown in Figure 7 highlights the difficulties encount-
ered during the analysis of waer in the presence of
hydrochloric acid.

A non-classical breakthrough has been observed
before by Koradia and Kiovsky during their work on
the drying of dichloropropane and dichlorobenzene
with Z200H. On the other hand, Goto and his coworkers
studied the drying of benzene over a 4A zeolite, at a
linear velocity of 7.0 cm/min (Re_p = 6.2) but at a
concentration of 665 ppm, and found an approximately
symmetrical breakthrough curve and a MTZ length of
10.3 cm. However, they also reported data for the
dehydration of ethanol over a 4A zeolite (Re_p = 2.5)
and found a non-symmetrical breakthtough curve, a
mass transfer zone length of 181 cm and capacities of
approximately 5%. Although they do not show the
breakthrough curve from the ethanol dehydration,
they do report a value of 0.37 for the fractional
ability of the mass transfer zone to adsorb solute;
a value of 0.5 represents symmetry. It is also
worth noting that the MTZ length for this system
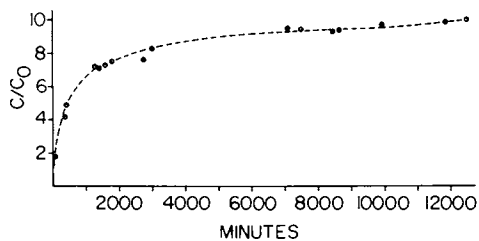
Figure 6.   Breakthrough curve for the butanediol–water–Z500 system
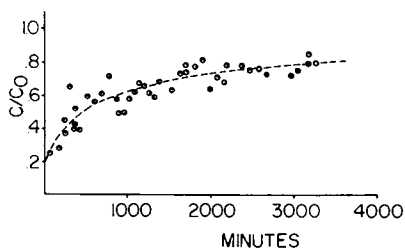
Figure 7.   Breakthrough curve for the benzene–water–HCl–Z200H system

TABLE IV

DYNAMIC TEST RESULTS

BENZENE Z200H

Run	Zeolon gms	Bed Length cm	Flow Rate cc/min	SLV cc/min	Inlet Water ppm	Inlet HCl ppm	Equilibrium Capacity, %	MTZ cm	Equilibrium Time, min
1	34.7	30.5	30.0	15.3	78.0	2000	8.8	62	3627
2	34.7	30.5	30.0	15.3	89.0	2513	7.0	115	2640
3	34.7	30.5	30.0	15.3	80.0	580	7.5	176	5460
4	34.7	30.5	30.0	15.3	72.3	3108	6.1	129	3687

was longer than the length of the adsorption
bed.

Koradia and Kiovsky attributed their non-symmet-
rical breakthrough curve to the presence of non-dis-
solved water, finely dispersed water droplets which
were present as a result of the way in which they pre-
pared their test solutions. While they may have had
a heterogeneous liquid mixture, their explanation can-
not be applied to the present cases of butanediol or
benzene.

For these cases, it is more likely that the dis-
placement of adsorbed organic by water is the control-
ling rate process (9, 10). This would also appear to
be the case in some of the studies reported by Goto
(7) where competitive co-adsorption was obviously
occurring (ethanol over 4A). In the absence of the
co-adsorption phenomenon, as for the case of benzene
drying over 4A (7), symmetric breakthrough is observed
along with small MTZ and high capacities.

Practical Drier Design

Several important aspects of practical drier
design have been covered in this article, and it is
worthwhile summarizing them and their implications.
First, the zeolite selection process has demonstrated
the need for a case-by-case examination based on fluid
characteristics and economic considerations. Con-
sequently, the choice of Z200H for the benzene-hydro-
chloric acid application and the chlorinated hydro-
carbon drying (3) was made because of the acid nature
of these fluids. On the other hand, the choice of
Z500 for butanediol drying was made because of strong
competitive co-adsorption (H-bonding) on Z200H and
the lower cost of Z500 compared to Z900Na.

Second, the length of the mass transfer zone and
the dynamic equilibrium capacity are greatly influenc-
ed by the presence of competitive co-adsorption which
appears to produce a very long zone (up to 180 cm)
with a non-symmetrical breakthrough profile and a
capacity of 5-10%. This type of behavior was observed
in the studies of benzene and butanediol drying re-
ported here and in the Series II studies of 1,2 dichlo-
ropropane reported by Koradia and Kiovsky where they
observed an MTZ length of 80-90 cm with a capacity
of 5-7%. Co-adsorption of ethanol on 4A produced an
MTZ length of 180 cm and reduced the equilibrium
capacity to 5-6% (7). However, co-adsorption is not
the only cause of long mass transfer zones. Koradia
and Kiovsky report that for the case where dispersed
water is present in 0-dichlorobenzene, they obtained

a very long MTZ (up to 140 cm) with a non-symmetrical breakthrough profile. However, they also observed very high capacities (approximately 40%). Consequently, if either competitive co-adsorption occurs or dispersed water drying is attempted, substantial penalties are incurred. However, for many applications, like some of the ones discussed here, there may be no better alternatives.

A third aspect of drier design of significant importance is the regeneration technique. This is of particular importance to liquid drying applications because of the possibility of decomposing organics to produce fouling or irreversible poisoning of the zeolite. It is, therefore, important to devise a regeneration procedure that will avoid shortening the zeolite life and adequately remove the adsorbed water. Several techniques have been employed in these studies, but all usually involve draining the liquid prior to a thermal regeneration. The use of DTA can help decide the approximate temperature and can also forewarn of undesirable reactions.

In this work we used a low-temperature nitrogen regeneration for benzene, but the vacuum technique employed for the chlorinated hydrocarbons (3) might have helped minimize the decomposition observed. A high-temperature regeneration using inert gas stripping was found to be adequate for the butanediol case. Other regeneration techniques that have been used include steam stripping, solvent washing prior to thermal regeneration and temperature-programmed desorption.

The bulk of this paper has described the results of some of the extensive testing needed to obtain design information for particular liquid phase applications. While we strongly recommend obtaining data like these for specifying a detailed design, we also recommend making an initial heuristic feasibility estimate. This process will permit not only a preliminary cost evaluation of the proposed system but, more importantly, will help prevent embarking on a lengthy and expensive test program with an inadequate zeolite or for an economically unrealistic application.

To help carry out such an evaluation we have prepared a flow chart, shown in Table V, which presents the important considerations in a systematic manner. These are two main branches, zeolite selection and process feasibility. The process feasibility initially assumes the worst case for the design parameter estimates, but these can be revised if the zeolite selection process indicates that higher capacity or shorter MTZ might be encountered. Having

TABLE V

PROCESS EVALUATION FLOW CHART
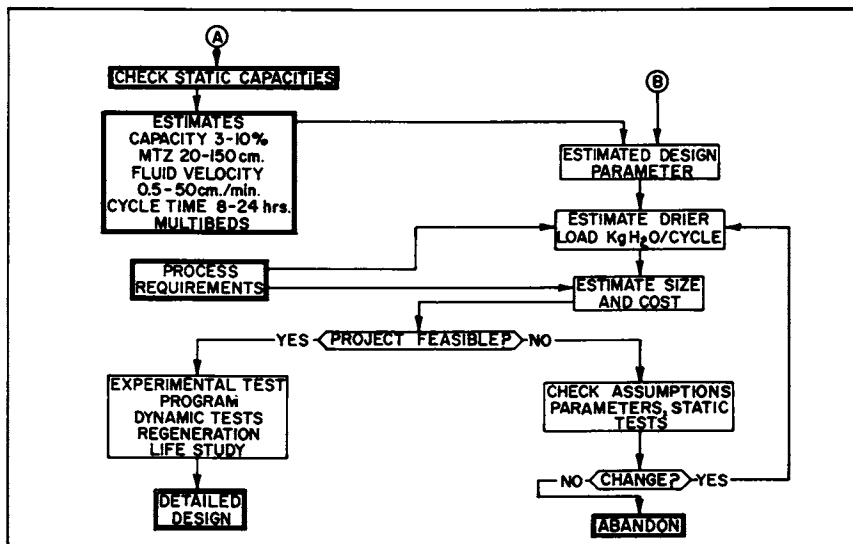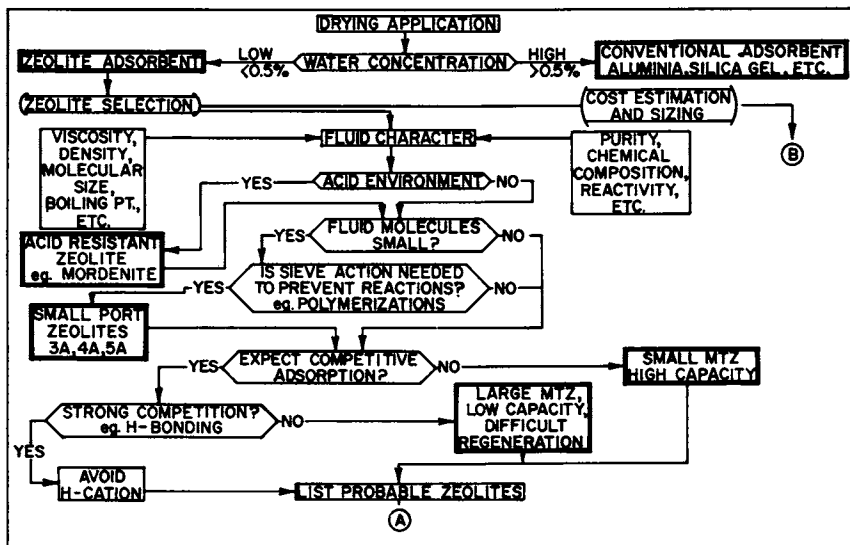
followed the flow chart, the outcome will be a list of potentially suitable zeolites, an economically feasible process, a possible regeneration scheme, and a much better appreciation of potential difficulties. With this knowledge, the detailed experimental program can be commenced and the specific design data obtained to permit the detailed engineering design of the drying system.

Acknowledgment

The authors wish to thank the Norton Company for support of this work and for permission to publish these findings.

Literature Cited

1. Hales, G.E., CEP, 1971, 67, (11), 45-48.

2. Dexant, A., LaTechnique Moderne, 1972, (Nov.),47-50.

3. Koradia, P.B., Kiovsky, J.R., CEP, 1977, 73, (4), 105-106.

4. Stannet, V.T., DuPlessis, T.A., Goineau, A.M., J. Appl. Polymer Sci., 1972, 16, 2847-2852.

5. Gehrhardt, H.M., Kyle, B.G., IEC (Process Design Development, 1967, 6, (3), 265-267.

6. Satterfield, C.N., Cheng, C.S., AIChE Journal, 1972, 18, (4), 720-723.

7. Goto, C., Joko, I., Tokunaga, K., Nippon Kagaku Kaishi, 1972, 2070-2075.

8. Michaels, A.S., IEC, 1952, 44, (8), 1922-1930.

9. Eagle, S., Scott, J.W., IEC, 1950, 42, (7), 1287-1294.

10. Kostecki, J.A., Manning, F.S., Cansar, L.N., AIChE Symposium Series, 1967, 63, (74), 90-95.

12

Separation of n-Paraffins from Wax Distillate with Supercritical Fluids and Molecular Sieves

PAUL BARTON and DAVID F. HAJNIK[1]

Chemical Engineering Department, The Pennsylvania State University,
University Park, PA 16802

An investigation was made to determine the feasibility of
the combination process of volatility amplification of non-
volatile mixtures by the addition of supercritical fluids follow-
ed by contacting the vapor with molecular sieves to separate
specific materials from the mixtures. Two potential advantages
of this novel combination become possible.
(1) With supercritical fluid volatility amplification, a
lower temperature can place a satisfactory concentration of the
material to be separated into the vapor phase, and since the
capacity of molecular sieves increases as the temperature is
lowered, a more economical process may be attainable. Higher
purity paraffin product may be produced without intermediate
washing or purging of the molecular sieves.
(2) At a given temperature level of operation, supercriti-
cal fluid volatility amplification makes it possible to increase
the molecular weight range of materials that can be volatilized
into the vapor phase in sufficient concentrations to be separated
satisfactorily by molecular sieve contacting.
In this study, C_{16}-C_{32} wax distillate is separated into $\underline{n}$-
paraffin and denormal oil fractions by vapor phase contacting
with type 5A molecular sieves. 2,2,4-Trimethylpentane (iso-
octane), 2,2-dimethylbutane, and 2-methylpentane are each used
as the supercritical fluid. Recovery of $\underline{n}$-paraffins from the
molecular sieves is accomplished by contacting with nitrogen or
ammonia gas.

Volatility Amplification with Supercritical Fluids

It is well established that supercritical gaseous phases are
capable of taking up classes of compounds under supercritical
conditions, the amount of material being taken up by the super-
critical gas being many times greater than would have been expec-
ted from the vapor pressure of these compounds at the temperature

---

[1]Current address: E. I. duPont de Nemours & Company, Towanda,
Pennsylvania   18848

of the treatment. Zhuze and Yushkevich (1) reported this phenom-
non for the extraction of a crude oil into methane. Studiengesell-
schaft Kohle m.b.H. (2) obtained patent coverage for a variety
of separations based on supercritical gas extraction. Paul and
Wise (3) presented an overview of the subject area. Gangoli and
Thodos (4) reviewed supercritical gas extraction for recovering
liquid fuels and chemical feedstocks from coal. Panzer et. al.
(5) reported on the supercritical gas extraction of the constit-
uents in a tar sand and a peat.

The data of Zhuse and Yuskevich (1) show that increasing
pressure increases the solubility of a Russian crude in methane
(T_c = 191 K, P_c = 4.64 MPa) at 313 K and that the solubility de-
creases as the percent stripped increases due to the decreasing
vapor pressure of the residue. Solubilities of the crude in the
vapor are 30 g/ℓ at 20 MPa, 80 g/ℓ at 50 MPa, and 220 g/ℓ at 80
MPa (790 atm). Up to 90% of the oil could be stripped at 80 MPa.

Zhuse and Yuskevich (6) also show that the nearness to the
critical temperature affects the gas phase solubility. With fuel
oil residue at 378 K, a vapor phase concentration of 0.7 g/ℓ
(upon expansion to standard T and P) is reached at a pressure of
9 MPa with propane (T_c = 370 K, P_c = 4.26 MPa) and propene (T_c =
365 K, P_c = 4.62 MPa), whereas a pressure of 50 MPa is needed
with ethylene (T_c = 283 K, P_c = 5.12 MPa).

Studiengesselschaft Kohle m.b.H. (2) reported the effect of
temperature on solubility level in supercritical gas. The solu-
bility is highest within 20 K of the critical temperature and
decreases as temperature is raised to 100 K above the critical
temperature. At temperatures near the critical temperature, a
sharp rise in solubility occurs as the pressure is increased to
the vicinity of the critical pressure and increases further as
the pressure is further increased. Less volatile materials are
taken up to a lesser extent than more volatile materials, so the
vapor phase has a different solute composition than the residual
material. There does not seem to be substantial heating or cool-
ing effects upon loading of the supercritical gas. It is claimed
that the chemical nature of the supercritical gas is of minor
importance to the phenomenon of volatility amplification. Ethy-
lene, ethane, carbon dioxide, nitrous oxide, propylene, propane,
and ammonia were used to volatilize hydrocarbons found in heavy
petroleum fractions.

Panzer et al. (5) extracted Athabasca tar sand in two steps,
the first with compressed n-pentane (T_c = 570 K, P_c = 3.37 MPa)
and the second with compressed benzene (T_c = 563 K, P_c = 4.92
MPa). At 533-563 K and 2.0-7.7 MPa, n-pentane extracted 95% of
the maltenes and asphaltenes from the tar sand, whereas at atmos-
pheric pressure only 75% was extracted. Further extraction with
benzene at 633 K and 2.0 MPa removed the remaining higher molecu-
lar weight asphaltenes. This indicates that the chemical nature
of the dense gas is important in some applications.

The large changes in the activities of the constituents of a

mixture at and adjacent to the critical temperature and pressure
of one of the constituents has been demonstrated by Powell (7).
He extracted water from sulfuric acid solutions containing
metal salts using n-heptane as the supercritical solvent. The
large change in the volatility of water at the critical point of
n-heptane is evidenced in Figure 1, with a substantial decrease
as the temperature is raised 20 K above the critical temperature
of n-heptane.

Thermodynamic Foundation. An expression relating the vapor
phase mole fraction (y_2) of a low volatility component (subscript
2) in a compressed gas to the liquid (or solid) phase mole frac-
tion (x_2) is given by (8):

$$y_2 = \left(\frac{x_2 \, P_2^\circ}{P}\right) \left[\frac{\gamma_{2,L} \, \phi_{2,L} \, \exp \displaystyle\int_{P_2^\circ}^{P} \frac{V_{2,L} \, dP}{RT}}{\gamma_{2,V} \, \phi_{2,V}}\right] \qquad (1)$$

The first term is the ideal gas prediction of y_2 and the second
term, the enhancement factor, corrects for nonidealities. The
liquid phase fugacity coefficient ($\phi_{2,L}$) of pure component 2 is
evaluated at the system temperature and its pure component
vapor pressure (P_2°). Its value is usually slightly less than
unity. The exponential term is the Poynting correction; it shows
that increasing pressure increases the enhancement factor though
its effect is not expected to be large. The vapor phase fuga-
city coefficient ($\phi_{2,V}$) of pure component 2 is evaluated at the
system temperature and the system pressure. At mixture reduced
temperatures and reduced pressures just above the critical point,
the value of the fugacity coefficient decreases from 0.7 to 0.2.
At lower values of mixture reduced temperature, fugacity coef-
ficients less than 0.01 are possible. This factor can contrib-
ute significantly to volatility enhancement. The chemical nature
of the solvent gas affects both the vapor phase activity coef-
ficient ($\gamma_{2,V}$) and the liquid phase activity coefficient ($\gamma_{2,L}$).
The net effect on the enhancement is difficult to predict.
    What is desirable in volatility amplification is a high
value of concentration of component 2 in the vapor on a mass
per unit volume basis. This is related to mole fraction by:

$$C_2 = \frac{y_2 \, M_2 \, N}{V} \qquad (2)$$

Increasing the system pressure increases the total moles N in
vapor volume V, thus increasing the concentration C_2 of com-
ponent 2 in the vapor on a g/ℓ basis. The system temperature
should also be high enough to give a high enough value of vapor
pressure of component 2 to provide a substantial y_2.
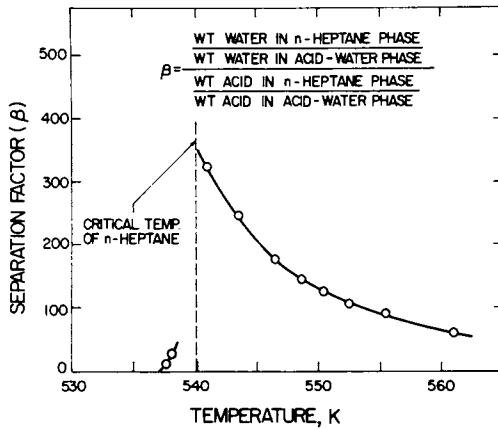
Figure 1.   The effect of temperature on the separation factor (β) for n-heptane extraction of acid mine water (pH = 2.35)

The choice of supercritical fluid for use in combination
with molecular sieves is thus influenced by the preceding con-
siderations.

Molecular Sieve Separations

In order to justify the combination volatility amplifica-
tion-vapor phase molecular sieve process, one must first preclude
the direct use of liquid phase molecular sieve contacting. We
are interested in applying the process to separate n-paraffins
with type 5A molecular sieves from petroleum fractions in the
gas oil through the medium lubricating oil boiling range (560-
740 K). For the only commercial liquid phase molecular sieve
process (Molex), light gas oil with a 605 K end point is listed
as the heaviest charging stock (9). A larger holdup of non-
adsorbable raffinate in the voids around the molecular sieve
crystals is given as a significant disadvantage of liquid phase
operation (10). Most of these non-normal compounds must be re-
moved from the molecular sieve vessel prior to desorption in
order to produce high-purity normals. Vapor phase operation
results in less non-normal compounds, which must be removed, and
more efficient removal of the non-normal compounds which are
present (11). Diffusion of n-paraffin molecules is important in
three zones: (1) the void spaces external to the molecular
sieves, (2) the interconnected macropores or channels within the
molecular sieves, and (3) the micropores or cages which branch
from these channels. Rates of diffusion thus play a critical
role in adsorption and desorption. Cooper et al. (11) state
that substantially better desorption rates can be obtained if
the operations are conducted in the vapor phase rather than in
the liquid phase. Conversely, better adsorption rates are to be
expected in vapor phase operations. O'Connor et al (12) show
that it takes substantial time to quantitatively adsorb long
chain paraffins from liquid solution onto type 5A molecular
sieves. It takes 0.7, 1.5, and 3 hours for C_{20}, C_{28}, and C_{32}
n-paraffins, respectively, when dissolved in 2,2,4-trimethyl-
pentane at 372 K. Therefore, vapor phase contacting becomes the
preferred mode of operation.

In conventional vapor phase molecular sieve operations, the
operating temperature must be high and the operating pressure
must be in the vacuum range in order to get the high molecular
weight molecules into the vapor phase for contacting with the
molecular sieves. The use of volatility amplification with
supercritical fluid obviates these requirements.

In conventional vapor phase molecular sieve operations, the
operating temperature must be even higher and the operating
pressure must be even lower than that required by the dew point
curve for the high boiling constituents. These extra require-
ments are needed to prevent capillary condensation. Condensa-

tion of feedstock in the capillaries of the molecular sieves de-
creases the diffusion rate and increases the holdup of non-ad-
sorbable raffinate on the molecular sieves. LaPlante and Symon-
iak (13) show that a typical light gas oil has a capillary
condensation temperature of 623 K at an operating pressure of
0.1 MPa (1 atm); this is 39 K higher than the dew point tempera-
ture. Asher et al. (14) have shown that the addition of a gas
to the feed to reduce the partial pressure of the feed reduces
capillary condensation. As an example, when operating at 0.78
MPa and 589 K, the purity of a C_9/C_{18} product was increased from
93.1 to 95.1 percent by adding 0.5 moles ammonia per mole of
feed. The dilution provided by supercritical gas in our process
may have a similar effect on the phenomenon of capillary conden-
sation.
    Several other factors enter into the choice of operating
temperature and pressure for the adsorption step. The maximum
temperature must be restricted to avoid excessive cracking and
rapid deactivation of the molecular sieve capacity. The capacity
of the molecular sieves to adsorb n-paraffins at equilibrium in-
creases with decreasing temperature. For example, for type 5A
molecular sieves with n-dodecane at 0.1 MPa, the molecular sieve
capacity changes from 7 to 15 wt % upon decreasing temperature
from 636 to 504 K (11). At 589 K, the equilibrium loading in-
creases from 6 wt % at 0.0007 MPa to 9 wt % at 0.5 MPa. With
C_{13} to C_{20} n-paraffins at 673 K, Burgess et al. (15) show little
pressure effect on equilibrium sieve capacity in the pressure
range of 0.02 to 0.04 MPa, with capacity ranging from 6.5 to 8.9
g/100 g sieve for these homologs, respectively. Higher temp-
eratures have the advantage of increased mass transfer rates.
This presumably could show up in the breakthrough capacity of an
operating molecular sieve bed. Breakthrough capacity is shown
to increase from 4 to 6.7 g n-paraffin introduced from feed per
100 g of molecular sieves upon increasing the temperature from
548 to 604 K, followed by a decrease to 6.3 g/100 g upon further
increasing the temperature to 634 K (10).
    It is desirable to operate the molecular sieve bed in the
adsorption mode at the same temperature as in the desorption
mode. Sista and Srivastava (16) show that temperatures in excess
of 533 K are needed to desorb by vacuum C_{12} to C_{32} n-paraffins
from type 5A molecular sieves at a pressure of 13 Pa (0.1 mm Hg).
Only 5% of n-C_{32} is removed at 636 K. Asher et al. (14) show
that, whereas it is possible to remove 98% of C_9/C_{18} n-paraffins
from type 5A molecular sieves with ammonia at 589 K, only 79%
removal is attained with C_{15}/C_{33} n-paraffins even though the
temperature is higher (658 K). Some of the retained material
over a long period of exposure to high temperature gradually
forms a carbonaceous deposit which reduces the adsorption capac-
ity of the molecular sieve; this coke deposit must be occasion-
ally removed by a controlled oxidation step which eventually
reduces molecular sieve life. Desorption rates increase with

increasing temperature. The desorption time of n̲-paraffins from 422–478 K naphtha with n̲-C$_5$ decreases from 42 to 11 minutes upon increasing the temperature from 508 to 660 K (11̲). Stripping curves show that the amount of n̲-C$_6$ needed to desorb paraffin product at a loading of 3.9 g/100 g of molecular sieves at 658 K is 60% of that required at 575 K (13̲). Generally, such curves have shown the optimum temperature to be 589–617 K for paraffins in the kerosene range and 589–672 K for paraffins in the gas oil range.

It appears that temperatures in the range of 500·to 670 K for the adsorption of n̲-paraffins in the 560–740 K boiling range on type 5A molecular sieves should be considered for investigating the combination supercritical fluid volatility amplification–vapor phase molecular sieve process. The pressure of operation will be governed by the critical pressures of potential solvents with critical temperatures in this range. The supercritical solvent of choice should not be adsorbable on type 5A molecular sieves and should not be expensive.

Because of the high molecular weight materials at the upper end of the boiling range for medium lube oil stocks, the desorption technique of choice should probably employ a displacement chemical with a high heat of adsorption, in order to overcome the high heat of adsorption of the n̲-paraffins. Ammonia at temperatures near 660 K and near atmospheric pressure appears to have good potential.

In the present study, the petroleum fraction used is a 560–740 K wax distillate obtained from Kendall Refining Company of Bradford, Pennsylvania (17̲). The supercritical fluids employed are: 2,2,4-trimethylpentane (T_c = 544 K, P_c = 2.57 MPa) at 522 to 578 K and 1.2 to 11.7 MPa; 2,3-dimethylbutane (T_c = 500 K, P_c = 3.13 MPa) at 508–512 K and 4.10–4.37 MPa; 2-methylpentane (T_c = 498 K, P_c = 3.01 MPa) at 514 K and 4.37 MPa. The desorption fluids employed are: nitrogen at 658 K and atmospheric pressure; ammonia at 616 to 730 K and atmospheric pressure.

Experimental Procedures

The apparatus used to contact the heavy petroleum liquids with supercritical fluid and for contacting the vaporized materials with molecular sieves is shown in Figure 2. The high pressure chamber is a one-gallon autoclave with a packless magnetically-driven stirrer, manufactured by Autoclave Engineers, Inc. It is constructed of 316 stainless steel and has a rated working pressure of 34 MPa at 616 K. Linde type 5A 3.2-mm calcium-form molecular sieves (230–400 g) are supported in the vapor space in a basket constructed of wire mesh. The heated chamber on top of the autoclave and the autoclave flange are removed to add and remove the molecular sieves. The sieve basket is surrounded by a cooling coil to freeze the loading on the molecular sieves during depressurization at the end of a test. The autoclave
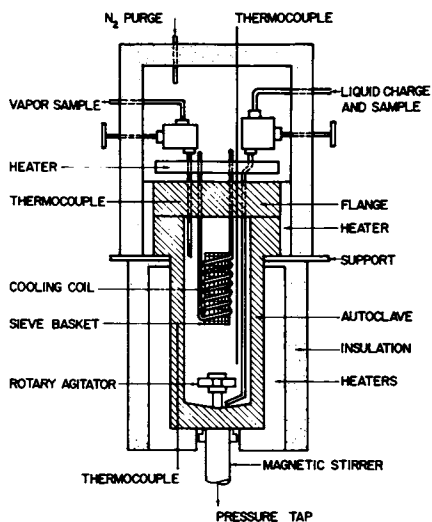
Figure 2.   High-pressure molecular sieve contactor

heaters and controls are able to keep the wall temperatures
throughout most of the vessel within 4 K of the temperature of
the equilibrated fluid within the vessel, as measured by annealed
copper-constantan thermocouples. The sample valves were main-
tained 15 K hotter than the autoclave to prevent condensation in
the vapor sample valve. An oil-filled pressure gage with a
precision of ±0.01 MPa is connected to the end of the bottom-
mounted magnetic stirrer casing.

Fresh molecular sieves were used in each test. They were
baked in an oven at 533 K for at least 5 hours. The molecular
sieves were weighed hot and placed in the autoclave under a
nitrogen purge. After fastening the flange, the autoclave was
pressure-tested with nitrogen. The autoclave was then evacuated
and the oil (60–113 g) and some of the solvent were added. The
initial charge solutions were usually less than 200 ml to avoid
wetting the molecular sieves as the liquid expanded during heat-
up. The autoclave was then heated to the operating temperature
near the critical temperature of the solvent; the heatup usually
required 1 to 2 hours. The remaining solvent was then pumped
in while stirring, to provide the desired operating pressure.
The total solvent ranged from 100 to 1700 g. The system was then
equilibrated while stirring at constant temperature for 1 to 3
hours. The vapor sample line was then purged and a small vapor
sample removed through a small condenser. The remaining super-
critical fluid and residual liquid, if any, were removed through
the liquid sample line and passed through a condenser cooled by
warm water (to avoid wax precipitation). The heaters were turned
off and the cooling water turned on during this draining and
depressurization step. In about 6 hours the autoclave was cold
enough to disassemble. After the flange was lifted, the molecu-
lar sieve basket was removed and weighed. The molecular sieves
were sealed in a glass jar after weighing.

The compounds adsorbed on the molecular sieves were desorbed
by elevating the temperature to 616 to 730 K and using either
nitrogen or ammonia purging at atmospheric pressure. The molecu-
lar sieves were placed and weighed in a stainless steel vessel
with tubing connections on each end. The vessel was placed in
an oven, and the inlet was connected to a flowmeter, regulator,
and gas source located outside the oven. The exit tubing went
out of the oven and into a 60-cm long 1.3-cm diameter vertical
glass tube. The tube cooled mixtures of purge gas and desorbed
products. The bottom of the tube was fitted into an Erlenmeyer
flask immersed in ice water to collect the adsorbate. The purge
gas exited through a cold trap cooled by dry ice to recover any
entrained adsorbate. When working with ammonia the system was
purged with nitrogen before and after the desorption. After the
furnace was hot, the purge gas flow rate was set between 150 and
250 ml/min. for 130 to 180 minutes. After cooldown, the loaded
molecular sieve chamber was weighed to determine net desorption.
Some residual ammonia remained in the molecular sieves.

The denormal oils recovered from the experiments were separated from the solvent by batch distillation. Vacuum and nitrogen stripping were applied towards the end, stopping when the oil temperature in the reboiler reached 473 K. Cloud and pour points were determined on the oil products.

Vacuum batch distillation in 25 ml stills was used to determine the oil-solvent composition of the small samples taken from the autoclave. The reboiler was exposed to a pressure of 2.7 kPa and a temperature of 373 K for 2 hours at the end of the distillation to remove the residual solvent. The composition was calculated from the weight of the feed and residual oil. The accuracy of the compositions determined by this procedure with 15-20 g samples is ±0.3 wt %.

The n-paraffin contents of the oil products were determined by a modification of the procedure described by O'Connor et al. (12). The separation of normals is accomplished by liquid phase adsorption onto type 5A molecular sieves using 2,2,4-trimethylpentane as solvent. The method determines normals content by weight of unadsorbed materials recovered from the solution after adsorption. First the molecular sieves are washed to remove dust and then vacuum baked. A weighed four-gram sample of oil is added to 40 grams of the molecular sieve pellets and 90 grams of distilled 2,2,4-trimethylpentane, and refluxed for 50 hours. The liquid is then collected. The molecular sieves are washed and refluxed for 30 minutes, and this wash liquid is added to the previous liquid. The solution is then evaporated and then dried at 473-498 K. Weighings at 10 minute intervals until constant weight is reached gives the amount of denormal oil. Loss of sample by occlusion, entrainment, and evaporation averaged 3%, so the normals content is adjusted downwards by 3 wt %. The accuracy of the normals contents determined by this procedure differs from that of O'Connor et al, which uses a simple washing step instead. With the latter procedure, an additional 7% of the denormal oil remains unrecovered from the molecular sieve macropores.

Gas chromatography was used to determine n-paraffin distribution in the oil and wax samples. An F and M Instrument Company Model 500 chromatograph was used with an uncompensated single column, a helium carrier gas flow rate of 25 ml/min., and a thermal conductivity detector. The column was 4.8 mm in diameter and 3.3 m in length, and was packed with 3% Dexil 300 on Chromosorb P. The block and injection port temperatures were maintained at 673 K. The column was temperature-programmed from 348 K to 673 K at a rate of 5.7 K per minute. Peak identification was aided by the use of internal standards of decane, dodecane, and hexadecane. The baseline was determined by heating without sample injection. Response values were not available for the various areas on the traces, so the analyses were reported as % by area.

Results and Discussion

Volatility Amplification. The solubility of the components in $C_{16}-C_{32}$ paraffinic wax distillate in supercritical 2,2,4-trimethylpentane was measured at 566 K. This was done by adding increased amounts of the solvent to a fixed amount (341 g) of oil in the autoclave in the absence of molecular sieves and sampling and analyzing the vapor phase. The results are presented in Table I. The pressures listed are those before and after sampling.

Table I

Solubility of $C_{16}-C_{32}$ Wax Distillate in Supercritical
2,2,4-Trimethylpentane at 566 K

Pressure, MPa	Wt 2,2,4-trimethylpentane/wt oil		Estimated oil solubility in vapor, g/ℓ
	In charge	In vapor	
1.32-1.21	0.61	12.0	5.3
1.89-1.82	1.11	18.1	6.3
2.50-2.45	2.01	21.4	9.5
2.97	3.59	3.50	91

The degree of volatility amplification is moderate at pressures of 1.2 to 2.5 MPa, with vapor compositions in the range of 4.5 to 7.7 wt % oil. Upon crossing the critical pressure of 2.56 MPa a dramatic increase in oil volatility occurs, reaching a composition of 22 wt % oil in the vapor. It is seen that at a solvent to oil ratio of 3.5 and a pressure of 2.97 MPa, the wax distillate is completely volatilized. The oil concentration in the vapor reached 91 g/ℓ.

It is apparent that quantitative vaporization of medium lube oil range petroleum stocks can be achieved under rather mild conditions.

n-Paraffin Separation. The $C_{16}-C_{32}$ paraffinic wax distillate was processed by volatility amplification into supercritical solvent and contacting the vapor with 5A molecular sieves. The operating conditions for tests using 2,2,4-trimethylpentane, 2,3-dimethylbutane, 2-methylpentane, and no solvent are presented in Table II. The product yields and properties are presented in Table III.

Run 2 represents a base case in the absence of supercritical solvent; it was run at the vapor pressure (0.1 MPa) of the wax distillate at 528-539 K. A gas chromatograph trace of the feed oil is shown in Figure 3. The oil is seen to consist pre-

Table II. Operating Conditions for Separation of $\underline{n}$-Paraffins from C_{16}-C_{32} Wax Distillate With Supercritical Solvent Volatility Application and 5A Molecular Sieves

Run	Charge		Adsorption				Gas	Desorption	
	$\dfrac{\text{Wt sieves}}{\text{Wt oil}}$	$\dfrac{\text{Wt solvent}}{\text{Wt oil}}$	Temp., K	Pressure, MPa	Time at equil. T, hr	$\dfrac{\text{g adsorbed}^a}{100 \text{ g sieves}}$		Temp., K	Time, hr
2	2.33	0	528-539	0.1	1	6.31	NH$_3$	662	3.5
Solvent: 2,2,4-trimethylpentane									
3	1.81	7.23	550-561	2.65-2.79	3.0	10.0	NH$_3$	654	---
6	2.20	15.9	551-553	9.06-9.61	2.6	8.79	N$_2$	658	2.0
4	2.38	2.00	554	1.34-1.41	1.2	6.51	NH$_3$	662	3.6
5	2.48	0.995	571-575	1.58-1.65	2.3	7.97	NH$_3$	661	3.3
13	2.78	0.886	522-578	1.20-1.57	3.0	6.61	NH$_3$	730	---
12	3.97	1.01	525	1.96	1.6	2.84	NH$_3$	675	2.7
8	4.09	26.3	566-578	9.61-11.68	1.9	6.76	N$_2$	658	3.7
7	5.14	4.09	548-555	1.45-1.49	2.2	4.89	NH$_3$	718	1.3
14	6.24	22.6	550	3.68	2.6	3.20	NH$_3$	662	2.3
Solvent: 2,3-dimethylbutane									
16	6.39	21.3	508-512	4.10-4.37	2.4	5.73	NH$_3$	647	2.5
Solvent: 2-methylpentane									
15	5.85	20.1	514	4.37	1.4	12.2	NH$_3$	616	---

^{a}This weight includes the adsorption of n-paraffin in the molecular sieve cages, oil raffinate and solvent adsorbed in the voids and macropores, and water adsorbed during molecular sieve transfer to and from autoclave.

Table III.   Products from Separation of C_{16}-C_{32} Wax Distillate
With Supercritical Solvent Volatility Amplification
and 5A Molecular Sieves.

Run	Yield,[a] wt % of feed	Denormal Product			Area % n-paraffin in chromatograph of desorbed wax product
		Cloud point, K	Pour point, K	n-paraffin content, wt %	
Feed	100	306	294	16.7	
2	85.3	---	294	7.0	95
Solvent:	2,2,4-trimethylpentane				
3	81.9	303	289	4.8	66
6	80.7	291	286	7.2	98 N_2 desorbed
4	84.5	---	291	7.8	43
5	80.5	301	291	7.8	38
13	81.6	---	289	6.3	45
12	88.7	301	294	7.7	37
8	72.3	---	280	6.5	58 N_2 desorbed
7	74.8	---	294	8.0	51
14	80.0	271	266	3.2	63
Solvent:	2,3-dimethylbutane				
16	63.3	276	266	2.0	44
Solvent:	2-methylpentane				
15	---	285	283	3.8	--

$-$ $-$ $-$ $-$

[a]Calculated from molecular sieve weight increase during adsorption assuming only oil and wax adsorbed. This calculation ignores water adsorption during molecular sieve transfer and adsorption of solvent. Consequently, these values are low.
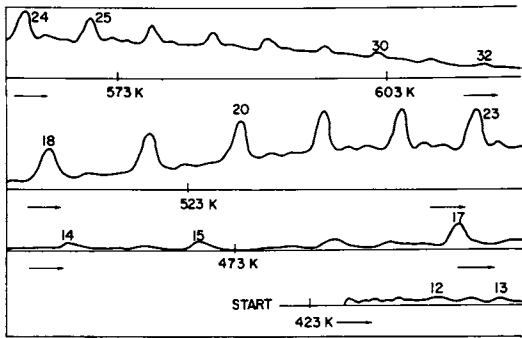
Figure 3. Chromatogram of Kendall paraffinic wax distillate
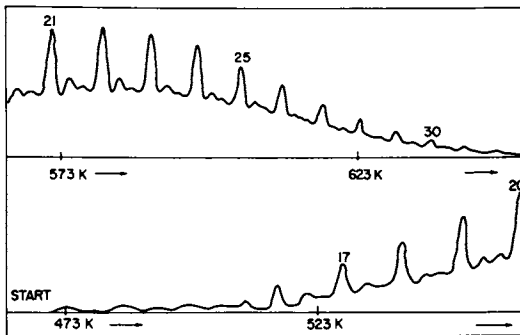
Figure 4. Chromatogram of Run 2 denormal oil

dominantly of C_{16} to C_{32} hydrocarbons, which boil at 560 to 740
K at atmospheric pressure, along with some C_{15} and lower light
ends. It is these light ends which generated atmospheric pres-
sure in the autoclave; otherwise the unit would have been under
vacuum. With a molecular sieve to oil weight ratio of 2.33, a
molecular sieve loading of 6.3 g adsorbate/100 g of molecular
sieves resulted. The hydrocarbon content of the adsorbate is
unknown because of water adsorbed from the atmosphere during
transfer of the sieves to and from the autoclave. The normals
content was reduced from 16.7 wt % in the feed oil to apparently
7.0 wt % in the product oil, but the pour point was not reduced
from the original 294 K. Figure 4 shows a gas chromatograph
trace of the product oil. The tall peaks represent n-paraffins;
the area above the base line and under the tall peaks represent
the non-normal compounds in the oil. Upon comparing Figure 4
with Figure 3, there doesn't appear to be any reduction in the
area of the n-paraffin peaks compared to the rest of the area in
Run 2. In view of conflicting analyses of the denormal oil in
Run 2, additional work is needed to establish base cases upon
which to compare the results with supercritical solvents.

The material adsorbed on the molecular sieves in Run 2 was
desorbed by ammonia. A gas chromatogram of this material is
shown in Figure 5; the n-paraffin peak area represents 95% of
the total area of the trace. The n-paraffins present are pre-
dominantly in the C_{12} to C_{23} range, with maxima at C_{18} through
C_{21}. Upon comparing Figures 4 and 5, it is apparent that the
C_{24}^+ n-paraffins didn't significantly volatilize and adsorb on
the molecular sieves.

Nine runs were made with 2,2,4-trimethylpentane as the
supercritical solvent at varying solvent/oil ratio, molecular
sieve/oil ratio, temperature, and pressure. The runs are listed
in the order of increasing molecular sieve/oil ratio in Tables
II and III.

The molecular sieve loadings reported in Table II include
the n-paraffins adsorbed in the molecular sieve cages, oil raf-
finate adsorbed in the voids and macropores, water in the molecu-
lar sieve cages adsorbed during transfer of the molecular sieves
to and from the autoclave, and solvent in the macropores. For
example, in the gas chromatographic trace for Run 6 desorbed
product, 19% of the area represented 2,2,4-trimethylpentane. The
molecular sieve loading appears to be predominantly controlled by
the molecular sieve/oil ratio. In Figure 6, the molecular sieve
loading is plotted as a function of the oil charge/molecular
sieve ratio. The data correlate; loading increases proportion-
ately to the oil charge at low loadings, with a tapering off in
the vicinity of 10 g adsorbed/100 g of molecular sieves. The
three data points below the curve in Figure 5, including the
one for Run 2 with no solvent, are for the shorter equilibration
times (1 to 1.6 hr) at temperatures around the critical tempera-
ture of 2,2,4-trimethylpentane coupled with operating pressures
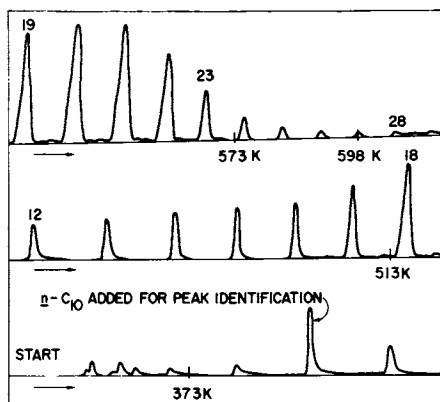
Figure 5.   Chromatogram of Run 2 desorbed product

Figure 6.   Molecular sieve loading as function of oil to molecular sieve ratio using 2,2,4-trimethylpentane supercritical solvent at 522–578 K and 1.34–11.68 MPa
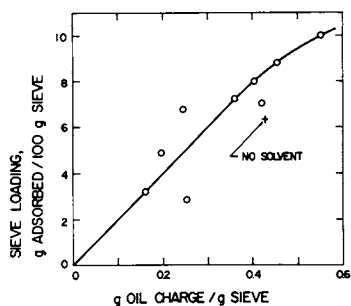
(0.1-1.96 MPa), in the region of no or low volatility amplification, below the critical pressure of 2.57 MPa of 2,2,4-trimethylpentane. This indicates that these three runs (2, 4, 12) were mass transfer rate-limited.

A high molecular sieve to oil ratio and conversely low molecular sieve loading are required to reduce the n-paraffin content of the wax distillate to low values. For example, in Run 6 with a molecular sieve/oil ratio of 2.20 and a loading of 8.79 g/100 g of molecular sieves, the normals content of the oil is reduced from 16.7 to just 7.2 wt % and the pour point is reduced from 294 to 286 K. In Run 14 with a molecular sieve/oil ratio of 6.24 and a loading of 2.30 g/100 g of molecular sieves, the normals content is reduced by 81% to 3.2 wt % and the pour point is reduced to 266 K. The yield of denormal oil as calculated from the molecular sieve weight gain, neglecting water and solvent adsorption, is 80%; this checks the material balance value of 79% calculated using the denormal product and n-paraffin product analyses in Table II. The gas chromatograms for these two runs are reproduced in Figures 7 and 8. In Run 6, the sizes of the n-paraffin peaks are greatly reduced, with the fractional reduction being about the same at all carbon numbers. In Run 14, the n-paraffin peaks are virtually obliterated.

A low molecular sieve/oil ratio, which results in high molecular sieve loading, in combination with a high solvent to oil ratio are needed to prepare high purity n-paraffinic product using supercritical solvent volatility amplification. In Run 6 with a loading of 8.79 g/100 g of molecular sieves and a 2,2,4-trimethylpentane/oil ratio of 15.9, n-paraffins with a purity of 98% are produced. In Run 14 with a loading of 3.20 g/100 g of molecular sieves and a 2,2,4-trimethylpentane/oil ratio of 22.6, the n-paraffin area on the gas chromatograph trace is reduced to 63% of the total area, because of condensation of raffinate in void spaces and in the macropores of the molecular sieves. This hints that capillary condensation may be a function of molecular sieve loading. Gas chromatographic traces for the normal products from Runs 6 and 14 are reproduced in Figures 9 and 10. Run 6 product was desorbed with nitrogen at 658 K and atmospheric pressure. Note the high purity attainable with volatility amplification without the need for an intermediate washing or purging step. Nitrogen is incapable of desorbing the C_{23}^{+} n-paraffins; 57% of the adsorbate remained on the molecular sieves, as calculated from molecular sieve weight loss during desorption. Since the raffinate in the voids and macropores is removed before or along with the adsorbate, as evidenced by the large 2,2,4-trimethylpentane peak, the normals remaining on the molecular sieves should have the same high purity. Run 14 product was desorbed with ammonia at 662 K and atmospheric pressure. Ammonia is capable of desorbing n-paraffins up to C_{28} with equal efficacy at all carbon numbers. The trace also indicates that the molecular sieves adsorb all carbon number n-paraffins in the wax distillate
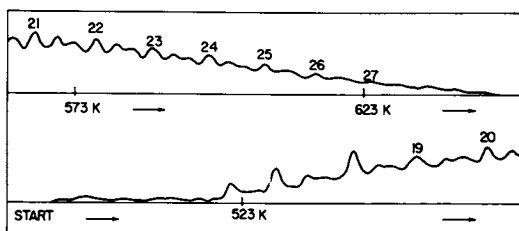
Figure 7.   Chromatogram of Run 6 denormal oil
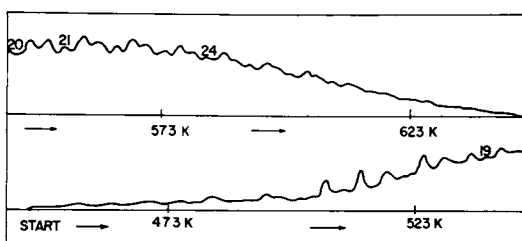
Figure 8.   Chromatogram of Run 14 denormal oil
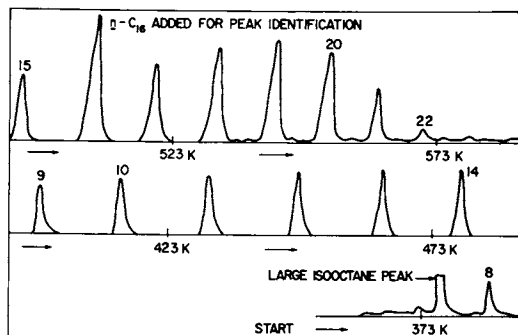
Figure 9.   Chromatogram of Run 6 desorbed product
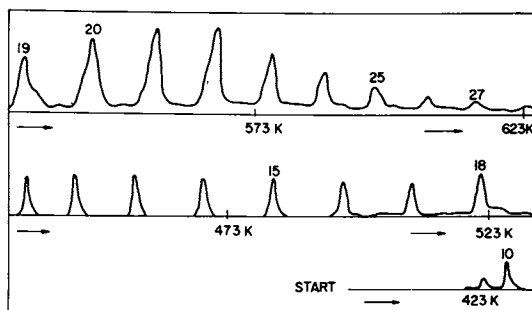
Figure 10.   Chromatogram of Run 14 desorbed product

with high effectiveness. The average molecular weight of the n-paraffins recovered corresponds to two carbon numbers higher with volatility amplification than with no volatility amplification. The amount of n-paraffins not desorbed from the molecular sieves could not be determined from the weight change of the molecular sieves due to the ammonia adsorbed.

The high pressure (9.06-9.61 MPa) used in Run 6 is probably not necessary for the production of high purity n-paraffinic product. It may be possible to achieve the same results with pressures of 2.6-3.7 MPa. High pressure was also used in Run 8 along with a moderate molecular sieve loading, yet the normals area % was only 58%; so it appears that the molecular sieve loading is the important variable.

The selectivity of the sieves for n-paraffins decreases as the ratio of supercritical fluid to wax distillate feed is decreased. n-Paraffin content is shown as a function of this ratio in Figure 11, at both high and low-to-moderate molecular sieve loadings.

A test was made with 2,3-dimethylbutane as the supercritical solvent; it has a lower critical temperature than 2,2,4-trimethylpentane. Operating at a temperature of 508-512 K, a pressure of 4.10-4.37 MPa, a molecular sieve/oil ratio of 6.39, and a solvent/oil ratio of 21.3, the molecular sieve capacity attained is 5.73 g/100 g of molecular sieves (as compared to 3.2 g/100 g of molecular sieves with 2,2,4-trimethylpentane at 550 K). The n-paraffin content of the wax distillate was reduced by 88% to a level of 2 wt %, giving a pour point of 266 K. The yield of denormal oil was lower (63%) and the n-paraffin content of the desorbate was lower (44%) at this lower temperature level. This is probably due to increased capillary condensation. Conversely, operation at temperatures greater than 550 K should produce less capillary condensation and purer n-paraffin product. It would be interesting to try supercritical solvents with critical temperatures in the 600-670 K range.

A test was made with 2-methylpentane as the supercritical solvent at 514 K and 4.37 MPa, at a molecular sieve to oil ratio of 5.85 and a solvent to oil ratio of 20.1. The n-paraffin content of the wax distillate was reduced by 77% to a level of 3.8 wt %. In this test, an extraordinary gain in molecular sieve weight occurred. A significant amount of the 2-methylpentane was recovered upon desorption of the molecular sieves with ammonia. For some reason unknown to us, a large amount of 2-methylpentane became adsorbed on the molecular sieves at its critical point.

Comparison of Molecular Sieve and Ketone Dewaxing. To serve as a basis for comparison, a sample of the C_{16}-C_{32} wax distillate was dewaxed using conventional procedures. The oil feed was dissolved in ketone solvent and cooled at a rate of 1.3 K per minute with stirring to 260 K. The slurry was filtered with a 20-35 μm cloth filter and the cake was washed with additional solvent to

remove some of the occluded oil. The products were then stripped
of ketone and the yields and properties measured. The results
are presented in Table IV. The results of Run 14 from the super-
critical solvent volatility amplification-molecular sieve process
are also shown in Table IV for comparison. The results are quite
similar. Dewaxed oil with a pour point of 264-266 K (15-20F) is
produced in both processes in 79-80% yield. The theoretical
(maximum) denormal oil and n-paraffin product yields differ from
the theoretical (maximum) dewaxed oil and wax yields producible
by conventional solvent dewaxing.

The oil yields calculated from the analyses of the denormal
products in Table III are plotted versus denormal product pour
point in Figure 12. It is seen that 60% of the n-paraffins must
be removed before the pour point begins to decrease. Further
extraction of the n-paraffins to 88% of the theoretical (maximum)
yield of 16.7 wt % n-paraffins then reduces the pour point from
294 K to 266 K. It appears that extraction of the remaining n-
paraffins may lower the pour point to the desirable range of 261-
255 K. It would be interesting to determine the effect of pour
point depressants on the denormal oil product.

For comparison, the theoretical oil yield data for dewaxing
by cooling is also shown in Figure 12. This curve is from Morales
(17) and from additional ketone dewaxing tests performed in this
study. The technique used to calculate the theoretical yield
curve from actual yield and product composition data has been
described by Passut et al. (18). The theoretical yield curve in
ketone dewaxing differentially removes all materials including
n-paraffins in the order of melting points, whereas some of these
other higher melting point materials remain in the molecular sieve
denormal product.

Figure 13 shows a gas chromatographic trace of a 261 K pour
point dewaxed oil from a conventional ketone dewaxing. Note the
absence of C_{25}^+ n-paraffins and the prevalence of C_{21}^- n-paraffins.
It is evident that conventional dewaxing removes constituents by
order of melting point, starting with the highest carbon number
on down. The theoretical oil yields of denormal oil and dewaxed
oil of this pour point are both 85%. The potential exists for
the production of 261 K pour point denormal oil in a higher actual
yield than the actual yield of 261 K pour point conventionally
dewaxed oil.

Future Studies

The combination supercritical fluid volatility amplification-
molecular sieve process has the potential for producing two val-
uable products simultaneously from gas oil-lube oil petroleum
stocks. In a flow-through molecular sieve bed, the leading ad-
sorption front operates in the lean molecular sieve loading
range, providing the conditions needed for the n-paraffin removal
needed to produce low pour lube oil, while the trailing adsorption

Table IV. Comparison of Dewaxing of C_{16}–C_{32} Wax Distillate by Volatility Amplification-Molecular Sieves With Conventional Ketone Dewaxing.

| | Feed | Molecular Sieve Process | | Ketone Dewaxing | |
		Denormal oil	n-Paraffins	Dewaxed oil	Wax[a]
Solvent (by weight)		2,2,4-trimethylpentane		1 Methylisobutyl ketone	1 Methylethyl ketone
Wt solvent/wt oil		22		1.5	
Wt molecular sieve/wt oil		6			
Pressure, MPa		3.7			
Temperature, K		550		260	
Pour point, K	294	266	—	264	
Cloud point, K	306	276	—	270	
Yield, wt %					
Actual		79	21	80	20
Theoretical		83	17	87	13
Occluded oil, wt %			37		35
Viscosity, cm2/s					
@ 311 K	0.1322			0.1406	
@ 372 K	0.0315			0.0331	
Viscosity Index	100			96	

[a] Wax cake was washed with 1 methylisobutyl ketone/1 methylethyl ketone at a wash to cake ratio of 1.35.
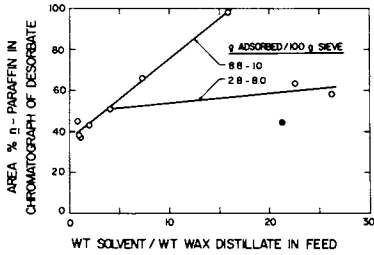
Figure 11. Molecular sieve selectivity for supercritical-fluid–molecular-sieve extraction: (○) 2,2,4-trimethylpentane; (●) 2,3-dimethylbutane
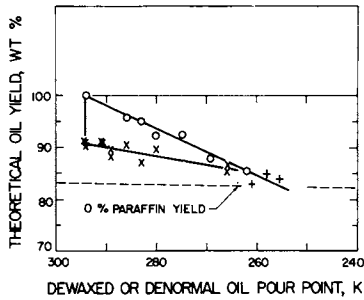
Figure 12. Theoretical yield curves for solvent (ketone) dewaxing: (○) Morales, (+) this work; and supercritical-fluid–molecular-sieve extraction of C_{16}–C_{32} wax distillate: (X) supercritical sieve extraction
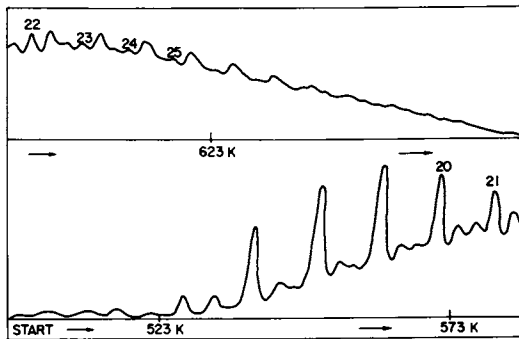
Figure 13. Chromatogram of solvent-dewaxed oil from C_{16}–C_{32} wax distillate

front operates in the high molecular sieve loading range, provid-
ing the conditions needed to produce high-purity n-paraffins.
Pilot plant studies are needed to investigate operation in this
mode. The improvements in operating conditions and products
attainable by sieve washing and purging between the adsorption
and desorption steps should be investigated. Operation at higher
temperatures needs to be evaluated. Work needs to be done with
cycled adsorbent. Application of this technique to the gas oil
feedstocks currently processed commercially should be evaluated.

Nomenclature

C =   mass per unit volume concentration in vapor phase

M =   molecular weight

N =   total moles of vapor

P =   system pressure

P° =   pure component vapor pressure

R =   gas constant

T =   temperature

V =   vapor volume

V_L =   molar liquid volume

x =   mole fraction in liquid phase

y =   mole fraction in vapor phase

Greek Letters

γ =   activity coefficient

ϕ =   fugacity coefficient

Subscripts

2 =   component 2

c =   thermodynamic critical point

L =   liquid phase

V =   vapor phase

Abstract

A method is developed to separate n-paraffins from petroleum fractions utilizing the combination of (1) volatility amplification of the liquid into a supercritical fluid, and (2) vapor-phase molecular sieve contacting. This can possibly extend molecular sieve operations to higher molecular weight oils or allow operating commercial molecular sieve processes at lower temperatures where molecular sieve capacity is higher and to produce purer n-paraffins without intermediate molecular sieve washing or purging. With C_{16}-C_{32} wax distillate and 2,3-dimethyl-butane supercritical solvent at 511 K and 4.27 MPa, or 2,2,4-trimethylpentane at 550 K and 3.68 MPa, a solvent/oil ratio of 22 and a molecular sieve/oil ratio of 6.3 gives 88 or 81% n-paraffin removal, respectively, and denormal oil with a 266 K pour point. Regeneration of the molecular sieves at 658 K with nitrogen desorbs n-paraffins up to C_{23}, and with ammonia, n-paraffins up to C_{28}. The desorbed products without an intermediate molecular sieve washing step contain from 38 to 98% n-paraffins. n-Paraffin purity can be increased by operating at a higher temperature to reduce capillary condensation and by intermediate washing or purging of the molecular sieves.

Acknowledgement

Literature Cited

1. Zhuze, T. P., Yushkevich, G. N., *Izvest. Akad. Nauk S.S.S.R., Odel. Tekh Nauk*, 1957, 11, 63.

2. Studiengesellschaft Kohle m.b.H., Mulheim-Ruhr, British Patent 1,057,911, 1967.

3. Paul, P. F. M., Wise, W. S., "The Principles of Gas Extraction", Mills and Boon Limited, London, 1971.

4. Gangoli, N., Thodos, G., *Ind. Eng. Chem., Prod. Res. Dev.*, 1977, 16(3), 208.

5. Panzer, F., Ellis, S. R. M., Bott, T. R., ISEC, 1977, CIM 21, 685.

6. Zhuze, T. P., Yushkevich, G. N., *Isvest. Akad. Nauk S.S.S.R., Odel. Tekh. Nauk*, 1957, 12, 83.

7. Powell, R. W., "Hydrocarbon Extraction of Acid Mine Drainage,"

M.S. Thesis, The Pennsylvania State University, University Park, PA, 1972.

8. Hajnik, D. F., "Separation of n-Paraffins from a Wax Distillate with Molecular Sieves and Critical Fluids", M.S. Thesis, The Pennsylvania State University, University Park, PA, 1980.

9. Anon., Hydrocarbon Processing, 1974, 53(9), 203.

10. Ponder, T. C., Hydrocarbon Processing, 1969, 48(10), 141.

11. Cooper, D. E., Griswold, H. E., Lewis, R. M., Stokeld, R. W., Chemical Engineering Progress, 1966, 62(4), 69.

12. O'Connor, J. G., Burow, F. H., Norris, M. S., Anal. Chem., 1962, 34(1), 82.

13. LaPlante, L. J., Symoniak, M. F., Hydrocarbon Processing, 1970, 49(12), 77.

14. Asher, W. J., Campbell, M. L., Epperly, W. R., Robertson, J. L., Hydrocarbon Processing, 1969, 48(1), 134.

15. Burgess, C. G. V., Duffett, R. H. E., Minkoff, G. J., Taylor, R. G., J. Appl. Chem., 1964, 14, 350.

16. Sista, V. R., Srivastava, G. C., Anal. Chem., 1976, 48(11), 1582.

17. Morales, J. A., "Dewaxing of Gas Oil by Adsorption on Activated Carbon", M.S. Thesis, The Pennsylvania State University, University Park, PA, 1977.

18. Passut, C. A., Barton, P., Klaus, E. E., Tewksbury, E. J., Ind. Eng. Chem., Process Des. Dev., 1977, 16(1), 120.

Polybed[1] Pressure-Swing Adsorption Hydrogen Processing

R. T. CASSIDY

Union Carbide Corporation, Linde Division/EP&P, Tarrytown, NY 10591

A process has been commercialized which repre-
sents a breakthrough in the production of high purity
hydrogen in the quantities needed for large hydrogen
plants serving the refining, chemicals production,
and fertilizer manufacturing industries. The patent-
ed process employs multiple adsorbent beds in a pres-
sure-swing cycle to separate hydrogen from a variety
of hydrogen-bearing feed streams. The process is
characterized by simple plant design, high product
purities and recoveries, and low energy requirements.
Commercial systems have proven stable and reliable in
operation and are non-polluting.

Hydrogen is important for a multitude of indus-
trial processes including hydrogenation, hydrocrack-
ing, ammonia and methanol syntheses, etc. Tradition-
ally hydrogen has been available at purities up to
about 97% in large plants. Although pressure-swing
adsorption technology is capable of providing ultra-
pure hydrogen, it had previously been limited to
relatively low recoveries and capacities.

Union Carbide engineers developed a new concept
in pressure-swing adsorption technology which solves
many of the problems inherent in conventional hydrogen
processing and extends the capacity range considerably
beyond that of previous pressure-swing processes. The
concept utilizes several adsorbers in an integrated
cycle that improves adsorbent productivity and product
recovery. The technique was applied to a steam re-
forming plant to replace the conventional hydrogen
purifications steps (1). Optimization of the pres-
sure-swing system resulted in the POLYBED PSA system.

---

[1]POLYBED is a trademark of Union Carbide Corporation.

Background

Pressure-Swing Adsorption

Adiabatic pressure-swing adsorption (PSA) process-
es using molecular sieves, activated carbon and silica
gel have become widely accepted as vital processing
tools in the petrochemical, chemical, petroleum refin-
ing and atmospheric gas separation industries during
the past ten years. Applications include purification
of hydrogen, helium, and methane; separation of iso-
and normal-paraffins; and air separation. The basic
process is cyclic in nature consisting of several
steps by which a gaseous product is separated from a
mixture at moderate to high pressure. The adsorbent
regeneration is carried out at low pressure.
     In the simplest type of PSA system, an adsorber
separates the desired product from the feed mixture at
feed pressure and ambient temperatures. When the ad-
sorbent bed has been saturated with impurities, it is
depressurized to a lower pressure and in a direction
countercurrent to the feed flow direction. The depres-
surization (blowdown) causes desorption and removal of
much of the impurities from the adsorbent. The bed is
then purged, also countercurrently to the feed flow
direction, with product gas to complete the removal of
impurities to a low residual level. Alternately,
the bed may be evacuated to a sub-atmospheric pressure
to remove impurities. The adsorber is then pressurized
with product gas and it is put back on line to begin
the adsorption step once again.
     The earlier PSA units typically utilized 2,3, or
4 adsorber beds in a cyclic sequence in which one of
the beds was always on an adsorption step while the
other bed or beds were being regenerated. However,
these systems were inherently inefficient for two
reasons. First, the blowdown from adsorption pressure
to the low waste pressure caused large losses of the
desired product gas which was stored in the bed at
high pressure. Second, some pure product gas was cy-
cled to waste since it was used to purge a regenerating
bed.
     Improved cycles were developed to increase the
efficiencies of PSA systems. The innovation consisted
of withdrawing product-quality gas from an adsorber
that has completed its adsorption step by depressuriz-
ing the bed cocurrently, in the direction of feed and
product flow, to some intermediate pressure. By con-
trol of the mass-transfer fronts of the impurities,
the purity of this lower-pressure gas is maintained at

a high level, and it is used to perform some of the
pressurization and all of the purging of other adsorb-
ers in the cycle. Thus, the product gas previously
lost in these functions can be recovered as product
at the plant battery limits. Also, since blowdown
starts at much lower pressure, losses of product stored
within the bed are reduced.

A cycle sequence chart for a PSA system incorpor-
ating these innovations is shown in Figure 1. The gas
for pressurization of adsorbers is transferred via
equalizations in pressure between the bed supplying
the gas and the bed receiving it. The system is ar-
ranged so that one adsorber is always "on-line" sup-
plying product gas.

The advantages of PSA systems over other process-
ing schemes are:

o   Ultra-high purity - preferred for hydrogen,
     helium and methane purifications with virtu-
     ally total removal of impurities.

o   No external heat input required for regenera-
     tion.

o   Single step processing - several constituents
     in a gas stream can be removed in one step,
     e.g., CO, CH_4 and CO_2 from hydrogen-bearing
     streams.

o   Long adsorbent life - original adsorbent
     charge generally lasts the life of the plant.

Traditionally PSA processes have found particu-
larly widespread application in hydrogen production
systems wherein the PSA unit is used to produce ultra-
high purity hydrogen (99.999%+) from steam-reformed
hydrocarbons and other hydrogen sources. However, sev-
eral limitations have existed with these processes.
The recovery of hydrogen, even in the more efficient
Union Carbide four-bed system, is typically 70-75%.
The size of the adsorbent beds is limited by factors
such as the physical strength of the adsorbent mater-
ials, vessel transportation, efficiency of flow dis-
tribution and other practical considerations. As a
result of recovery and bed size limitations, the pro-
duction rate of 2-, 3-, or 4-bed systems generally has
an upper limit of 12-13 MMSCFD.

During the 1970's the trend in the petrochemical
industry shifted to synthesis gas as a basic raw mater-
ial, and the need for higher-octane gasoline created
major new demands for hydrogen in petroleum refining.
It was recognized that conventional PSA units were
not broadly applicable in these areas because of their

VESSEL
NUMBER

1	ADSORPTION	EQ1	C D	EQ2	C D	PURGE	EQ2	EQ1	R

2	C D	PURGE	EQ2	EQ1	R	ADSORPTION	EQ1	C D	EQ2

3	EQ1	C D	EQ2	C D	PURGE	EQ2	EQ1	R	ADSORPTION

4	EQ1	R	ADSORPTION	EQ1	C D	EQ2	C D	PURGE	EQ2

EQ — EQUALIZATION   ↑ ———— COCURRENT FLOW
C D↑ — COCURRENT DEPRESSURIZATION   ↓ — COUNTERCURRENT FLOW
C D↓ — COUNTERCURRENT DEPRESSURIZATION
R — REPRESSURIZATION
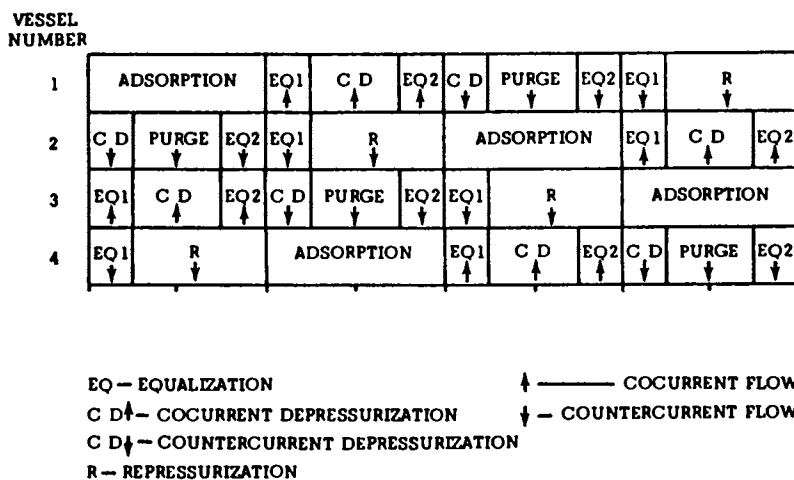
Figure 1.   Generalized PSA cycle sequence chart

limited production capacity. Furthermore, the concept
of simply using several of these units in parallel was
not truly viable. Their relatively low product recov-
ery (70-75%) in large units would result in large
quantities of low-value fuel-gas or waste gas.

It was evident that a new-generation, high-capa-
city, high-recovery system was needed. The problem
became one of making more efficient use of the adsorb-
ents used in these systems and, concurrently, making
a major increase in unit capacity.

The POLYBED PSA System

Since the previously stated limitations on ves-
sel size were still in effect, it was decided to pur-
sue a route using multiple adsorber beds in a highly
integrated system. It was necessary to define inte-
grated high-capacity systems with at least 80% product
recovery and to devise control schemes for such sys-
tems.

While optimizing purity and recovery for the
large-scale system, some of the concerns were:

- o   Determination of the minimum number (N)
  of hydrogen recovery stages, and number of
  adsorbers for a wide range of operating
  parameters.

- o   For each N, a definition of optimum feed-to-
  purge pressure ratios.

- o   Definition of the minimum final purge condi-
  tion which still provides necessary adsorb-
  ent cleanup.

- o   Determination of mass-transfer fronts, shapes
  and movement during each step.

- o   Avoidance of buildup of "heavy" impurities
  which could cause irreversible adsorbent
  deactivation.

- o   Design of a reliable process control system.

In dealing with the problems mentioned above,
consideration was given to those occurrences in the
process which were largely unsteady-state phenomena.
In each step in the process there is a change in the
adsorbate (impurity) loading on the adsorbent bed and
a change in the total gas storage within the adsorber
vessel. These changes are caused by:

- o   Pressure change such as depressurization
  and repressurization.

o   Loading changes which are the result of
    changing partial pressures of the impurities
    within the system.

o   Temperature changes within the adsorbers
    caused by expansion or contraction of gas
    during pressure changes, and the heat of
    adsorption and desorption.

o   Movement of the mass-transfer fronts in each
    adsorber as a result of changes in pressure,
    loading (i.e., movement along the isotherms),
    temperature, flow direction and volumetric
    flow.

o   Changes in composition of the gas entering
    and leaving each adsorber, caused by items
    mentioned above.

When dealing with seven to ten, or more, adsorb-
ers and additional intermediate pressure levels, as
well as the dynamic behavior of the adsorbent system
itself, the process must also be subjected to more
sophisticated control than when dealing with four or
fewer adsorber beds and only one or two intermediate
pressure levels.

Process Description

The POLYBED PSA hydrogen system uses five or more
adsorbers in a staggered sequence. Several adsorbers
are on adsorption steps at any time while the others
are in various stages of regeneration. The different
cycle steps which an adsorber experiences during one
complete cycle are summarized below and in Table I.

Adsorption

The feed gas enters the adsorber at relatively
high pressure (typically 250 to 600 psig). All impur-
ities are selectively adsorbed and purified hydrogen
product is delivered at about 5 psi less than feed
pressure. The adsorption step is terminated when the
mass transfer front reaches a predetermined point in
the bed.

Hydrogen Recovery Steps

The adsorber is depressurized in stages to recov-
er hydrogen from the void spaces in the bed. Purity
of the hydrogen taken from the bed during these steps
is maintained. This is achieved by controlling the

TABLE I

CYCLE STEPS

Steps	Functions
Adsorption	Trap impurities
Hydrogen Recovery Stages	Recover H_2 stored in the adsorbent bed to pressurize and purge other adsorbers.
Blowdown	Desorb impurity.
Regeneration	Purge impurities from adsorbent and restore pressure in vessel prior to adsorption step.

depressurizations to keep the impurity front within the bed at all times. The control system routes the gas to other adsorbers for repressurization and purging.

Blowdown

A final controlled depressurization occurs in which the vessel is brought to its lowest pressure. Impurities are desorbed and removed to some extent.

Regeneration

The adsorber is purged at tail gas pressure with hydrogen recovered from other adsorbers. The gas desorbs impurities from the adsorbent and flows out the tail gas line. The impurity front is returned to the feed end of the adsorbent bed. The tail gas can be used as fuel or for subsequent processing.

Recovered hydrogen from other adsorbers is used to repressurize the vessel in several stages to intermediate levels. Some product gas is introduced to complete the repressurization.

This sequence of steps completes one cycle on an adsorber. After the repressurization is completed, the adsorber is again switched to the adsorption step and the sequence is repeated.

Integration of Process Steps

As was mentioned before, several of the adsorbers in a POLYBED system are on adsorption steps at any time. However, the sequencing is staggered so that the adsorbers are in different phases of their adsorption steps. For example, as a bed begins its adsorption step, one of the others could be one-quarter to one-half of the way through its adsorption step. Still another adsorber could be one-half to three-quarters through adsorption. The remaining vessels are in various stages of hydrogen recovery or regeneration.

The integrated sequencing provides the opportunities for more efficient hydrogen recovery through extra steps compared to traditional PSA cycles. Improvements of better than ten percentage points have been realized (2). Adsorbent utilization is improved so that productivity, i.e., hydrogen produced per mass unit adsorbent, increased by 10 to 20%.

The sophisticated sequencing and the requirements for control of the transfer of gas streams among the adsorbers presented a challenge in control system design. Through use of solid state programmable hardware

and modern pressure control techniques, highly effici-
ent and reliable control systems were implemented (2,3).

Conventional Hydrogen Production Using Liquid Absorption Purification

A review of conventional hydrogen production via
steam reforming is useful to appreciate the advantages
of the POLYBED PSA system. The conventional system
consists of a feed desulfurizer, reforming furnace,
high-temperature and low-temperature shift converters,
CO_2 removal system and a methanator (see Figure 2).
The operation of the reforming section is dependent on
the degree of CO conversion in the shift converters
and the extent of CO_2 removal from the hydrogen stream.
Less CO conversion and CO_2 removal result in greater
hydrogen losses in the methanator. In turn, a greater
steam-to-carbon ratio is required in the reformer to
maintain a product purity of 97% hydrogen. Generally,
the hydrogen purity attainable by conventional systems
is 97-98%.

Although the reformer catalyst tends to be rugged
and reliable, the catalyst in the low-temperature shift
converter and the methanator tends to be less so. In
addition, the potential exists for temperature excur-
sions in the methanator in the event of CO_2 breakthrough
from the wash system. The CO_2 removal system requires
a significant heat input and a corrosive solvent, which
can present difficulties.

"Conventional" technology is therefore character-
ized by:

o   Hydrogen recoveries of 90-95%.

o H_2 purity limited to 97-98%.

o   Complex flow scheme for impurity removal.

o   Wet processing, using corrosive solvent
     which may present handling and operational
     problems.

Integration into Hydrogen Plant

The POLYBED PSA system replaces several of the
units associated with hydrogen purification in a con-
ventional plant -- specifically, the low temperature
shift converter, the CO_2 removal system and the methan-
ator (see Figure 2). The tail gas from the PSA system
is used as fuel to the reformer and it is supplemented
by an external supply. However, the amount of fuel
consumed is greatly reduced. Because some hydrogen
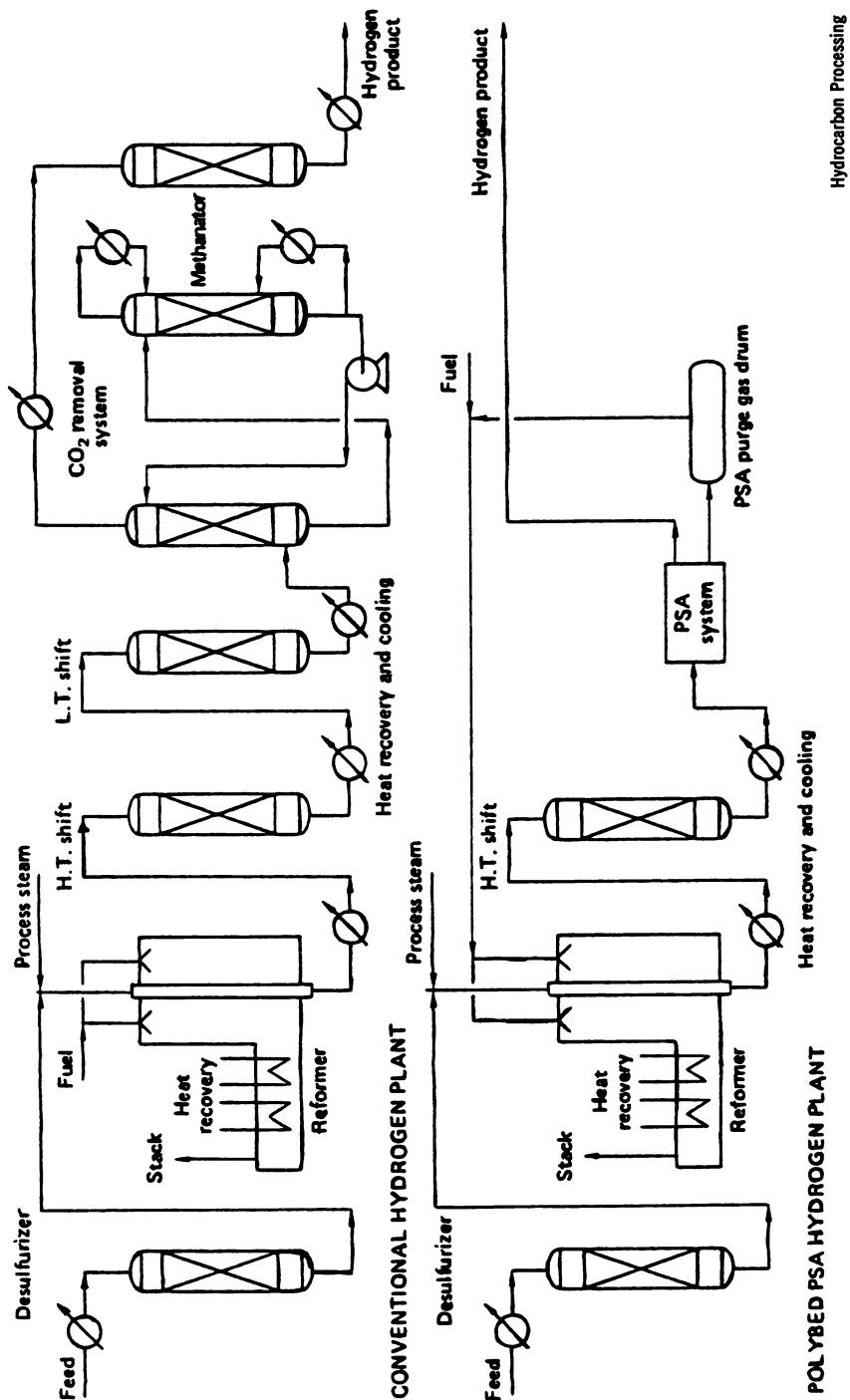
Figure 2.   Conventional and PSA steam reformer hydrogen plants

is lost to fuel through the tail gas of the POLYBED PSA
unit, more hydrogen must be produced in the reforming
section. This increases the feed requirement and the
size of the furnace. Off-setting this disadvantage
is a more efficient heat recovery with the net effect
that the overall hydrogen production costs, both oper-
ating and capital, are less than those of a convention-
al plant (1).
    One of the major technical problems that had to
be overcome to integrate the POLYBED system with the
steam reformer was the variation in tail gas flow and
composition. Because of the cyclic nature of the pro-
cess, tail gas is rejected by the POLYBED unit during
blowdown and purge with significant flow and composi-
tion variations. The fluctuations would have made it
impossible to use the tail gas for fuel and a sophis-
ticated system was developed to balance tail gas heat-
ing value. This buffer/mixing tank system has proven
to be very reliable in holding heat input variation
to ± 1% (2).

Commercial Operation

    The first commercial unit went on stream at Win-
tershall AG's Refinery in Lingen, West Germany in
August 1977. It produces 41 MMSCFD of 99.999% purity
hydrogen at a recovery of 86%. This is 3% above design
and lowers the costs for feed and utilities by 2% com-
pared to previously published comparisons.
    Both flexibility and reliability are enhanced by
an additional feature of the system: the two sections
of five adsorbers can be decoupled to permit operation
on a single train of five beds. This allows hydrogen
production to continue at some reduced level if a pro-
blem occurs with part of the unit. When operating in
this mode, the Wintershall plant has produced between
50-60% of the full design product flow for ten-bed
operation. Very good recovery has been realized in
this mode as well (2).
    The first domestic hydrogen plant utilizing POLY-
BED PSA was recently brought onstream at Ashtabula,
Ohio for Union Carbide's Linde Division. The system
is designed to produce 9 MMSCFD of hydrogen. The pur-
ity is 99.9999% since only 1 ppm total impurities can
be tolerated in a liquefaction system downstream of the
POLYBED unit. Several other hydrogen plants which in-
tegrate steam reforming with POLYBED PSA are in various
stages of design and construction (3).

Other Applications of the POLYBED PSA Concept

The applicability of POLYBED is not restricted to steam reforming hydrogen plants. The advantages of high capacity, high recovery and high purity make the concept suitable for economic purification of hydrogen from a variety of process streams. Other applications include:

o   Refinery H_2 Upgrading - substitute for cryo-
      genic processing (an energy-intensive process).

o   Ammonia Loop Vent Streams - hydrogen or a
      hydrogen/nitrogen mixture can be recovered
      while rejecting inerts.

o   Ethylene Plant Off-Gas - H_2 can be recovered
      from streams containing C_2's and other hydro-
      carbons.

o   Coal Gasification/Liquefaction - the sizes of
      even demonstration plants require large-scale,
      efficient hydrogen recovery/purification.

o   Partial oxidation systems.

o   Methanol Purge.

o   Coke Oven Gases.

Environmental Considerations

The POLYBED PSA system is clean and non-polluting. The only materials leaving the unit are product and a tail gas which is used for fuel or subsequent process-ing. The system requires no water, combustion air, or fuel, and discharges nothing to the atmosphere. Exist-ing commercial units are distinguished by their clean appearance and freedom from odor and corrosion problems.

Conclusion

The development and commercialization of the POLYBED PSA system opens the door to a new generation of applications in gas processing. High volume, high recovery and high purity can all be provided with a single unit. The development effort required an in-depth understanding of the theory and practical oper-ating constraints of adsorption systems as a basis for innovative design. The successful commercialization resulted from the application of basic chemical engineer-ing concepts and implementation of modern control tech-nology. In recognition of the development of POLYBED PSA, Union Carbide received an honors award from the

Kirkpatrick Award Committee and Chemical Engineering
Magazine in December 1979 (4).

Literature Cited

(1)   Heck, J. L., and Johansen, T., "Process Improves
       Large Scale Hydrogen Production", Hydrocarbon
       Processing, January 1978, pp. 175-179.

(2)   Corr, F., Dropp, F., and Rudelstorfer, E., "PSA
       Produces Low-Cost High-Purity H$_2$", Hydrocarbon
       Processing, March 1979, pp. 119-122.

(3)   Heck, J. L., "A Report on the Performance of
       the First 'POLYBED' PSA Unit Operating in the
       United States", Oil and Gas Journal,
       February 11, 1980, pp. 122-130.

(4)   Chemical Engineering, December 3, 1979, pp. 90-91.

Separation of Hydrogen Sulfide–Hydrogen Mixtures by Heatless Adsorption

M. D. WHITLEY[1] and C. E. HAMRIN, JR.

Department of Chemical Engineering and Institute for Mining and Minerals Research, University of Kentucky, Lexington, KY 40506

Many processes have been developed for the removal of hydrogen sulfide from gas streams. They can be classified as liquid absorption, liquid oxidation, dry oxidation, and adsorption. One of these processes is usually included in a coal gasification or liquefaction flowsheet since the coal sulfur is converted to H_2S and finally elemental sulfur. The Stretford and Townsend direct H_2S to S processes and the Rectisol process followed by a Claus plant are frequently included on coal conversion flowsheets (1). Kohl and Riesenfeld (2) present pertinent details for many commercial processes.

Cyclic adsorption processes such as parametric pumping, cycling zone adsorption and heatless adsorption have received much attention both theoretically and experimentally in the past several years (3). Skarstrom (4) has reviewed applications of heatless adsorption (synonymous with pressure swing adsorption) to air drying, hydrogen purification and air fractionation. Stewart and Hack (5) have presented operating characteristics of pressure swing adsorption systems for reducing impurities in a hydrogen stream from 40 vol percent to 1 ppm. Impurities included ammonia, water, methane, carbon monoxide, carbon dioxide, nitrogen, and several hydrocarbons. In this study heatless adsorption is used to separate hydrogen sulfide-hydrogen mixtures and the experimental results are compared with theoretical models.

Process Description

Heatless adsorption is a cyclical process for the purification of gaseous mixtures by the separation of the gas into two streams. One stream which contains more of the more strongly adsorbable materials is called the purge. The other process stream is called the product stream and contains less of the more-adsorbable components. Pressure reduction during the purging cycle coupled with the use of product purge gas and short cycles allows the process to operate without the use of heat for bed

[1]Current address: Shell Oil Co., New Orleans, LA 70161

regeneration and without an excessive demand for purge volume.
When operated at the proper purge gas fraction with relatively
short cycles, the process can reduce the content of more strongly
held components in the product to exceedingly low levels.

A duo-bed heatless adsorption cycle has been described by
Shendalman and Mitchell (6). The cycle consists of four distinct
steps (Figure 1).

Step 1: Feed gas mixture flows into column 2 while product
         flows out. A portion of this product is passed
         through column 1 at a lower pressure acting as a
         purge.

Step 2: Column 2 originally at feed pressure is reduced to
         a lower pressure (blowdown) while column 1 is
         increased to feed pressure (repressurization).

Step 3: Feed flows into column 1 at high pressure with a
         portion of the product used to purge column 2 at
         reduced pressure.

Step 4: Column 1 undergoes blowdown while column 2 is
         repressurized.

Diagrams showing the pressures, feed, product and purge flow
rates for each column during a cycle are presented by Weaver and
Hamrin (7).

This system has certain characteristics which are not pre-
sent in conventional adsorption processes. A loss in recovery of
material is experienced during both blowdown and purging. The
volume of gas lost during blowdown is dependent on the pressure
differential; the higher the pressure differential the more gas
lost. The length of the cycle time also affects the amount lost
during blowdown. The purge losses depend only on the chosen
purge rate.

Theory

Shendalman and Mitchell (6) have developed an equilibrium
model which assumes that the adsorption isotherm is linear. The
model predicts the limiting product composition for varying oper-
ating conditions as well as the product composition as a function
of cycle number for the initial transient period.

The equation for the product concentration, Y_n^{Pr}, of the more
strongly adsorbed component is

$$Y_n^{Pr} = Y_0^F \left(\frac{P_L}{P_H}\right)^{2nk(1-\epsilon)/[\epsilon+k(1-\epsilon)]} \tag{1}$$

where Y_0^F is the feed concentration of the more strongly adsorbed

component and the subscripts L and H refer to low and high pres-
sure respectively, n is the half cycle number, k is the partition
coefficient, P is the pressure in the column, and ε is the bed
void fraction.

The mass balance model of Weaver and Hamrin (7) was modified
to describe the operation of this system. A series of mass bal-
ances were written around columns 1 and 2 describing the varying
steps in the process. The balances were written with respect to
the more strongly adsorbed component, hydrogen sulfide. Due to
the fact that hydrogen does not adsorb on the molecular sieve,
this makes the expression less complicated and less difficult to
solve than the original model. Details are presented elsewhere
(8).

Experimental Apparatus and Procedure

The experimental system used in this study was modeled after
the heatless adsorber used by Shendalman and Mitchell (6) and
constructed by Weaver and Hamrin (7) for hydrogen isotope separa-
tion (Figure 2).

Two columns of brass tubing having dimensions of 0.94 cm
inside diameter and 87.6 cm length were utilized as the adsorbing
unit. Both columns were packed with Union Carbide Molecular
Sieve Type 4A, 8x12 mesh beads. Molecular Sieve Type 4A is an
alkali metal alumino-silicate containing the sodium form of the
Type A crystal. Column 1 was packed with 38.8 gms of adsorbent
and column 2 with 39.0 grams. The approximate length of the bed
in column 1 was 81.9 cm, and in column 2 it was 82.8 cm. In
order to determine the void fraction of the column, the skeletal
density of the adsorbent was determined by isopropanol displace-
ment in a volumetric flask. The density of the adsorbent was
found to be 1.74 g/cc. Using this value for the density, a void
fraction of 0.61 was calculated for the bed.

Feed from one of two Matheson gas cylinders was directed
into a column and purged out of the other column alternately by
a 4-way solenoid valve which was activated by a cam timer for
runs of 2 minutes and by hand for runs of 6, 12, and 24 minutes.
Operating pressure of 80 psig was maintained by a cylinder regu-
lator and a back pressure regulator. A Masonielan back pressure
regulator was used on the purge line to maintain it at 5 psig.
One feed mixture was 3.01 volume % hydrogen sulfide and the other
6.32 volume % hydrogen sulfide, with the remainder of both being
hydrogen (99.999% minimum purity).

The purge and analysis flowrates were kept constant by dif-
ferential flow controllers used in tandem with Nupro Double Pat-
tern Fine Metering Valves. By varying the position of these
valves it was possible to change the purge and product flowrates.
In doing this the total feed rate was also varied. With the
capacity to vary the purge rate and feed rate by this method, one
can vary the purge to feed ratio. The purge, product, and
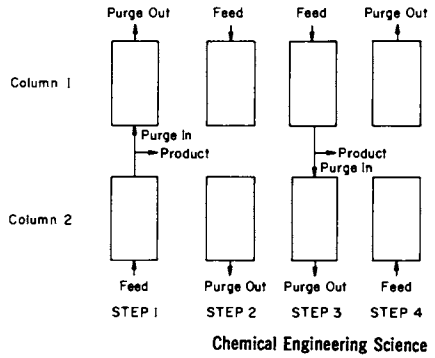
Figure 1. *Steps in heatless adsorption cycle (7)*

Chemical Engineering Science
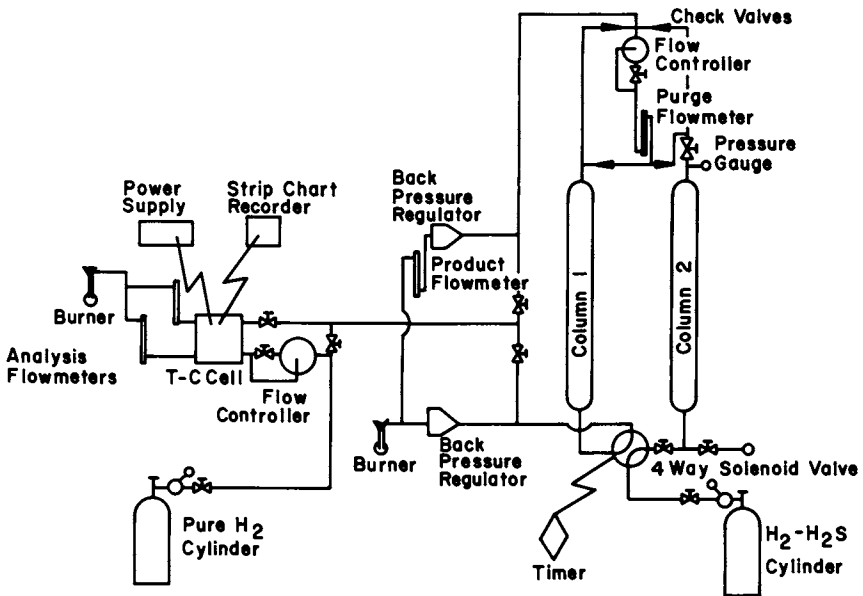
Figure 2. *Schematic of system*

analysis flowrates were measured by flowmeters which were cali-
brated by a bubblemeter and stopwatch. In the tubing above the
columns, four Nupro check valves were employed to prevent the
pressure from equalizing in the two columns. Standard 1/4" brass
tubing was used throughout the system.

For determing the concentration of hydrogen sulfide in the
product gas, a Gow-Mac thermal conductivity cell (Model #10-952)
was used. The cell was equipped with four matched pairs of AuW
filaments, especially used because of their resistance to corro-
sion from the hydrogen sulfide. Layers of styrofoam were used to
insulate the cell from changes in ambient temperature. This
detector was found to be very sensitive to changes in the flow-
rate.

Ultra-high-purity hydrogen (99.999% minimum purity) served
as the zero gas by passing it through the reference side of the
cell. Constant current of 250 ma was directed to the cell by a
Gow-Mac power supply. The resulting signal was amplified and
sent to a Honeywell Electronik 19 stripchart recorder. All the
gases leaving the system were directed to one of two bunsen burn-
ers for safety.

Before making any runs it was necessary to make a calibra-
tion curve for the thermal conductivity cell by measuring the
voltage, $\Delta \upsilon$, output from the cell for a known gas mixture. Be-
fore passing any mixtures through the cell, the zero point was
established. This was done by passing ultra-high-purity hydrogen
through both sides of the cell; zero was then set on the recorder
and a value of $\Delta \upsilon$ was then found for each of the known gas mix-
tures. A plot of $\Delta \upsilon$ versus vol % hydrogen sulfide was found to
be linear in the region under investigation.

Heatless Adsorption Runs. The heatless adsorption runs were
preceded by saturating column 1 with feed at 80 psig and satura-
ting column 2 with feed at 5 psig. In order to warm up the
thermal conductivity cell, ultra-high-purity hydrogen was passed
through the reference side of the cell while the hydrogen sulfide
mixture was passed through the unknown side. Due to the corro-
sive properties of hydrogen sulfide the warm up procedure was
later modified and ultra-high-purity hydrogen was passed through
both sides of the cell. It was then necessary to pass the hydro-
gen sulfide mixture through the cell briefly to allow the cell to
come to equilibrium with the temperature in the columns. A vari-
ety of total flow rates was investigated, ranging from 95 to 435
SCCM. For all runs, 25 SCCM of product was diverted to the ther-
mal conductivity cell. A start-up flow rate of 450 SCCM was used
to expedite the reaching of steady state. This flow rate was
achieved by utilizing the maximum product and purge flow rates
available. Steady state conditions were reached in a time of
approximately 4 hours. The product and purge flow rates were
then corrected to the desired run conditions. A run was then
begun by activating the timer which controlled the position of

the 4-way solenoid valve. This directed the flow into column 2.
The flow was alternately directed into one column while purge was
allowed to escape from the other. This was switched at the end
of every half cycle interval. A continuous read-out of the pro-
duct gas concentration was recorded for the run of generally 30
half cycles.

Breakthrough Runs. For a breakthrough run the columns were
first swept free of the hydrogen sulfide by flowing pure hydrogen
up through the columns. After the gas from the columns had
reached its lowest steady state value of near zero concentration
the flowrates were set for the run and the hydrogen sulfide gas
mixture was passed through the column. A continuous record of
the product gas concentration was made. The run was finished
when the product gas concentration reached the feed concentration.
The time that this required depended upon the feed rate and pres-
sure.

Results and Discussion

Separations of hydrogen sulfide from hydrogen were achieved
in a continuous manner using the heatless adsorption process.
The purge to feed ratio, γ, the cycle time, and total feed rate
were all shown to have an effect on the degree of removal of the
hydrogen sulfide. Seventeen runs were made with a feed gas hav-
ing a composition of 3.01% hydrogen sulfide followed by eight
runs with a 6.32% hydrogen sulfide feed gas. Feed rates from
55 to 435 SCCM were investigated. Cycle times of 2, 3, 6, 12
and 24 minutes were used and purge to feed ratios were varied
from 0.52 to 4.2. All concentrations reported in this discussion
are given in terms of the mole fraction or percent of hydrogen
sulfide in the product stream.
A typical stripchart trace for a run is depicted in Figure
3. The concentration vs. half cycle number for the first 12 half
cycles is given. During the first two half cycles, the largest
amount of separation takes place. The cycling of the concentra-
tion is due to the fact that the two columns did not start at the
same equilibrium loading of hydrogen sulfide. It is believed
that the minimums do not occur at the end of the half cycle due
to holdup in the lines leading to the detector. In all subse-
quent figures, the concentration of hydrogen sulfide was that at
the end of each half cycle.

Effect of Cycle Time on Separation. Figures 4 and 5 show
the effect of varying cycle times for constant feed rates and
purge to feed ratios. From both of the Figures it is apparent
that the concentration of hydrogen sulfide in the product stream
decreases with increasing cycle time. Figure 4 compares runs
with a feed rate of 190 SCCM and a purge to feed ratio of 2.88.
Another set of data for the same cycle times but a purge to feed
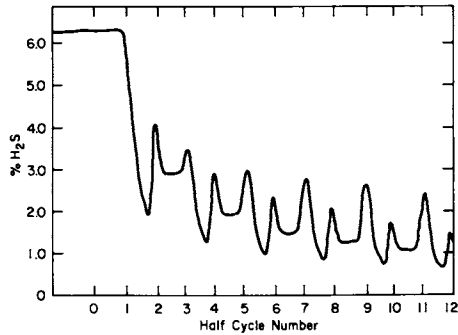
Figure 3. Recorder output (feed rate = 55 SCCM, γ = 2.88, cycle time = 12 min)
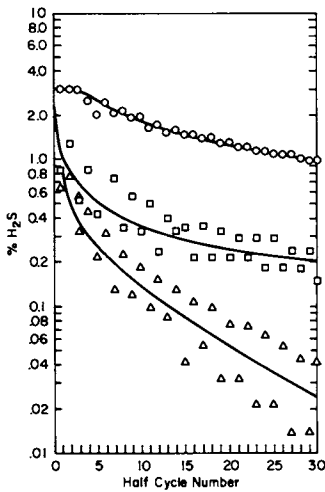
Figure 4. Effect of cycle time on removal of H_2S, constant feed rate of 190 SCCM, and purge/feed ratio of 2.88; cycle times: (○) 2 min, (□) 6 min, and (△) 12 min

Figure 5. Effect of cycle time on removal of H₂S, constant feed rate of 190 SCCM, and purge/feed ratio of 2.88; cycle times: (○) 6 min, (□) 12 min, and (△) 24 min
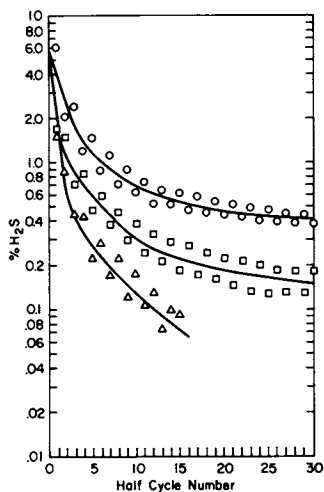
Figure 6. Effect of purge/feed ratio on removal of H₂S, constant feed rate of 190 SCCM, and cycle time of 12 min; γ: (○) 2.38, (△) 2.88, and (□) 4.19
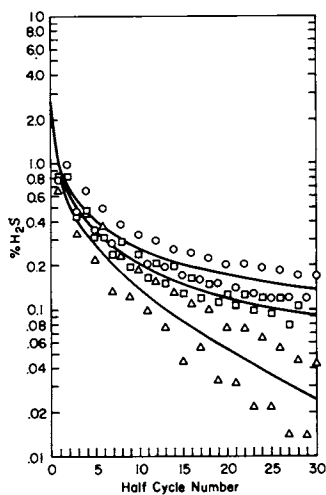
ratio of 4.2 gave identical results for the 6 and 12 minute cycle
times but slightly higher H2S concentration for the longest cycle
time. Figure 5 compares runs with a feed composition at 6.32%
hydrogen sulfide, a feed rate of 190 SCCM, and purge to feed
ratio of 2.88. This plot shows that at higher feed composition
a longer cycle time (24 min) is required to get a hundredfold
reduction in H2S content, whereas for the 3.01% H2S feed only a
12 min cycle time is necessary.

    <u>Effect of Purge/Feed on Separation</u>. The purge to feed ratio
effect is shown in Figure 6 for a cycle time of 12 minutes and
a feed rate of 190 SCCM.
    The results of these runs show that the removal of hydrogen
sulfide goes through a maximum with increasing γ. There is an
apparent optimum value of γ between 2.88 and 4.19, which is much
higher than the value of 1.3 suggested by Skarstrom (<u>4</u>). An-
other series of runs, however, with the higher feed composition
and a 280 SCCM flow rate indicated that γ = 2.88 was not adequate
for good separation.

    <u>Effect of Feed Rate on Separation</u>. The results of runs at
three flow rates varying from 55 to 280 SCCM are compared in
Figure 7 to show the effect of feed rate on the product concen-
tration for a constant γ = 2.88 and cycle time of 12 minutes.
The effect of increasing feed rate is not as marked as changing
the purge to feed ratio or cycle time; however, it is evident
that at the lowest feed rate the product concentration is high-
est in hydrogen sulfide. The overlap of the 190 and 280 SCCM
flow rates shows that there is little if any difference in sepa-
rating capacity at these flows.

    <u>Comparison of Experimental Data and Theoretical Models</u>. The
predictions made by the Shendalman and Mitchell model and the
mass balance model developed in this study are shown in Figure 8.
Only one prediction of the Shendalman-Mitchell model is shown
because of the nature of the equation. The predictions of the
model depend on the feed concentration, void fraction of the bed,
k, the partition coefficient, and the ratio of the purge pressure
to the feed pressure. Since these remain constant for the runs
shown, only one line is predicted, which is much lower than the
experimental values. After only the first half cycle the concen-
tration is predicted as 0.0056%. The lowest experimental concen-
tration measured was 0.014% after 30 half cycles. This over-
prediction was found by Shendalman and Mitchell for the CO_2-He
system and explained as due to phenomena occurring during repres-
surization. No doubt this effect is important in these experi-
ments, but intraparticle diffusion is probably even more signifi-
cant. The Lennard-Jones diameter of H2S is 3.62Å (<u>9</u>) which is
only slightly less than the pore diameter of 4.0Å suggesting the
importance of pore resistance. Further experiments with a larger

Figure 7. Effect of feed rate on the removal of H_2S for constant γ of 2.88 and cycle time of 12 min; feed rates: (○) 55 SCCM, (□) 190 SCCM, and (△) 280 SCCM
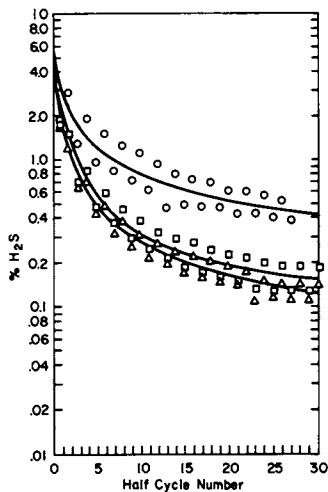
Figure 8. Predictions of (– –·–) Shendalman's model and (———) mass balance model: (○) feed rate = 160 SCCM and γ = 2.4, (□) feed rate = 190 SCCM and γ = 1.0
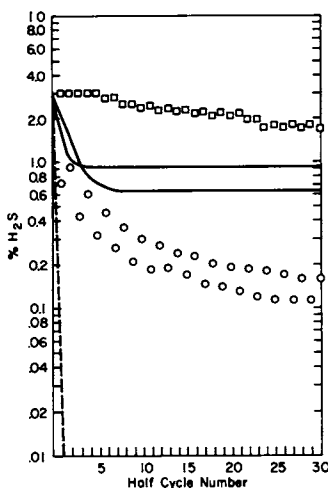
pore adsorbent would help to determine the relative importance of these effects.

Figure 8 also shows the mass balance model predictions for two runs. The mass balance model does a reasonable job of predicting the product concentration for the low cycle time. Here the predicted values are lower than the experimental values, differing by a factor of approximately two. However, for a cycle time of 12 minutes, the prediction falls short of the experimentally determined value. The critical value of γ = 1.0 was used in the model calculations. If 1.3 were used for the purge to feed ratio as suggested by Skarstrom (4), or a value closer to 3 as found in these experiments, the agreement would be slightly better for both runs.

Although the purpose of this investigation was to study the initial transient behavior of heatless adsorption, the best removal of hydrogen sulfide occurred in the run with 3.01% H_2S and a γ = 2.88, cycle time of 12 minutes and feed rate of 190 SCCM. Removal was down to 99.55% in three hours. For the 6.32% feed the best removal for the same time period was 98.49%.

Mitchell and Shendalman (10) discuss the importance of dynamic capacity on the performance of the heatless adsorption system. Dynamic capacity is defined as the product of the space velocity and half cycle duration. Space velocity is expressed in terms of the volumetric feed rate per volume of adsorbent. The units of dynamic capacity thus become the volume fed during saturation per unit volume of the adsorbent. Table 1 shows the effect of dynamic capacity at constant purge to feed ratio and half cycle time. As the dynamic capacity increases from 5.77 to 29.4 V/V/half cycle the minimum hydrogen sulfide content at the 30th half cycle decreases from 0.37% to 0.117% for a γ = 2.88. In all cases it shows that as the dynamic capacity increases, the separation of hydrogen sulfide increases, resulting in lower product concentration. These results are in partial agreement with the findings of Mitchell and Shendalman (10) for the CO_2-He-silica gel system. These authors found the CO_2 concentration decreased initially with an increase in dynamic capacity, but then increased. It is believed the higher value of γ in this study accounts for the lack of a minimum in the range of dynamic capacity investigated.

Breakthrough Runs

Three runs were made to determine the length of time elapsed before the product stream concentration reached that of the feed. One run was made at the start-up feed rate of 450 SCCM to determine if sufficient time had elapsed in start-up for the columns to reach saturation equilibrium conditions. Figure 9 shows that approximately 2 hours was necessary for the columns to reach equilibrium. This confirmed that, indeed, sufficient time had expired, since start-up was approximately 4 hours.

TABLE 1 Effect of Dynamic Capacity at
Constant γ and Half Cycle Time

Dynamic Capacity	Min. H$_2$S in 30th
V/V/1/2 cycle	1/2 cycle, %
3.01% H$_2$S, γ = 0.96-1.05 Half Cycle Time = 1 min.	
2.80	1.52
3.32	1.37
4.37	1.32
3.01% H$_2$S, γ = 2.4 Half Cycle Time = 6 min.	
16.8	0.16
25.2	0.087
6.32% H$_2$S, γ = 2.88 Half Cycle Time = 6 min.	
5.77	0.37
19.9	0.13
29.4	0.117
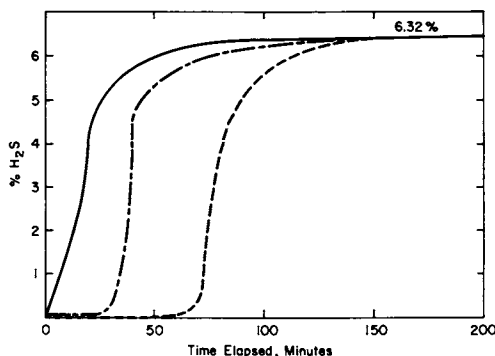
Figure 9. Breakthrough curves: (———) feed rate = 190 SCCM and pressure = 5 psig, (— — —) feed rate = 450 SCCM and pressure = 80 psig, (– – –) feed rate = 190 SCCM and pressure = 80 psig

The most common feed rate in this study is also shown in Figure 9. The feed rate of 190 SCCM at high pressure is shown to take approximately 2.5 hours for the product concentration to reach that of the feed. The low pressure feed takes a shorter time of about 1.5 hours. These runs were conducted after the heatless adsorption runs and indicate no significant deterioration of the adsorbent had occurred during the course of the experiments.

Abstract

Continuous separations of hydrogen sulfide-hydrogen gas mixtures of 3.01% and 6.32% hydrogen sulfide were accomplished in a single-stage, heatless adsorption unit. Removals of 99.6 and 98.5 percent were achieved for the two feeds, respectively, during the initial, transient period of study. The effects of purge to feed ratio, cycle time, and total feed rate were investigated in 25 runs using 4 A molecular sieves as the adsorbent. Comparisons between the experimental results and those predicted by a mass balance model and an equilibrium model were made.

Literature Cited

1.   "International Coal Technology Summary Document", U.S. Dept. of Energy, HCP/P-3885, 1978, pp. 44-45.

2.   Kohl, A.L., and F.C. Riesenfeld, "Gas Purification", McGraw-Hill (1960).

3.   Wankat, D.C., Sep. Sci., (1974) 9, 85.

4.   Skarstrom, C.W., "Heatless Fractionation of Gases Over Solid Adsorbents", in "Recent Developments in Separation Science", Vol. II, Li, N.N., Ed., CRC Press, Cleveland, Ohio, 1972.

5.   Stewart, H.A., and J.L. Heck, Chem. Eng. Progr., (1969), 65, 78,

6.   Shendalman, L.H., and J.E. Mitchell, Chem. Eng. Sci., (1972), 27, 1449.

7.   Weaver, K., and C.E. Hamrin, Jr., Chem. Eng. Sci., (1974), 29, 1873.

8.   Whitley, M.D., "Separation of Hydrogen Sulfide-Hydrogen Mixtures by Heatless Adsorption", MS Thesis, University of Kentucky, 1975.

9. Sherwood, T.K., R.L. Pigford, and C.R. Wilke, "Mass Trans-
    fer", McGraw-Hill (1975).

10. Mitchell, J.E., and L.H. Shendalman, AIChE Symp. Ser., No.
    134, (1973), 69, 25.

A New Process for Adsorption Separation of Gas Streams

GEORGE E. KELLER II and RUSSELL L. JONES

Union Carbide Corporation, Box 8361, South Charleston, WV 25303

Separation of gas streams by adsorption is becoming increasingly popular as improved technology comes on the market. Some examples of commercially practiced adsorption processes are shown in Table 1. These processes take advantage of the selective adsorption properties of a number of microporous adsorbents, including activated carbon, silica, alumina, and various synthetic and natural zeolites.

There are fundamentally two types of gas adsorption processes, which can be differentiated by the way in which adsorbed species are desorbed. In one type the adsorbed species are removed by raising the temperature of the adsorbent, thereby decreasing its capacity. In the second type the partial pressures of the adsorbed species are reduced to effect desorption. Of course a combination of the two desorption techniques can be and is sometimes used. In Figure 1 an isotherm diagram is shown which depicts these desorption techniques.

If the adsorbing material constitutes only a small portion of the feed gas - usually a mole percent or two or less - regeneration of the adsorbent by temperature increase is the preferred mode. However for higher concentrations of adsorbing materials - bulk separations - pressure reduction is the preferred mode of regeneration. The reasons for using a pressure-swing process for bulk separations are (i) adsorption-plus-regeneration times are much shorter (minutes vs. hours to days for temperature-increase) and (ii) the large temperature increases experienced during adsorption are largely cancelled out by the endothermic desorption of the adsorbed material, thereby eliminating large temperature excursions within the bed.

Processes involving total-pressure reduction to remove the adsorbed species, called pressure-swing adsorption (PSA) or heatless adsorption, are mechanically complex, since they must include separate adsorption, depressurization, desorption, and repressurization steps. To accommodate a steady flow of feed and products, several beds - usually three or more in parallel - are used. A typical four-bed process flowsheet is shown in

TABLE 1

IMPORTANT COMMERCIAL ADSORPTIVE GAS SEPARATIONS

Material Adsorbed	Process Stream
Ammonia	Cracked Ammonia, Reformer Hydrogen
Carbon Dioxide	Ethylene, Air, Inert Atmospheres, Flue Gas
Carbon Monoxide	Hydrogen
Gasoline Components	Natural Gas
Hydrogen Sulfide	Natural Gas, Reformer Hydrogen
Iso-olefins	Normal Olefins
Krypton	Hydrogen
Mercaptans	Propane
Mercury	Hydrogen
Methane	Hydrogen
Nitrogen	Hydrogen, Air
Nitrogen Oxides	Nitrogen, Air
Normal Paraffins	Kerosine, Gasoline
Oil Vapor	Compressed Gases
Oxygen	Argon
Sulfur Dioxide	Vent Streams
Water	Acetylene, Air, Argon, Carbon Dioxide, Chlorine, Cracked Gas, Ethylene, Helium, Hydrogen, Hydrogen Chloride, Hydrogen Sulfide, Natural Gas, Nitrogen, Oxygen, Reformer Hydrogen, Sulfur Hexafluoride

Figure 2. An additional problem is the fact that only one highly purified (less-adsorbed) product can be produced, since part of this product is used to purge the more tightly adsorbed product and is lost with that product.

   Despite these problems, PSA is often used for oxygen and hydrogen purification, and a recent runner-up Kirkpatrick Award for Union Carbide's Polybed hydrogen process (1) attests to the fact that it is now both practical and economical to perform bulk separations on feed streams in excess of one million cubic feet per hour.

   The objectives of the present study were to decrease the basic complexity of PSA and to increase its productivity - the amount of product produced per unit time per unit weight of adsorbent. Success in both of these areas should further enhance process economics and increase the potential application for pressure-swing-adsorption-based processes.

   The new process is called either pressure-swing parametric pumping or rapid pressure-swing adsorption; the former name will be used here. The name parametric pumping was coined by Wilhelm (2), who described an adsorption-based separation process involving reversing flows. When the flow is in one direction a parameter, such as temperature, which influences adsorptivity, is at one value, while the parameter is changed to another value when the flow is in the opposite direction. Such a process will create a separation between components with different adsorp-tivities. Chen (3) has correctly pointed out that pressure-swing adsorption processes consitute a subset of parametric pumping, in which pressure is the parameter used to influence adsorptivity.

Process Description

   This section outlines the basic pressure-swing parametric pumping process, which will be described below in the context of oxygen production from air. The preferred adsorbent for this separation can be either 5A or 13X zeolite.

   Flowsheet. A schematic diagram is shown in Figure 3. The process consists of a single bed of relatively small adsorbent particles (40 to 80 mesh, or 177 to 420 microns, for example). The bed length can vary from about one to four or more feet. Feed gas is supplied in pulses of up to about a second in length from a compressor and a surge tank. The pulse is controlled by a solenoid valve and a timer. During this feed pulse the exhaust solenoid valve is closed. Following the feed pulse both valves at the feed end are closed for about 0.5 to three seconds; this period is called the delay. Finally the solenoid valve on the exhaust or purge line opens for a period of about five to 20 seconds. Since the pressure in this line is maintained below that in the feed line, a reverse flow of gas from the bed occurs.

   However, while pressures and flow directions are fluctuating substantially at the feed end of the bed, a continuous flow
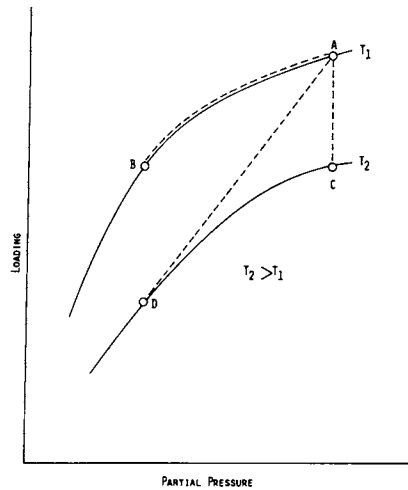
Figure 1.   Typical loading vs. partial
            pressure curves
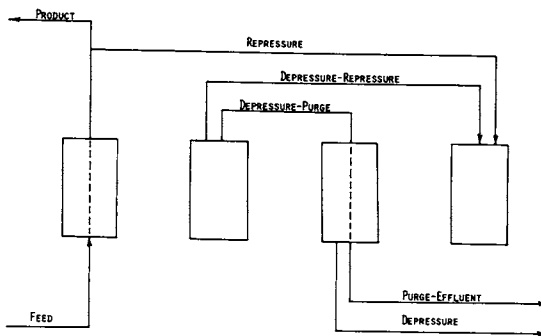
Figure 2.   Pressure-swing adsorption system using four beds

emerges from the product end and through a small surge tank.
This flow is enriched in less tightly adsorbed components; in the
case of air separation, the product consists typically of 90 to
95 percent oxygen, with the balance argon and a small amount of
nitrogen. Conversely the exhaust stream is somewhat depleted in
oxygen and argon.

     The net effect of this process is to produce, using a single
adsorbing bed and two surge tanks, a constant flow of less tightly
adsorbed product - primarily oxygen in this case - from a constant
flow of air from a compressor.

     <u>Adsorbent</u>. Standard 5A and 13X zeolite can be used in
pressure-swing parametric pumping to produce enriched oxygen.
However, it is essential that the adsorbent be finely divided,
and in the case of oxygen production, about a 40 to 80 mesh
particle size is optimal. (The reasons for using small particles
will be discussed later.) Such a material can be produced by
crushing and screening the pellets, spheres, etc., normally used
in other adsorption processes. Following this procedure, the
zeolite particles are activated at the same conditions as would
be used for regular-size particle activation and are then packed
in the adsorbent bed.

     A major potential problem with the use of such small
particles is fluidization of the adsorbent following opening of
the exhaust valve and reversal of the gas flow in the bed.
Fluidization of the bed under the pressure gradients developed
causes rapid particle attrition, attendant loss of adsorbent
through the restraining screens, and cessation of separating
ability. Fluidization can be prevented by applying a sufficient
force to the upper hold-down plate, e.g., by use of a spring or
a hydraulically balanced floating head. Efficient pre-settling
of the adsorbent particles while packing the bed will also tend
to prevent fluidization later, as the bed is subjected to
repeated pressure fluctuations.

     An important feature of the adsorbent bed in this process is
its ability to accept a water-saturated feed without displaying
any tendency for the zeolite to become deactivated by water
adsorption. The reverse flow of gas during the exhaust part of
the cycle stabilizes the water penetration to no more than about
one-fourth to one-half inch from the top of the bed. As a result,
no need exists for pre-drying the feed air or supplying a
desiccant at the inlet to the bed.

Process Performance

     The key feature of pressure-swing parametric pumping is the
unusual pressure versus distance and time feature of the bed.
In PSA, pressure drop is purposely minimized, so that, although
the pressure within a bed changes substantially during a cycle,
the pressures at various points in a bed at a given time are
virtually the same. In pressure-swing parametric pumping, large
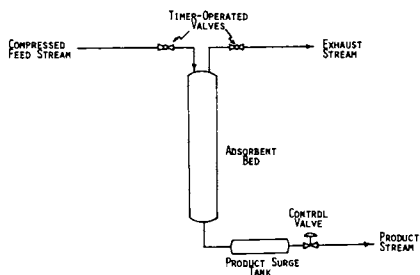
Figure 3.   Schematic of pressure-swing parametric pump
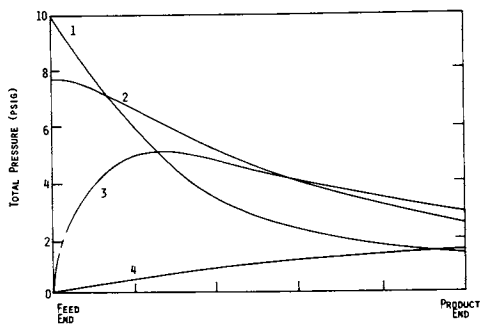
Figure 4.   Pressure profiles in an adsorbent bed producing 90 mol % oxygen:
1, middle of feed; 2, middle of delay; 3, early in exhaust; 4, late in exhaust

pressure differences are developed in the bed during the cycle; this can be seen by reference to Figure 4. The curves in this Figure were obtained from a bed equipped with a number of fast-response pressure transducers along its length. The feed pressure was 10 psig and the exhaust pressure 0 psig.

During the feed period (which lasts about one second or less), a large pressure gradient develops (see curve 1) as feed gas rushes into the bed. If the feed period were extended much longer, it would not be possible to produce the desired 90+ per-cent oxygen product. Following the feed period, the delay period (curve 2) permits the pressure wave to penetrate further into the bed without overloading the bed with extra feed. The slope of the pressure curve is essentially zero at the feed end of the bed, attesting to the fact that no gas entering or leaving this end. Part of the time during the exhaust period, gas actually flows simultaneously toward both ends of the bed (curve 3) from a pressure maximum. As the exhaust period continues, the pressure maximum both declines and moves toward the product end, so that near the end of the exhaust period the maximum is essentially at the product end. Thus, all parts of the bed ultimately are subjected to the reverse flow necessary to purge adsorbed nitrogen. The fact that the purge gas for regenerating the adsorbent comes from the bed itself constitutes a major difference between this process and PSA, in which purge gas comes primarily from another bed.

The pressure at the product end fluctuates about two psi; the amount of this fluctuation can be controlled to some extent by the size of the product surge tank and the length of the exhaust part of the cycle. This surge tank permits a constant product flow to be maintained in spite of these small fluctuations.

The small adsorbent particles are obviously responsible for the substantial pressure gradients in the bed. The use of larger particles in the same bed results in decreased separating ability, i.e., the high degree of separation cannot be maintained at the same productivity. Extending the length of the bed in combina-tion with the use of larger particles (to maintain the same overall flow restance) also results in a deteriorating produc-tivity and eventually in the inability to make high-purity product. The larger particles have larger intra-particle resis-tances, and these larger resistances may become an important factor in bed performance with the fast cycle times used in pressure-swing parametric pumping.

Using particles substantially smaller than about 40 to 80 mesh leads to too large a flow resistance, and productivity drops. Thus, an optimal particle size exists, and in general this will lie in the range of 20 to 120 mesh.

In Figure 5 are shown the concentration profiles of oxygen in the gas phase during various times in the cycle. These curves were obtained from the same bed as the one used for the pressure data. As would be expected, the S-shaped curve moves toward the
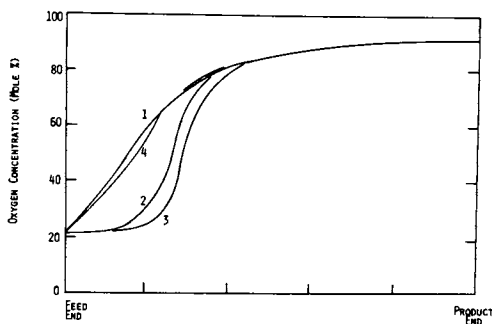
*Figure 5. Concentration profiles in an adsorbent bed producing 90 mol % oxygen:
1, middle of feed; 2, middle of delay; 3, early in exhaust; 4, late in exhaust*

*Figure 6.   Effect of feed pressure on
productivity and recovery for producing
a 98 mol % hydrogen stream from a
33/67 mol ratio methane/hydrogen feed:
bed length, 4 ft; exhaust pressure, 0 psig;
temperature, ambient; adsorbent, 30/60
to 40/80 mesh activated carbon; cycle,
0.5 sec feed—1.0 sec delay—5.0 sec
exhaust*
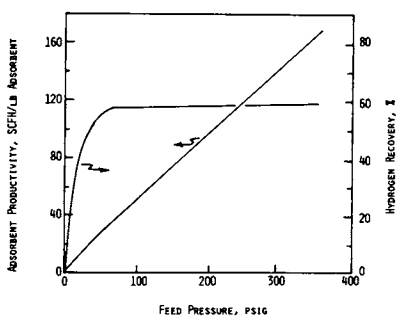
product end during the feed and delay periods, and then toward
the feed end during the exhaust period.

The net effect of the pressure and concentration profiles
is to produce a high-productivity, simple process. In Table 2
is shown a comparison of performance between PSA and pressure-
swing parametric pumping. Most notable is the four-to-five-fold
increase in productivity for the latter over the former. This
increase is achieved with a fundamentally simpler process and
only a slightly higher power input per cubic foot of product.
(Higher power input is related to higher air supply pressure
and lower oxygen recovery.)

A second example of separation performance is shown in
Figure 6. The feed mixture was a one-to-two mol ratio of
methane to hydrogen, which is typical of the composition of the
light fraction from steam-cracking of a mixture of ethane and
propane. The product was 98 mol percent hydrogen, and the
Figure shows the effect of varying the feed pressure to the
column. Productivity was found to increase almost linearly with
feed pressure, and values reached at the upper range were very
high. Thus, at a feed pressure of 350 psig, a column with a
cross-sectional area of one square-foot could produce about
25,000 standard cubic feet per hour of 98 percent hydrogen.
Hydrogen recovery, on the other hand, reached a value of slightly
less than 60 percent at a feed pressure of 50 psig and remained
virtually constant at higher pressures.

Prior Literature

Although pressure-swing parametric pumping is quite
different from the more traditional temperature-swing parametric
pumping first promulgated by Wilhelm (2), there is some prece-
dent in the literature for this type of operation. Turnock (4),
Turnock and Kadlec (5), Kowler (6) and Kowler and Kadlec (7,8)
studied a similar pressure-swing device for separating nitrogen
and methane. However, they were unable to solve the problem of
long-term mechanical stability of the adsorbent, and the time
cycles used were substantially different than those suggested
here. Their cycles limited both adsorbent productivity and
product recovery. The preferred cycles for pressure-swing
parametric pumping are the subject of a recent patent application
(9).

Applications of Pressure-Swing Parametric Pumping

Pressure-swing parametric pumping would seem to have many
applications for separation of from very small to quite large
gas streams. One area of promise is the production of oxygen
from air. Union Carbide is currently marketing a small device
for producing up to about six liters per minute of 90+ percent
oxygen for medical use in homes. This device actually contains

TABLE 2

COMPARISON OF PRESSURE-SWING ADSORPTION AND PRESSURE-SWING

PARAMETRIC PUMPING FOR PRODUCTION OF OXYGEN FROM AIR

	Pressure-Swing Adsorption	Pressure-Swing Parametric Pumping
Number of Adsorbent Beds	3	1
Supply Pressure (psig)	45	50
Adsorbent Bed Length (ft)	6-10	3-4
Adsorbent Particle Size	1/16 inch pellets	40-80 mesh granules
Pressure Cycle Length	3-4 minutes	18.5 seconds
Exhaust Pressure (psig)	0	0
Product Pressure (psig)	2-5	2-5
Product Purity (Mol % Oxygen)	90	90
Oxygen Recovery, %	40	38
Adsorbent Productivity (Ton 100% Oxygen/Ton Adsorbent)	0.5	2.3

three small beds in parallel, eliminating surge tanks by proper
sequencing of the bed time cycles. Pressure-swing parametric
pumping can also be used to produce oxygen in up to tonnage
quantities for hospitals, welding units, waste-water treatment,
etc.

    Many other applications exist for separation of various
chemical and refinery streams. For instance, Union Carbide has
demonstrated on a pilot scale the feasibility of producing
hydrogen, as shown in Figure 6, from both high- and low-pressure
hydrogen-methane and hydrogen-carbon monoxide streams. Another
major area of application is the removal of organics from vent
and other waste gas streams. A commercial unit has been in
operation for over a year at Union Carbide's Texas City, TX,
plant, processing a stream containing primarily nitrogen and
ethylene. An enriched nitrogen "product" is vented from the
process, while an enriched ethylene stream - the exhaust - is
recycled to the process. Two other pilot plants are in operation
making other separations of importance.

    A major concern regarding the use of this technology under
such rapidly fluctuating pressures is the stability of the
adsorbent. Long-term testing of several types of synthetic
zeolites and activated carbon in bench-scale, large-pilot-scale,
and commercial units has demonstrated that adsorbent lifetimes
of well over one year are to be expected in most applications.

Summary

    Pressure-swing parametric pumping is a recently commercial-
ized, simple, pressure-swing adsorption process. Compared to
standard PSA, pressure-swing parametric pumping accomplishes all
of the four basic operations - pressurization, adsorption,
depressurization and desorption - in a single bed in such a way
that a continuous flow of less tightly adsorbed product is
produced. With the aid of a surge tank on the feed line, the
process also accepts a constant feed flow. The overall cycle time
is in the order of about 20 seconds or less, compared to several
minutes for PSA.

    The adsorbent particles in pressure-swing parametric pumping
are substantially smaller than those in PSA and produce rapidly
fluctuating pressure profiles in the bed during a cycle. These
profiles and the cycle times which influence them are responsible
for the continuous product flow, the high productivities and the
high product purities which can be attained in the process.

    The process is capable of performing a number of commer-
cially important separations, using a wide range of adsorbents.
For oxygen production from air, either 5A or 13X zeolite can be
used as the adsorbent. Particle sizes are in the range of 40 to
80 mesh, and oxygen productivity is about five times that of PSA
for similar feed pressures.

Literature Cited

1. Corr, F.; Dropp, F.; Rutelstorfer, E., Hydrocarbon Processing, 1979, 58, 119.
2. Wilhelm, R. H., Ind. Eng. Chem. Fund., 1966, 5, 141.
3. Chen, H. T., "Parametric Pumping"; in Schweitzer, P. A., Ed., "Handbook of Separation Techniques for Chemical Engineers"; McGraw-Hill: New York, N. Y., 1979; p. 1-467.
4. Turnock, P. H., "The Separation of Nitrogen and Methane by Pulsating Flow Through a Fixed, Molecular Sieve Bed"; Ph.D. Thesis, Univ. of Michigan, Dept. of Chemical and Metallur-gical Engineering: Ann Arbor, MI, 1968.
5. Turnock, P. H.; Kadlec, R. H., A.I.Ch.E.J., 1971, 17, 335.
6. Kowler, D. E., "Optimization of the Cyclic Operation of a Molecular Sieve Adsorber"; Ph.D. Thesis, Univ. of Michigan, Dept. of Chemical and Metallurgical Engineering: Ann Arbor, MI, 1969.
7. Kowler, D. E.; Kadlec, R. H., A.I.Ch.E.J., 1972, 18, 1207.
8. Kowler, D. E.; Kadlec, R. H., A.I.Ch.E.J., 1972, 18, 1212.
9. Jones, R. L.; Keller, G. E.; Wells, R. C., U. S. and foreign patents applied for.

INDEX

Ion
  –dipole energy 8
  energies, Cu(II) 172
  exchange
    ammonium 177–178
    cesium 133
    copper(II) 178
    isotherms 197
    mass transfer for 211
    of zeolite Na-A,Cd 187–198
    of zeolite Na-A,Pb 187–198
  –quadrupole energy 8
Ionic radius
  barium 144
    crystal 137
  copper(II) 182
  ammonium 184
  sodium 144
Isomers, separation of aromatic 132–133
Isoparaffins separation from
  aromatics 130
Isosteric heats of sorption 116–120
Isotherm(s)
  adsorption 207, 262
    for *p*-bromophenol 31*f*
    for dodecyl benzene sulfonate 32*f*
    for phenol 31*f*
    for *p*-toluene sulfonate 32*f*
  binary 63
    equation 57
  cadmium ion-exchange 190
  constants 33*t*
  Freundlich 30
  ion-exchange 197
    lead 188–190
  Langmuir 30, 34
  single solute 28
  sorption 56–57
    equilibrium 75
    nitrogen 111*f*
Isotropic refinement 140
Isotropic thermal ellipsoids 150

J

Jahn–Teller
  coupling constant 165–166
  distortion 162, 166–167, 172
  spin orbit splitting 164*f*

K

Ketone-dewaxed oil, chromatogram .. 243*f*
Ketone dewaxing 240–242, 243*f*
Krypton
  mixture equilibria of methane and 55–70
  sorption 60–70

L

Langmuir
  isotherm 30, 34
  model 113
    binary 66
  parameters 115*t*
Laser, pulsed nitrogen 159
Lattice solution sites 11, 17, 19
Lattice theory of solutions 3–6
Lead ion exchange of zeolite Na-A 187–198
Least-squares refinement 144
Lennard–Jones diameter of H_2S 269
Lennard–Jones potential 10
  equation 7
Linear regression 113, 116
Liquid absorption purification,
  hydrogen production 255
Liquid phase
  drying 201–219
  equilibrium sorption 130–131
  sorption, competitive 131–132
Lithium cation, geometric
  arrangement 13*f*
Loading(s)
  impurity 251–252
  and partial pressure 278*f*
  ratio correlation 75–76, 89*f*
  stoichiometric 89*f*
  of supercritical gas 222
  zeolite 235, 236*f*
Localized adsorption 4
Luminescence
  decay curve 160*f*
  decay time 159
  intensity and decay lifetime 163*f*
  spectrometer 157–159

M

Macropores, surface diffusion 82–84
Mass
  balance equation 76
  balance model 269–271
  transfer
    coefficient 29, 35–38,
                                        82–84, 98, 99*f*
      for dodecyl benzene sulfonate   49
      for phenol 49
    data, correlation 90*f*, 94*f*, 96*f*, 98*f*
    equations 76–77
    fronts 248, 252
    for ion exchange 211
    packed bed breakthrough
      method 74
    rate 28
    resistance(s) 73, 75, 95
Matrix diagonalization 172